UC San Diego
UC San Diego Electronic Theses and Dissertations

Title

Cyclic (alkyl)(amino)carbenes: from Replacing Metals to Metal Replacement

Permalink

https://escholarship.org/uc/item/6rr51823

Author

Peltier, Jesse Lawrence

Publication Date

2020

Peer reviewed|Thesis/dissertation

UNIVERSITY OF CALIFORNIA SAN DIEGO

Cyclic (alkyl)(amino)carbenes: from Replacing Metals to Metal Replacement

A dissertation submitted in partial satisfaction of the requirements for the degree of
Doctor of Philosophy

in

Chemistry

by

Jesse Lawrence Peltier

Committee in charge:

       Professor Guy Bertrand, Chair
       Professor Adah Almutairi
       Professor Seth M. Cohen
       Professor Michael K. Gilson
       Professor Arnold L. Rheingold

2020

The dissertation of Jesse Lawrence Peltier is approved, and it is acceptable in quality and form for publication on microfilm and electronically:

_____

_____

_____

_____

_____

Chair

University of California San Diego
2020

iii

DEDICATION

This dissertation is dedicated first and foremost to my fiancée, Cassi Pinion, whose enduring love, patience, and support gave me the strength to overcome many challenging times throughout my academic career. My fondest memories are those spent with her. She is truly my best friend and partner in crime.

Next, my Mom and Dad who always stressed the importance of an education, persevering, and reciprocity. Every time I look in the mirror, I see them. Although I was far away, they were always with me in lab. This success is as much theirs as it is mine. Last but certainly not least, my relatives, ancestors and tribes, Turtle Mountain Anishinaabe and White Bear Nakoda, whose survivance is the reason I have had many opportunities in this life. It is on their shoulders that I stand.

TABLE OF CONTENTS

LIST OF ABBREVIATIONS

ACN: Acetonitrile

Ad: Adamantyl

AGR: Anti-galvanic replacement

aNHC: Abnormal N-heterocyclic carbene

Ar: Aromatic

BAr^F: Tetrakis(perfluorophenyl)borate

BCF: Tris(pentafluorophenyl)borane

BICAAC: Bicyclic (alkyl)(amino)carbene

$B_2(Neop)_2$: Bis(neopentyl-glycolato)diboron

CAAC: Cyclic (alkyl)(amino)carbene

COD: 1,5-Cyclooctadiene

CzCN: 3,5-Dicyano-9-H-carbazole

CzOMe: 3,5-Dimethoxy-9-H-carbazole

Cp: Cyclopentadienyl

CV: Cyclic Voltammetry

Cz: Carbazole

DAC: N,N'-diamidocarbene

DCM: Dichloromethane

DFT: Density functional theory

Dipp: 2,6-Diisopropylphenyl

DMF: Dimethylformamide

DTE: Dithienylethene

e: electron

E_a: Activation energy

ELF: Electron Localization Function

EML: Emissive layer

ENHC: Ender's N-heterocyclic carbene

EQE_{max}: maximum external quantum efficiency

Equiv.: Equivalent

Et: Ethyl

ETL: Electron transport layer

EtOH: Ethanol

HBPin: Pinacol borane

HOMO: Highest occupied molecular orbital

HR-MS: High resolution mass spectrometry

ICT: Interligand charge transter

*i*Pr: Isopropyl

IPr: 1,3-Bis(2,6-diisopropylphenyl)-1,3-dihydro-2H-imidazol-2-ylidene

IPr*: 1,3-bBs(2,6-bis(diphenylmethyl)-4-methylphenyl)imidazo-2-ylidene

ir: Irreversible

ISC: Intersystem Crossing

k_{nr}: Rate of nonradiative decay

k_r: Rate of radiative decay

LLCT: Ligand-to-ligand charge transfer

LUMO: Lowest unoccupied molecular orbital

mCBP: 3,3′-Bis(carbazol-9-yl)biphenyl

mCP: Dicarbazolyl-3,5-benzene

MD: Molecular Dynamics

Me: Methyl

MeCy: methylcyclohexane

^{Me}Cz: 1,8-dimethyl-9-H-carbazole

Menth: Menthyl

MeOH: Methanol

Mes: Mesityl

MIC: Mesoionic carbene

MLCT: Metal-to-ligand charge transfer

M^0: Metal in the zero oxidation state

M^I: Metal in the first oxidation state

NHC: N-heterocyclic carbene

NICS: Nuclear Independent Chemical Shift

NICS-Scan: Nuclear Independent Chemical Shift Scan

NMR: Nuclear Magnetic Resonance

OLED: Organic Light Emitting Diode

O^{t}Bu: *tert*-Butoxide

OTf: Trifluoromethanesulfonate

Ph: Phenyl

Ppm: Parts per million

PS: polystyrene

Quin-1: 9,10-Phenanthrenequinone

Quin-2: 1,10-Phenanthroline-5,6-dione

RASI: Rotationally assisted spin-state inversion

RT: Room temperature

saNHC: Saturated abnormal carbene

SOC: Spin-Orbit Coupling

SS: Solid state

S/T: Singlet-triplet

S_0: Ground state

S_1: Lowest excited singlet state

TADF: Thermally Activated Delayed Fluorescence

t-Bu: *tert*-Butyl

TDDFT: Time Dependent Density Functional Theory

TEP: Tolman electronic parameter

THF: Tetrahydrofuran

THT: Tetrahydrothiophene

TON: Turnover Number

T_1: Lowest excited triplet state

UGH3: 1,3-Bis(triphenylsilyl)benzene

up-ISC: Up-intersystem crossing

^{1}ICT: Singlet interligand charge transfer

2-MeTHF: 2-methyltetrahydrofuran

^{3}Cz: Triplet carbazole

^{3}ICT: Triplet interligand charge transfer

^{3}LE: Closest-lying ligand localized triplet state

^{3}NPh$_2$: Triplet state localized on the amide moiety

%V_{bur}: Percent buried volume

ξ: Spin-orbit coupling parameter

λ_{max}: Maximum Wavelength

Φ_{PL}: Photoluminescent quantum yield

τ: Excited state lifetime

LIST OF FIGURES

xiii

LIST OF SCHEMES

LIST OF TABLES

ACKNOWLEDGEMENTS

To start, I would like to thank the committee members for their time and effort in reading and commenting on this dissertation: Prof. Adah Almutairi, Prof. Seth Cohen, Prof. Michael Gilson and Prof. Arnold Rheingold.

My greatest acknowledgement is to my advisor, Prof. Guy Bertrand, for welcoming me into the group and for his steadfast dedication to science. He gave me the independence to explore my curiosities and was willing to constantly refine those ideas on a regular basis. In that regard, I appreciated his frequent lab walkthroughs where he would ask me, "what's new?" He taught me the importance of thinking about the overarching narrative when writing a manuscript and how to know when to drop a project. He always has his eye on the prize while retaining the student's best interest in mind. I am fortunate to have had the opportunity to be a researcher in his lab. I also want to express my deepest gratitude to him for helping me secure a postdoctoral position at UC Berkeley.

Next, Dr. Rodolphe Jazzar aka Rudy has become one of my best friends and colleagues. When there were moments that I was filled with self-doubt and a touch of imposter syndrome, he always believed in me and encouraged me to continue investigating my ideas. His collaborative spirit has inspired me throughout graduate school and his lighthearted nature made it a laughter filled experience. Especially, when he would share his crazy stories and life experiences. Moreover, we both loved to debate on a range of topics, constantly challenging the other's assumptions. I am also grateful that he pushed me to pursue research in France. It was a once in a lifetime experience that illuminated my world view. Furthermore, he showed me how to always see the best in every student and how to foster each student's unique talents. I hope to emulate his mentoring style one day. I also hope we get the chance to collaborate in the future.

I would also like to thank Dr. Michele Soleilhavoup. She spent tremendous amounts of effort to keep the lab running smoothly and safely. She would order chemicals and consumables for the entire lab in a timely manner which is no small feat. She also impressed upon me the importance of cleanliness in the

lab and although I missed the mark sometimes, I can honestly say that it helped me to build better habits that I will carry into the future.

I want to thank Dr. David Martin for welcoming me into his lab in Grenoble, France. I was fortunate enough to experience research abroad for over three months towards the end of my Ph.D. He took the time to teach me the intricacies of electrochemistry and EPR, and I plan to use these techniques in the future. Also, I really appreciated his sense of humor and lighthearted jokes. I would especially like to thank him for being willing to host me for several dinners at his home, introduce me to his beautiful family, and showcase French cuisine. Along those lines, I am thankful to one of my great friends, Dr. Eder Tomás González de Mendivil, who also welcomed me to the lab in France. He has a great temperament and made working in lab more enjoyable. I would like to thank him for grabbing the occasional beer with me throughout my stay, for taking me on hikes, and for introducing me to several of his friends and colleagues.

I would also like to thank Dr. Erik Romero who would always be there to discuss ideas. Together with Rudy, we would always be laughing. He was also a great motivating force as he would push himself and others to work as hard as possible. I appreciate him for hosting me during my interview for a postdoctoral position at UC Berkeley. Although I forgot my suit jacket for my interview, he lent me his which I greatly appreciate. Throughout my graduate studies, he became one of my great friends, and I hope we get see each other again soon.

Thanks are due to my great friend, Dr. Daniel Tolentino. I appreciated his dark sense of humor and that we got to commiserate on the challenges of graduate school. I look back fondly on the coffee breaks and lunches that we took where we discussed ideas and life.

Also, I would like to thank one of my great friends, Glen Junor, who helped teach me DFT. He has a great sense of humor and was always willing to discuss ideas. I especially appreciated the fact that he often had a different perspective than most people do which lead to many fruitful conversations.

Additionally, he always made me feel supported as he was an ally on many topics. As a scientist and as a person, his growth mindset made him an ideal lab mate and friend.

I would like to acknowledge one of my best friends and mentors, Dr. Cory Cornelius. He originally pushed me to pursue research opportunities early on in my undergraduate studies. Later, he encouraged me to pursue a PhD for which I am forever grateful. I also appreciate the fact that he and Čante Nakanishi always have an annual trip with Cassi and I. Plus, I appreciate that they were willing to explore Paris with Cassi and I during my research abroad in France. I am fortunate to have friends like them in my life.

Furthermore, I would like to acknowledge Prof. David Glueck who helped guide me through my undergraduate research and for helping me in my graduate school applications. I appreciate that he was a very patient mentor and that he has continued to support me in my academic career.

I would also like to thank the American Indian Science and Engineering Society (AISES) for helping me believe that I belong in academia. I would especially like to thank Prof. Mary Jo Ondrechen who would check in on me frequently and make sure that I was doing well. I appreciate her support and for encouraging me to pursue academia. I have been lucky to have her as a mentor, and she has made me feel like I do indeed have a place in science. She has worked tirelessly to bolster the number of native peoples in STEM and I hope to achieve her level of reciprocity one day.

Of course, I would like to thank my parents. They convinced me early on to focus on my education and taught me determination and perseverance. Without their love and support, I wouldn't be half the man that I am today. My Dad showed me how to be a Native man in this world and I am forever grateful for his lessons. My Mom is one of the most kind and caring individuals on this planet, and she taught me how to express my emotions which made me whole. Furthermore, my relatives have always been there for me and helped me learn the true meaning of family. I would also like to thank my tribes: Turtle Mountain Anishinaabe and White Bear Nakoda.

I am tremendously grateful for my fiancée, Cassi Pinion. She was always a constant source of support and love during my PhD experience. Through the ups and downs, she has always been there for me. When I would come home after a difficult day in lab, she would uplift my spirit again. She constantly

encouraged me and helped me believe in my abilities. I am home when I am with her. She is the reason that I understand the meaning of the word love.

Thanks are also due to all of my lab mates from past to the present: Francois Vermersch, Delphine Pichon, Jan Lorkowski, Dr. Pauline Olsen, Dr. Ryo Nakano, Dr. Fatme Dahcheh, Dr. Jiaxang Chu, Dr. Liqun Jin, Dr. David Ruiz, Dr. Liu Liu, Domenik Schleier, Dr. Mael Poizat, Dr. Xingbang Hu, Dr. Lilja Kristinsdottir, Dr. Connor Pranckevicius, Dr. Vianney Regnier, Dr. Mohand Melaimi, Dr. Janell Mahoney, Sima Yazdani, Victor Wang, Adam Vianna, Melinda Serrato, Nahal Soltani, Sebastian Nider, and Joseph Hunter. Special thanks to Dr. Anthony Mrse, Dr. Milan Gembicky, Dr. Cory Weinstein, Dr. Dominik Munz, and Dr. Max M. Hansmann.

Chapter 2 is adapted, in part, from the submitted manuscript, Peltier, J. L.; Tomás-Mendivil, E.; Tolentino, D. R.; Hansmann, M. M.; Jazzar, R.; Bertrand, G. "Organocatalyzed Carbonylation Reaction with Carbon Monoxide," **2020**. Permission to use copyrighted images and data was obtained from Eder Tomás-Mendivil, Daniel R. Tolentino, Max M. Hansmann, Rodolphe Jazzar, and Guy Bertrand. The dissertation author was the first author and primary investigator of this manuscript.

Chapter 3 is adapted, in part, from, Hamze, R.; Peltier, J. L.; Sylvinson, D.; Jung, M.; Cardenas, J.; Haiges, R.; Soleilhavoup, M.; Jazzar, R.; Djurovich, P. I.; Bertrand, G.; Thompson, M. E. "Eliminating nonradiative decay in Cu(I) emitters: >99% quantum efficiency and microsecond lifetime." *Science* **2019**, *363*, 601–606. This article is copyrighted by The American Association for the Advancement of Science 2019. Permission to use copyrighted images and data was obtained from Rasha Hamze, Daniel Sylvinson, Moon Chul Jung, Jose Cardenas, Ralf Haiges, Michele Soleilhavoup, Rodolphe Jazzar, Guy Bertrand, and Mark E. Thompson. The dissertation author was the second author of the manuscript.

Chapter 4 is adapted, in part, from the submitted manuscript, Peltier, J. L.; Soleilhavoup, M..; Martin, D.; Jazzar R.; Bertrand, G. "Absolute Templating of M(111) Cluster Surrogates by Galvanic Exchange," **2020**. Permission to use copyrighted images and data was obtained from Michele Soleilhavoup, David Martin, Rodolphe Jazzar, and Guy Bertrand. The dissertation author was the first author and primary investigator of the manuscript.

Chapter 5 is adapted, in part, from, Peltier, J. L.; Jazzar, R.; Mohand, M.; Bertrand, G. "Ancillary Ligand-free Copper Catalysed Hydrohydrazination of Terminal Alkynes with NH_2NH_2." *Chem. Commun.* **2016**, *52*, 2733–2735. This article is copyrighted by The Royal Society of Chemistry 2016. Permission to use copyrighted images and data was obtained from Rodolphe Jazzar, Mohand Melaimi, and Guy Bertrand. The dissertation author was the first author and primary investigator of this manuscript.

VITA

EDUCATION

DOCTOR OF PHILOSOPHY: CHEMISTRY
University of California San Diego   *2020*
Advisor: **Guy Bertrand**

MASTER OF SCIENCE: CHEMISTRY
University of California San Diego   *2016*

BACHELOR OF ARTS: DOUBLE MAJOR IN CHEMISTRY & NATIVE AMERICAN STUDIES
Dartmouth College   *2014*
Advisor (Chemistry): **David S. Glueck**

PUBLICATIONS

1. Peltier, J. L.; Soleilhavoup, M.; Martin, D.; Jazzar, R.; Bertrand, G. Absolute Templating of Coinage Metal Clusters by Galvanic Exchange: M(111) Surface Surrogates. *Submitted*.
2. Peltier, J. L.; Tomás-Mendivil, E.; Tolentino, D. R.; Hansmann, M. M.; Jazzar R.; Bertrand, G. Metal-Free Carbene-Catalyzed Carbonylation Reaction with Carbon Monoxide. *Submitted*.
3. Yazdani, S.; Junor, G. P.; Peltier, J. L.; Gembicky, M.; Jazzar, R.; Grotjahn, D. B.; Bertrand, G. Influence of Carbene and Phosphine Ligands on the Catalytic Activity of Gold Complexes in the Hydroamination and Hydrohydrazination of Alkynes. *ACS Catal.* **2020**, *10*, 5190–5201. DOI: 10.1021/acscatal.0c01352
4. Gibbons, S. K.; Valleau, C. R. D.; Peltier, J. L.; Cain, M. F.; Hughes, R. P.; Glueck, D. S.; Golen, J. A.; Rheingold, A. L. Diastereoselective Coordination of P-Stereogenic Secondary Phosphines in Copper(I) Chiral Bis(phosphine) Complexes: Structure, Dynamics, and Generation of Phosphido Complexes. *Inorg. Chem.* **2019**, *58*, 8854–8865. DOI: 10.1021/acs.inorgchem.9b01263
5. Hamze, R.; Shi, S.; Kapper, S. C.; Sylvinson, D., Estergreen, L.; Jung, M.; Tadle, A. C.; Haiges, R.; Djurovich, P. I.; Peltier, J. L.; Jazzar, R.; Bertrand, G.; Bradforth, S. E.; Thompson, M. E. Quick-Silver' from a systematic study of highly luminescent, 2-coordinate, d^{10} coinage metal complexes. *J. Am. Chem. Soc.* **2019**, *141*, 8616–8626. DOI: 10.1021/jacs.9b03657
6. Hamze, R.; Peltier, J. L.; Sylvinson, D.; Jung, M.; Cardenas, J.; Haiges, R.; Soleilhavoup, M.; Jazzar, R.; Djurovich, P. I.; Bertrand, G.; Thompson, M. E. Eliminating nonradiative decay in Cu(I) emitters: >99% quantum efficiency and microsecond lifetime. *Science* **2019**, *363*, 601–606. DOI: 10.1126/science.aav2865
7. Romero, E. A.; Peltier, J. L.; Jazzar, R.; Bertrand, G. Catalyst-free Dehydrocoupling of Amines, Alcohols, and Thiols with Pinacol Borane and 9-borabicyclononane (9-BBN). *Chem. Commun.* **2016**, *52*, 10563–10565. DOI: 10.1039/C6CC06096J
8. Li, Z.; Chen, X.; Benkő, Z.; Liu, L.; Ruiz, D. A.; Peltier, J. L.; Bertrand, G.; Su, C.-Y.; Grützmacher, H. N-Heterocyclic Carbenes as Promoters for the Rearrangement of Phosphaketenes to Phosphaheteroallenes: A Case study for OCP to OPC Constitutional Isomerism. *Angew. Chem. Int. Ed.* **2016**, *55,* 6018–6022. DOI: 10.1002/anie.201600903
9. Peltier, J. L.; Jazzar, R.; Melaimi, M.; Bertrand, G. Ancillary Ligand-Free Copper Catalysed Hydrohydrazination of Terminal Alkynes with NH_2NH_2. *Chem. Commun.* **2016**, *52*, 2733–2735. DOI: 10.1039/C5CC10427K

FELLOWSHIPS, AWARDS & HONORS

UNIVERSITY OF CALIFORNIA PRESIDENT'S POSTDOCTORAL FELLOWSHIP
University of California, Berkeley   *April 2020*

BOUCHET GRADUATE HONOR SOCIETY
University of California, San Diego Graduate Division   *February 2020*

CARL STORM UNDERREPRESENTED MINORITY FELLOWSHIP
Organometallic Chemistry Gordon Research Conference   *May 2018*

NATIONAL SCIENCE FOUNDATION GRADUATE RESEARCH FELLOWSHIP
University of California, San Diego   *October 2016 – October 2019*

HONORABLE MENTION: FORD FOUNDATION PREDOCTORAL FELLOWSHIP
University of California, San Diego   *March 2016*

TRIBAL MEMBERSHIP INITIATIVE FELLOWSHIP
University of California, San Diego   *October 2015 – October 2016*

HONORABLE MENTION: FORD FOUNDATION PREDOCTORAL FELLOWSHIP
University of California, San Diego   *March 2015*

LIGHTING THE PATHWAY TO FACULTY CAREERS FOR NATIVES IN STEM
American Indian Science & Engineering Society   *October 2014 – October 2016*

AMERICAN INSTITUTE OF CHEMISTS FOUNDATION STUDENT AWARD
Dartmouth College Chemistry Department Faculty   *June 2014*

DANIEL SIMON PRIZE IN NATIVE AMERICAN STUDIES
Dartmouth College Native American Studies Faculty   *June 2014*

ZABRISKIE SUMMER UNDERGRADUATE RESEARCH FELLOWSHIP
Dartmouth College Chemistry Department   *June – September 2013*

A.T. ANDERSON MEMORIAL SCHOLARSHIP
American Indian Science & Engineering Society   *June 2013*

PAUL K. AND EVALYN E. COOK RICHTER MEMORIAL FUND FOR UNDERGRADUATE RESEARCH
Dartmouth College   *June – September 2012*

JUNIOR RESEARCH SCHOLARSHIP
Dartmouth College   *January – April 2012*

POSTERS & PRESENTATIONS

SYNTHESIS & REACTIVITY OF A WELL-DEFINED MIXED-VALENT COPPER (0)/(I) NANOCLUSTER
Journées de Chimie Organique 2019
École polytechnique de Palaiseau, France   *October 2019*

SYNTHESIS AND REACTIVITY OF A WELL-DEFINED MIXED-VALENT COPPER (0)/(I) NANOCLUSTER
258th American Chemical Society National Meeting & Exposition
San Diego, CA   *August 2019*

STRIKING GOLD WITH COPPER
UCSD Inorganic Seminar
University of California, San Diego   *August 2019*

READILY AVAILABLE CYCLIC (ALKYL)(AMINO)CARBENES: UNRAVELING COPPER LUMINESCENCE
Southern California Inorganic Photochemistry Conference
Catalina, CA   *April 2019*

DIVERGENT SYNTHESIS OF WELL-DEFINED COPPER NANOCLUSTERS
SoCal Organometallics Meeting
University of Southern California   *February 2019*

COPPER: LET THERE BE LIGHT!
UCSD Graduate Student Seminar
University of California, San Diego   *November 2018*

DIVERGENT SYNTHESIS OF WELL-DEFINED COPPER (0) AND COPPER HYDRIDE NANOCLUSTERS
Organometallic Chemistry Gordon Research Conference
Salve Regina University   *July 2018*

DIVERGENT SYNTHESIS OF WELL-DEFINED COPPER (0) AND COPPER HYDRIDE NANOCLUSTERS
Organometallic Chemistry Gordon Research Seminar
Salve Regina University   *July 2018*

ANCILLARY LIGAND-FREE COPPER CATALYZED HYDROHYDRAZINATION OF TERMINAL ALKYNES
American Indian Science & Engineering Society National Conference
Minneapolis, MN   *November 2016*

ANCILLARY LIGAND-FREE COPPER CATALYZED HYDROHYDRAZINATION OF TERMINAL ALKYNES
University of California Symposium on Chemical Sciences
Lake Arrowhead, CA   *March 2016*

ANCILLARY LIGAND-FREE COPPER CATALYZED HYDROHYDRAZINATION OF TERMINAL ALKYNES
251st American Chemical Society National Meeting & Exposition
San Diego, CA   *March 2016*

ANCILLARY LIGAND-FREE COPPER CATALYZED HYDROHYDRAZINATION OF TERMINAL ALKYNES
Graduate Division Native American Student Research Symposium
University of California, San Diego   *November 2015*

TRANSITION METAL CHEMISTRY OF BIS(SECONDARY PHOSPHINES)
22nd Annual Karen E. Wetterhahn Symposium
Dartmouth College   *May 2013*

FLUXIONAL PROCESS IN COPPER BIS(SECONDARY PHOSPHINE) COMPLEXES
Graduate Research Colloquium in Organometallic Chemistry
Dartmouth College   *November 2013*

ABSTRACT OF THE DISSERTATION

Cyclic (alkyl)(amino)carbenes: from Replacing Metals to Metal Replacement

by

Jesse Lawrence Peltier

Doctor of Philosophy in Chemistry

University of California San Diego, 2020

Professor Guy Bertrand, Chair

Cyclic (alkyl)(amino)carbenes (CAACs) have been recognized as a class of carbenes adept at activating small molecules and stabilizing a wide array of highly reactive compounds. Herein, we outline the impact of CAACs in a variety of applications, *e.g.*, as a catalyst replacing metals, and as ligands promoting metal replacement. Moreover, we delineate that in some transformations, and in marked contrast with the literature, CAACs, or any ligand for that matter, are superfluous in achieving high catalytic activity.

Unlike traditional carbene-catalysts that act as Lewis bases, CAACs are ambiphilic enough to activate carbon monoxide, thus mimicking the behavior of metals. In chapter two, we demonstrate that, without the need for a metal, sterically encumbered CAACs can catalytically transform and transfer CO in carbonylation. This highlights that ambiphilic carbenes can open new avenues in carbene-organocatalysis.

Next, light emitting devices are traditionally made using scarce heavy metals (*e.g.,* Ir, and Pt). The use of copper, however, would constitute a major innovation by replacing those metals, but it is plagued by

weak spin-orbit coupling as well as high reorganization energies. In chapter three, we demonstrate that having copper sandwiched between an electron-donor (carbazole) that is rigidly pointed at an electron-acceptor (CAAC) enables record photoluminescent properties akin to heavy metals. Significantly, we exploited this copper system to fabricate a rare example of a high energy blue OLED device.

In chapter four, upon taking advantage of CAAC's ambiphilicity, we stabilized an active copper cluster and used it as a template via absolute galvanic metal replacement to isolate the coinage metal family of clusters. Moreover, analogous to M(111) surfaces, we demonstrated that copper is unique among coinage metals as it can transform CO_2 into CO, further delineating the intermediacy of clusters between homogenous and heterogeneous processes.

In the last chapter, we discuss the challenges of the parent hydrazine in catalytic transformations. As a substrate, it typically requires gold catalysts stabilized by strongly donating carbene ligands. Although we found that (CAAC)Cu cationic complexes could catalyze this difficult transformation, we discovered that commercially available copper salts, unlike gold, were highly efficient catalyst precursors in the absence of ancillary ligands.

Chapter 1 – General Introduction

1.1 Modern-day Alchemy

Since time immemorial, the concept of changing one substance into a more useful one, through human ingenuity, has captivated the imaginations of various cultures. Early on, one way this was accomplished was through extractions and separations with water, the universal solvent, such as the Dakota people who drank a willow-bark tea, containing salicylic acid, to restore themselves mentally and physically,[1] or the use of fire for cooking or smelting processes. However, as peoples' philosophical and cultural understandings of the world changed, so too did their ideas on what was in the realm of possibility. The general impetus being how to modify the world around them to create something valuable or useful. Along those lines, after several hundred years into the common era, the origins of alchemy can be traced to Greco-Roman Egypt followed by a diaspora throughout Africa, Europe and East Asia.[2] Amongst the various principles of alchemy, there was the notion of transmuting a base metal into a more valuable or useful one. Through the lens of the modern era, however, these strategies were not achievable, but this central paradigm of human society has persisted and expanded through time. Although the underpinnings of Alchemy led to pseudoscience, a modern-day version of this concept exploits the idea of transmutation. Nowadays, with our more advanced understanding of chemistry and physics, the modern-day alchemist is no longer concerned with changing an element of the periodic table into another (with the exception of fusion and fission), but instead focused on altering chemical conditions to force a cheaper, more earth abundant element to behave analogously to a rare and useful one. A couple of ways in which this can manifest includes forcing an abundant first-row transition metal to react like a rarer third row transition metal, or upon taking a main group element and forcing it to react like a metal. To accomplish this task, a highly advanced understanding of molecular structure-behavior relationships had to be developed which led to the advancement of highly reactive main group ligands. Some of the most powerful ligands, capable of engendering profound new properties are carbenes and their analogues. However, the highly reactive nature of carbenes led to rocky beginnings in their development. Eventually, amongst the various carbene classes developed, ambiphilic carbenes, such as cyclic (alkyl)(amino) carbenes (CAACs), are rising to the occasion.

1.2　The Quest for a Stable Carbene

Despite their desirability, historically, carbenes were fugacious. Although the first attempted isolation of a monomeric carbene, notably before the concept of orbitals, was by Dumas in 1835 from the dehydration of methanol (Scheme 1.1),[3] the idea of a carbene wasn't formally developed until 1903 by Buchner.[4]
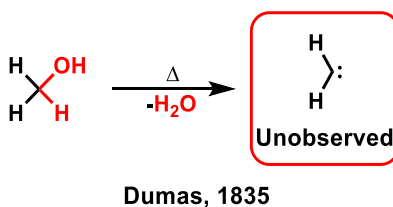
Scheme 1.1: Initial attempt at the isolation of a free carbene.

Soon after, in 1912, Staudinger reported the photolysis of diazomethane and trapped the transient parent carbene through an N-H insertion on hydrazine (Scheme 1.2).[5] Thus, demonstrating that at the very least, carbenes were metastable intermediates. Early in their exploration, much to the frustration of synthetic chemists, carbenes largely behaved as transient intermediates and could only be trapped by organic substrates.
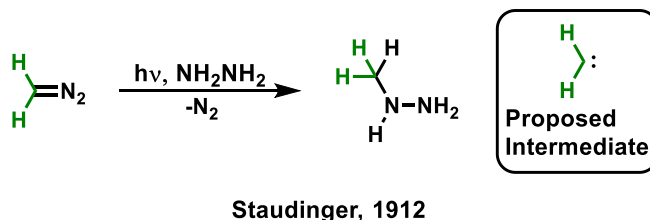
Scheme 1.2: Historical trapping of a carbene after photolysis of the diazoprecursor.

Without proper stabilization, these divalent two-coordinate carbon-based species, with a valence shell configuration of $2s^2 2p^2$, tend to exist in a highly reactive triplet state. In the linear form, there is no hybridization and the two nonbonding electrons occupy the two degenerate sets of empty p-orbitals (p_x and

p$_y$) with parallel spins (Figure 1.1).[6] As diradicals, these highly reactive species only have a fleeting existence as they simply react too rapidly with their environment or dimerize.[7]
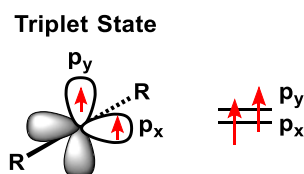
Triplet State

Figure 1.1: Triplet state carbenes feature a degenerate set of p-orbitals occupied by nonbonding electrons with parallel spin (left) and a depiction of the Singly Occupied Molecular Orbitals (SOMOs) (right).

Continuing along this trajectory, in 1952, the synthetic utility of carbenes was realized and popularized in organic chemistry by Doering in a cyclopropanation reaction of cyclohexene involving the deprotonation of chloroform or bromoform to form a transient carbene (Scheme 1.3).[8] However, the quest for a stable carbene persisted. In a brazen attempt to isolate the monomeric carbene, in the 1960s, Wanzlick reported that the thermolysis of an unhindered *N*-heterocyclic carbene (NHC) chloroform adduct yielded a tetraazafulvalene (Scheme 1.4).[9,10] This dimer was proposed to arise from and be in equilibrium with the transient monomeric carbene. Of course, Wanzlick's equilibrium came about from a lack of kinetic stabilization through steric bulk, but by using an amino substituent, this breakthrough highlighted the importance of heteroatom stabilization. However, the isolation of the challenging free carbene continued to elude synthetic chemists.

Doering, 1954
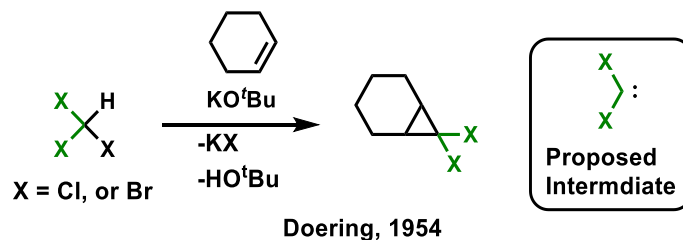
Scheme 1.3: Triplet carbenes can undergo cyclopropanation reactions which highlighted their synthetic utility.

Wanzlick, 1962
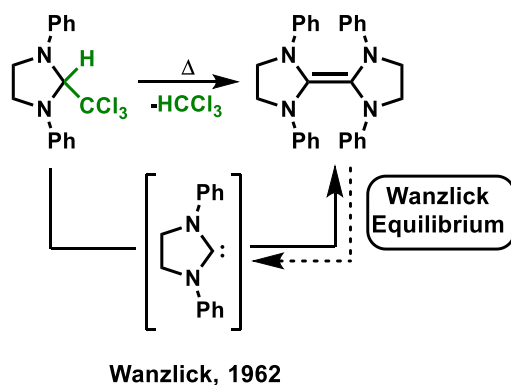
Scheme 1.4: Unhindered carbenes stabilized by heteroatoms undergo the Wanzlick Equilibrium.

In 1980, Schoeller[11] and Pauling[12] elucidated the framework necessary to stabilize a singlet carbene: substituents adjacent to the carbene need to preserve its electroneutrality through mesomeric and inductive effects. When the two nonbonding electrons are paired in the same σ orbital (originally referred to as p_x), this engenders the singlet state which is a closed shell species and inherently more stable than a diradical triplet state (Figure 1.2). To favor the singlet state, the degeneracy of the σ and p_π (originally known as p_y) orbitals must be broken which can be achieved through two different substitution patterns (although exceptions to these rules have been discovered).[6]
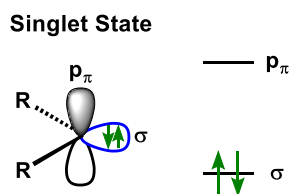
Figure 1.2: (Left) Singlet state carbene featuring a nondegenerate set of p-orbitals occupied by nonbonding electrons with opposite spin; (right) a depiction of the Highest Occupied Molecular Orbital (HOMO) and Lowest Unoccupied Molecular Orbital (LUMO).

The first strategy, and currently the most widely utilized, hinges on two π-donor substituents α to the carbene center which can donate a lone pair into the empty p_π. From these donating substituents, the degeneracy is broken by an increase in electron-electron repulsion in the Lowest Unoccupied Molecular

5

Orbital (LUMO). Plus, it decreases the overall electrophilicity of the species which can be difficult to tame. Furthermore, this separation in the energetics of the p-orbitals is enhanced by the inductive effect of these two electronegative groups. Each of them pulls density from the filled σ orbital thereby stabilizing the Highest Occupied Molecular Orbital (HOMO). Therefore, colloquially, this method amounts to a "push-push" mesomeric, "pull-pull" inductive stabilization (Figure 1.3, left).

The second option involves a combination of a π-donor and a π/σ-acceptor type substituent, and of course, the π-donor substituent stabilizes the carbene singlet state in the previously mentioned fashion. The difference with this strategy is the presence of the π/σ -acceptor type substituent which causes the carbene σ lone pair to mesomerically donate into the π/σ-accepting group thereby aiding in breaking degeneracy. The result is that the HOMO is significantly stabilized over the LUMO through the delocalization of electrons leading to a more favorable singlet state. Colloquially, this substitution pattern is known as "push-pull mesomeric" stabilization (Figure 1.3, right). Notably, these strategies proved seminal in the advancement of carbene and carbenoid technology and finally led to the isolation of the monomeric species.

D= electronegative π-donor
A= electropositive π/σ acceptor
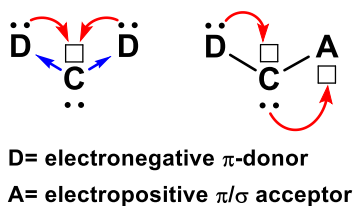
Figure 1.3: Methods for the stabilization of singlet carbenes: "push-pull" mesomeric stabilization (on the left) and "push-push" mesomeric, "pull-pull" inductive stabilization (on the right).

In 1988, Bertrand *et al.* irradiated (trimethylsilyl)[bis(diisopropylamino)phosphino]diazomethane to engender a phosphinosilylcarbene, the first persistent singlet carbene, upon extrusion of dinitrogen (Scheme 1.5).[13] Markedly, the α-substituents exploited in stabilizing this moiety rested on a "push-pull mesomeric" strategy. Of course, as part of the pnictogen family, the phosphino substituent with a lone pair acts as the π-donor whereas the silyl group acts as the acceptor with the presence of its low lying σ* orbital. While this discovery was contested in part due to the presence of resonance forms such as a zwitterionic phospha-allene and a phospha-acetylene, the subsequent carbenoid reactivity (*e.g.*, insertion into the

diisopropyl substituent, the cyclopronation with alkenes, and cyclization with carbonyls) clearly demonstrated that these species can be regarded as singlet carbenes.[14]
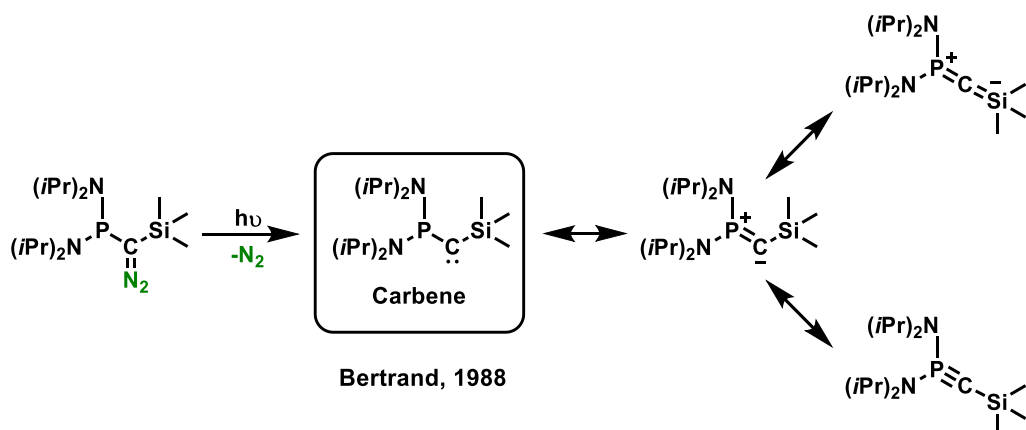
Scheme 1.5: The first isolated carbene with bonafide reactivity: the phosphino(silyl)carbene and all of its potential resonance forms.

A few years after this initial discovery and building on the equilibrium discovered by Wanzlick, Arduengo *et al.* isolated the first crystalline carbene.[15] To achieve this feat, the sterically bulky 1,3-di-1-adamantylimidazolium chloride was deprotonated to form the kinetically protected 1,3-di-1-adamantylimidazol-2-ylidene (Scheme 1.6). Cleverly, this carbene is kinetically stabilized by the bulkier adamantyl substitutents and thermodynamically stabilized by the unsaturated backbone which adds the additional benefit of aromaticity. Resting upon the other strategy to engender a singlet carbene, this NHC exploited the "push-push mesomeric, pull-pull inductive" stabilization by the two electronegative amino substituents, both with lone pairs for π donation. Due in part to the ease of synthesis and accessibility, *N*-heterocyclic carbenes (NHCs) opened the flood gates for stable carbenes to flourish with a broad range of applications. The foundations for singlet carbene chemistry had been finally realized.
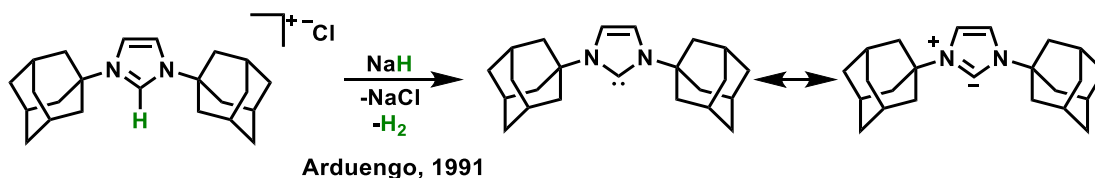
Scheme 1.6: The first monocrystalline carbene: the NHC that also shows one of its ylide resonance forms.

1.3   High Tunability of Carbenes

After those seminal discoveries, carbene chemistry began to blossom and this can be largely attributed to their tunable electronic properties. Since they possess an empty p_π orbital and a filled σ donating orbital, they have the potential to be ambiphilic in nature. Singlet carbenes are, therefore, nucleophilic, with the ability for strong σ donation, and electrophilic, with the ability to be strong π-acids. Among the various tunable features, several key components have arisen (Figure 1.4).[16] First, the heteroatom substitution pattern around the carbene center has large impact on the electronics, but due to its stabilizing prowess, nitrogen is the most prevalent heteroatom.[17,18] Notably, carbenes stabilized by other heteroatoms do exist but to a lesser extent (*e.g.*, phosphorus, oxygen, sulfur).[19,20] Next, the carbene backbone represents a tunable feature (including cyclic versus acyclic variants but this dissertation will focus on the more widely used cyclic variants)[21] such as benzannulated moieties that can lower the LUMO through delocalization. Another significant feature is ring size which increases the bond angle at a carbene center and causes the HOMO to raise in energy.[17,22] Lastly, steric properties are easily modifiable through the adjacent substituents and by the ring size. Taken together, these alterations highlight the tunable features that have led to the development of an extensive library of singlet carbenes at the disposal of chemists. Because of this vast array of alterable properties, there has been the development of strategies to gauge the resulting electronic and steric properties.
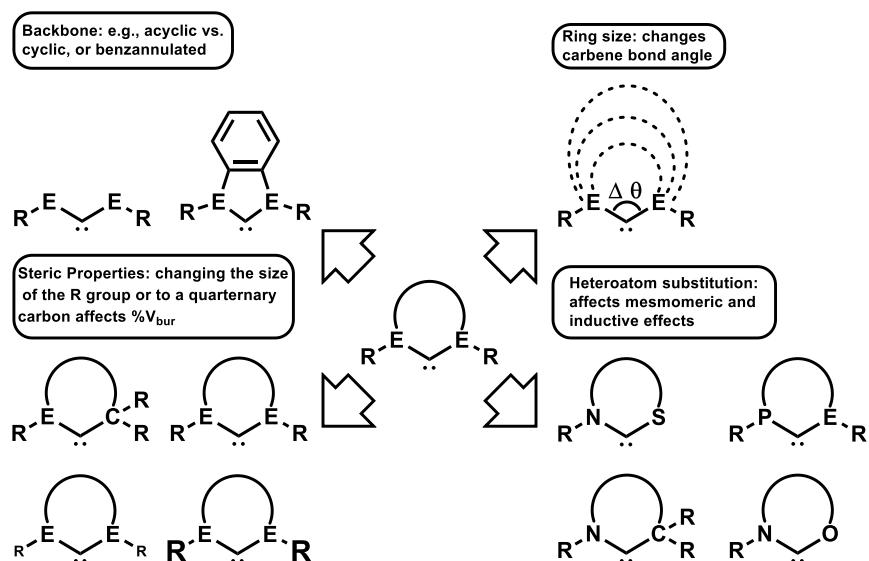
Figure 1.4: Carbenes can be tuned in a myriad of fashions giving the impression of seemingly endless possibilities: backbone alterations such as an increased aromatic network (top left); ring size changes which affect the carbene bond angle (top right); steric properties from big R groups to small (bottom left); heteroatom substitutions, *e.g.*, nitrogen to sulfur, phosphorus, or carbon (bottom right).

For the steric properties of carbenes, Nolan and Cavallo developed percent buried volume ($\%V_{bur}$).[23] This is defined as the percent of the total volume occupied by a ligand in a sphere with a defined radius (r = 3.5 Å) whose volume represents the potential coordination space occupied by a ligand.[24,25] As for the electronic properties, Density Functional Theory (DFT) can qualitatively gauge the frontier energetics of carbenes, but experimental measurements have been developed to ground the results and quantitatively determine chemical properties. The overall donating ability can be determined through the Tolman Electronic Parameter (TEP) which relies on the *cis*-[(carbene)Rh(CO)$_2$Cl] complex's CO stretching frequency in the IR spectrum.[17,26] Importantly, the TEP value is useful for determining overall donating ability, but to disentangle the σ-donating ability from the π-acidity, the TEP must be used in tandem with another technique. Therefore, Bertrand *et al.*[27] and Hudnall *et al.*[28] determined the π-accepting character for a series of carbenes and established the "P-scale"[26,29] based on the ^{31}P NMR of a carbene-phosphinidene adduct. Together, these tools have become pervasive in determining donating ability and π-acidity.

1.4   Carbene Classes

With experimental techniques to determine steric and electronic properties in hand, the rational design and utilization of carbenes could proceed. As previously mentioned, heteroatom substitution, especially heteroatoms adjacent to the carbene center, have a substantial impact through mesomeric and inductive effects. Out of this concept, sprung forth several groups of cyclic carbene classes with distinct electronic properties.
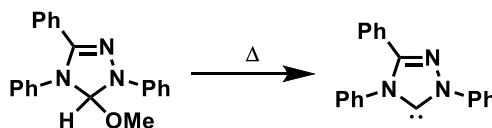
Scheme 1.7: Vacuum pyrolysis of methanol bound to a 1,2,4-triazole ring to form Ender's carbene.

In relation to the initially discovered NHCs, which have two amino substituents partially quenching the empty LUMO, there are carbenes that have been designed to be weaker nucleophiles. In 1995, soon after the discovery of a crystalline carbene, Ender discovered a carbene through vacuum pyrolysis of methanol from a methoxy bound to a 1,2,4-triazole ring (Scheme 1.7).[30] This engendered the eponymously known Ender's carbene (ENHC) which is a much weaker nucleophile than NHCs (TEP: 2050.7 cm^{-1}) as exemplified by its TEP value of 2057.3 cm^{-1} (Figure 1.5).[17] Starting from an unsaturated NHC, these carbenes simply replace one of the carbon substituents on the backbone of the five membered ring with a nitrogen. By doing so, this demonstrates the profound effect of remote substitution. The attenuation of nucleophilicity is achieved by the electronegativity of the β-nitrogen which inductively pulls more electron density from the HOMO, thus making them weaker nucleophiles. This electronic difference makes ENHCs better leaving groups which has led to pronounced nucleophilic organocatalytic activity (*e.g.*, benzoin condensation and Stetter reactions).[31]
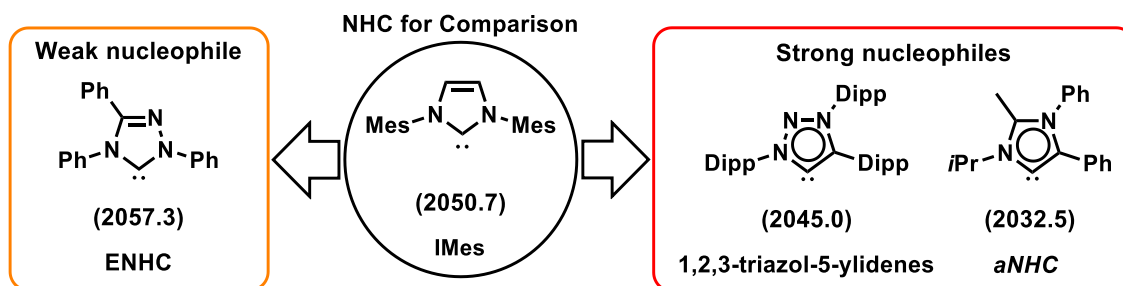
Figure 1.5: Comparing the donor ability with TEP values (in parenthesis with units of cm^{-1}) between strongly nucleophilic carbenes and weakly nucleophilic carbenes with an NHC for comparison (mes = mesityl and dipp = 2,6-diisopropylphenyl).[17]

On the other hand, there are also carbenes that have been discovered to be strong nucleophilic σ donors. A representative of this class is mesoionic carbenes (MICs) which encompass a relatively broad range of 5 membered ring variants. Initially discovered by trying to ligate an NHC to IrH$_5$(PPh$_3$)$_2$, in 2001, Crabtree *et al.* serendipitously found a new binding mode in the less acidic C-5 position via an oxidative addition.[32] These first versions of MICs came to be known as *a*NHCs. Following this discovery, in 2009, Bertrand *et al.* were able to synthesize the free *a*NHC by blocking the NHC's C-2 position with a phenyl group.[33] Furthermore, Bertrand *et al.* were able to contribute to the MIC family upon synthesizing the 1,2,3-triazol-5-ylidenes.[34] Although these species have a different overall number of heteroatoms in the ring, all feature an adjacent carbon that forms an alkene with the carbene center (forming a zwitterion) in addition to the typical amino substituent. The defining feature of these zwitterionic compounds, however, is that canonical resonance structures of the carbene cannot be drawn without formal charges (Figure 1.6).
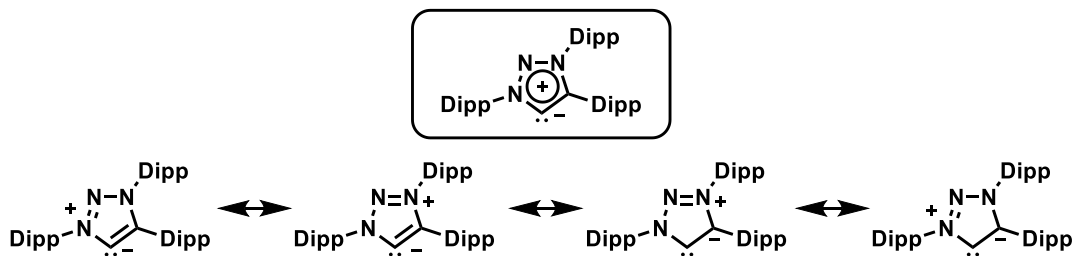
Figure 1.6: Resonance forms of 1,2,3-triazol-5-ylidenes highlighting the mesionic nature of MICs.

Therefore, the LUMO of these moieties is always filed to a large extent by a pi bond with one of the adjacent substituents. Notably, they feature an anionic charge at the carbene center. With virtually no empty LUMO, a strong partial negative charge on the carbene, and only one amino substituent to pull e-density from the HOMO compared to NHCs, these MICs are exceptionally strong nucleophiles. Applications for these electronic properties tend to be focused on transition metal catalysis where strong σ donation is often beneficial (*e.g.*, water oxidation, hydrogen transfer, and cross coupling to name a few).[35,36] Moreover, MICs have also found use as organocatalysts (*e.g.*, ring opening polymerization, and formyl H/D exchange).[44,36,46] In fact, the field of carbene organocatalysis is dominated by carbenes used as Lewis bases such as NHCs, ENHC, and MICs. Later in this dissertation, we demonstrate that ambiphilic carbenes can also behave as organocatalysts.

As opposed to MICs with a high-HOMO and -LUMO, carbenes can also have a low-HOMO and -LUMO thereby having weaker nucleophilicity but pronounced electrophilicity. In 2009, Bielawksi *et al.* deprotonated the pyrimidinium salt to engender a *N,N'*-diamidocarbenes (DACs), a representation of electrophilic carbenes.[38] The electrophilic properties of the DAC family results from the amide backbone which features a low-lying π^* orbital. By delocalizing the nitrogen atoms' π electrons away from the carbene p_π orbital, these functional groups attenuate the α nitrogen atoms' ability to mesomerically donate into the carbene center. This results in a more Lewis acidic carbene and is highlighted by the P-scale value of +83 ppm for the 6-membered DAC and +78.6 ppm for the 5-membered DAC which is significantly higher than IMes (-23.0 ppm for comparison) (Figure 1.7).[27,28] Additionally, while the other carbenes' LUMOs were stabilized by aromaticity, ones that are like the 6-membered DAC also features enhanced electrophilicity due to its nonaromatic ring structure. The importance of this carbene electrophilicity is highlighted by the reactivity of DACs which are capable of binding small molecules and activating E-H bonds (E = heteroatom).[39–41] Despite a lower lying HOMO because of the stronger induction by the amide, this reactivity demonstrates the non-negligible σ-donor ability that is a property of virtually all carbenes.
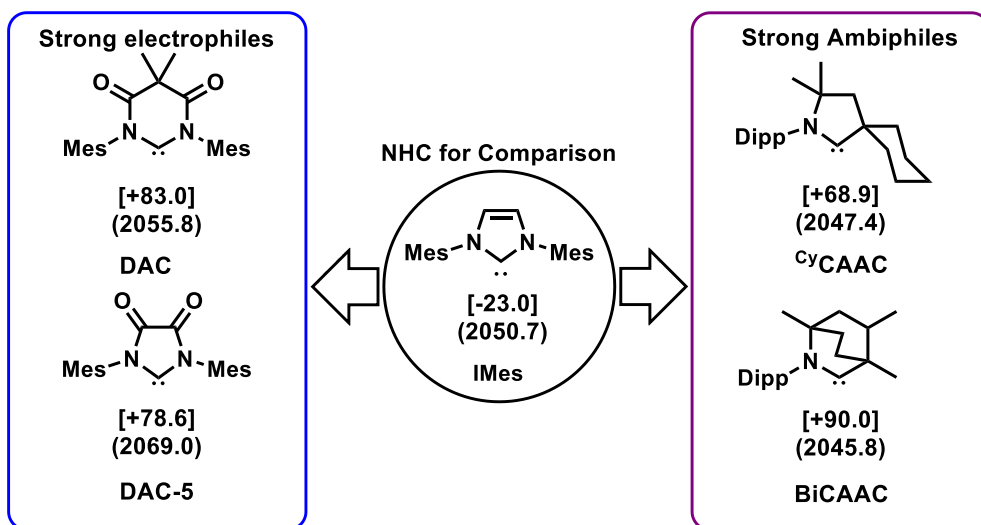
Figure 1.7: Comparing the donor and acceptor ability—TEP values (in parenthesis with units of cm^{-1} in DCM)[17,42,43] and P-scale values [in brackets with units of ppm in C_6D_6][27,28]—between the strongly electrophilic DAC family and the strongly ambiphilic CAAC family with an NHC for comparison (mes = mesityl and dipp = 2,6-diisopropylphenyl).

Amongst the various carbene electronic properties, a special class involves those that are strong nucleophiles and electrophiles thereby being highly ambiphilic. Undoubtedly, cyclic (alkyl)(amino)carbenes (CAACs) discovered by Bertrand *et al.* in 2005,[44] and followed by the bicyclic (alkyl)(amino)carbene (BICAACs) by Bertrand *et al.* in 2017[42] are some of the most highly ambiphilic carbenes to date: as stronger donors, their TEP Value is much lower than the DAC and NHC family,[17,42,43] and they have comparable or even greater π-acidity to DACs as represented by their P-scale values (Figure 1.7).[27,28] Notably, CAACs and BICAACs feature one nitrogen and one quaternary carbon atom α to the carbene center. Since there is only one σ-accepting and π-donating group to stabilize the carbene, these species feature a higher HOMO and a lower LUMO. These strong σ-donor and π-acceptor capabilities outperform other carbenes in several applications—*e.g.*, stabilizing metals in unusually low oxidation states and coordination numbers,[45] extremely robust interactions to stabilize transition metals in homogenous catalysis,[46,47,48] carbon-centered[49–51] and main group radicals[52,53] stabilized by the strong "push-pull" captodative effects, and low valent main-group compounds that were previously unisolable.[43,46]

13

The rapid advancement of carbene chemistry is thanks in part to rigorous experimental techniques to gauge their stereoelectronic properties which have parsed out key differences in the subtle variations between carbene motifs. This led to the rise of several carbene classes. Amidst the various classes, CAACs stand out due to their pronounced ambiphilicity. For example, the ambiphilic character of CAACs, often displayed by metals capable of backbonding, enabled reactivity analogous to transition metals. CAACs can activate several challenging small molecules (*e.g.*, H_2, NH_3, and CO) akin to metals.[54] Furthermore, they can form extremely robust interactions with transition metals.[55] Hence, they are one of the most capable carbene species that can achieve the replacement of more expensive metal processes.

1.5   Ambiphilic Cyclic (alkyl)(amino)carbene Enabled Transmutation

Using CAACs, this dissertation serves to expand upon the notion of forcing a more abundant element into behaving like a more valuable one. The peculiar stereoelectronic properties of CAACs led to our advancement in the transition metal analogy through organocatalysis. Furthermore, by expanding and developing several novel applications in earth abundant copper chemistry, CAACs caused copper to behave like a 3rd row transition metal.[55] Through our investigations, the distinct ambiphilicity of CAACs was found to be crucial in finding ways in which these ligands could supplant transition metal processes, enable copper to behave like an expensive transition metal, and lead to galvanic metal replacement in clusters, taking a 1st row transition metal cluster and turning it into its gold analogue.

1.6   References

(1)   Andros, F. THE MEDICINE AND SURGERY OF THE WINNEBAGO AND DAKOTA INDIANS. *JAMA* **1883**, *I*, 116–118.

(2)   Cobb C, G. H. *Creations of Fire: Chemistry's Lively History From Alchemy to the Atomic Age*; Plenum Press, New York, 1995.

(3)   Dumas, J. B.; Peligot, E. Mémoire Sur l'esprit de Bois et Sur Les Divers Composés Éthérés Qui En Proviennent. *Ann. Chim. Phys.* **1835**, *58*, 5.

(4)   Buchner, E.; Feldmann, L. Diazoessigester Und Toluol. *Berichte der Dtsch. Chem. Gesellschaft.*

1903, *36*, 3509.

(5)   Staudinger, H.; Kupfer, O. Über Reaktionen Des Methylens. III. Diazomethan. Berichte Der Dtsch. Chem. Gesellschaft. *Berichte der Dtsch. Chem. Gesellschaft* **1912**, *45*, 501–509.

(6)   Bourissou, D.; Guerret, O.; Gabbaï, F. P.; Bertrand, G. Stable Carbenes. *Chem. Rev.* **2000**, *100*, 39–91.

(7)   Hirai, K.; Itoh, T.; Tomioka, H. Persistent Triplet Carbenes. *Chem. Rev.* **2009**, *109*, 3275–3332.

(8)   Doering, W. von E.; Hoffmann, A. K. The Addition of Dichlorocarbene to Olefins. *J. Am. Chem. Soc.* **1954**, *76*, 6162–6165.

(9)   Wanzlick, H.-W.; Schikora, E. Ein neuer Zugang zur Carben-Chemie. *Angew. Chem.* **1960**, *72*, 494.

(10)   Wanzlick, H. W. Aspects of Nucleophilic Carbene Chemistry. *Angew. Chem. Int. Ed. Engl.* **1962**, *1*, 75–80.

(11)   Schoeller, W. W. When Is a Singlet Carbene Linear? *J. Chem. Soc. Chem. Commun.* **1980**, 124–125.

(12)   Pauling, L. The Structure of Singlet Carbene Molecules. *J. Chem. Soc. Chem. Commun.* **1980**, 688–689.

(13)   Igau, A.; Grutzmacher, H.; Baceiredo, A.; Bertrand, G. Analogous α,α'-Bis-Carbenoid Triply Bonded Species: Synthesis of a Stable Λ3-Phosphinocarbene-Λ5-Phosphaacetylene. *J. Am. Chem. Soc.* **1988**, *110*, 6463–6466.

(14)   Igau, A.; Baceiredo, A.; Trinquier, C.; Bertrand G. [Bis(Diisopropylamino)Phosphino] Trimethyl-Silylcarbene : A Stable Nucleophilic Carbene. *Angew. Chem. Int. Ed. Engl.* **1989**, *28*, 621–622.

(15)   Arduengo, A. J.; Harlow, R. L.; Kline, M. A Stable Crystalline Carbene. *J. Am. Chem. Soc.* **1991**, *113*, 361–363.

(16)   Hopkinson, M. N.; Richter, C.; Schedler, M.; Glorius, F. An Overview of N-Heterocyclic Carbenes. *Nature* **2014**, *510*, 485–496.

(17)   Nelson, D. J.; Nolan, S. P. Quantifying and Understanding the Electronic Properties of N-Heterocyclic Carbenes. *Chem. Soc. Rev.* **2013**, *42*, 6723–6753.

(18)   Bernhammer, J. C.; Frison, G.; Huynh, H. V. Electronic Structure Trends in N-Heterocyclic Carbenes (NHCs) with Varying Number of Nitrogen Atoms and NHC-Transition-Metal Bond Properties. *Chem. Eur. J.* **2013**, *19*, 12892–12905.

(19)   Canac, Y.; Soleilhavoup, M.; Conejero, S.; Bertrand, G. Stable Non-N-Heterocyclic Carbenes (Non-NHC): Recent Progress. *J. Organomet. Chem.* **2004**, *689*, 3857–3865.

(20)   Melaimi, M.; Soleilhavoup, M.; Bertrand, G. Stable Cyclic Carbenes and Related Species beyond Diaminocarbenes. *Angew. Chem. Int. Ed.* **2010**, *49*, 8810–8849.

(21)   Martin, D.; Canac, Y.; Lavallo, V.; Bertrand, G. Comparative Reactivity of Different Types of Stable Cyclic and Acyclic Mono- and Diamino Carbenes with Simple Organic Substrates. *J. Am.*

Chem. Soc. **2014**, *136*, 5023–5030.

(22)   Weinstein, C. M.; Junor, G. P.; Tolentino, D. R.; Jazzar, R.; Melaimi, M.; Bertrand, G. Highly Ambiphilic Room Temperature Stable Six-Membered Cyclic (Alkyl)(Amino)Carbenes. *J. Am. Chem. Soc.* **2018**, *140*, 9255–9260.

(23)   Hillier, A. C.; Sommer, W. J.; Yong, B. S.; Petersen, J. L.; Cavallo, L.; Nolan, S. P. A Combined Experimental and Theoretical Study Examining the Binding of N-Heterocyclic Carbenes (NHC) to the Cp*RuCl (Cp* = H5-C5Me5) Moiety: Insight into Stereoelectronic Differences between Unsaturated and Saturated NHC Ligands. *Organometallics* **2003**, *22*, 4322–4326.

(24)   Díez-González, S.; Nolan, S. P. Stereoelectronic Parameters Associated with N-Heterocyclic Carbene (NHC) Ligands: A Quest for Understanding. *Coord. Chem. Rev.* **2007**, *251*, 874–883.

(25)   Clavier, H.; Nolan, S. P. Percent Buried Volume for Phosphine and N-Heterocyclic Carbene Ligands: Steric Properties in Organometallic Chemistry. *Chem. Commun.* **2010**, *46*, 841–861.

(26)   Huynh, H. V. Electronic Properties of N-Heterocyclic Carbenes and Their Experimental Determination. *Chem. Rev.* **2018**, *118*, 9457–9492.

(27)   Back, O.; Henry-Ellinger, M.; Martin, C. D.; Martin, D.; Bertrand, G. 31P NMR Chemical Shifts of Carbene-Phosphinidene Adducts as an Indicator of the π-Accepting Properties of Carbenes. *Angew. Chem. Int. Ed.* **2013**, *52*, 2939–2943.

(28)   Rodrigues, R. R.; Dorsey, C. L.; Arceneaux, C. A.; Hudnall, T. W. Phosphaalkene vs. Phosphinidene: The Nature of the P–C Bond in Carbonyl-Decorated Carbene → PPh Adducts. *Chem. Commun.* **2014**, *50*, 162–164.

(29)   Vummaleti, S. V. C.; Nelson, D. J.; Poater, A.; Gómez-Suárez, A.; Cordes, D. B.; Slawin, A. M. Z.; Nolan, S. P.; Cavallo, L. What Can NMR Spectroscopy of Selenoureas and Phosphinidenes Teach Us about the π-Accepting Abilities of N-Heterocyclic Carbenes? *Chem. Sci.* **2015**, *6*, 1895–1904.

(30)   Enders, D.; Breuer, K.; Raabe, G.; Runsink, J.; Teles, J. H.; Melder, J.; Ebel, K.; Brode, S. Preparation, Structure, and Reactivity of 1,3,4- Triphenyl-4,5-Dihydro-LH-l,2,4-Triazol-5-Ylidene, a New Stable Carbene. *Angew. Chem. Int. Ed. Engl.* **1995**, *34*, 1021–1023.

(31)   Enders, D.; Niemeier, O.; Henseler, A. Organocatalysis by N-Heterocyclic Carbenes. *Chem. Rev.* **2007**, *107*, 5606–5655.

(32)   Gründemann, S.; Kovacevic, A.; Albrecht, M.; Faller, J. W.; Crabtree, R. H. Abnormal Ligand Binding and Reversible Ring Hydrogenation in the Reaction of Imidazolium Salts with IrH5(PPh3)2. *J. Am. Chem. Soc.* **2002**, *124*, 10473–10481.

(33)   Eugenia Aldeco-Perez, Amos J. Rosenthal, Bruno Donnadieu, Pattiyil Parameswaran, Gernot Frenking, G. B. Isolation of a C5-Deprotonated Imidazolium, a Crystalline "Abnormal" N-Heterocyclic Carbene. *Science* **2009**, *326*, 556–559.

(34)   Guisado-Barrios, G.; Bouffard, J.; Donnadieu, B.; Bertrand, G. Crystalline 1H-l,2,3-Triazol-5-Ylidenes: New Stable Mesoionic Carbenes (MICs). *Angew. Chem. Int. Ed.* **2010**, *49*, 4759–4762.

(35)   Vivancos, Á.; Segarra, C.; Albrecht, M. Mesoionic and Related Less Heteroatom-Stabilized N-

Heterocyclic Carbene Complexes: Synthesis, Catalysis, and Other Applications. *Chem. Rev.* **2018**, *118*, 9493–9586.

(36)   Sau, S. C.; Hota, P. K.; Mandal, S. K.; Soleilhavoup, M.; Bertrand, G. Stable Abnormal N-Heterocyclic Carbenes and Their Applications. *Chem. Soc. Rev.* **2020**, *49*, 1233–1252.

(37)   Wei Liu, Liang-Liang Zhao, Mohand Melaimi, Lei Cao, Xingyu Xu, Jean Bouffard, Guy Bertrand, X. Y. Mesoionic Carbene (MIC)-Catalyzed H/D Exchange at Formyl Groups. *Chem* **2019**, *5*, 2484–2494.

(38)   Hudnall, T. W.; Bielawski, C. W. An N,N′-Diamidocarbene: Studies in C-H Insertion, Reversible Carbonylation, and Transition-Metal Coordination Chemistry. *J. Am. Chem. Soc.* **2009**, *131*, 16039–16041.

(39)   Siemeling, U. Yes They Can: Small-Molecule Activation with Stable Diaminocarbenes. *Aust. J. Chem.* **2011**, *64*, 1109–1112.

(40)   Moerdyk, J. P.; Schilter, D.; Bielawski, C. W. N,N'-Diamidocarbenes: Isolable Divalent Carbons with Bona Fide Carbene Reactivity. *Acc. Chem. Res.* **2016**, *49*, 1458–1468.

(41)   Song, H.; Kim, Y.; Park, J.; Kim, K.; Lee, E. Activation of Small Molecules at N-Heterocyclic Carbene Centers. *Synlett* **2016**, *27*, 477–485.

(42)   Tomás-Mendivil, E.; Hansmann, M. M.; Weinstein, C. M.; Jazzar, R.; Melaimi, M.; Bertrand, G. Bicyclic (Alkyl)(Amino)Carbenes (BICAACs): Stable Carbenes More Ambiphilic than CAACs. *J. Am. Chem. Soc.* **2017**, *139*, 7753–7756.

(43)   Melaimi, M.; Jazzar, R.; Soleilhavoup, M.; Bertrand, G. Cyclic (Alkyl)(Amino)Carbenes (CAACs): Recent Developments. *Angew. Chem. Int. Ed.* **2017**, *56*, 10046–10068.

(44)   Lavallo, V.; Canac, Y.; DeHope, A.; Donnadieu, B.; Bertrand, G. A Rigid Cyclic (Alkyl)(Amino)Carbene Ligand Leads to Isolation of Low-Coordinate Transition-Metal Complexes. *Angew. Chem. Int. Ed.* **2005**, *44*, 7236–7239.

(45)   Roy, S.; Mondal, K. C.; Roesky, H. W. Cyclic Alkyl(Amino) Carbene Stabilized Complexes with Low Coordinate Metals of Enduring Nature. *Acc. Chem. Res.* **2016**, *49*, 357–369.

(46)   Soleilhavoup, M.; Bertrand, G. Cyclic (Alkyl)(Amino)Carbenes (CAACs): Stable Carbenes on the Rise. *Acc. Chem. Res.* **2015**, *48*, 256–266.

(47)   Moock, D.; Wiesenfeldt, M. P.; Freitag, M.; Muratsugu, S.; Ikemoto, S.; Knitsch, R.; Schneidewind, J.; Baumann, W.; Schäfer, A. H.; Timmer, A.; Tada, M.; Hansen, M. R.; Glorius, F. Mechanistic Understanding of the Heterogeneous, Rhodium-Cyclic (Alkyl)(Amino)Carbene-Catalyzed (Fluoro-)Arene Hydrogenation. *ACS Catal.* **2020**, *10*, 6309–6317.

(48)   Nascimento, D. L.; Fogg, D. E. Origin of the Breakthrough Productivity of Ruthenium-Cyclic Alkyl Amino Carbene Catalysts in Olefin Metathesis. *J. Am. Chem. Soc.* **2019**, *141*, 19236–19240.

(49)   Hansmann, M. M.; Melaimi, M.; Bertrand, G. Organic Mixed Valence Compounds Derived from Cyclic (Alkyl)(Amino)Carbenes. *J. Am. Chem. Soc.* **2018**, *140*, 2206–2213.

(50)   Mahoney, J. K.; Regnier, V.; Romero, E. A.; Molton, F.; Royal, G.; Jazzar, R.; Martin, D.; Bertrand, G. The Serendipitous Discovery of a Readily Available Redox-Bistable Molecule Derived from Cyclic (Alkyl)(Amino)Carbenes. *Org. Chem. Front.* **2018**, *5*, 2073–2078.

(51)   Mahoney, J. K.; Martin, D.; Thomas, F.; Moore, C. E.; Rheingold, A. L.; Bertrand, G. Air-Persistent Monomeric (Amino)(Carboxy) Radicals Derived from Cyclic (Alkyl)(Amino) Carbenes. *J. Am. Chem. Soc.* **2015**, *137*, 7519–7525.

(52)   Kundu, S.; Sinhababu, S.; Chandrasekhar, V.; Roesky, H. W. Stable Cyclic (Alkyl)(Amino)Carbene (CAAC) Radicals with Main Group Substituents. *Chem. Sci.* **2019**, *10*, 4727–4741.

(53)   Martin, C. D.; Soleilhavoup, M.; Bertrand, G. Carbene-Stabilized Main Group Radicals and Radical Ions. *Chem. Sci.* **2013**, *4*, 3020–3030.

(54)   Martin, D.; Soleilhavoup, M.; Bertrand, G. Stable Singlet Carbenes as Mimics for Transition Metal Centers. *Chem. Sci.* **2011**, *2*, 389–399.

(55)   Jazzar, R.; Soleilhavoup, M.; Bertrand, G. Cyclic (Alkyl)- And (Aryl)-(Amino)Carbene Coinage Metal Complexes and Their Applications. *Chem. Rev.* **2020**, *120*, 4141–4168.

Chapter 2 – Organocatalyzed Carbonylation with

Carbon Monoxide

2.1   Introduction

2.1.1   Carbene Organocatalysis: Limited to Lewis Bases.

A myriad of organic and main group compounds can accelerate and enable chemical reactions when used in substoichiometric quantities via a process known as organocatalysis. These organocatalysts have historically fallen into four different categories (or a combination thereof): Lewis bases, Lewis acids, Brønsted bases, and Brønsted acids.[1–4] Amongst the various organic compounds known to act as catalysts, C-nucleophiles, principally carbenes, have become powerful metal-free catalysts. The origins and capacity for carbenes to behave as organocatalysts can be traced back to 1958 when Breslow postulated that in the active site of thiamine-dependent decarboxylase enzymes, thiazolin-2-ylidene (**2.1**) was responsible for the in-vivo umpolung reactivity of aldehydes in benzoin condensations (Figure 2.1).[5] Since then, the field of carbene organocatalysis has largely relied on the Lewis basic nature of carbenes[4,6–12] although there is evidence for the possibility of radical catalysis.[13–15]
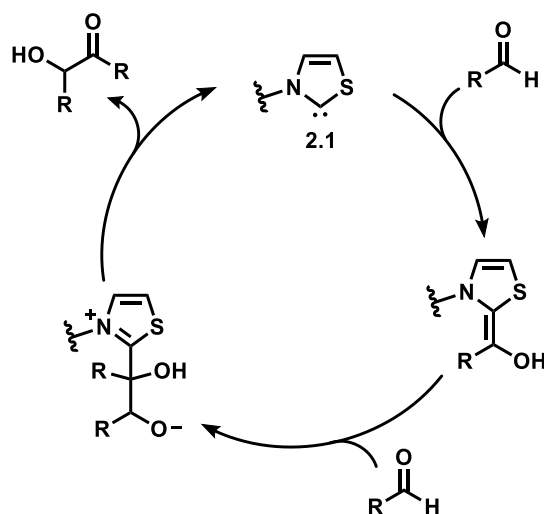
Figure 2.1: Catalytic cycle for nucleophilic carbene enabled Umpolung reactivity in the active site of thiamine based enzymes.

To extend the reach of carbenes beyond simply acting as Lewis bases in organocatalysis, we were inspired by a transition metal analogy. Ambiphilic carbenes, which possess a lone pair of electrons and an accessible vacant orbital, resemble transition metals.[16] Akin to metals, ambiphilic carbenes can activate

small molecules with the potential to engage in their catalytic transformation which would highlight ambiphilic carbenes' potential in organocatalysis.

2.1.2 Ambiphilic Carbene: Reductive Elimination.

The divergence between nucleophilic carbenes and ambiphilic carbenes lies in the ability for more ambiphilic carbenes to mimic the frontier orbital layout of transition metals, leading to challenging bond activation (Figure 2.2).[17] For ambiphilic carbenes such as CAACs, this analogy led to the oxidative addition of enthalpically strong E-H bonds (*e.g.*, E = H, B, N, Si, P),[16,18–20] but their exclusion from organocatalysis firmly rested upon the challenge of the reverse reaction, namely reductive elimination. This is a natural consequence of the stronger donating and accepting properties that are characteristic of highly ambiphilic carbenes. There are, however, a couple of recent examples that highlight strategies to enforce reductive elimination type processes and thereby, finally enable ambiphilic carbenes to achieve organo-carbene-catalysis beyond simply acting as a Lewis base.
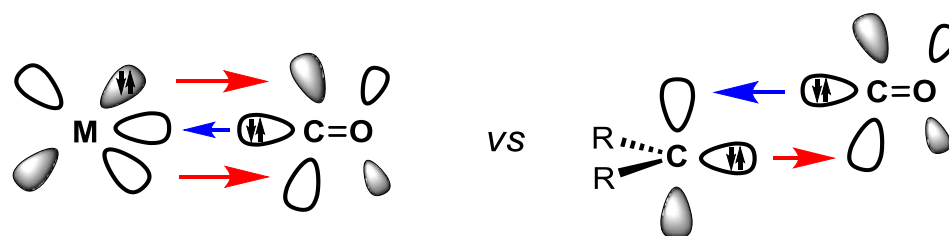
Figure 2.2: Ambiphilic orbital interactions are required for transition metals to coordinate and activate small molecules such as carbon monoxide (left). Since carbene's frontier orbitals are ambiphilic like transition metals, this enabled them to mimic the same behavior (right).

2.2.A

λ > 500 nm

NH₃

2.2.C

λ = 313 nm

2.2.B

λ > 500 nm

λ = 313 nm

NH₃
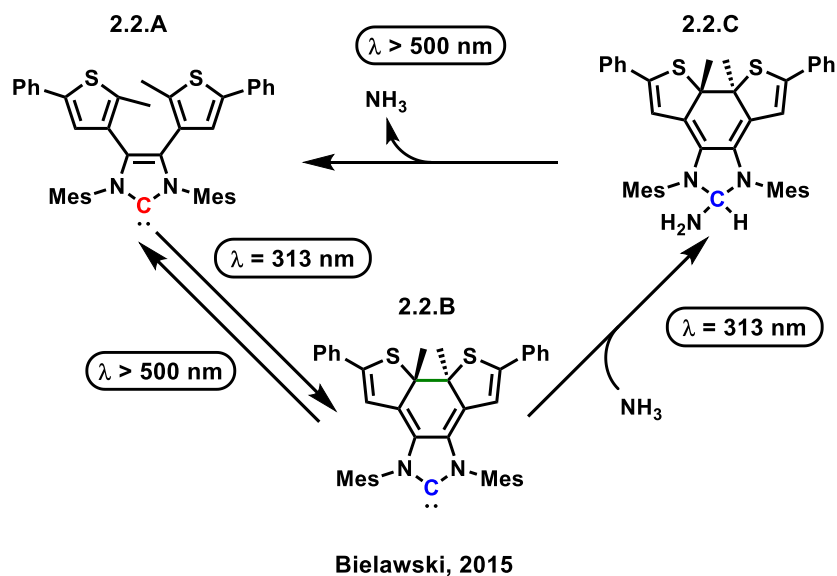
Bielawski, 2015

Scheme 2.1: Photoswitchable carbene leads to reversible bond activation of ammonia.

In 2015, Bielawski *et al.* installed a light responsive dithienylethene (DTE) backbone on an NHC to oscillate the electronics of the carbene.[21] Upon irradiating the free carbene (**2.2.A**) at 313 nm, the DTE backbone photoisomerized to engender a 6-membered ring on the backbone. This newly formed extended conjugated backbone predominantly resulted in further delocalization of electron density at the carbene center thereby significantly lowering the LUMO and leading to a more ambiphilic carbene (**2.2.B**). Additionally, through variations in the wavelength of irradiation, this carbene could cycle back and forth through **2.2.A** and **2.2.B**. Due to the change in electronics, however, **2.2.B** could then activate ammonia to generate the adduct (**2.2.C**). Notably, **2.2.A** was incapable of cleaving the challenging N-H bond. Upon irradiating the sample at >500 nm, the backbone ring opened and released ammonia to regenerate the free carbene of **2.2.A** (Scheme 2.1). This strategy highlights that the rational incorporation of photoswitchable functional groups can enable electronic fluctuation which leads to reductive elimination. Although the challenge of incorporating functional groups that are photoresponsive, limits the breadth of this type of strategy. However, a methodology that relies on a more readily tunable feature has also been recently developed to enable reductive elimination.
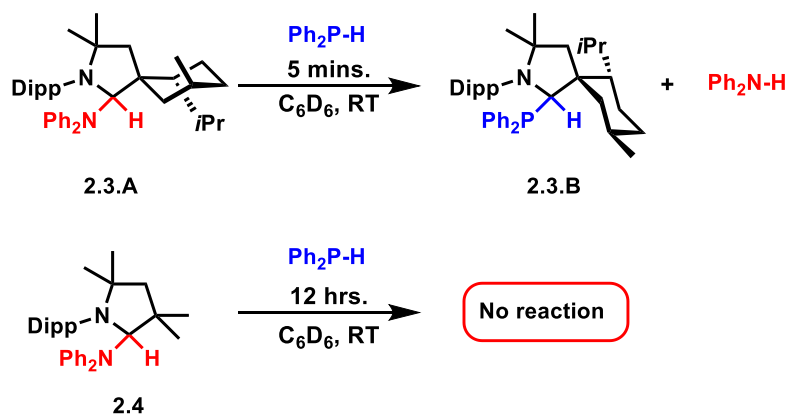
Bertrand, 2019

Scheme 2.2: The bulk of a CAAC determines whether or not reductive elimination occurs readily at room temperature. On top, the [Menth]CAAC's steric bulk enables the substrate substitution of diphenylamine for diphenylphosphine whereas on bottom, less bulky [Me]CAAC doesn't lead to an observable exchange at room temperature.

Another strategy demonstrates the ability for the readily tunable steric properties to induce difficult reductive eliminations in ambiphilic carbenes. Initially, in 2017, Radius *et al.* had discovered that CAACs could cleave the B-C(sp^2) bonds of organoboronates, and upon heating, they provided some preliminary evidence that this reaction was reversible.[22] However, in 2019, Bertrand *et al.* elucidated how sterically bulky CAACs could force reductive elimination to occur[23] which furthers the analogy in mimicking transition metal catalysts.[24] For instance, this behavior parallels the rate enhancement for reductive elimination observed in chelating bis(phosphine)Pd(II) complexes.[25] The rate of reductive elimination was dramatically increased with steric crowding at the active site induced by larger bite angles in the bis(phosphine) ligand. As for CAACs, the sterically bulky [Menthyl]CAAC was found to exchange the diphenylamine adduct in **2.3.A** for the more favorable P-C bond of diphenylphosphine to afford complex **2.3.B** (Scheme 2.1, top). The importance of the sterics is demonstrated by the contrast with the significantly less bulky [Me]CAAC whose diphenyl amine adduct (**2.4**) doesn't exchange with diphenylphosphine (Scheme 2.2, bottom).[23] Finally, as a proof of principle, a Lewis base catalyzed hydrophosphination reaction, known for nucleophilic NHCs,[26] was investigated for CAAC catalysts. The catalytic activity of the CAAC catalyst was reflected in its steric bulk in that the bulkiest [Menthyl]CAAC was the only one found to give complete

conversion to the alkene products (E/Z isomers) whereas the much smaller ^{Me}**CAAC** gave no conversion (Scheme 2.3).[23]
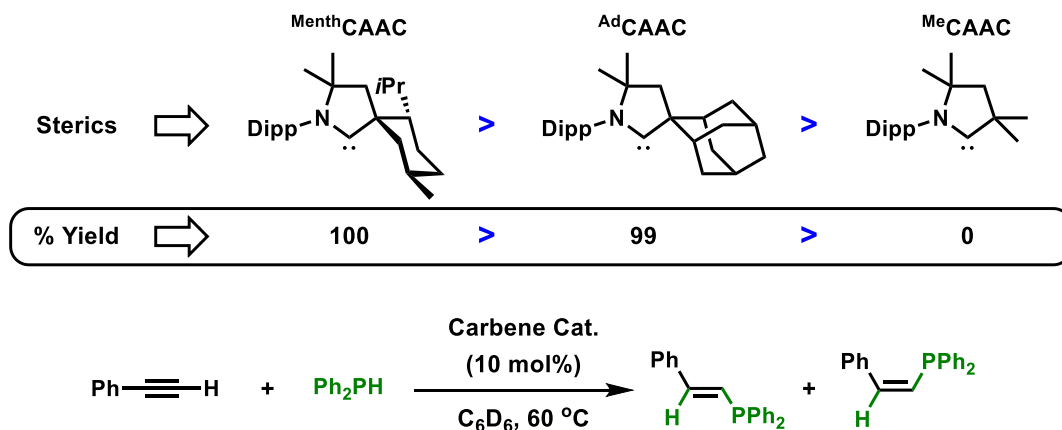
Scheme 2.3: Greater steric bulk parallels greater catalytic activity for CAAC in the hydrophosphination of phenylacetylene with diphenylphosphine, a transformation catalyzed by Lewis basic carbenes.

While this result, discovered through the analogy with transition metals, emphasized the importance of the steric environment around the carbene center, it was still a process known to be catalyzed by Lewis basic carbenes. Nevertheless, this study has led to a greater understanding of how to achieve the most challenging step for ambiphilic carbenes, reductive elimination and emphasized the importance of sterics as being the key to unlock their full potential in organocatalysis. To truly highlight the utility of ambiphilic carbenes in this type of catalysis, it is critical to exploit differences in their reactivity with carbenes that function predominantly as nucleophiles (*e.g.*, NHCs, ENHCs, and MICs).

2.1.3   Ambiphilic Carbenes: Activation of Carbon Monoxide.

Small molecules (*e.g.*, H_2, NH_3, CO, P_4) are notoriously difficult to activate as a result of their inherent thermodynamic stability.[27] Ambiphilic carbenes, however, can activate small molecules. Therefore, a niche wherein they can potentially catalyze processes distinct from their Lewis base-catalyst counterparts would be in small molecule activation. Carbon monoxide, for instance, has historically and predominantly been tamed by transition metals[28,29] but has been extremely challenging for main group species to coordinate. In carbene chemistry, only the most ambiphilic ones can coordinate and activate

carbon monoxide. Therefore, its transfer would emphasize ambiphilic carbenes' abilities in organocatalysis, namely carbonylation catalysis.
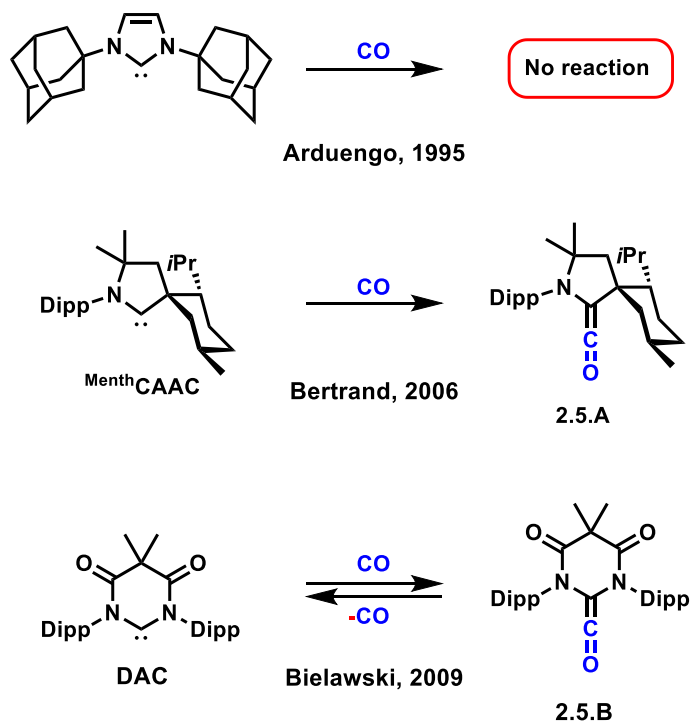
Scheme 2.4: 5-membered ring NHCs are incapable of forming a bond with carbon monoxide (top); however, the bulky 5-membered ^{Menth}CAAC is able to bind CO to afford the resulting (amino)ketene (middle); the **DAC** can also bind CO, but its weaker σ-donation leads to reversibility (bottom).

Soon after the discovery of NHCs, Arduengo *et al.* attempted to react CO with the 1,3-di-1-adamantylimidazol-2-ylidene to afford an (amino)ketene, but since there was no reaction, computational results were used to find that the only interaction was, "a non-bonded weakly interacting (van der Waals) complex," (Scheme 2.4, top).[30] This result was rather unsurprising given that amino(ketenes) were already described, at the time, as highly reactive transient intermediates.[31] To demonstrate that singlet carbenes were actually capable of fixating CO, in 2006, Bertrand *et al.* demonstrated that ^{Menth}CAAC (and an acyclic(alkyl)(amino) carbene) could react with carbon monoxide to afford the resulting (amino)ketene (**2.5.A**) (Scheme 2.4, middle).[32] Subsequently, in 2009, Bielawski reported the use of the *N,N′*-Diamido carbene (**DAC**) to bind CO which also affords an (amino)ketene (**2.5.B**), but due to the weaker σ-donating ability, the binding of CO was highly reversible (Scheme 2.4, bottom).[33] The reversibility of the **DAC**

coordination does suggest an important concept in organocatalysis: the potential for a carbene's leaving group ability to enhance the elimination of a potential product. Nonetheless, this difference between the **MenthCAAC** and **DAC** further demonstrates the importance of ambiphilicity in the activation and coordination of small molecules such as CO.
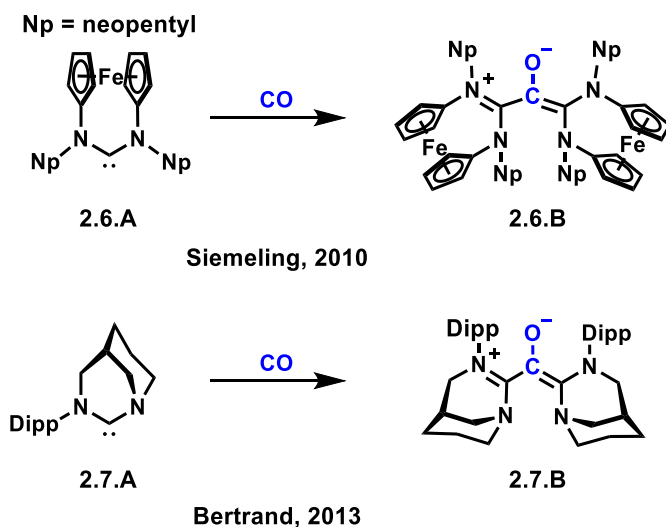
Scheme 2.5: Ambiphilic, sterically unencumbered carbenes add CO, but then immediately react with another equivalent of the carbene to form betaines.

Although the electronics of a carbene enable the activation of carbon monoxide, another important factor that has been discovered while investigating carbon monoxide reactivity is sterics. Siemeling *et al.* showcased this phenomenon upon using a [3]ferrocenophane-type NHC (**2.6.A**) — which features two pyramidalized amino substituents, due to the ferrocene backbone, leading to strong π-acidity coupled to a lesser amount of sterics at the carbene — to react with carbon monoxide.[34] Immediately, this ambiphilic carbene forms the (amino)ketene moiety from the CO; however, it then rapidly proceeds to react with another equivalent of carbene in solution to form the betaine (**2.6.B**) presumably due to reduced steric congestion at the carbene center (Scheme 2.5, top).[34] The importance of sterics was further exemplified by the reactivity of CO and the electrophilic anti-Bredt NHC (**2.7.A**). As described by Bertrand *et al.*, **2.7.A** features virtually no steric bulk on the pyramidalized nitrogen, which leads to the second nucleophilic attack of **2.7.A** to engender the oxyallyl or betaine moiety (**2.7.B**) (Scheme 2.5, bottom).[35] Therefore, it is clear

that bulky ambiphilic and to a lesser extent, electrophilic carbenes are capable of fixating CO provided that the steric bulk is adequate.

2.1.4   CAAC-catalyzed Carbonylation with Carbon Monoxide.

While the concept of transition metal mimicry has been limited to the previously mentioned fundamental stoichiometric processes such as oxidative addition, reductive elimination, and carbon monoxide fixation (Figure 2.3, A-C), these steps laid the foundation to push the analogy into the realm of catalysis that so far is reserved predominantly for transition metals.
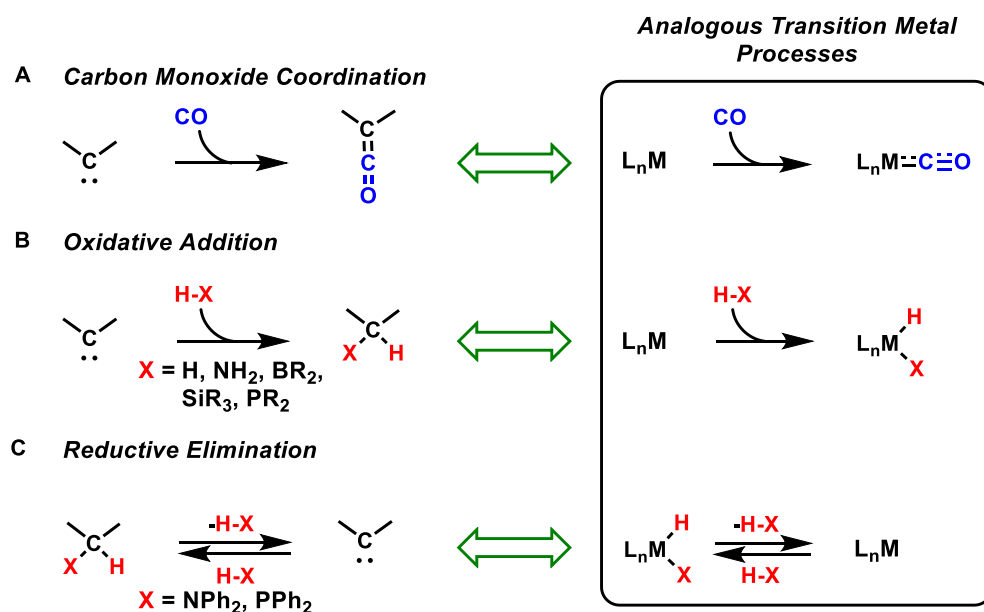
Figure 2.3: **(A)** The activation of carbon monoxide is not limited to transition metals. **(B)** Ambiphilic singlet carbenes can engage in a formal oxidative addition. (**C)** Despite the strong ambiphilicity of carbenes, reductive elimination is now tunable.

With these fundamental studies in mind, the key to the catalytic carbonylation hinges on transforming the carbon monoxide bound in the (amino)ketene and releasing the new compound by using appropriate sterics or electronics by reductive elimination. To achieve the goal of (amino)ketene transformation, we were inspired by the reactivity of alkyl and aryl substituted ketenes (RR'C=C=O). These ketenes are known to react with *ortho*-quinones leading to the corresponding spirolactones,[36–39] and therefore, we hypothesized that the more reactive (amino)ketenes should react similarly (Scheme 2.6).
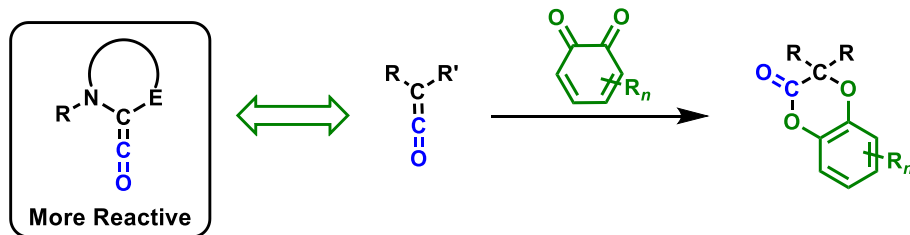
Scheme 2.6: The more reactive (amino)ketenes should react analogously to their alkyl and aryl substituted ketene (RR'C=C=O) equivalents which are known to react with *o*-quinones to give spirolactones.

This prompted us to envisage a singlet carbene catalyzed carbonylation of *ortho*-quinones into cyclic carbonates using carbon monoxide which would demonstrate that ambiphilic carbenes can indeed facilitate catalytic carbonylation (Figure 2.4). We anticipated that an accessible ketene (*Step 1*), should react with a quinone to afford the corresponding [4+2] cycloadducts (*Step 2*). These adducts should then undergo reductive elimination thanks to the steric bulk or electronic properties provided by the carbene catalyst, thus closing the cycle (*Step 3*). Herein, we illustrate through our mechanistic study that catalysis is possible with 9,10-phenanthrenequinone (**Quin-1**) as a model substrate. Then, we demonstrated catalysis as a proof of concept.
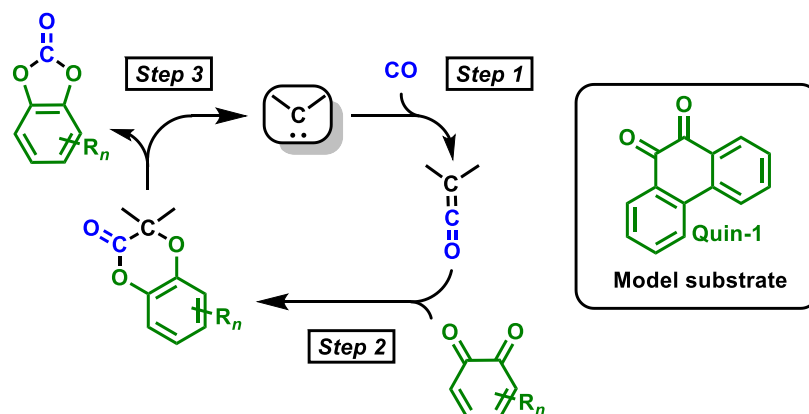
Figure 2.4: Proposed mechanistic cycle for the carbonylation of *ortho*-quinones using singlet-carbenes as catalysts with 9,10-phenanthrenequinone (**Quin-1**) as a model substrate.

2.2   Results & Discussion

We began our study by examining the stoichiometric reactivity of ^MenthCAAC with carbon monoxide and

9,10-phenanthrenequinone (**Quin-1**). As previously mentioned, the **DAC** is one of the handful of carbenes known to bind CO,[33] but it also functions as an excellent leaving group; therefore, we also considered it as a carbene catalyst. Furthermore, it has been shown that only a few other stable singlet carbenes, featuring a sufficiently small singlet-triplet (S/T) gap,[40] could add CO to afford the corresponding ketenes. So, we also considered our recently reported bicyclic (alkyl)(amino)carbene (**BiCAAC**) with a smaller S/T gap of 45.7 kcal/mol as compared to the ^{Menth}**CAAC** which has a S/T gap of 49.2 kcal/mol.[41] To begin, we synthesized the corresponding (amino)ketenes for the CAAC family of ligands which were synthesized by simply reacting ^{Menth}**CAAC**, and **BiCAAC** with carbon monoxide at room temperature in benzene to afford (amino)ketenes, **2.5.A** and **2.5.C** respectively (Scheme 2.7). With each of these ketenes in hand, their reactivity with **Quin-1** was investigated at room temperature in benzene. We discovered that the **2.5.A** and **2.5.C** both resulted in clean quantitative conversion to the corresponding [4+2] cycloadducts. These complexes were isolated as single diastereomers, **2.8.A** and **2.8.C** respectively, and confirmed by an X-ray crystallographic study (Scheme 2.7).
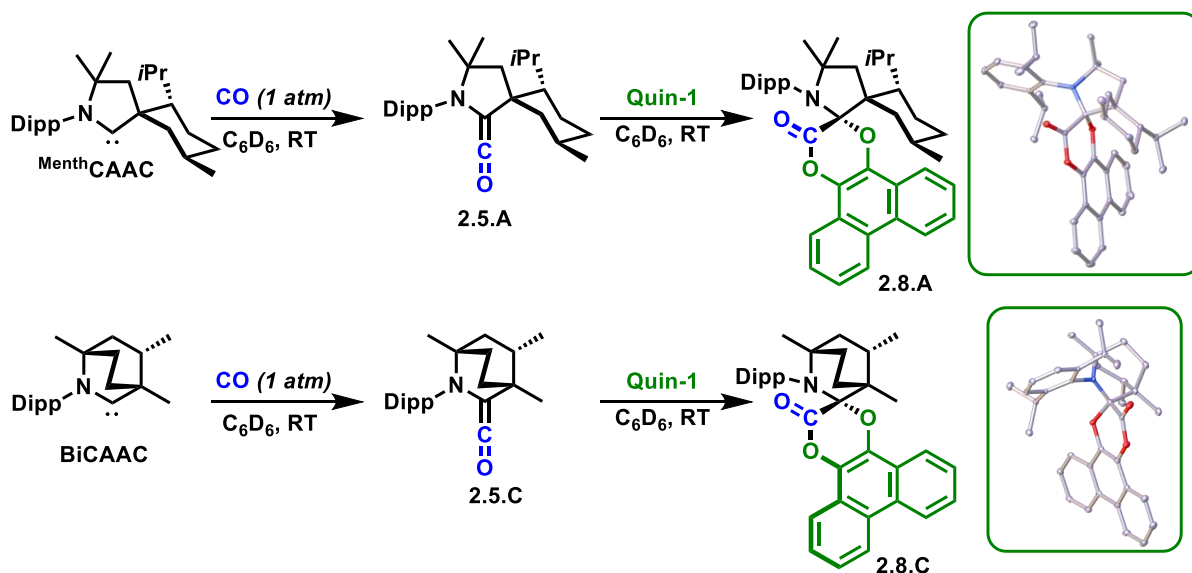
Scheme 2.7: The CAAC (^{Menth}**CAAC** and **BiCAAC**) family of carbenes form (amino)ketenes (**2.5.A** and **2.5.C** respectively) with carbon monoxide which can subsequently react with *ortho*-quinones to form their corresponding spirolactones (**2.8.A** and **2.8.C** respectively).

However, the less basic **DAC** was confirmed to react with CO to give in equilibrium with (amino)ketene

2.5.B. Subsequently, this mixture led to two products upon reacting with **Quin-1**: the desired spirolactone, **2.8.B**, and the presence of another product **2.9.B** which we postulated was the *o*-quinone adduct (Scheme 2.8). This presumably resulted from **Quin-1** reacting with **DAC** free carbene because of the reversible coordination of carbon monoxide.
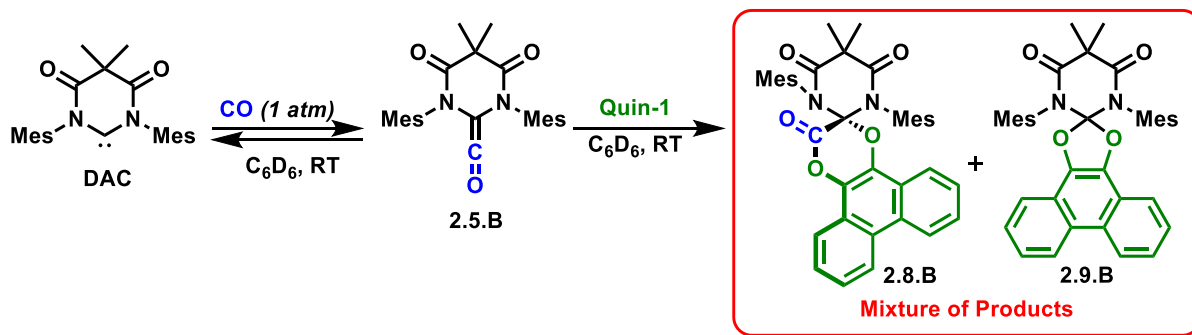
Scheme 2.8: The **DAC** reversibly binds CO to form (amino)ketene **2.5.B** which gives a mixture of products: one of which is the corresponding spirolactone (**2.8.B**), but the other involves a reaction between **DAC** and the **Quin-1** to afford the adduct (**2.9.B**).

To verify this hypothesis, we independently investigated the reaction between the **DAC** and **Quin-1** which did indeed afford **2.9.B** as exemplified by X-ray crystallography (Scheme 2.9, top). Notably, this reactivity highlighted a catalyst deactivation pathway where the free carbene itself reacts with the substrate before the (amino)ketene has a chance to form. At this juncture, we thought it prudent to probe the reactivity of each carbene catalyst with this substrate and as expected, the unhindered **BiCAAC** reacted with **Quin-1**. Yet again, we observed the rapid, irreversible formation of a spirocyclic compound **2.9.C** (Scheme 2.9, bottom). These results precluded the use of both of these carbenes as catalysts due to the irreversibility of the chelated quinone-adduct.
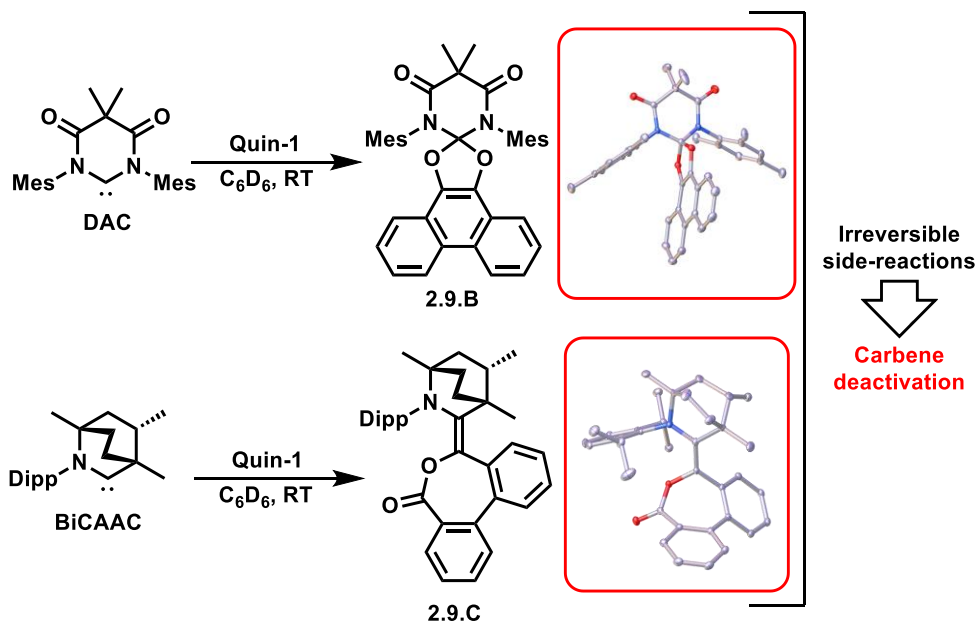
Scheme 2.9: **DAC** and **BiCAAC** react with the **Quin-1** to afford **2.9.B** and **2.9.C** respectively thereby preventing carbonylation catalysis.

In marked contrast, ^{Menth}CAAC remained unreacted under the same conditions, which we attributed to the significantly greater steric protection at the carbene center provided by the Menthyl substituent (Scheme 2.10, top). To confirm the necessity of sterics for this lack of reactivity, we proceeded to react the much less bulky ^{Me}CAAC with **Quin-1** and immediately found that it engendered a carbene catalyst deactivated product **2.9.D** (Scheme 2.10, bottom).
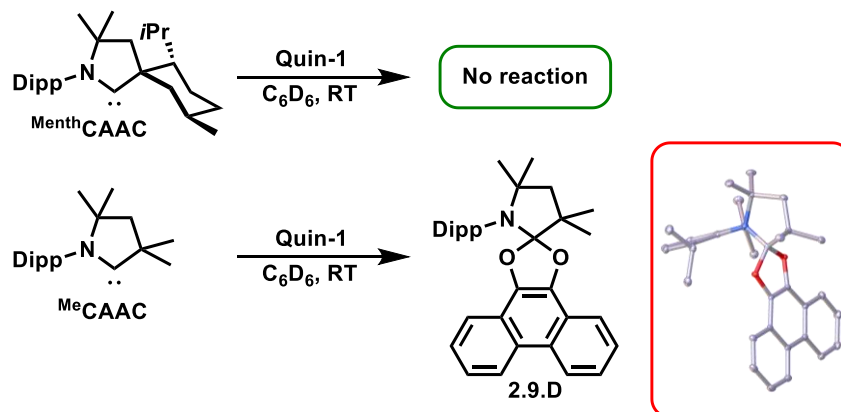
Scheme 2.10: Sterically bulky ^{Menth}CAAC does not react with **Quin-1** whereas the unencumbered ^{Me}CAAC reacts irreversibly to afford **2.9.D** preventing its use as a carbonylation catalyst.

31

We then continued to demonstrate a stepwise mechanistic pathway with the only viable catalyst readily available, [Menth]CAAC. After demonstrating that **2.8.A** can form from **2.5.A**, we sought to investigate the most challenging step of the sequence, the reductive elimination. We hypothesized that thanks to the steric bulk of the menthyl substituent, which was previously found to block the substrate from deactivating the catalyst, there should be an equilibrium occurring to reversibly coordinate the product (Scheme 2.11).
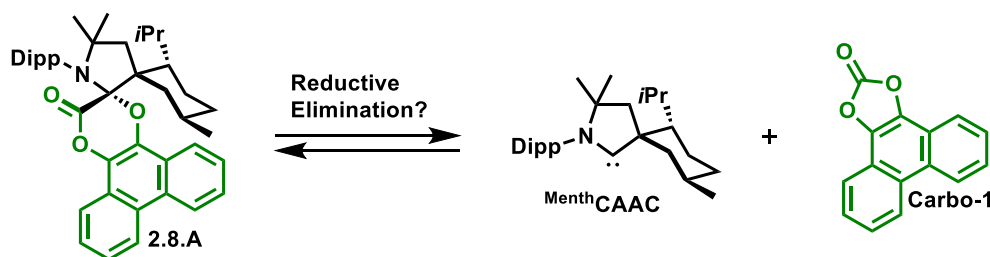
Scheme 2.11: [Menth]CAAC should be bulky enough to engender reductive elimination from **2.8.A** but it is not readily observable due to an equilibrium between the carbene and the product (**Carbo-1**).

Reaction of **2.8.A** with elemental sulfur (S_8), a classical trapping agent for singlet carbenes,[42] afforded the thiolactam (**2.10.A**) ($^{13}C\{^1H\}$ NMR characteristic carbene carbon signal of **2.10.A**:[23] 209.9 ppm in THF-d_8), along with the free carbonate **Carbo-1** in quantitative yield, thus confirming an equilibrium between **Carbo-1** and the adduct, **2.8.A**, in solution at room temperature (Scheme 2.12, and $^{13}C\{^1H\}$ NMR data for reaction: Figure 2.5).
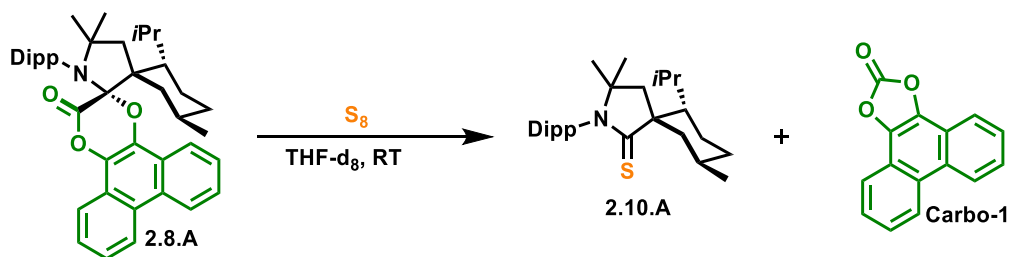
Scheme 2.12: Because of the sterics of [Menth]CAAC, the free carbene can be trapped with S_8 due to the room temperature reversible release of **Carbo-1** from **2.8.A** to afford the thiolactam (**2.10.A**).
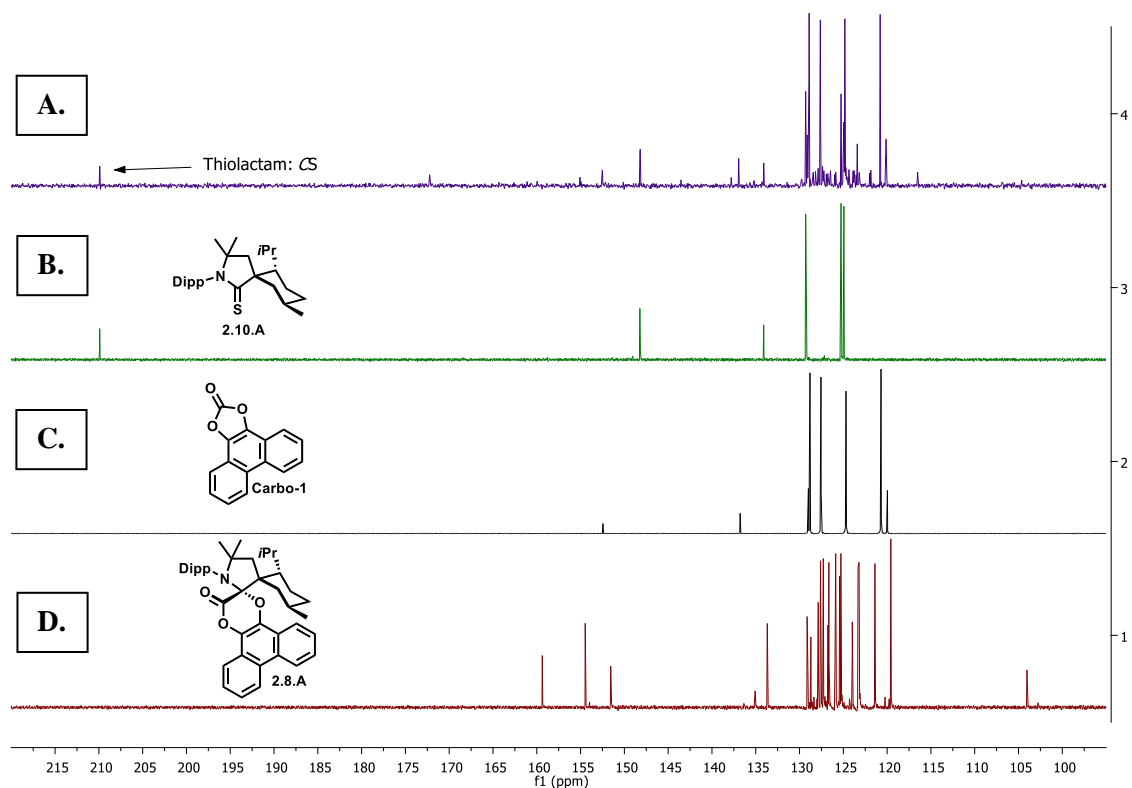
Figure 2.5: Stacked $^{13}\text{C}\{^1\text{H}\}$ NMR (125.7 MHz, THF-d_8) spectra showing room temperature reductive elimination from **2.8.A** by trapping the carbene as **2.10.A**; **A.** *In situ* reaction mixture of **2.8.A** with elemental sulfur at room temperature after 16 hours (characteristic *C*S signal at 209.9 ppm); **B.** Isolated **2.10.A**; **C.** Isolated **Carbo-1**; **D.** Isolated **2.8.A**.

Next, we set out to probe whether the catalyst could regenerate **2.5.A** from **2.8.A** despite the equilibrium. This would conclusively demonstrate that the catalyst can undergo a turnover in the catalytic cycle. To confirm this possibility, we proceeded to trap $^{\text{Menth}}$**CAAC** as **2.5.A** with the carbon monoxide substrate, thus mimicking our proposed catalytic conditions (Scheme 2.13). Unsurprisingly, 1 bar of CO was insufficient; however, we were pleased to observe the formation of **2.5.A** ($^{13}\text{C}\{^1\text{H}\}$ NMR characteristic *CC*O ketene signal:[32] 278.8 ppm in THF-d_8) and **Carbo-1** when using 4 bar of CO, supporting a pressure dependent equilibrium (Scheme 2.13, $^{13}\text{C}\{^1\text{H}\}$ NMR data for the reaction: Figure 2.6).

33
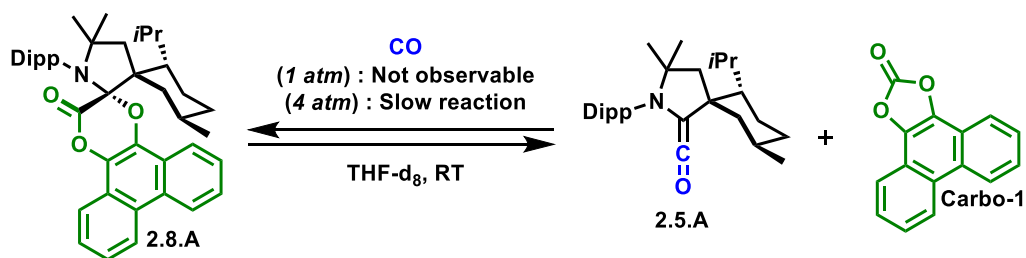
Scheme 2.13: Observation that **2.8.A** can reductively eliminate **Carbo-1** at room temperature and reform **2.5.A** which demonstrates the possibility for catalysis.

Curious to understand the nature of the reductive elimination step, we also confirmed the existence of an equilibrium between **2.5.A** and ^{Menth}**CAAC** upon slow dissociation of CO under vacuum over 24 hours (Scheme 2.14). The accessibility of ^{Menth}**CAAC**, from **2.5.A**, led us to examine the reaction between ^{Menth}**CAAC** and **Carbo-1**, which afforded the intermediate cycloadduct **2.8.A**, thus demonstrating the reversibility of the reductive elimination step (Scheme 2.14). This is in marked contrast with **2.5.A** which did not react at an appreciable rate with **Carbo-1** under the same conditions, but instead, only reacts slowly at higher temperatures to give **2.8.A**, presumably limited by the slow dissociation of CO under an argon atmosphere (Scheme 2.14). Therefore, nearly every intermediate in the catalytic cycle is reversible to some extent. The only irreversible process is the reaction between **Quin-1** and **2.5.A** to form **2.8.A**. This reaction's irreversibility, therefore, is essential in driving the catalytic cycle forward in productive catalysis.
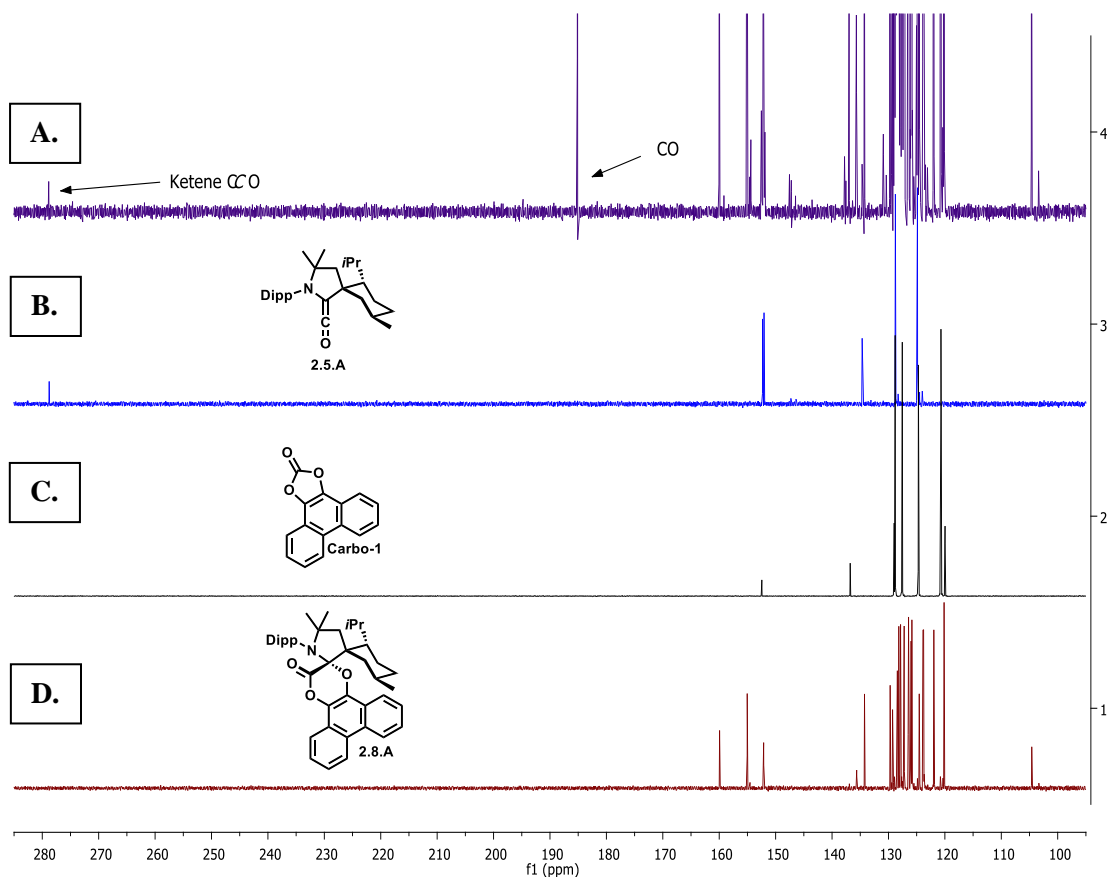
Figure 2.6: Stacked $^{13}C\{^1H\}$ NMR (125.7 MHz, THF-d_8) spectra showing room temperature reductive elimination from **2.8.A**; **A.** *In situ* reaction mixture of **2.8.A** with $CO_{(g)}$ (4 atm) at room temperature after 48 hours (characteristic (amino)ketene CCO signal at 278.8 ppm); **B.** Isolated **2.5.A**; **C.** Isolated **Carbo-1**; **D.** Isolated **2.8.A**.
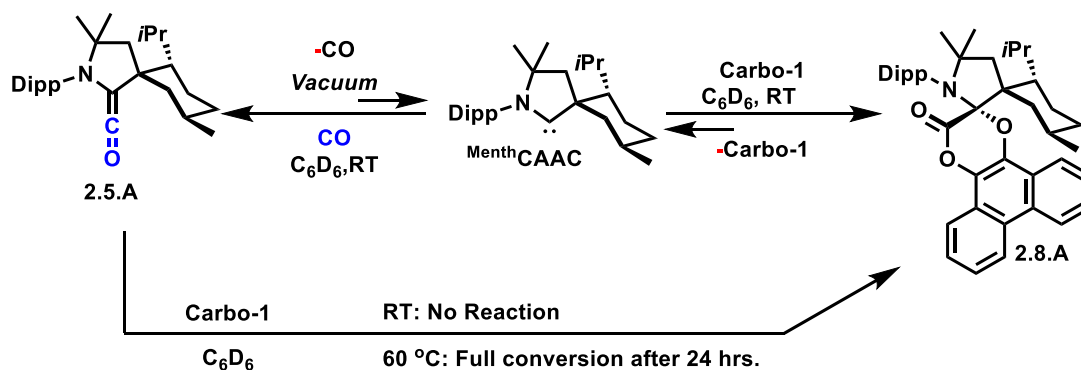
Scheme 2.14: (Amino)ketene **2.5.A** dissociates CO gas to form ^{Menth}**CAAC** which can subsequently oxidatively add **Carbo-1** to generate **2.8.A.** Additionally, **2.5.A** can add **Carbo-1** at 60 °C to form **2.8.A** showing the reversibility of our potential catalytic process.

35

From this short mechanistic investigation, it appeared that the formation of compound **2.8.A** can be generated either from the reaction of a quinone with a ketene, or reversibly from the insertion of ^{Menth}CAAC into the C-O single bond of the carbonate product, **Carbo-1**. To confirm these findings and get a more accurate depiction of this process, DFT analysis was performed (Figure 2.7). We found that the formation of **2.8.A** involves addition of the *o*-quinone on the highly polarized **2.5.A** resulting in a transient zwitterionic adduct **2.11**. Moreover, and in line with our experimental results, we found the formation of **2.8.A** to be exergonic with respect to **2.5.A**, but also with respect to the elimination of the product **Carbo-1**, which suggests that the reductive elimination of the carbonate is rate limiting. The reductive elimination is proposed to occur through an accessible kinetic diastereomer **2.8.A'** but was unobservable for the sterically encumbered ^{Menth}CAAC.
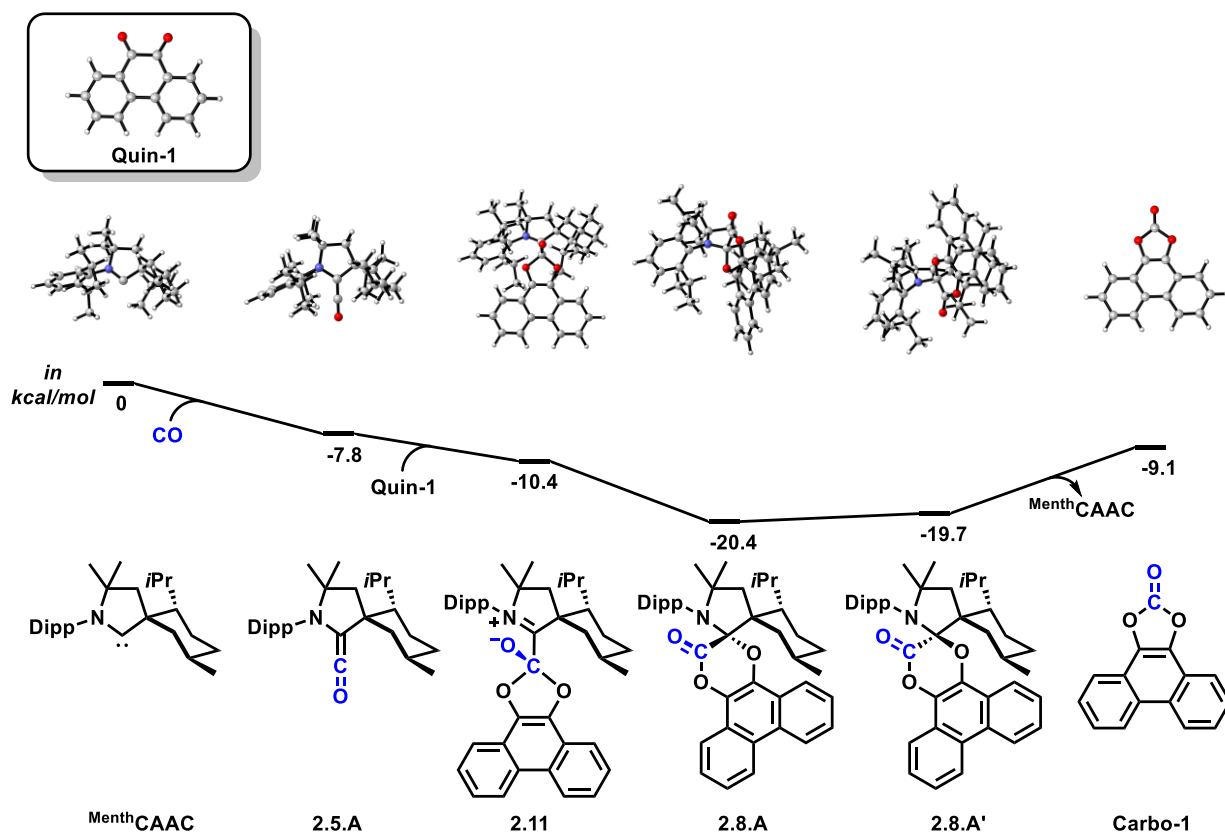
Figure 2.7: Computed free energy profile for the proposed and isolated catalytic intermediates, and product that demonstrates the exergonic nature of the reaction of ^{Menth}CAAC, CO gas, and **Quin-1** as a model substrate to generate **Carbo-1** (B3LYP/def2-TZVP level).[43,44]

36

Table 2.1: CAAC-catalyzed carbonylation with carbon monoxide.
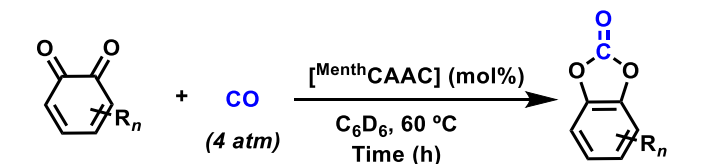
Entry	Quinone	[MenthCAAC] (mol%)	Time (h)	Yield (%)	TON	Carbonate
1	Quin-1	20	24	100[a]	5	Carbo-1
2	Quin-1	-	24	0	0	-
3	Quin-1	10	24	100[a]	10	Carbo-2
4	Quin-1	10	40	79.6[b]	8	Carbo-1
5	Quin-2	5	40	94.5[b]	19	Carbo-2

Quin-1   Quin-2

Carbo-1   Carbo-2
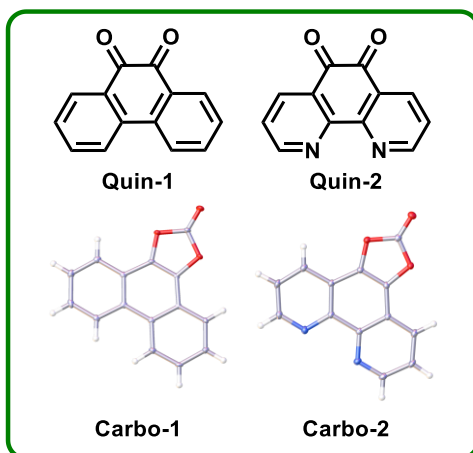
(a) Yield determined by ^1H NMR analysis
(b) Isolated Yield

With a clear mechanistic pathway in mind, and with a favorable energetic landscape highlighted by DFT, we set out to investigate our overarching catalytic objective: to demonstrate for the first time that ambiphilic carbenes are capable of mimicking metals in catalytic carbonylation using carbon monoxide as a C_1 source. As confirmed experimentally and computationally, the release of **Carbo-1** required elevated tempertures. After initial optimization (Table 2.2), gratifyingly, we found that **MenthCAAC** was capable of catalytically generating **Carbo-1** in benzene after 24 hours at 60 °C under 4 bar of CO gas (N.B. we found that **DAC**, **BiCAAC**, and **MeCAAC** do not catalyzed the process). Indeed, with a 20 mol% catalyst loading under these conditions, we achieved 5 TON and 100% conversion (Table 2.1, entry 1). The formation of

Carbo-1 was established by ^{1}H and ^{13}C{^{1}H} NMR, and further demonstrated by an X-ray diffraction study. To unambiguously confirm the catalytic activity of [Menth]CAAC, the reaction was repeated in the absence of catalyst under the optimized conditions. Unsurprisingly, no conversion was observed under these conditions even after 24 hours (Table 2.1, entry 2). As proposed previously, the reductive elimination step in this system is rate limiting. To confirm this hypothesis and push the catalysis further, we reasoned that a substrate with a better leaving group ability than **Quin-1** could overcome the challenging reductive elimination step. This was achieved upon using 1,10-phenanthroline-5,6-dione, **Quin-2**, which features an electron-withdrawing bipy backbone. Using the initially optimized conditions, we achieved 100% conversion and 10 TON using 10 mol% of catalyst (Table 2.1, entry 3). Here also, we fully established the structure of **Carbo-2** spectroscopically and by X-ray diffraction. Finally, lowering the catalyst loading and running the reaction for 40 hours at 60 °C allowed us to achieve 8 TON and 19 TON upon isolation of **Carbo-1** and **-2** respectively (Table 2.1, entry 4 and 5).

2.3   Conclusion

Until now, the only carbenes considered for organocatalysis have been limited to Lewis bases that engage in nucleophilically catalyzed processes. The catalysts typically feature weak bases that can behave as good leaving groups with a large HOMO/LUMO gap (*e.g.*, NHCs and ENHCs) and this trope has precluded the consideration of ambiphiles which tend to be stronger donors and worse leaving groups. Fortunately, we have shown that this barrier can be overcome through the careful design of more sterically hindered carbene catalysts. Additionally, this work demonstrates that strongly ambiphilic carbenes such as CAACs can be highly desirable in catalysis as their electronic properties allow for coordinating and activating challenging small molecules. Analogous to the foundation of organometallic chemistry, where the first carbonyl complexes opened the path to highly desirable catalytic carbonylation reactions, we believe that our stepwise mechanistic investigation and catalytic proof of principle have led to a paradigm shift in that ambiphilic carbenes can now be considered as organocatalysts in carbonylation reactions.

Therefore, this investigation has further advanced their analogy with transition metals. Since several other low-valent main-group compounds, such as silylenes,[45] phosphinidenes[46–48] and borylenes[49–52] are able to bind CO these findings pave the way for the discovery of other metal-free catalyzed carbonylation reactions.[53]

2.4 Appendix

2.4.1 General Methods & Materials.

All manipulations were performed — unless otherwise noted — under an atmosphere of dry argon using standard Schlenk or dry box techniques. Solvents were dried by standard methods and distilled under argon. ^{1}H, ^{13}C NMR spectra were recorded on a Varian VX 500, Bruker 300, and Jeol 500 spectrometer. Chemical shifts are given in ppm and are referenced to $SiMe_4$ (^{1}H, ^{13}C). Coupling constants *J* are given in Hertz as positive values regardless of their real individual signs. NMR multiplicities are abbreviated as follows: s = singlet, d = doublet, t = triplet, q = quartet, sept = septet, m = multiplet, br = broad signal. All spectra were obtained at 25 °C in the solvent indicated. For all neat or solid-state samples, FTIR spectra were collected on thin-film samples using a JASCO FTIR-4100 fitted with an ATR accessory (ZnSe plate). Solution phase FTIR spectra were recorded on a Thermo-Nicolet iS10 FTIR spectrometer. Samples were prepared as solutions with the corresponding solvent and injected into a ThermoFisher solution cell equipped with KBr windows. Solvent peaks were digitally subtracted from all solution FTIR spectra by comparison with an authentic solvent spectrum obtained prior to that of the sample. The intensities of the selected peaks are abbreviated as follows: s = strong, m = medium, w = weak, br = broad. UV-Vis spectra were recorded on a Shimadzu UV–3600 UV/vis/NIR spectrometer, and samples were prepared as solutions under argon and transferred to an air-tight cuvette (l= 1.0 mm). The Mass spectra were performed at the UC San Diego Mass Spectrometry Laboratory on an Agilent 6230 Accurate-Mass TOFMS spectrometer. Single crystal X-ray diffraction data were collected on Bruker Apex diffractometers at the UC San Diego Crystallography Facility. **BiCAAC**,[41] ^{Menth}**CAAC**,[54] **DAC**[55] and ^{Me}**CAAC**[56] were prepared as reported in

the literature, while all other starting materials were purchased from commercial sources and used without further purification.

2.4.2   Experimental Procedures & Characterization Data.

Reaction of ^{Menth}CAAC with carbon monoxide to afford 2.5.A.
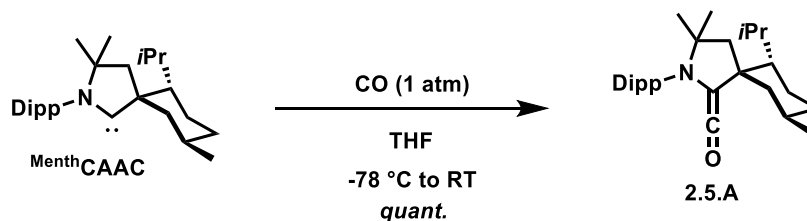
Scheme 2.15: Synthesis of known (amino)ketene (**2.5.A**) from ^{Menth}CAAC and CO$_{(g)}$.

In a J. Young NMR tube, ^{Menth}CAAC (0.2 g, 0.524 mmol) was dissolved in 1 mL of dry THF under argon atmosphere. The solution was cooled down to -78 °C and it was degassed under vacuum. Carbon monoxide (1 atm) was introduced into the tube and upon warming to room temperature, the solution turned blue. The degasification/CO gas introduction process was repeated three times until the solution was a deep blue. The conversion to the known **2.5.A**[32] was quantitative and clean in solution. Afterwards, to isolate the solid, volatiles were removed under vacuum at 0 °C and a minimum amount of dry pentane was added (1 mL). Upon storing the solution in the freezer (-40 °C) under an inert atmosphere (Argon filled glovebox) blue crystals appeared, which were decanted and dried. Yield 90% (0.193 g for preparative scale).
Characterization data: ^{1}**H NMR** (500 MHz, THF-d$_8$): δ = 7.26-7.10 (m, 3H), 3.65 (sept, J = 6.8, 1H), 3.57 (sept, J = 6.8, 1H), 2.59 (dt, J = 12.6, 2.3 Hz, 1H), 2.55 (d, J = 13.1 Hz, 1H), 2.39 (sept, J = 6.8 Hz, 1H), 1.85 (d, J = 13.1 Hz, 1H), 1.65-1.62 (m, 1H), 1.57-1.53 (m, 1H), 1.39-1.34 (m, 2H), 1.31-1.24 (m, 13H), 1.07 (d, J = 6.8 Hz, 3H), 1.02 (d, J = 6.8 Hz, 1H), 1.00 (d, J = 6.8 Hz, 3H), 0.90 (d, J = 6.6 Hz, 3H), 0.87-0.79 (m, 2H) ppm; ^{13}**C{^{1}H} NMR** (125.7 MHz, THF-d$_8$): δ = 278.8, 152.3, 152.1, 134.7, 128.8, 125.0, 124.8, 81.6, 64.9, 55.2, 53.9, 50.1, 50.0, 35.5, 31.4, 31.3, 30.6, 29.3, 29.2, 28.5, 26.9, 26.2, 23.9, 23.6, 22.8, 18.5 ppm.

Reaction of BiCAAC with carbon monoxide to afford 2.5.C.
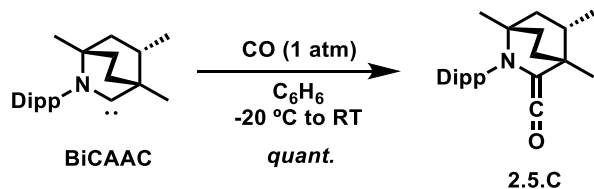
Scheme 2.16: Synthesis of (amino)ketene (**2.5.C**) from **BiCAAC** and $CO_{(g)}$.

In a pressure Schlenk (or Young NMR tube for small scale reaction) free **BiCAAC** (0.100 g, 0.32 mmol for preparative scale; 0.030 g, 0.096 mmol in Young NMR tube) was dissolved in 3 mL of dry benzene or 0.7 mL of dry deuterated benzene, respectively, under argon atmosphere. The solution was cooled down to -20 °C until the solvent froze and it was degassed under vacuum. Carbon monoxide was introduced into the flask and it was warmed to room temperature. The solution immediately turned blue when benzene melted (5 °C). The degasification/CO gas introduction process was repeated three times until the solution was deep blue. The conversion to **2.5.C** was quantitative and clean. In order to isolate the product as blue crystalline solid, volatiles were removed under vacuum and minimum amount of dry pentane was added (1 mL). Upon storing the solution in the freezer (-40 °C) under inert atmosphere (Argon filled glovebox), blue crystals appeared which were decanted and dried. Yield 85% (0.092 g for preparative scale). *(The reaction is instantaneous at RT and CO bubbling is neither needed nor recommended to avoid undesired side-products).* **Characterization data: IR** (20 mg/mL in pentane): $\nu_{(CO\ stretching)}$ = 2080 cm^{-1}; **UV-vis**. (20 mg/mL in pentane): broad band from 500 to 700 nm (λ_{max} 580 nm); **^{1}H NMR** (500 MHz, C_6D_6): δ = 7.14-7.08 (m, 1H), 7.05-7.01 (m, 2H), 3.71 (sept, J = 6.9 Hz, 1H), 3.60 (sept, J = 6.9 Hz, 1H), 2.10-1.99 (m, 2H), 1.71-1.59 (m, 4H), 1.46-1.40 (m, 1H), 1.31 (d, J = 6.9 Hz, 3H), 1.28-1.23 (m, 9 H), 1.09 (d, J = 6.5 Hz, 3H), 0.74 (s, 3H), 0.69 (s, 3H), ppm; **^{13}C{^{1}H} NMR** (125.7 MHz, C_6D_6): δ = 270.7, 150.8, 150.7, 138.4, 128.3, 124.6, 124.2, 78.7, 52.4, 46.5, 37.2, 36.4, 35.5, 33.6, 28.9, 28.6, 26.0, 25.3, 24.6, 24.2, 23.6, 21.0, 18.6 ppm.
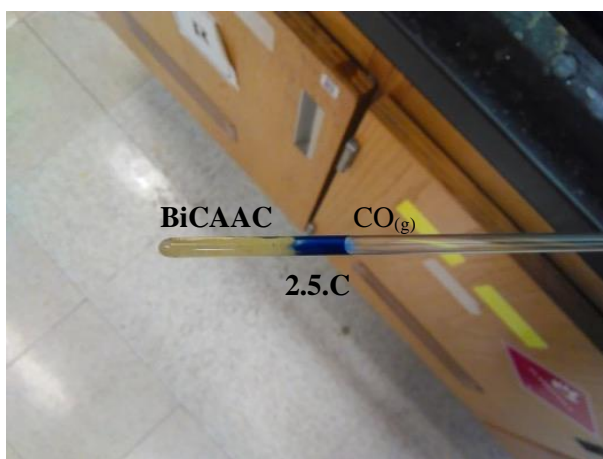
Figure 2.8: Synthesis of (amino)ketene **2.5.C** in a J. Young NMR tube. From left to right: **BiCAAC** in a frozen C_6D_6 solution is colorless to pale yellow; upon melting the solution, **2.5.C** is formed as evidenced by the deep blue color of the solution; and the $CO_{(g)}$ atmosphere in the headspace.

Routes to 2.8.A.
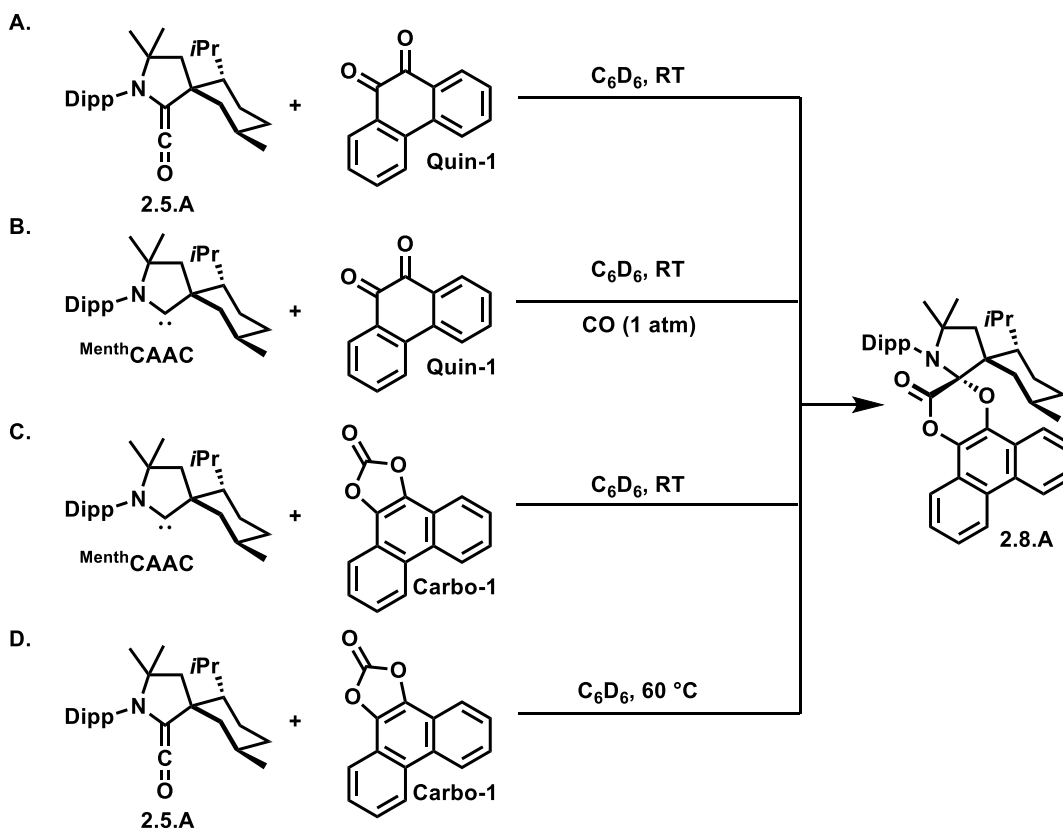
Scheme 2.17: Synthetic routes to **2.8.A**; **A. 2.5.A** reacts with **Quin-1**; **B.** Upon mixing ^MenthCAAC and **Quin-1**, no reaction occurs until after CO(g); **C. Carbo-1** can directly add to ^MenthCAAC demonstrating an equilibrium; **D.** An equilibrium exists at 60 °C as **2.5.A** can release CO(g) and add **Carbo-1** when under argon.

Route A: Reaction of 2.5.A with Quin-1 to afford 2.8.A.

In a J. Young NMR tube, free ^{Menth}CAAC (0.030 g, 0.079 mmol) was dissolved in 0.7 mL of dry deuterated benzene under an argon atmosphere. The solution was cooled down to -20 °C until the solvent froze, and it was degassed under vacuum. Carbon monoxide was introduced into the tube and it was warmed to room temperature. The solution immediately turned blue when the benzene melted. The degasification/CO gas introduction process was repeated three times until the solution was a deep blue. The tube was introduced into a glovebox filled with dry Argon and opened to exchange the CO atmosphere with Argon. Then, 1,9-phenanthrenequinone (**Quin-1**; 0.0164 g, 0.079 mmol) was introduced, the solution immediately turned yellowish-orange and then became colorless. NMR analysis showed clean and quantitative formation of a single diastereomer of the resulting carbonate adduct **2.8.A**. After volatiles were removed under vacuum, the solid was washed with 1 mL of pentane, and a white solid was isolated. Yield 97% (0.047 g). **Crystallization of 2.8.A:** Crystals were grown overnight from a saturated benzene solution. **Characterization data**: ^{1}**H NMR** (500 MHz, C$_6$D$_6$): δ = 8.44 (d, J = 8.0 Hz, 1H), 8.34 (d, J = 8.3 Hz, 1H), 8.28 (d, J = 8.2 Hz, 1H), 8.10 (d, J = 8.0 Hz, 1H), 7.45 (t, J = 7.5 Hz, 1H), 7.36 (t, J = 7.7 Hz, 1H), 7.30 (dd, J = 7.7, 1.6 Hz, 1H), 7.26 (t, J = 7.4 Hz, 1H), 7.23-7.19 (m, 1H), 7.12 (t, J = 7.7 Hz, 1H), 6.97 (dd, J = 7.6, 1.4 Hz, 1H), 4.42 (br, 1H), 4.19 (sept, J = 6.6 Hz, 1H), 3.35 (d, J = 12.2 Hz, 1H), 2.98 (br, 1H), 2.63 (br, 1H), 2.15 (tt, J = 11.0, 5.5 Hz, 1H), 1.86 (d, J = 6.4 Hz, 3H), 1.75-1.67 (m, 2H), 1.58 (s, 3H), 1.42 (d, J = 6.6 Hz, 3H), 1.34 (s, 3H), 1.38-1.25 (m, 5H), 1.14 (d, J = 6.6 Hz, 3H), 1.02 (d, J = 6.2 Hz, 3H), 0.70 (br, 5H), 0.31 (d, J = 6.2 Hz, 3H), -0.23 (br, 3H) ppm; ^{13}**C{^{1}H} NMR** (125.7 MHz, C$_6$D$_6$): δ = 159.7, 154.6, 151.7, 135.1, 133.9, 129.2, 128.4, 127.6, 127.2, 126.6, 126.5, 126.3, 126.2, 125.7, 125.5, 124.3, 123.4, 123.0, 121.4, 120.2, 104.3, 63.6, 62.4, 59.0, 51.8, 34.0, 30.7, 29.5, 29.4, 28.4, 26.9, 26.8, 26.6, 24.7, 23.6, 19.8 ppm; **IR** (neat): 2990 (m), 2952 (s), 2922 (s), 2865 (s), 1785 (s), 1661(m), cm^{-1}; **HRMS** (ESI): *m/z* calculated for C$_{42}$H$_{52}$NO$_3$ [M+H]$^+$ 618.3942; found 618.3934; **X-ray** see below.

Route B: Reaction of ^{Menth}CAAC with Quin-1 under CO to afford 2.8.A.

In a J. Young NMR tube, free ^{Menth}**CAAC** (0.030 g, 0.079 mmol) and 1,9-phenanthrenequinone (**Quin-1**; 0.0164 g, 0.079 mmol) were dissolved in 0.7 mL of dry deuterated benzene under an argon atmosphere. Then, the solution was cooled down to -20 °C until the solvent froze, and it was degassed under vacuum. The degasification/CO gas introduction process was repeated three times. NMR analysis showed clean and quantitative formation of a single diastereomer of the resulting carbonate adduct **2.8.A**.

Route C: Reaction of ^{Menth}CAAC with Carbo-1 to afford 2.8.A.

In a J. Young NMR tube, free ^{Menth}**CAAC** (0.030 g, 0.079 mmol) and **Quin-1** (0.0186 g, 0.079 mmol) were dissolved in 0.7 mL of dry deuterated benzene under an argon atmosphere. After 30 minutes, NMR analysis showed clean and quantitative formation of a single diastereomer of the carbonate adduct **2.8.A**.

Route D: Reaction of ^{Menth}CAAC with Carbo-1 to afford 2.8.A.

In a J. Young NMR tube, free ^{Menth}**CAAC** (0.030 g, 0.079 mmol) was dissolved in 0.7 mL of dry deuterated benzene under an argon atmosphere. The solution was cooled down to -20 °C until the solvent froze, and it was degassed under vacuum. Carbon monoxide was introduced into the tube and it was warmed to room temperature. The solution immediately turned blue when the benzene melted. The degasification/CO gas introduction process was repeated three times until the solution was a deep blue. The tube was introduced into a glovebox filled with dry Argon and opened to exchange the CO atmosphere with Argon. Then, **Quin-1** (0.0186 g, 0.079 mmol) was added to the blue solution. Upon sonication or heating the solution to 60 °C for 1 hour, the mixture became colorless. NMR analysis showed clean and quantitative formation of a single diastereomer of the carbonate adduct **2.8.A**.

Routes to 2.8.C
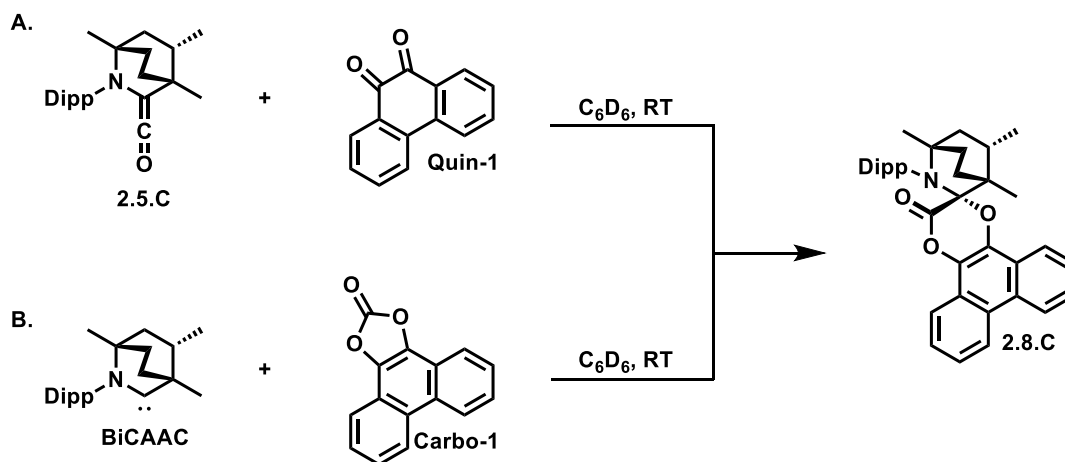
Scheme 2.18: Synthetic routes to **2.8.C**; **A. 2.5.C** can react with an *ortho*-quinone, **Quin-1**; **B. BiCAAC** can react with **Carbo-1** thereby showing the reversibility of reductive elimination.

Route A: Reaction of 2.5.C with Quin-1 to afford 2.8.C.

In a Young NMR tube free **BiCAAC** (0.030 g, 0.096 mmol) was dissolved in 0.7 mL of dry deuterated benzene under an argon atmosphere. The solution was cooled down to -20 °C until the solvent froze and it was degassed under vacuum. Carbon monoxide was introduced into the flask and the flask was warmed to room temperature. The solution immediately turned blue when the benzene melted (see protocol for (amino)ketene **2.5.C**). The degasification/CO gas introduction process was repeated three times until the solution was deep blue. The tube was introduced into a glovebox filled with dry Argon and opened to exchange the CO atmosphere with Argon. Then, the corresponding 9,10-phenanthrenequinone (**Quin-1**; 0.096 mmol) was introduced and the solution immediately turned dark green-orange with some dark precipitate in suspension. NMR analysis showed clean and quantitative formation of the corresponding adduct **2.8.C**. **Crystallization of 2.8.C:** In a Teflon sealed pressure Schlenk, free **BiCAAC** (0.030 g, 0.096 mmol) was dissolved in 1 mL of dry Et$_2$O under argon atmosphere. At room temperature, carbon monoxide was introduced in the flask (no bubbling, just replacement of the atmosphere). The solution immediately turned blue. The solution was stirred for 15 minutes, until it turned deep blue. The flask was sealed and introduced in a glovebox filled with dry Argon and opened to exchange the CO atmosphere with Argon.

Then, 9,10-phenanthrenequinone (**Quin-1**; 0.020 g, 0.096 mmol) was added and the solution immediately turned dark green. After 15 minutes stirring at room temperature, some black precipitate formed, and it was removed by filtration. The clear greenish solution was sealed and stored in a freezer at -40 °C until yellow crystals grew for X-ray analysis. Yield 74% (0.036 g). **Characterization data: ^{1}H NMR** (500 MHz, C_6D_6): $\delta = 8.51$ (d, $J = 8.1$ Hz, 1H), 8.28 (d, $J = 8.3$ Hz, 1H), 8.23-8.16 (m, 1H), 7.97-7.91 (m, 1H), 7.46 (t, $J = 7.3$ Hz, 1H), 7.31 (t, $J = 7.3$ Hz, 1H), 7.19-7.11 (m, 3H), 6.97 (t, $J = 7.7$ Hz, 1H), 6.80 (d, $J = 7.7$, 1H), 4.18 (sept, $J = 6.6$ Hz, 1H), 3.99 (sept, $J = 6.6$ Hz, 1H), 2.93 (dd, $J = 19.6, 11.6$ Hz, 1H), 2.46 (dd, $J = 16.6, 6.3$ Hz, 1H), 2.08 (t, $J = 11.5$ Hz, 1H), 1.82-1.76 (m, 1H), 1.75 (d, $J = 6.4$ Hz, 3H), 1.58-1.51 (m, 2H), 1.44-1.08 (m, 2H), 1.26 (d, $J = 6.8$ Hz, 3H), 1.23 (d, $J = 7.1$ Hz, 3H), 1.18 (d, $J = 6.8$ Hz, 3H), 0.91 (s, 3H), 0.84 (s, 3H), 0.55 (d, $J = 6.6$ Hz, 3H) ppm; **^{13}C{^{1}H} NMR** (125.7 MHz, C_6D_6): $\delta = 159.6, 153.0, 152.2, 137.6, 134.9, 129.4, 129.1, 128.7, 128.4, 127.5, 126.4, 126.3, 125.6, 125.5, 125.4, 125.3, 125.2, 124.4, 123.7, 123.3, 122.7, 120.4, 103.3, 55.4, 47.5, 44.0, 36.7, 34.8, 33.0, 29.6, 29.2, 27.0, 26.6, 26.2, 26.0, 25.2, 19.6, 18.3$ ppm; **HRMS** (ESI): *m/z* calculated for $C_{37}H_{42}NO_3$ [M+H]$^+$ 548.3159; found 548.3155; **X-ray** see below.

Route B: Reaction of BiCAAC with Carbo-1 to afford 2.8.C.

To probe the nature of the equilibrium, **BiCAAC** (0.050 g, 0.16 mmol) was dissolved in 0.7 mL of dry deuterated benzene under an argon atmosphere. Then, **Carbo-1** (0.038 g, 0.16 mmol) was added to the solution which immediately turned dark green. NMR analysis showed clean and quantitative formation of the corresponding adduct **2.8.C**.

Reaction between DAC and Quin-1 under CO to form 2.8.B and 2.9.B.
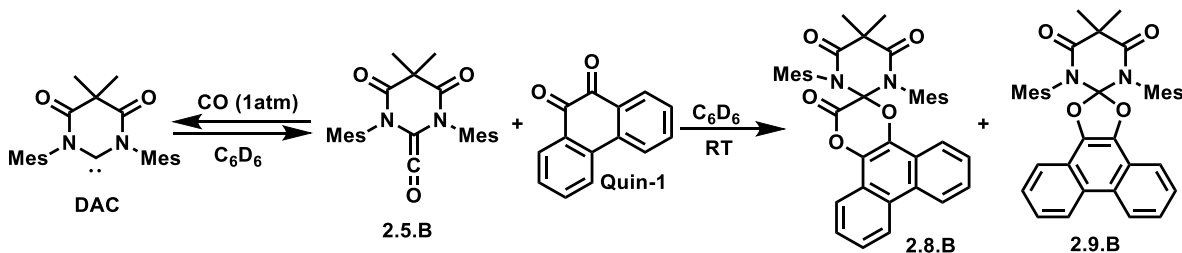
Scheme 2.19: Synthetic route to **2.8.B** from **2.5.B** leads to mixture with catalyst deactivation product **2.9.B**.

In a Young NMR tube, **DAC** (30 mg, 0.08 mmol) was dissolved in 0.7 mL of dry deuterated benzene under an argon atmosphere. The solution was cooled down to -20 °C until the solvent froze, and it was degassed under vacuum. Carbon monoxide was introduced in the flask and let it warm to room temperature. The solution immediately turned a reddish-purple when the benzene melted. The degasification/CO gas introduction process was repeated three times and led to an mixture of **DAC** and the known **2.5.B**.[55] The tube was introduced in a glovebox filled with dry Argon and 1,9-phenanthrenequinone (**Quin-1**; 16.6 mg, 0.08 mmol) was quickly added to the solution to give a mixture of products including **2.8.B** and **2.9.B**. See NMR spectra of the mixture (Section below: 2.4.5). **Characterization data for 2.8.B by subtraction of 2.9.B from the mixture**: **^{1}H NMR** (500 MHz, C_6D_6): δ = 8.10 (dd, J = 8.2, 0.8 Hz, 1H), 8.02 (d, J = 8.4 Hz, 1H), 7.99-7.95 (m, 1H), 7.71 (d, J = 9.5 Hz, 1H), 7.33-7.28 (m, 1H), 7.19 (d, J = 7.1 Hz, 1H), 7.11-7.06 (m, 2H), 6.36 (s, 2H), 6.27 (s, 2H), 2.44 (s, 6H), 2.40 (s, 6H), 2.23 (s, 3H), 2.13 (s, 3H), 1.61 (s, 6H) ppm; **^{13}C{^{1}H} NMR** (125.7 MHz, C_6D_6; characteristic peaks): δ = 171.8 (N-C=O), 159.1 (O-C=O), 94.7 ($C_{carbene}$) ppm.

Catalyst deactivation study.

Control experiment: reaction between DAC and Quin-1.
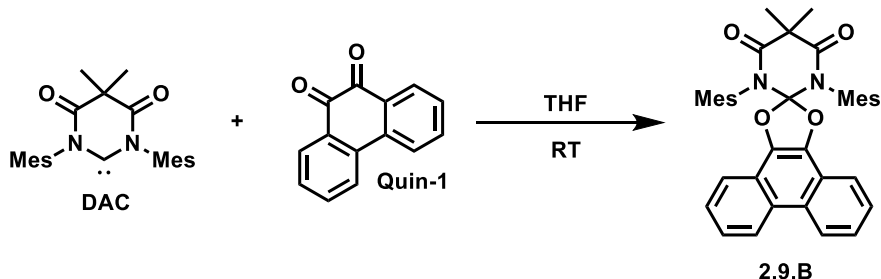
Scheme 2.20: Catalyst deactivation of **DAC** by substrate **Quin-1** leading to the synthesis of **2.9.B**.

In a Young NMR tube, free **DAC** (30 mg, 0.08 mmol) was dissolved in 0.7 mL of dry THF under an argon atmosphere and **Quin-1** (16.6 mg, 0.08 mmol) was added to the solution. After 15 minutes, THF was removed under vacuum to give a white solid, **2.9.B** (45.2 mg, 97 % yield). Crystals were grown from THF layered with pentane. **Characterization data**: ^{1}**H NMR** (500 MHz, C_6D_6): δ = 7.85 (d, J = 8.4 Hz, 2H), 7.75-7.73 (m, 2H), 7.25-7.21 (m, 2H), 6.99 (ddd, J = 8.4, 7.1, 1.3 Hz, 2H), 6.38 (s, 4H), 2.55 (s, 12H), 2.03 (s, 6H), 1.51 (s, 6H) ppm; ^{13}**C{^{1}H} NMR** (125.7 MHz, C_6D_6): δ = 169.9, 138.3, 138.1, 135.9, 130.7, 129.7, 127.3, 127.2, 124.9, 123.9, 123.0, 119.8, 119.2, 47.2, 25.2, 20.5, 19.5 ppm; **HRMS** (ESI): *m/z* calculated for $C_{38}H_{37}N_2O_4$ [M+H]$^+$ 585.2748; found 585.2737.

Reaction of BiCAAC with Quin-1.
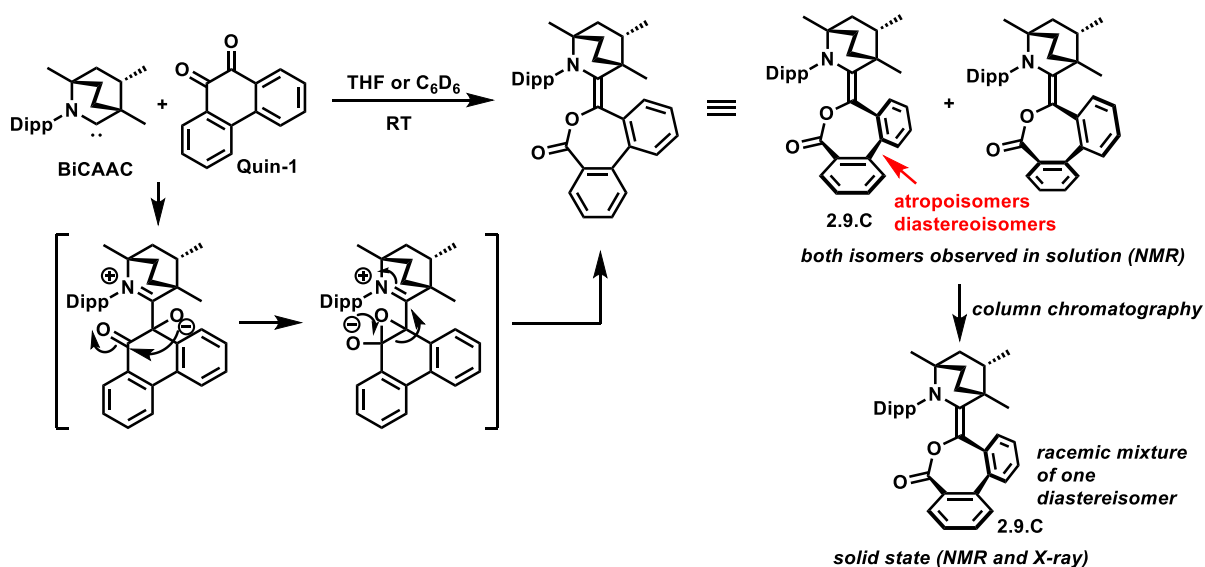
Scheme 2.21: Catalyst deactivation of **BiCAAC** by substrate **Quin-1** with proposed mechanism leading to a diastereomeric mixture of atropisomers, and the subsequent purification to isolate **2.9.C** by silica gel column chromatography.

BiCAAC (0.050 g, 0.16 mmol) was dissolved in 1 mL of dry THF under an Argon atmosphere at room temperature. Then, 9,10-phenanthrenequinone (**Quin-1**) was added (0.027 g, 0.13 mmol) forming a homogeneous deep purple-reddish solution. After stirring for 10 minutes, volatiles were removed. The mixture was analyzed by means of NMR spectroscopy showing variable mixture of isomers in each batch (around 1:1). The product was purified by silica-gel column chromatography (eluent hexane/DCM (1:2)). A single isomer, **2.9.C**, was isolated as a pale-yellow product ($R_f = 0.3$). Yield 39% (0.030 g). X-ray quality crystals were grown after slow evaporation of the solvent. **Characterization data**: **^{1}H NMR** (500 MHz, CDCl$_3$): $\delta = 7.64$ (d, $J = 7.8$ Hz, 1H), 7.51 (t, $J = 7.4$ Hz, 1H), 7.45-7.32 (m, 4H), 7.31-7.25 (m, 2H), 7.18 (s, 1H), 7.17 (s, 1H), 3.40 (sept, $J = 6.8$ Hz, 1H), 3.28 (sept, $J = 6.8$ Hz, 1H), 2.12-2.00 (m, 2H), 1.92-1.86 (m, 1H), 1.65-1.56 (m, 3H), 1.53-1.49 (m, 1H), 1.36 (d, $J = 6.8$ Hz, 3H), 1.31 (t, $J = 7.0$ Hz, 3H), 1.29 (t, $J = 7.0$ Hz, 3H), 1.22 (d, $J = 6.8$ Hz, 3H), 0.74 (s, 3H), 0.41 (d, $J = 7.0$ Hz, 3H), 0.34 (s, 3H), ppm; **^{13}C{^{1}H}**

NMR (125.7 MHz, CDCl$_3$): $\delta = 169.6, 147.7, 146.7, 141.0, 140.5, 140.1, 139.6, 133.3, 132.8, 131.4, 131.3, 128.9, 127.6, 127.4, 127.1, 127.0, 127.0, 123.8, 123.7, 118.9, 56.5, 43.7, 40.3, 39.0, 36.0, 35.0, 28.7, 28.4,$

27.4, 26.2, 26.1, 25.3, 24.9, 24.0, 18.2 ppm; **IR** (neat): $\nu_{(CO\ stretching)}$ = 1716.3 (s) cm^{-1}; **HRMS** (ESI): *m/z*

calculated for $C_{36}H_{42}NO_2$ [M+H]$^+$ 520.3210; found 520.3207; **X-ray** see below.

Control experiment: reaction between ^{Menth}*CAAC and Quin-1.*
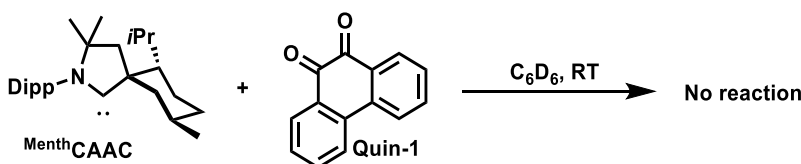
Scheme 2.22: Sterically bulky ^{Menth}**CAAC** as an active catalyst does not react with substrate **Quin-1**.

As observed before in the synthesis of compound **2.8.A** (procedure **A**), there is no reaction between

free ^{Menth}**CAAC** (0.030 g, 0.079 mmol) and 1,9-phenanthrenequinone (**Quin-1**; 0.0164 g, 0.079 mmol) in

0.7 mL of dry deuterated benzene under an argon atmosphere.

Control experiment between ^{Me}*CAAC and Quin-1.*
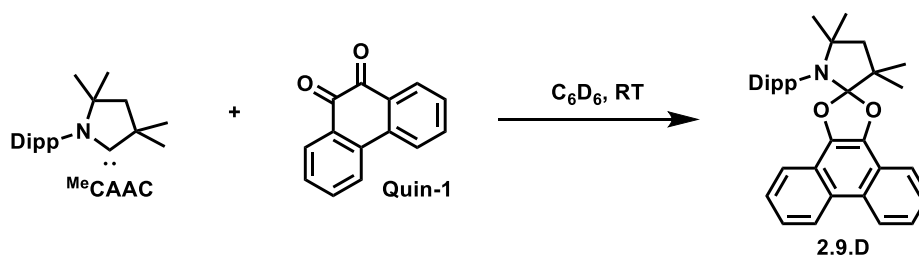
Scheme 2.23: Catalyst deactivation of sterically unencumbered ^{Me}**CAAC** by substrate **Quin-1** leading to the synthesis of **2.9.D**.

^{Me}**CAAC** (0.050 g, 0.175 mmol) and **Quin-1** (0.0365 g, 0.175 mmol) were dissolved in 0.7 mL of

benzene to give the quantitative and clean formation of **2.9.D**. Volatiles were removed under vacuum and

the solid was washed with 1 mL of pentane. X-ray quality crystals were grown by the slow evaporation of

a saturated solution in benzene. Yield 87.9% (0.076 g). **Characterization data**: **^{1}H NMR** (500 MHz,

C_6D_6): δ = 8.37 (d, *J* = 8.4 Hz, 2H), 8.10 (dd, *J* = 8.1, 0.8 Hz, 2H), 7.38 (dt, *J* = 7.5, 0.8 Hz, 2H), 7.23 (dt,

J = 7.7, 1.3 Hz, 2H), 7.08 (br, 3H), 4.03 (sept, *J* = 6.8 Hz, 2H), 1.90 (s, 2H), 1.37 (d, *J* = 6.8 Hz, 6H), 1.34-

1.33 (m, 12H), 1.22 (s, 6H) ppm; $^{13}C\{^1H\}$ **NMR** (125.7 MHz, C$_6$D$_6$): δ = 152.8, 138.4, 134.9, 132.1, 128.5, 127.0, 126.8, 124.9, 124.1, 123.7, 121.6, 120.7, 62.0, 52.4, 46.7, 30.6, 29.2, 27.6, 27.1, 24.6 ppm; **X-ray** see below.

Reactivity of 2.8.A.
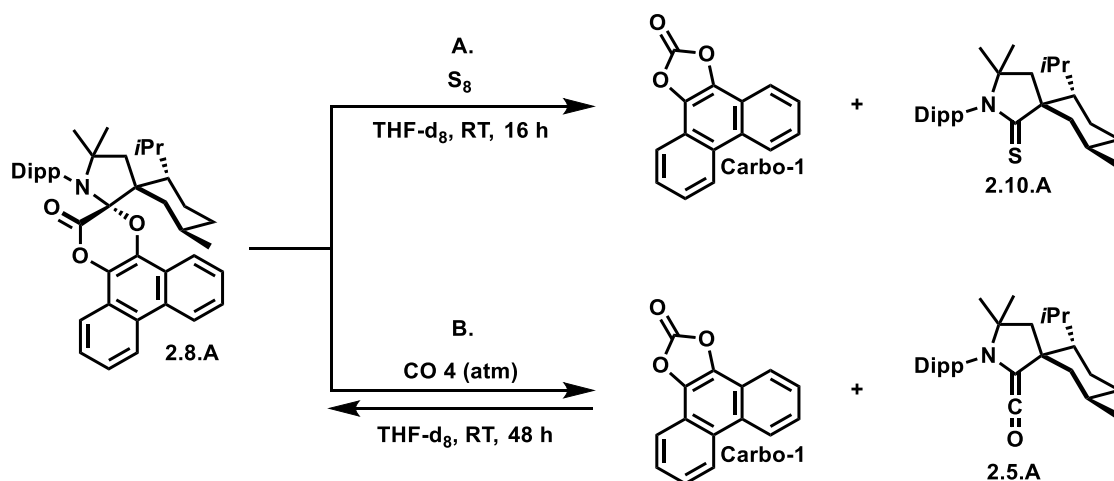
Scheme 2.24: Forcing reductive elimination from **2.10.A**; **A.** Upon adding elemental sulfur, a classical carbene trapping reagent, **2.10A** is synthesized and **Carbo-1** is released; **B.** Under 4 atm of CO$_{(g)}$, **2.5.A** is formed from the free-carbene upon eliminating **Carbo-1**.

Route A: Forcing reductive elimination from 2.8.A in the presence of S$_8$.

In a J. Young NMR tube, **2.8.A** (0.050 g, 0.0809 mmol) was dissolved in 0.7 mL of dry deuterated tetrahydrofuran under an argon atmosphere. Then, 1 equiv. of sulfur, S$_8$ (0.0026 g, 0.0101 mmol), was added to the colorless solution which immediately began to turn light yellow. After 16 hours, NMR analysis showed quantitative formation of **Carbo-1** and the thiolactam **2.10.A**. To confirm, each component of the reaction mixture was purified by silica-gel column chromatography (eluent hexane/DCM (2:1) and its NMR matched against known literature.[23] **2.10.A** was isolated as a white solid. **Characterization data**: **^{1}H NMR** (500 MHz, THF-d$_8$): δ = 7.31-7.27 (m, 1H), 7.22-7.19 (m, 2H), 2.93-2.80 (m, 4H), 2.50 (d, J = 13.6 Hz, 1H), 2.14 (dt, , J = 13.6, 2.8 Hz, 1H), 2.05 (sept, J = 7.0 Hz, 1H), 1.97 (d, J = 13.6 Hz, 1H), 1.87-1.83 (m, 1H), 1.43-1.37 (m, 1H), 1.33 (s, 3H), 1.26-1.25 (m, 6H), 1.23 (s, 3H), 1.22-1.21 (m, 1H), 1.18-1.15 (m,

6H), 1.07 (d, J = 6.9 Hz, 3H), 1.01 (d, J = 6.9 Hz, 3H), 0.81 (d, J = 6.6 Hz, 3H) ppm; $^{13}C\{^{1}H\}$ NMR (125.7

MHz, THF-d$_8$): δ = 209.9, 148.2, 148.2, 134.1, 129.3, 125.3, 124.9, 68.6, 58.4, 54.2, 53.0, 51.9, 36.6, 30.3,

30.3, 30.1, 30.0, 29.3, 27.9, 26.8, 26.6, 23.7, 23.4, 23.1, 23.0, 20.1 ppm.

Route B: Forcing reductive elimination from 2.8.A in the presence of CO$_{(g)}$.

In a heavy wall J. Young NMR tube, **2.8.A** (0.005 g, 0.00809 mmol) was dissolved in 0.1 mL of

dry deuterated tetrahydrofuran under an argon atmosphere. The solution was cooled down with liquid

nitrogen until the solvent froze, and it was degassed under vacuum. Carbon monoxide (4 atm) was

introduced into the tube and it was warmed to room temperature. The degasification/CO gas introduction

process was repeated three times. The tube was left at room temperature for 95 hours. Over the course of

that period, NMR was used to monitor the solution and probe the equilibrium. $^{13}C\{^{1}H\}$ NMR analysis

confirmed the presence of the **2.5.A** in the mixture.

Reactivity of 2.8.C.
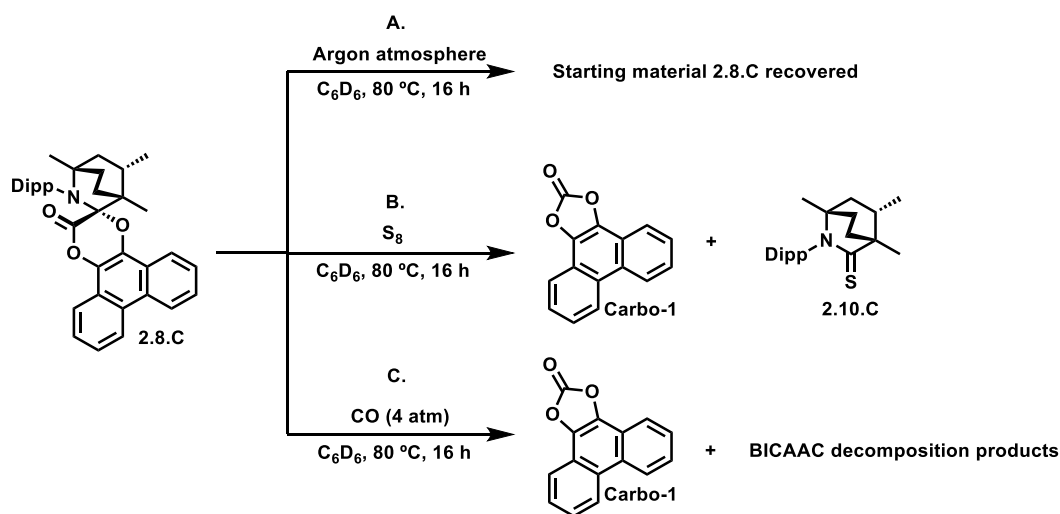
Scheme 2.25: Probing the reductive elimination from **2.8.C**; **A.** No reductive elimination occurs under argon despite high temperature; **B.** Equilibrium of adding and eliminating **Carbo-1** is established at 80°C by trapping the carbene as **2.10.C** with elemental sulfur; **C.** Despite reversible reductive elimination occuring, **BiCAAC** decomposes under CO$_{(g)}$ at 80°C.

Route A: Attempt at reductive elimination from 2.8.C at high temperature.

In a J. Young NMR tube, **2.8.C** (0.0527 g, 0.096 mmol) was dissolved in 0.7 mL of C_6D_6 under an argon atmosphere and heated to 80 °C overnight. NMR analysis showed no reaction which suggested that if **BiCAAC** and **Carbo-1** are liberated via a formal reductive elimination at carbon, the reverse occurs rapidly such that no observable reaction takes place upon cooling to room temperature.

Route B: Forcing reductive elimination from 2.8.C in the presence of S_8.

In a J. Young NMR tube, **2.8.C** (0.0527 g, 0.096 mmol) was dissolved in 0.7 mL of C_6D_6 and then, charged with S_8 (2 equivalents, 0.062 g, 0.024 mmol). The tube was sealed and heated to 80 °C for 16 hours. $^{13}C\{^1H\}$ NMR analysis showed the clean formation of the thiolactam, **2.10.C**, together with the cyclic carbonate, **Carbo-1**. To confirm, each component of the reaction mixture was purified by silica-gel column chromatography (eluent hexane/DCM (2:1), the NMR matched against known literature.[41] **2.10.C** was isolated as a pale-white solid. **Characterization data**: ^1H **NMR** (500 MHz, CDCl$_3$): δ = 7.35 (t, J = 7.7 Hz, 1H), 7.21 (d, J = 7.4 Hz, 2H), 2.92 (sept, J = 6.8 Hz, 1H), 2.63 (sept, J = 6.8 Hz, 1H), 2.11-2.05 (m, 2H), 2.02-1.93 (m, 1H), 1.91-1.84 (m, 1H), 1.81-1.70 (m, 2H), 1.65 (dd, J = 7.8, 3.4 Hz, 1H), 1.43 (s, 3H), 1.28-1.22 (m, 12H), 1.06 (d, J = 6.5 Hz, 3H), 0.93 (s, 3H) ppm; $^{13}C\{^1H\}$ **NMR** (125.7 MHz, CDCl$_3$): δ = 209.2, 145.7, 145.6, 138.0, 128.6, 124.7, 124.4, 61.7, 48.7, 44.6, 36.8, 34.4, 34.0, 29.3, 28.8, 25.6, 25.5, 24.9, 24.8, 24.5, 23.7, 19.0 ppm; **IR** (neat): 3057, 2959 (strong), 2927, 2866, 1669, 1446 (strong), 1392 (strong), 1265, 1178, 1065, 935, 794 (strong), 745 cm^{-1}; **HRMS** (ESI): m/z calculated for $C_{22}H_{34}NS$ [M+H]$^+$ 344.2406; found 344.2406. **Carbo-1** was isolated as a white crystalline solid. ^1H **NMR** (500 MHz, CDCl$_3$): δ = 8.76-8.74 (m, 2H), 8.09-8.05 (m, 2H), 7.78-7.71 (m, 4H) ppm; $^{13}C\{^1H\}$ **NMR** (125.7 MHz, CDCl$_3$): δ = 152.4, 136.2, 128.4, 128.2, 127.1, 123.8, 120.5, 119.2 ppm; **IR** (neat): $\nu_{(CO\ stretching)}$ = 1819.5 cm^{-1}. **HRMS** (ESI): m/z calculated for $C_{14}H_9O_2$ [M-CO+H]$^+$ 209.0597; found 209.0596.

Route C: Forcing reductive elimination from 2.8.C in the presence of CO(g).

In a J. Young NMR tube, **2.5.C** (0.0527 g, 0.096 mmol) was dissolved in 0.7 mL of C_6D_6 under an argon atmosphere. The solution was cooled down to -20 °C until the solvent froze, and it was degassed under vacuum. Carbon monoxide (4 atm) was introduced into the tube and it was warmed to room temperature. The degasification/CO gas introduction process was repeated three times. Afterwards, the tube was sealed, and heated to 80 °C for 16 hours. $^{13}C\{^1H\}$ NMR analysis showed the corresponding carbonate **Carbo-1** was formed along with a variety of decomposition products of the **BiCAAC** skeleton. **2.5.C** was not observed in the reaction mixture which suggests that indeed (when compared to **Route A**), free carbene is released, but after reacting with CO, it decomposes at 80 °C in the mixture.

^{Menth}CAAC-catalyzed carbonylation of quinones with CO(g).

Quin-1, X = CH
Quin-2, X = N

Carbo-1, X = CH
Carbo-2, X = N
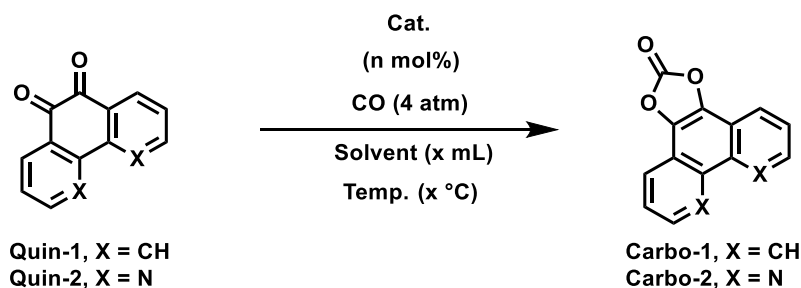
Scheme 2.26: Optimizing the catalytic carbonylation of *ortho*-quinones to cyclic carbonates by an ambiphilic carbene catalyst with CO(g).

Optimization: Procedure A for Table 2.1.

In a 100 mL Teflon-capped pressure Schlenk under an inert argon atmosphere in the glovebox, the corresponding amount of free-carbene cat. (n mol% catalyst loading, see table), and the corresponding amount of **Quin-1** (n mmol, see table) were added to solution, and then dry solvent (x mL, see table) was added to the mixture. The solution was cooled down until the solvent froze, and it was degassed under vacuum. Carbon monoxide (4 atm) was introduced into the flask and it was warmed to room temperature. The degasification/CO gas introduction process was repeated three times. The flask was sealed and stirred

at 500 RPM at the corresponding temperature (Temp. ℃, see table) for the desired duration of time (Time hours, see table). Upon completion of the catalysis, the vessel was removed from the heat, cooled to room temperature, and then the solvent was completely removed under vacuum. The resulting orange to pale yellow solid was then opened to the atmosphere, and the solid was completely dissolved in a 2 mL stock solution of CDCl$_3$ with 1,3,5-Trimethoxybenzene as a standard (5.95 mM). ^{1}H NMR analysis was then used to determine the TON and the conversion to the resulting cyclic carbonate with respect to the standard.

Optimization: Procedure B for Table 2.1.

In a 100 mL Teflon-capped pressure Schlenk, the corresponding amount of free-carbene cat. (n mol% catalyst loading, see table) was dissolved in 1/3 of the corresponding total dry solvent to be used in the catalysis (see below). After one freeze-pump-thaw, the solution was put under 1 atmosphere of CO. After the solution changed color, the pressure Schlenk was introduced into the glovebox, the corresponding amount of *ortho*-quinone, orange **Quin-1** or yellow **Quin-2**, (n mmol, see table) was added to solution, and the rest of the dry solvent was added to the mixture (total solvent x mL, see table). The solution was cooled down to -20 °C until the solvent froze, and it was degassed under vacuum. Carbon monoxide was introduced in the flask and let it warm to room temperature. The degasification/CO gas introduction process was repeated three times. The flask was sealed and stirred at 500 RPM at the corresponding temperature (Temp. ℃, see table) for the desired duration (Time hours, see table). Upon completion of the catalysis, the vessel was removed from the heat, cooled to room temperature, and then the solvent was completely removed under vacuum. The resulting solid was then opened to the atmosphere, completely dissolved in a stock solution of CDCl$_3$ with 1,3,5-Trimethoxybenzene as a standard (5.95 mM) (2 mL of stock solution for **Quin-1/Carbo-1** whereas 6 mL was required for **Quin-2/Carbo-2**). ^{1}H NMR was then used to determine the TON and the conversion to the resulting cyclic carbonate.

Table 2.2: Catalytic optimization for carbonylation reaction.

Procedure	*o*-quinone (mmol)	Cat. Loading (mol%)	T (°C)	t(hr)	Conv.% by ¹H NMR	Solvent (mL)	TON
A	**Quin-1** (0.131)	ᴹᵉⁿᵗʰCAAC (20)	60	24	100	Benzene (2)	5
A	**Quin-1** (0.262)	None	60	24	0	Benzene (2)	0
A	**Quin-1** (0.131)	**BiCAAC** (20)	60	24	0	Benzene (2)	0
A	**Quin-1** (0.131)	**DAC** (20)	60	24	0	Benzene (2)	0
A	**Quin-1** (0.131)	ᴹᵉCAAC (20)	60	24	0	Benzene (2)	0
A	**Quin-1** (0.262)	ᴹᵉⁿᵗʰCAAC (10)	60	24	33	Benzene (2)	3
A	**Quin-1** (0.262)	ᴹᵉⁿᵗʰCAAC (10)	60	24	8.2	THF (2)	0
A	**Quin-1** (0.262)	ᴹᵉⁿᵗʰCAAC (10)	60	24	7.5	Pentane (2)	0
A	**Quin-1** (0.262)	ᴹᵉⁿᵗʰCAAC (10)	60	24	23.5	Toluene (2)	2
A	**Quin-1** (0.262)	ᴹᵉⁿᵗʰCAAC (10)	60	24	5.5	Dioxane (2)	0
A	**Quin-1** (0.262)	ᴹᵉⁿᵗʰCAAC (10)	60	24	4.2	Dimethoxyethane (2)	0
A	**Quin-1** (0.262)	ᴹᵉⁿᵗʰCAAC (10)	60	24	8.3	Diethyl ether (2)	0
A	**Quin-1** (0.262)	ᴹᵉⁿᵗʰCAAC (10)	50	24	18.7	Benzene (2)	1
A	**Quin-1** (0.262)	ᴹᵉⁿᵗʰCAAC (10)	70	24	4.8	Benzene (2)	0
A	**Quin-1** (0.262)	ᴹᵉⁿᵗʰCAAC (10)	80	24	4.5	Benzene (2)	0
A	**Quin-1** (0.262)	ᴹᵉⁿᵗʰCAAC (10)	Sonic.	24	16.7	Benzene (2)	1
B	**Quin-1** (0.262)	ᴹᵉⁿᵗʰCAAC (10)	60	24	45.7	Benzene (2)	4
B	**Quin-1** (0.262)	ᴹᵉⁿᵗʰCAAC (10)	60	16	28.1	Benzene (2)	2
B	**Quin-1** (0.262)	ᴹᵉⁿᵗʰCAAC (10)	60	36	49.5	Benzene (2)	4
B	**Quin-1** (0.262)	ᴹᵉⁿᵗʰCAAC (10)	60	40	80.1[a]	Benzene (3)	8
B	**Quin-1** (0.262)	ᴹᵉⁿᵗʰCAAC (12.5)	60	40	100	Benzene (3)	8
B	**Quin-2** (0.262)	ᴹᵉⁿᵗʰCAAC (10)	60	24	100	Benzene (3)	10
B	**Quin-2** (0.524)	ᴹᵉⁿᵗʰCAAC (5)	60	24	55.6	Benzene (3)	11
B	**Quin-2** (0.524)	ᴹᵉⁿᵗʰCAAC (5)	60	40	100	Benzene (3)	20

[a]*Isolated yield by florisil column chromatography of small-scale reaction determined to be 79.6%.*

Catalytic procedure.

In a 500 mL Teflon-capped pressure Schlenk, the corresponding amount of ᴹᵉⁿᵗʰCAAC (12.5 mol% for **Quin1/Carbo-1**; or 5 mol% for **Quin-2/Carbo-2**) was dissolved in 1/3 of the corresponding total dry benzene to be used in the catalysis. After one freeze-pump-thaw, the solution was put under 1 atmosphere of CO. After the solution became dark blue, the pressure Schlenk was introduced into the glovebox, the corresponding amount of *ortho*-quinone (2.401 mmol of orange **Quin-1**; or 0.524 mmol of yellow **Quin-2**) was added to solution, and the rest of the dry benzene was added to the mixture (total of 27.5 mL for

Quin-1/Carbo-1; or total of 3 mL for **Quin-2/Carbo-2**). The solution was cooled down to -20 °C until the solvent froze, and it was degassed under vacuum. Carbon monoxide (4 atm) was introduced into the flask and it was warmed to room temperature. The degasification/CO gas introduction process was repeated three times. The flask was sealed and stirred at 500 RPM at 60 °C for 40 hours. Upon completion of the catalysis, the vessel was removed from the heat, cooled to room temperature, the solvent was completely removed under vacuum, and then the resulting mixture was purified (see below).

Catalysis: Quin-1, CO, and CAAC catalyst afford Carbo-1.
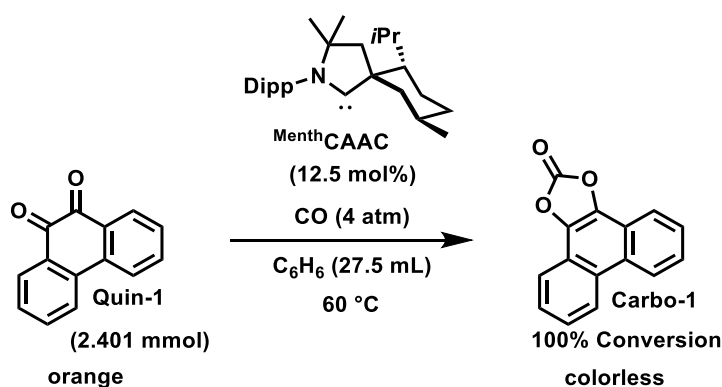
Scheme 2.27: Catalytic carbonylation of **Quin-1** to **Carbo-1** by $^{\text{Menth}}$**CAAC** catalyst with $CO_{(g)}$.

Purification: From the pale white solid, **Carbo-1** was purified via removing the $^{\text{Menth}}$**CAAC** decomposition product by simply washing with pentane (3 x 2 mL). NB: **Carbo-1** very slowly decomposes back to **Quin-1** if a silica gel or a neutral alumina column is used in the purification process. Therefore, if there is any **Quin-1** left in the mixture, a Florisil adsorbent must be used (eluent hexane/DCM (2:1)). **Carbo-1** yield 97.3% (0.552 g). **Carbo-1:** white crystalline solid. **Characterization data: ^{1}H NMR** (500 MHz, CDCl$_3$): δ = 8.76-8.74 (m, 2H), 8.09-8.05 (m, 2H), 7.78-7.71 (m, 4H) ppm; ^{13}C{^{1}H} **NMR** (125.7 MHz, CDCl$_3$): δ = 152.4, 136.2, 128.4, 128.2, 127.1, 123.8, 120.5, 119.2 ppm; **IR** (neat): $\nu_{\text{(CO stretching)}}$ = 1819.5 cm^{-1}; **HRMS** (ESI): m/z calculated for C$_{14}$H$_9$O$_2$ [M-CO+H]$^+$ 209.0597; found 209.0596; **X-ray** see below.

Catalysis: Quin-2, CO, and CAAC catalyst afford Carbo-2.
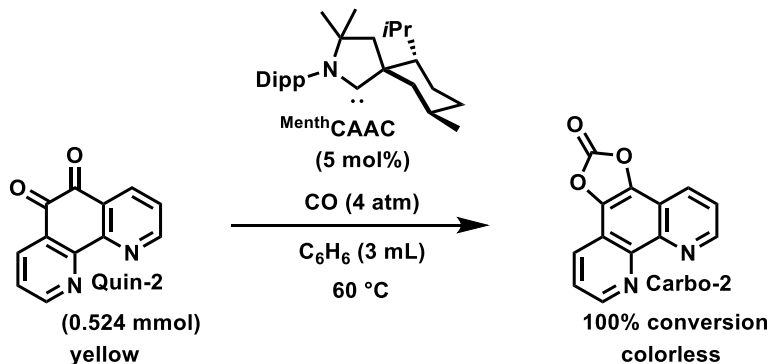
Scheme 2.28: Catalytic carbonylation of **Quin-2** to **Carbo-2** by ^MenthCAAC catalyst with $CO_{(g)}$.

Purification: From the pale white solid, **Carbo-2** was purified by removing the ^MenthCAAC decomposition product by simply washing with pentane (3 x 2 mL). **Carbo-2** yield 94.5% (0.118 g). **Carbo-2:** white crystalline solid. **Characterization data: ^{1}H NMR** (500 MHz, CDCl$_3$) δ = 9.28 (dd, J = 1.8, 4.4 Hz, 2H), 8.47 (dd, J = 1.8, 8.2 Hz, 2H), 7.80 (dd, J = 4.4, 8.2 Hz, 2H) ppm. ^{13}C{^{1}H} **NMR** (125.7 MHz, CDCl$_3$) δ = 151.6, 150.6, 143.8, 135.2, 128.5, 124.1, 116.5 ppm; **HRMS** (ESI): m/z calculated for $C_{13}H_7N_2O_3$ [M+H]$^+$ 239.0451; found 239.0455; **X-ray** see below.

2.4.3 X-Ray Crystal Structure Determination.

Olex2 software[57] was employed for the resolution, refinement, and generation of crystallographic information files of every structure. The structures were solved with the ShelXS9[58] structure solution program using Direct Methods and refined with the ShelXL9[58] refinement package using Least Squares minimization. During the final stages of the refinements, all the positional parameters and the anisotropic temperature factors of all the non-H atoms were refined. The H atoms were geometrically located and their coordinates were refined riding on their parent atoms.

X-Ray data and structure for 2.8.A.

Table 2.3: Crystal structure and refinement data for **2.8.A**.

Identification code	**2.8.A**
Empirical formula	$C_{42}H_{51}NO_3$
Formula weight	617.83
Temperature/K	100.0
Crystal system	monoclinic
Space group	$P2_1$
a/Å	9.6614(2)
b/Å	13.1385(2)
c/Å	13.6483(2)
α/°	90
β/°	100.9460(10)
γ/°	90
Volume/Å^3	1700.95(5)
Z	2
ρ_{calc}g/cm^3	1.206
μ/mm^{-1}	0.575
F(000)	668.0
Crystal size/mm^3	$0.2 \times 0.1 \times 0.05$
Radiation	CuKα (λ = 1.54178)
2Θ range for data collection/°	6.596 to 139.332
Index ranges	$-10 \leq h \leq 11$, $-15 \leq k \leq 15$, $-16 \leq l \leq 16$
Reflections collected	23828
Independent reflections	6223 [R_{int} = 0.0263, R_{sigma} = 0.0250]
Data/restraints/parameters	6223/1/424
Goodness-of-fit on F^2	1.036
Final R indexes [I>=2σ (I)]	R_1 = 0.0263, wR_2 = 0.0682
Final R indexes [all data]	R_1 = 0.0266, wR_2 = 0.0685
Largest diff. peak/hole / e Å^{-3}	0.17/-0.16
Flack parameter	0.03(4)
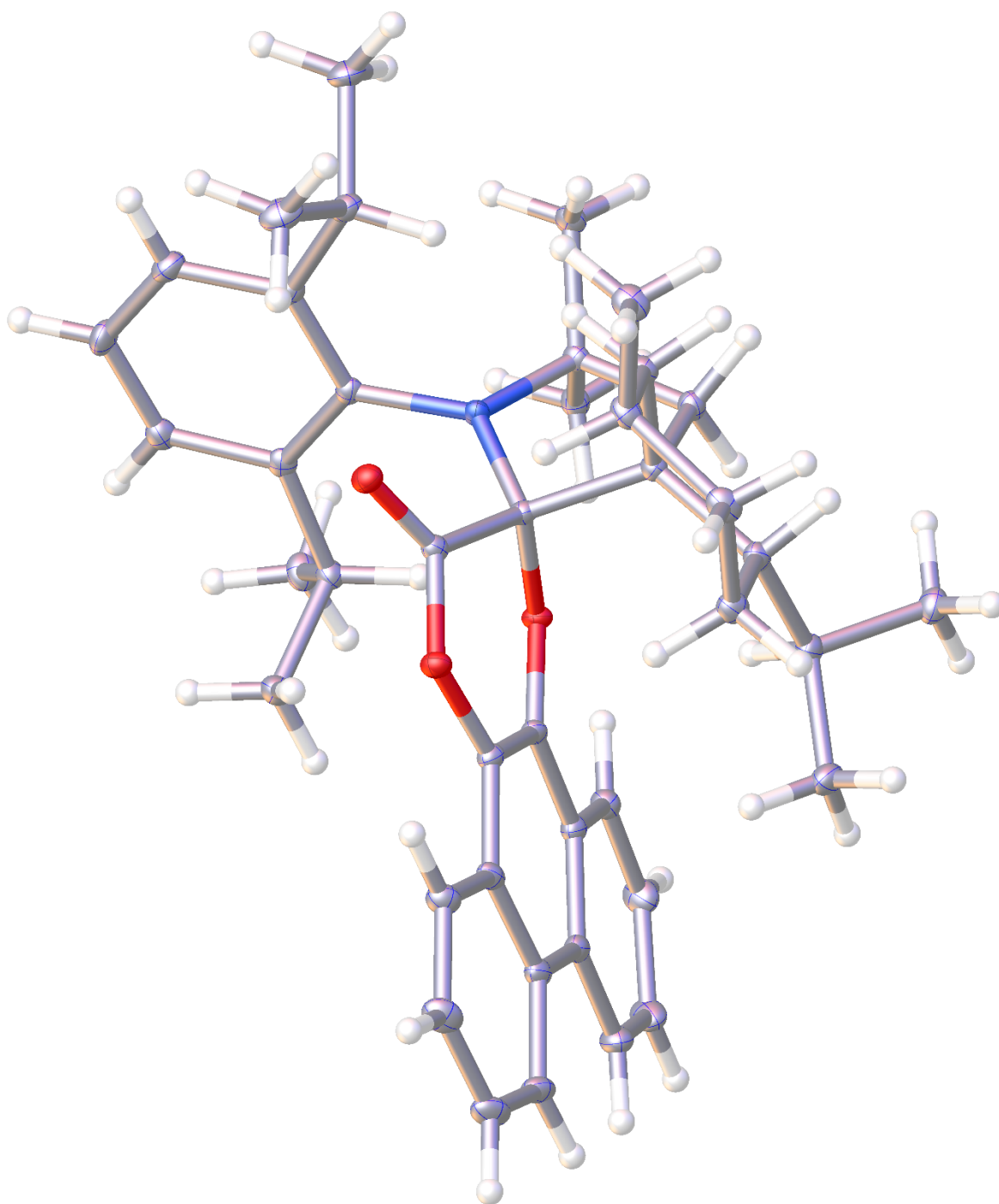
Figure 2.9: X-ray structure of **2.8.A** (ellipsoids shown at 30% probability).

X-Ray data and structure for 2.8.C.

Table 2.4: Crystal structure and refinement data for **2.8.C**.

Identification code	**2.8.C**
Empirical formula	$C_{37}H_{41}NO_3$
Formula weight	547.71
Temperature/K	100.0
Crystal system	triclinic
Space group	P-1
a/Å	13.522(2)
b/Å	14.662(2)
c/Å	15.587(3)
α/°	70.362(5)
β/°	82.086(6)
γ/°	89.869(5)
Volume/Å^3	2879.6(8)
Z	4
ρ_{calc}g/cm^3	1.263
μ/mm^{-1}	0.079
F(000)	1176.0
Crystal size/mm^3	$0.3 \times 0.1 \times 0.1$
Radiation	MoKα (λ = 0.71073)
2Θ range for data collection/°	2.952 to 50.884
Index ranges	$-16 \leq h \leq 14$, $-17 \leq k \leq 17$, $-18 \leq l \leq 18$
Reflections collected	60474
Independent reflections	10618 [R_{int} = 0.0469, R_{sigma} = 0.0320]
Data/restraints/parameters	10618/0/754
Goodness-of-fit on F^2	1.043
Final R indexes [I>=2σ (I)]	R_1 = 0.0431, wR$_2$ = 0.1031
Final R indexes [all data]	R_1 = 0.0557, wR$_2$ = 0.1114
Largest diff. peak/hole / e Å^{-3}	0.38/-0.25
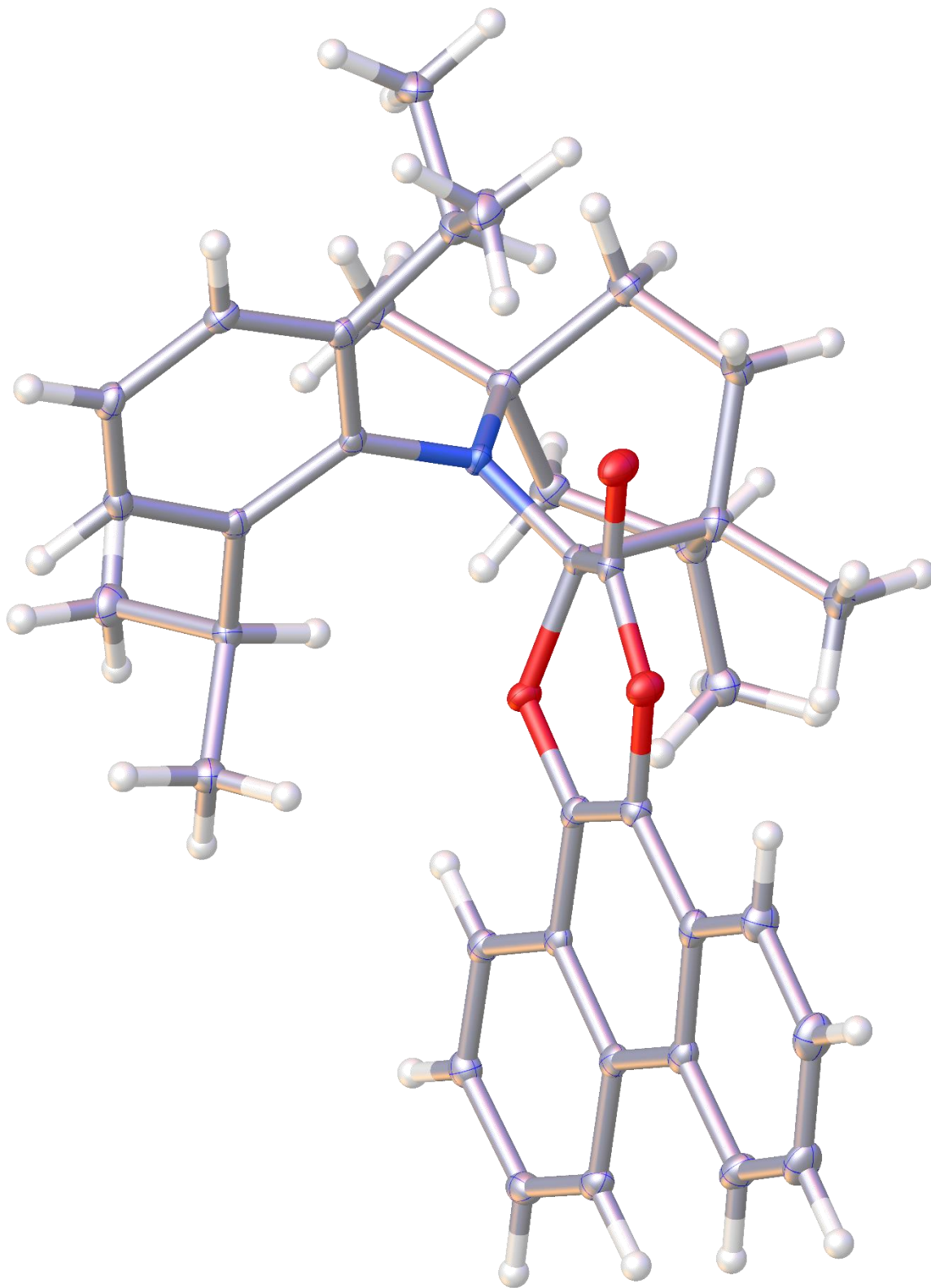
Figure 2.10: X-ray structure of **2.8.C** (ellipsoids shown at 30% probability).

X-Ray data and structure for 2.9.B.

Table 2.5: Crystal structure and refinement data for **2.9.B**.

Identification code	**2.9.B**
Empirical formula	$C_{38}H_{36}N_2O_4$
Formula weight	584.69
Temperature/K	100.0
Crystal system	monoclinic
Space group	$P2_1/c$
a/Å	24.7101(6)
b/Å	9.8702(2)
c/Å	25.3347(6)
α/°	90
β/°	95.1420(10)
γ/°	90
Volume/Å^3	6154.1(2)
Z	8
ρ_{calc}g/cm^3	1.262
μ/mm^{-1}	0.082
F(000)	2480.0
Crystal size/mm^3	$0.35 \times 0.1 \times 0.1$
Radiation	MoKα (λ = 0.71073)
2Θ range for data collection/°	3.494 to 50.806
Index ranges	$-29 \le h \le 29$, $-11 \le k \le 8$, $-30 \le l \le 30$
Reflections collected	64959
Independent reflections	11275 [R_{int} = 0.0591, R_{sigma} = 0.0451]
Data/restraints/parameters	11275/0/810
Goodness-of-fit on F^2	1.024
Final R indexes [I>=2σ (I)]	R_1 = 0.0414, wR_2 = 0.0898
Final R indexes [all data]	R_1 = 0.0679, wR_2 = 0.1016
Largest diff. peak/hole / e Å^{-3}	0.37/-0.29
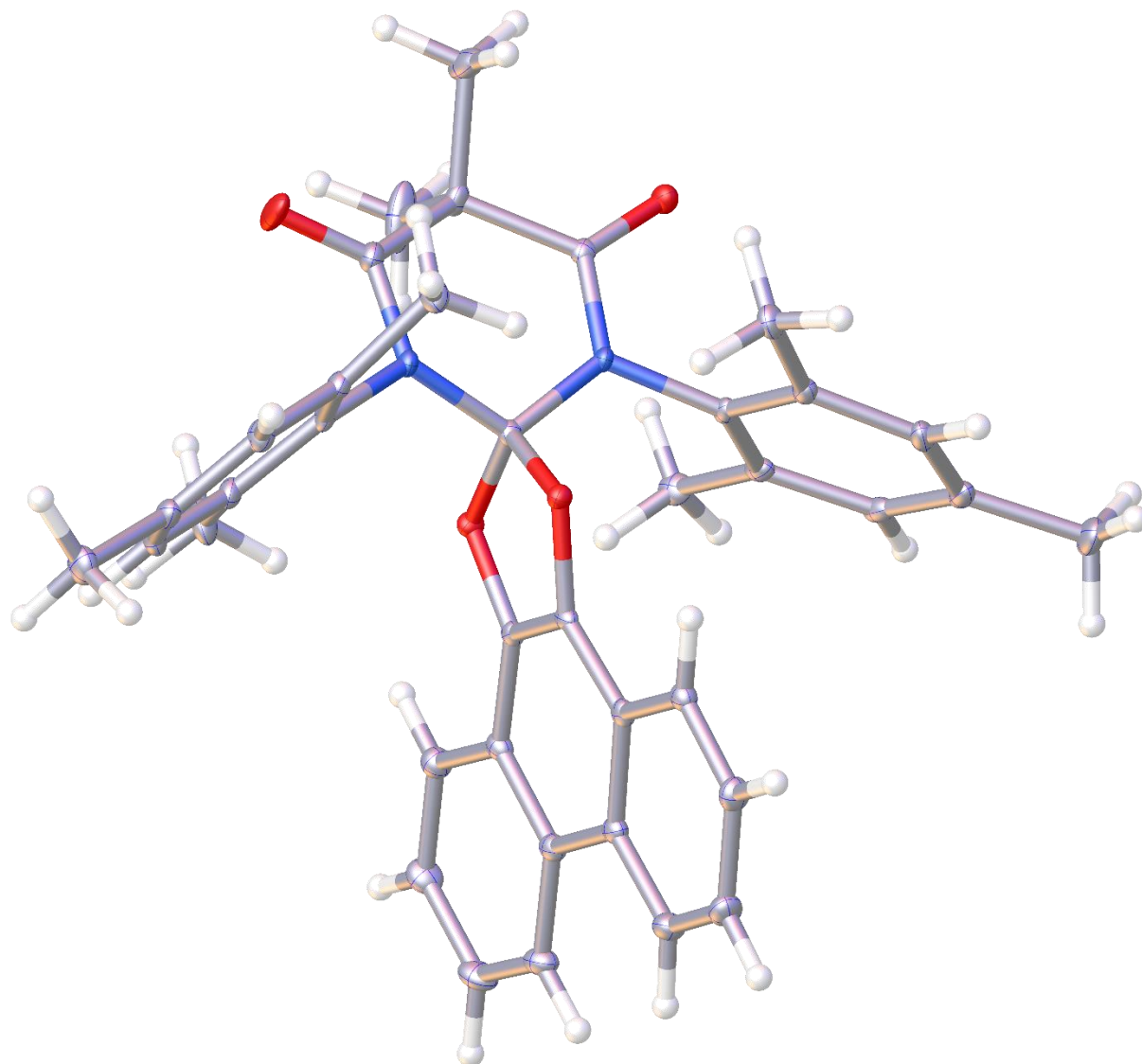
Figure 2.11: X-ray structure of **2.9.B** (ellipsoids shown at 30% probability).

X-Ray data and structure for 2.9.C.

Table 2.6: Crystal structure and refinement data for **2.9.C**.

Identification code	**2.9.C**
Empirical formula	$C_{36}H_{41}NO_2$
Formula weight	519.70
Temperature/K	100.0
Crystal system	monoclinic
Space group	$P2_1/c$
a/Å	12.3948(3)
b/Å	11.2872(2)
c/Å	20.5754(5)
$\alpha/°$	90
$\beta/°$	101.0280(10)
$\gamma/°$	90
Volume/Å^3	2825.40(11)
Z	4
$\rho_{calc}g/cm^3$	1.222
μ/mm^{-1}	0.074
F(000)	1120.0
Crystal size/mm^3	$0.05 \times 0.05 \times 0.05$
Radiation	MoKα ($\lambda = 0.71073$)
2Θ range for data collection/°	4.134 to 50.78
Index ranges	$-14 \leq h \leq 14, -13 \leq k \leq 13, -17 \leq l \leq 24$
Reflections collected	22153
Independent reflections	5183 [$R_{int} = 0.0344$, $R_{sigma} = 0.0341$]
Data/restraints/parameters	5183/0/398
Goodness-of-fit on F^2	1.030
Final R indexes [I>=2σ (I)]	$R_1 = 0.0423$, w$R_2 = 0.0945$
Final R indexes [all data]	$R_1 = 0.0586$, w$R_2 = 0.1026$
Largest diff. peak/hole / e Å^{-3}	0.54/-0.29
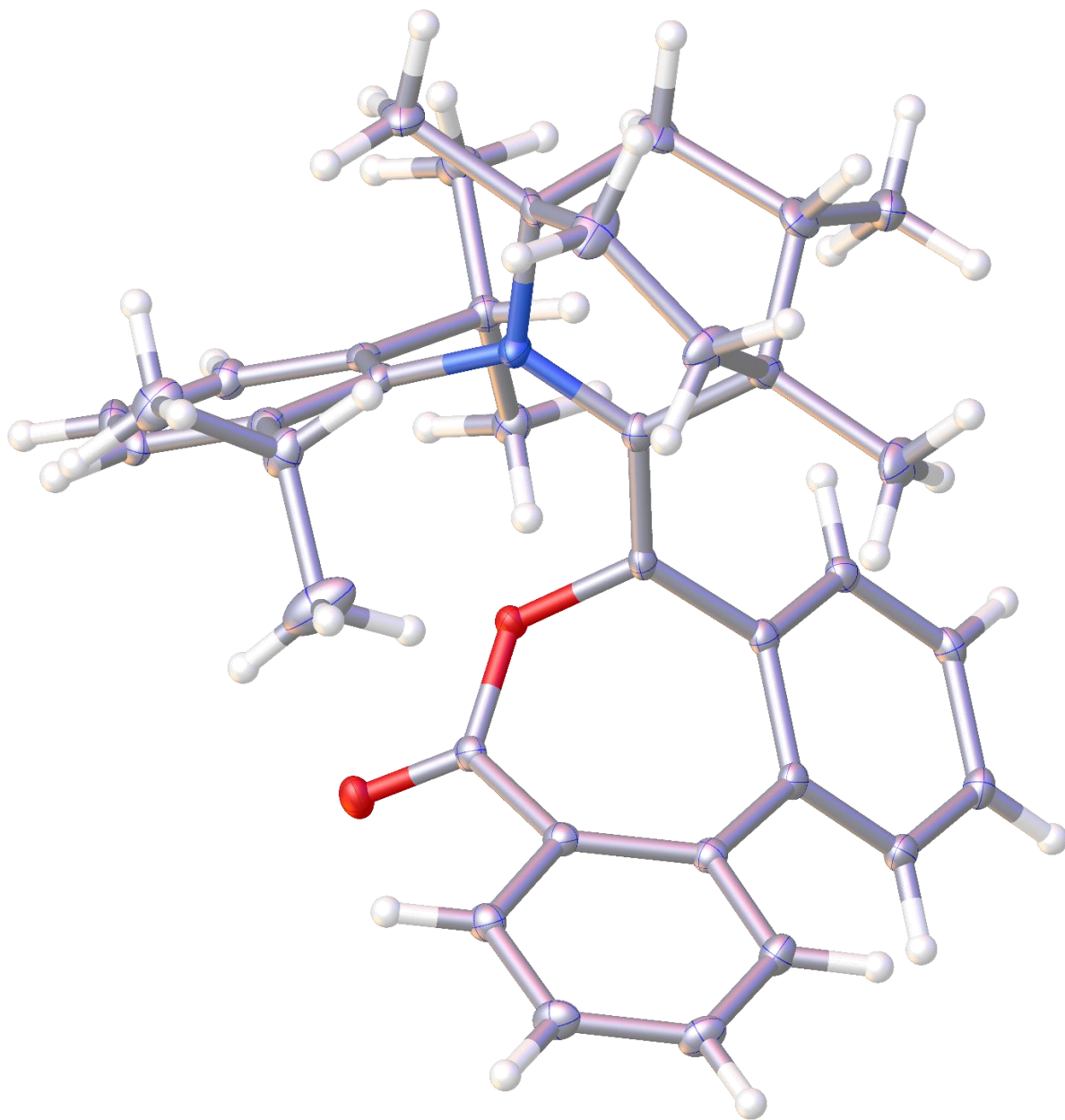
Figure 2.12: X-ray structure of **2.9.C** (ellipsoids shown at 30% probability).

X-Ray data and structure for 2.9.D.

Table 2.7: Crystal structure and refinement data for **2.9.D**.

Identification code	**2.9.D**
Empirical formula	$C_{34}H_{39}NO_2$
Formula weight	493.66
Temperature/K	100.15
Crystal system	monoclinic
Space group	$P2_1/n$
a/Å	10.042(3)
b/Å	13.464(3)
c/Å	20.119(5)
$\alpha/°$	90
$\beta/°$	90.293(9)
$\gamma/°$	90
Volume/$Å^3$	2720.3(12)
Z	4
$\rho_{calc}g/cm^3$	1.205
μ/mm^{-1}	0.074
F(000)	1064.0
Crystal size/mm^3	$0.25 \times 0.2 \times 0.1$
Radiation	MoKα ($\lambda = 0.71073$)
2Θ range for data collection/°	3.64 to 52.048
Index ranges	$-12 \leq h \leq 12$, $-16 \leq k \leq 16$, $-24 \leq l \leq 24$
Reflections collected	40418
Independent reflections	5351 [$R_{int} = 0.0780$, $R_{sigma} = 0.0461$]
Data/restraints/parameters	5351/0/343
Goodness-of-fit on F^2	1.045
Final R indexes [I>=2σ (I)]	$R_1 = 0.0418$, $wR_2 = 0.1007$
Final R indexes [all data]	$R_1 = 0.0569$, $wR_2 = 0.1108$
Largest diff. peak/hole / e $Å^{-3}$	0.28/-0.23
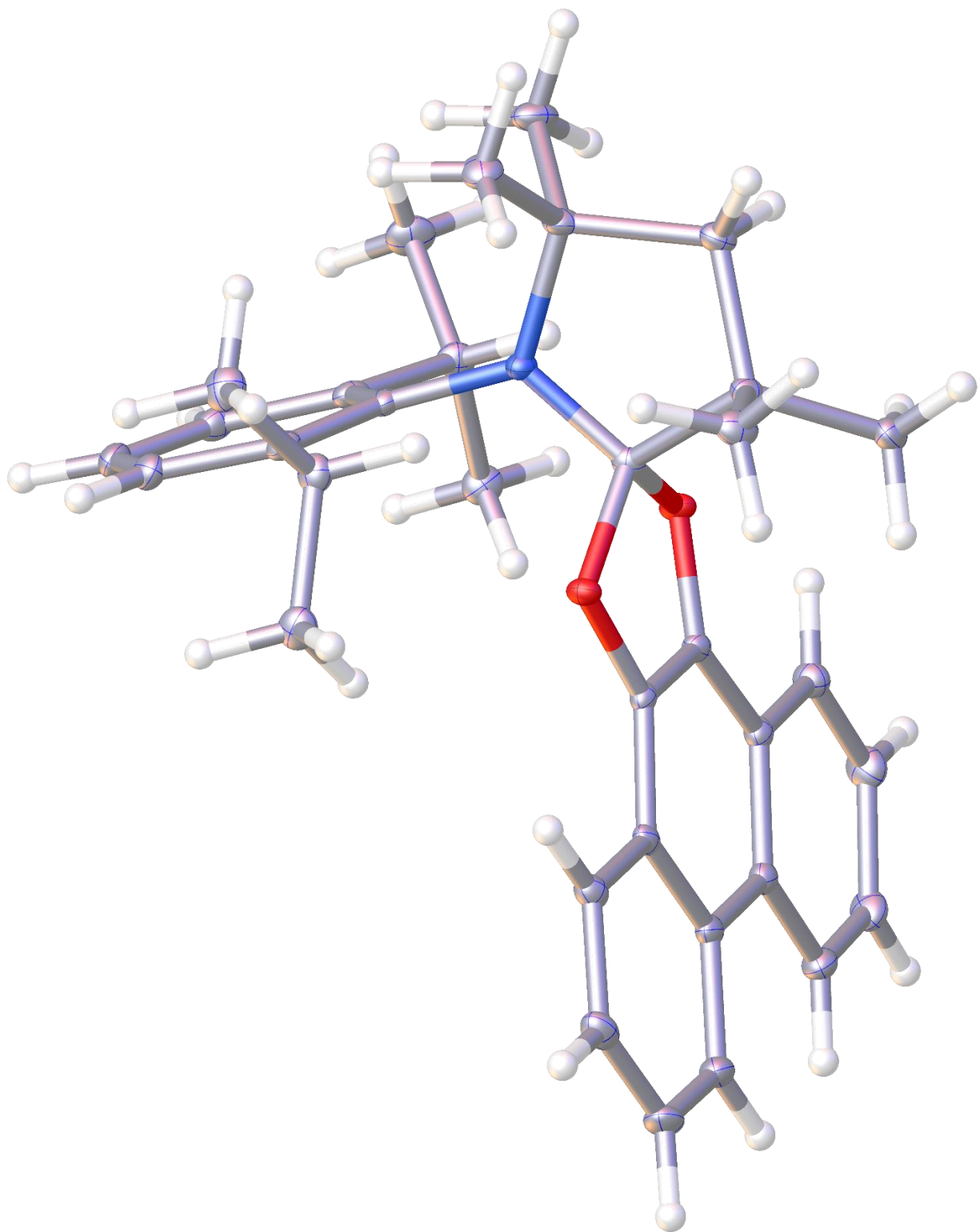
Figure 2.13: X-ray structure of **2.9.D** (ellipsoids shown at 30% probability).

X-Ray data and structure for Carbo-1.

Table 2.8: Crystal structure and refinement data for **Carbo-1**.

Identification code	**Carbo-1**
Empirical formula	$C_{15}H_8O_3$
Formula weight	236.21
Temperature/K	100.0
Crystal system	monoclinic
Space group	$P2_1/c$
a/Å	15.818(19)
b/Å	7.181(6)
c/Å	18.43(2)
$\alpha/°$	90
$\beta/°$	97.14(5)
$\gamma/°$	90
Volume/Å^3	2077(4)
Z	8
ρ_{calc}g/cm^3	1.511
μ/mm^{-1}	0.106
F(000)	976.0
Crystal size/mm^3	$0.3 \times 0.05 \times 0.05$
Radiation	MoKα ($\lambda = 0.71073$)
2Θ range for data collection/°	2.594 to 50.724
Index ranges	$-12 \leq h \leq 19$, $-8 \leq k \leq 8$, $-22 \leq l \leq 21$
Reflections collected	11759
Independent reflections	3783 [$R_{int} = 0.0501$, $R_{sigma} = 0.0595$]
Data/restraints/parameters	3783/0/325
Goodness-of-fit on F^2	1.036
Final R indexes [I>=2σ (I)]	$R_1 = 0.0828$, $wR_2 = 0.2192$
Final R indexes [all data]	$R_1 = 0.1087$, $wR_2 = 0.2400$
Largest diff. peak/hole / e Å^{-3}	0.87/-0.38
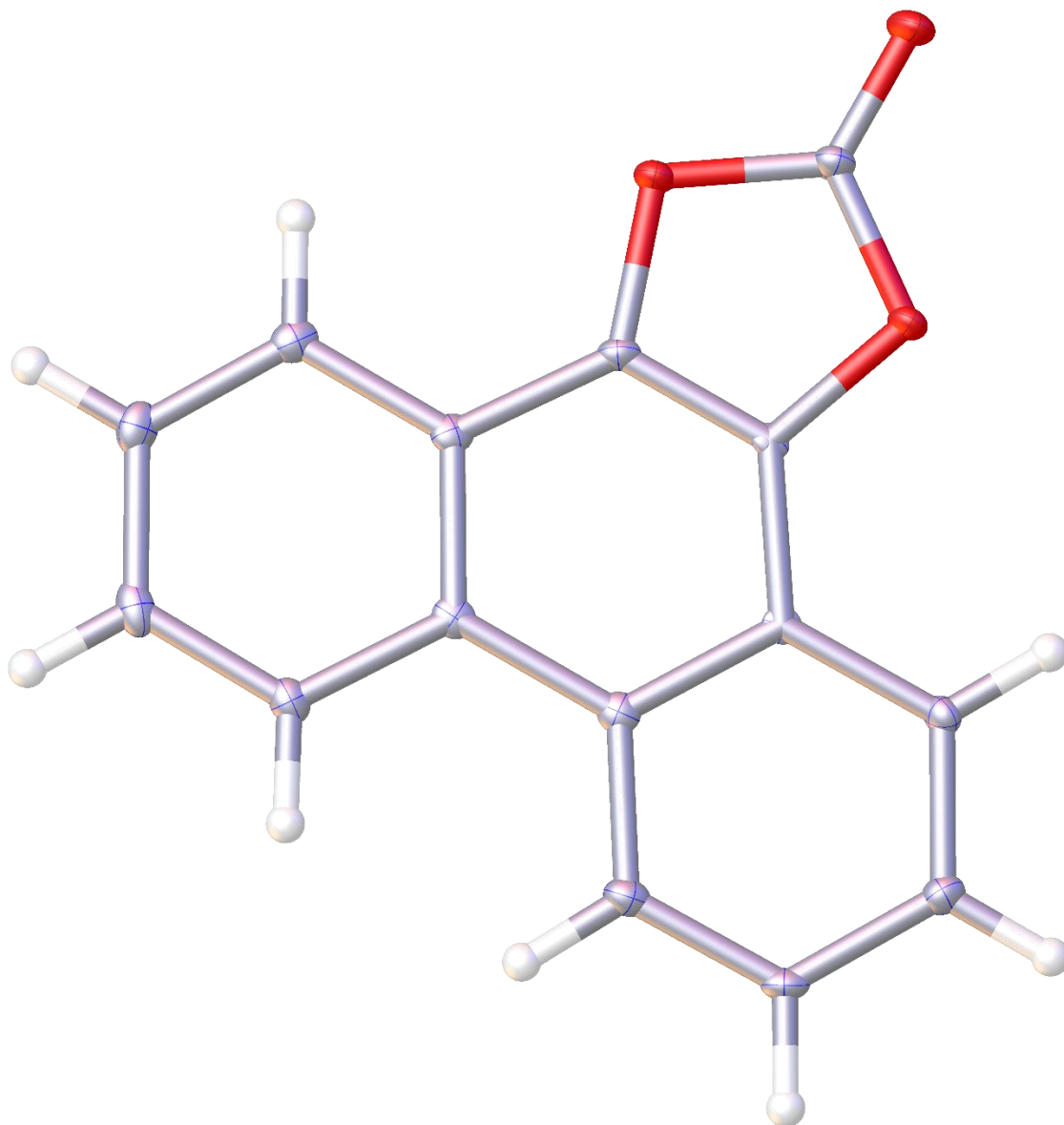
Figure 2.14: X-ray structure of **Carbo-1** (ellipsoids shown at 30% probability).

start Validation Reply Form

_vrf_PLAT097_**Carbo-1**;

PROBLEM: Large Reported Max. (Positive) Residual Density   0.87 eA-3

RESPONSE: Residual electron density was detected which can be attributed to a secondary orientation of

Carbo-1 in the lattice;

end Validation Reply Form.

X-Ray data and structure for Carbo-2.

Table 2.9: Crystal structure and refinement data for **Carbo-2**.

Identification code	**Carbo-2**
Empirical formula	$C_{14}H_7Cl_3N_2O_3$
Formula weight	357.57
Temperature/K	100.0
Crystal system	orthorhombic
Space group	Pbcm
a/Å	5.56110(10)
b/Å	18.7200(4)
c/Å	13.4542(3)
α/°	90
β/°	90
γ/°	90
Volume/Å^3	1400.63(5)
Z	4
ρ_{calc}g/cm^3	1.696
μ/mm^{-1}	6.066
F(000)	720.0
Crystal size/mm^3	$0.1 \times 0.1 \times 0.05$
Radiation	CuKα (λ = 1.54178)
2Θ range for data collection/°	9.448 to 136.938
Index ranges	$-6 \leq h \leq 6$, $-22 \leq k \leq 21$, $-16 \leq l \leq 15$
Reflections collected	13438
Independent reflections	1353 [R_{int} = 0.0367, R_{sigma} = 0.0259]
Data/restraints/parameters	1353/0/106
Goodness-of-fit on F^2	1.064
Final R indexes [I>=2σ (I)]	R_1 = 0.0284, wR_2 = 0.0703
Final R indexes [all data]	R_1 = 0.0289, wR_2 = 0.0707
Largest diff. peak/hole / e Å^{-3}	0.21/-0.29

Figure 2.15: X-ray structure of **Carbo-2** (ellipsoids shown at 30% probability).

2.4.4 Computational Details.

All calculations were performed with the Gaussian 16 program package[59] (version g16, rev.a03). The theoretical approach is based on the framework of density functional theory (DFT).[60,61] All calculations were performed with the B3LYP functional and Ahlrichs redefined triple-ζ basis set [def2-TZVP].[43,44] Grimme's D3 dispersion correction with Becke-Johnson damping was used in order to take dispersion effects into account.[62,63] Ground states were fully optimized without constraints at the corresponding level of theory and verified by a frequency calculation. Gibbs free reaction energies and enthalpies were calculated for standard conditions (p = 1 atm, T = 298 K) and are unscaled. For the visualization of molecular structures, CYLview was used.[64]

2.4.5 NMR Spectra of DAC Mixtures.
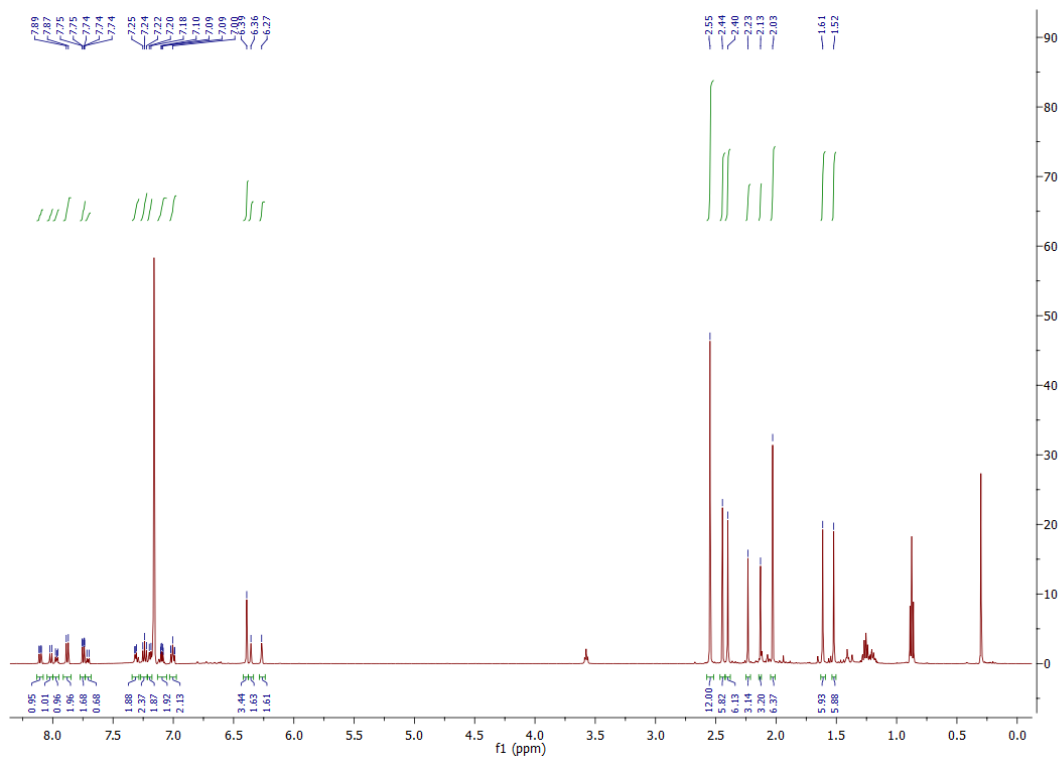
Figure 2.16: ^{1}H NMR (500 MHz, C$_6$D$_6$) of the mixture, **2.8.B** and **2.9.B**, immediately following reaction from **2.5.B** and **Quin-1**.
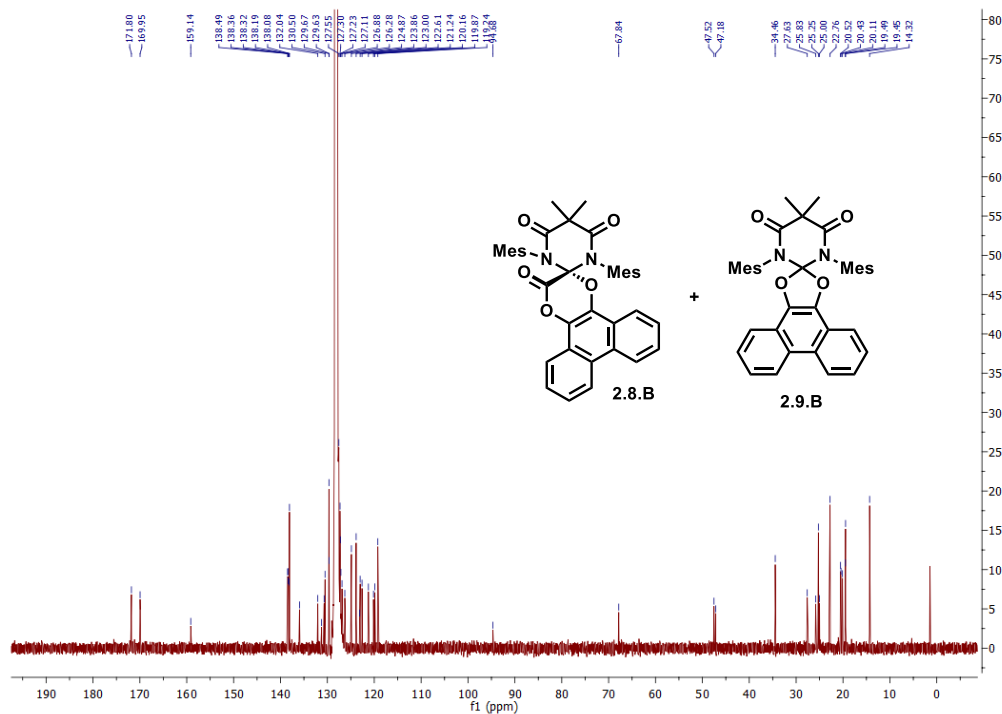
Figure 2.17: $^{13}C\{^1H\}$ NMR (125.7 MHz, C₆D₆) of the mixture, **2.8.B** and **2.9.B**, immediately following reaction from **2.5.B** and **Quin-1**.
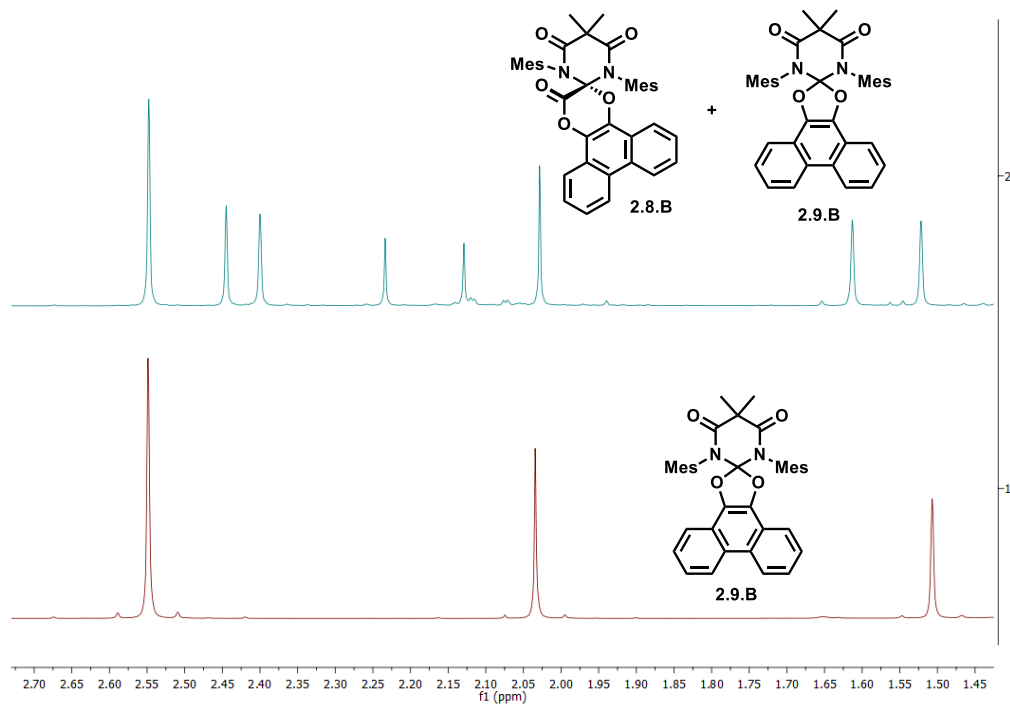
Figure 2.18: Stacked ^1H NMR (500 MHz, C₆D₆) spectra showing the mixture of **2.8.B** and **2.9.B** immediately following reaction from **2.5.B** and **Quin-1** (top) versus pure **2.9.B** (bottom).
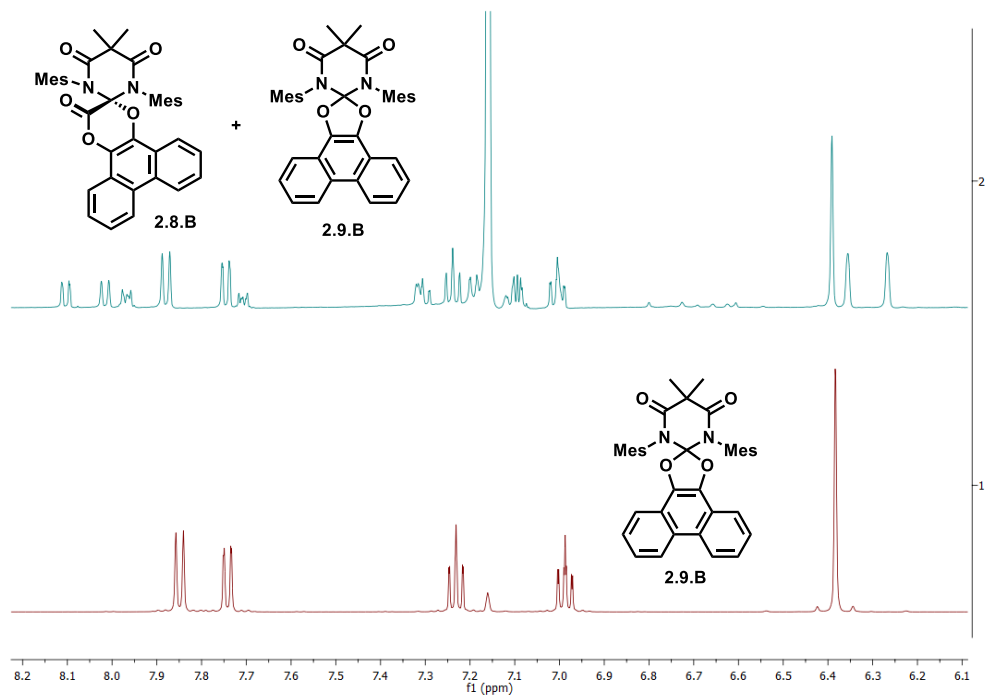
Figure 2.19: Stacked ^{1}H NMR (500 MHz, C$_6$D$_6$) spectra showing the mixture of **2.8.B** and **2.9.B** immediately following reaction from **2.5.B** and **Quin-1** (top) versus pure **2.9.B** (bottom).
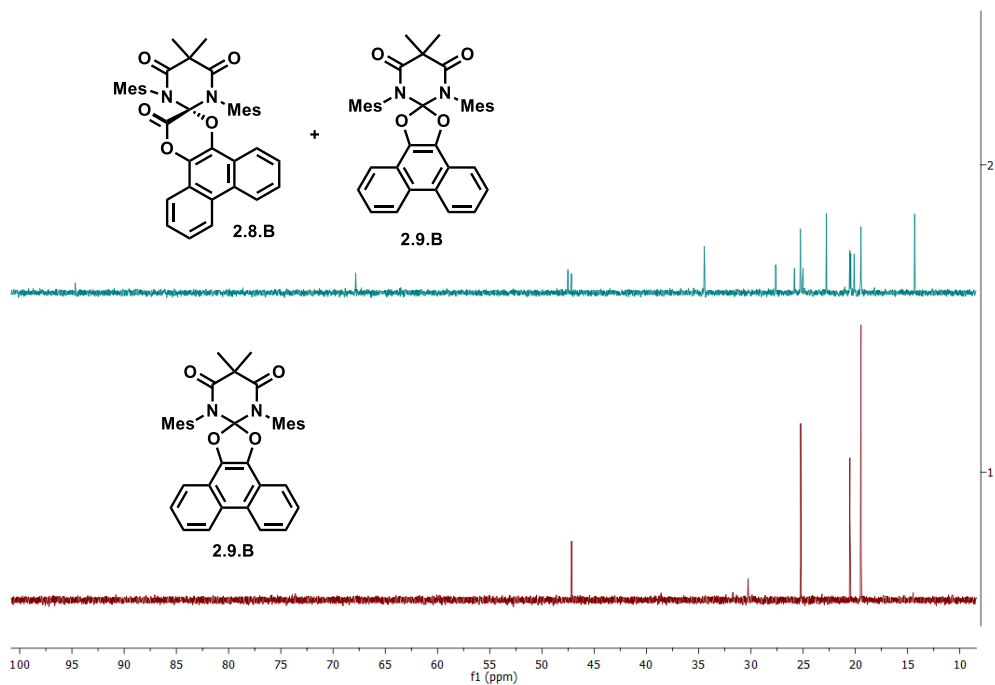
Figure 2.20: Stacked ^{13}C{^{1}H} NMR (125.7 MHz, C$_6$D$_6$) spectra showing the mixture of **2.8.B** and **2.9.B** immediately following reaction from **2.5.B** and **Quin-1** (top) versus pure **2.9.B** (bottom).

Figure 2.21: Stacked $^{13}C\{^1H\}$ NMR (125.7 MHz, C_6D_6) spectra showing the mixture of **2.8.B** and **2.9.B** immediately following reaction from **2.5.B** and **Quin-1** (top) versus pure **2.9.B** (bottom).

2.5 Acknowledgements

2.6 References

(1)   List, B. Introduction: Organocatalysis. *Chem. Rev.* **2007**, *107*, 5413–5415.

(2)   Bertelsen, S.; Jørgensen, K. A. Organocatalysis–after the Gold Rush. *Chem. Soc. Rev.* **2009**, *38*, 2178–2189.

(3)   Melen, R. L. Frontiers in Molecular P-Block Chemistry: From Structure to Reactivity. *Science* **2019**, *363*, 479–484.

(4)   Vogel, P.; Lam, Y. H.; Simon, A.; Houk, K. N. Organocatalysis: Fundamentals and Comparisons to Metal and Enzyme Catalysis. *Catalysts* **2016**, *6*, 128.

(5)   Breslow, R. On the Mechanism of Thiamine Action. IV. Evidence from Studies on Model Systems. *J. Am. Chem. Soc.* **1958**, *80*, 3719–3726.

(6)   Wang, N.; Xu, J.; Lee, J. K. The Importance of N-Heterocyclic Carbene Basicity in Organocatalysis. *Org. Biomol. Chem.* **2018**, *16*, 6852–6866.

(7)   Enders, D.; Balensiefer, T. Nucleophilic Carbenes in Asymmetric Organocatalysis. *Acc. Chem. Res.* **2004**, *37*, 534–541.

(8)   Grossmann, A.; Enders, D. N-Heterocyclic Carbene Catalyzed Domino Reactions. *Angew. Chem. Int. Ed.* **2012**, *51*, 314–325.

(9)   Naumann, S.; Dove, A. P. N-Heterocyclic Carbenes as Organocatalysts for Polymerizations: Trends and Frontiers. *Polym. Chem.* **2015**, *6*, 3185–3200.

(10)   Hollóczki, O. The Mechanism of N-Heterocyclic Carbene Organocatalysis through a Magnifying Glass. *Chem. Eur. J.* **2020**, *26*, 4885–4894.

(11)   Bugaut, X.; Glorius, F. Organocatalytic Umpolung: N-Heterocyclic Carbenes and Beyond. *Chem. Soc. Rev.* **2012**, *41*, 3511–3522.

(12)   Enders, D.; Niemeier, O.; Henseler, A. Organocatalysis by N-Heterocyclic Carbenes. *Chem. Rev.* **2007**, *107*, 5606–5655.

(13)   Regnier, V.; Romero, E. A.; Molton, F.; Jazzar, R.; Bertrand, G.; Martin, D. What Are the Radical Intermediates in Oxidative N-Heterocyclic Carbene Organocatalysis? *J. Am. Chem. Soc.* **2019**, *141*, 1109–1117.

(14)   Rehbein, J.; Ruser, S. M.; Phan, J. NHC-Catalysed Benzoin Condensation-Is It All down to the Breslow Intermediate? *Chem. Sci.* **2015**, *6*, 6013–6018.

(15)   Ishii, T.; Nagao, K.; Ohmiya, H. Recent Advances in N-Heterocyclic Carbene-Based Radical Catalysis. *Chem. Sci.* **2020**, *11*, 5630–5636.

(16)   Frey, G. D.; Lavallo, V.; Donnadieu, B.; Schoeller, W. W.; Bertrand, G. Facile Splitting of Hydrogen and Ammonia by Nucleophilic Activation at a Single Carbon Center. *Science* **2007**, *316*, 439–441.

(17)   Martin, D.; Soleilhavoup, M.; Bertrand, G. Stable Singlet Carbenes as Mimics for Transition Metal Centers. *Chem. Sci.* **2011**, *2*, 389–399.

(18)   Frey, G. D.; Masuda, J. D.; Donnadieu, B.; Bertrand, G. Activation of Si-H, B-H, and P-H Bonds at a Single Nonmetal Center. *Angew. Chem. Int. Ed.* **2010**, *49*, 9444–9447.

(19)   Moerdyk, J. P.; Blake, G. A.; Chase, D. T.; Bielawski, C. W. Elucidation of Carbene Ambiphilicity Leading to the Discovery of Reversible Ammonia Activation. *J. Am. Chem. Soc.* **2013**, *135*, 18798–

18801.

(20)   Zhukhovitskiy, A. V.; Mavros, M. G.; Queeney, K. T.; Wu, T.; Voorhis, T. Van; Johnson, J. A. Reactions of Persistent Carbenes with Hydrogen-Terminated Silicon Surfaces. *J. Am. Chem. Soc.* **2016**, *138*, 8639–8652.

(21)   Teator, A. J.; Tian, Y.; Chen, M.; Lee, J. K.; Bielawski, C. W. An Isolable, Photoswitchable N-Heterocyclic Carbene: On-Demand Reversible Ammonia Activation. *Angew. Chem. Int. Ed.* **2015**, *54*, 11559–11563.

(22)   Eichhorn, A. F.; Fuchs, S.; Flock, M.; Marder, T. B.; Radius, U. Reversible Oxidative Addition at Carbon. *Angew. Chem. Int. Ed.* **2017**, *56*, 10209–10213.

(23)   Tolentino, D. R.; Neale, S. E.; Isaac, C. J.; Macgregor, S. A.; Whittlesey, M. K.; Jazzar, R.; Bertrand, G. Reductive Elimination at Carbon under Steric Control. *J. Am. Chem. Soc.* **2019**, *141*, 9823–9826.

(24)   Hartwig, J. F. Carbon–Heteroatom Bond Formation Catalysed by Organometallic Complexes. *Nature* **2008**, *455*, 314.

(25)   Marcone, J. E.; Moloy, K. G. Kinetic Study of Reductive Elimination from the Complexes (Diphosphine)Pd(R)(CN). *J. Am. Chem. Soc.* **1998**, *120*, 8527–8528.

(26)   Blackaby, W. J. M.; Neale, S. E.; Isaac, C. J.; Sabater, S.; Macgregor, S. A.; Whittlesey, M. K. N-Heterocyclic Carbene Non-Innocence in the Catalytic Hydrophosphination of Alkynes. *ChemCatChem* **2019**, *11*, 1893–1897.

(27)   Crabtree, R. H. *The Organometallic Chemistry of the Transition Metals*; Wiley, 2009.

(28)   Colquhoun, H. M., Thompson, D. J., Twigg, M. V. *Carbonylation: Direct Synthesis of Carbonyl Compounds.*; Springer: New York, 1991.

(29)   Beller, M.; Wu, X.-F. *Transition Metal Catalyzed Carbonylation Reactions*; 2013.

(30)   Dixon, D. A.; Arduengo, A. J.; Dobbs, K. D.; Khasnis, D. V. On the Proposed Existence of a Ketene Derived from Carbon Monoxide and 1,3-Di-1-Adamantylimidazol-2-Ylidene. *Tetrahedron Lett.* **1995**, *36*, 645–648.

(31)   Gong, L.; McAllister, M. A.; Tidwell, T. T. Substituent Effects on Ketene Structure and Stability: An Ab Initio Study. *J. Am. Chem. Soc.* **1991**, *113*, 6021–6028.

(32)   Lavallo, V.; Canac, Y.; Donnadieu, B.; Schoeller, W. W.; Bertrand, G. CO Fixation to Stable Acyclic and Cyclic Alkyl Amino Carbenes: Stable Amino Ketenes with a Small HOMO–LUMO Gap. *Angew. Chem. Int. Ed.* **2006**, *45*, 3488–3491.

(33)   Hudnall, T. W.; Bielawski, C. W. An N,N′-Diamidocarbene: Studies in C-H Insertion, Reversible Carbonylation, and Transition-Metal Coordination Chemistry. *J. Am. Chem. Soc.* **2009**, *131*, 16039–16041.

(34)   Siemeling, U.; Färber, C.; Bruhn, C.; Leibold, M.; Selent, D.; Baumann, W.; von Hopffgarten, M.; Goedecke, C.; Frenking, G. N-Heterocyclic Carbenes Which Readily Add Ammonia, Carbon Monoxide and Other Small Molecules,. *Chem. Sci.* **2010**, *1*, 697–704.

(35) Martin, D.; Moore, C. E.; Rheingold, A. L.; Bertrand, G. An Air-Stable Oxyallyl Radical Cation. *Angew. Chem. Int. Ed.* **2013**, *52*, 7014–7017.

(36) Schoenberg, A.; Mustafa, A. 186. Photochemical Reactions in Sunlight. Part XII. Reactions with Phenanthraquinone, 9-Arylxanthens, and Diphenyl Triketone. *J. Chem. Soc.* **1947**, 997–1000.

(37) Erickson, J. L. E.; Dechary, J. M. The Addition of Diphenylketene to o-Benzoquinone. *J. Am. Chem. Soc.* **1952**, *74*, 2644–2646.

(38) Ried, W.; Radt, W. Ketene Capture by O-Quinones. *Angew. Chem. Int. Ed.* **1963**, *2*, 397.

(39) Ried, W.; Radt, W. Uber Die Reaktion Von Ketenen Mit O-Chinonen. *Justus Liebigs Ann. Chem.* **1964**, *17*, 110–114.

(40) Goedecke, C.; Leibold, M.; Siemeling, U.; Frenking, G. When Does Carbonylation of Carbenes Yield Ketenes? A Theoretical Study with Implications for Synthesis. *J. Am. Chem. Soc.* **2011**, *133*, 3557–3569.

(41) Tomás-Mendivil, E.; Hansmann, M. M.; Weinstein, C. M.; Jazzar, R.; Melaimi, M.; Bertrand, G. Bicyclic (Alkyl)(Amino)Carbenes (BICAACs): Stable Carbenes More Ambiphilic than CAACs. *J. Am. Chem. Soc.* **2017**, *139*, 7753–7756.

(42) Tretiakov, M.; Shermolovich, Y. G.; Singh, A. P.; Samuel, P. P.; Roesky, H. W.; Niepötter, B.; Visscher, A.; Stalke, D. Lewis-Base Stabilized Diiodine Adducts with N-Heterocyclic Chalcogenamides. *Dalt. Trans.* **2013**, *42*, 12940–12946.

(43) Weigend, F.; Ahlrichs, R. Balanced Basis Sets of Split Valence, Triple Zeta Valence and Quadruple Zeta Valence Quality for H to Rn: Design and Assessment of Accuracy. *Phys. Chem. Chem. Phys.* **2005**, *7*, 3297–3305.

(44) Weigend, F. Accurate Coulomb-Fitting Basis Sets for H to Rn. *Phys. Chem. Chem. Phys.* **2006**, *8*, 1057–1065.

(45) Ganesamoorthy, C.; Schoening, J.; Wölper, C.; Song, L.; Schreiner, P. R.; Schulz, S. A Silicon–Carbonyl Complex Stable at Room Temperature. *Nat. Chem.* **2020**, *12*, 608–614.

(46) Hansmann, M. M.; Jazzar, R.; Bertrand, G. Singlet (Phosphino)Phosphinidenes Are Electrophilic. *J. Am. Chem. Soc.* **2016**, *138*, 8356–8359.

(47) Hansmann, M. M.; Bertrand, G. Transition-Metal-like Behavior of Main Group Elements: Ligand Exchange at a Phosphinidene. *J. Am. Chem. Soc.* **2016**, *138*, 15885–15888.

(48) Puschmann, F. F.; Stein, D.; Heift, D.; Hendriksen, C.; Gal, Z. A.; Grützmacher, H. F.; Grützmacher, H. Phosphination of Carbon Monoxide: A Simple Synthesis of Sodium Phosphaethynolate (NaOCP). *Angew. Chem. Int. Ed.* **2011**, *50*, 8420–8423.

(49) Finze, M.; Bernhardt, E.; Terheiden, A.; Berkei, M.; Willner, H.; Christen, D.; Oberhammer, H.; Aubke, F. Tris(Trifluoromethyl)Borane Carbonyl, $(CF_3)_3BCO$ - Synthesis, Physical, Chemical and Spectroscopic Properties, Gas Phase, and Solid State Structure. *J. Am. Chem. Soc.* **2002**, *124*, 15385–15398.

(50) Dahcheh, F.; Martin, D.; Stephan, D. W.; Bertrand, G. Synthesis and Reactivity of a CAAC-Aminoborylene Adduct: A Hetero-Allene or an Organoboron Isoelectronic with Singlet Carbenes. *Angew. Chem. Int. Ed.* **2014**, *53*, 13159–13163.

(51) Braunschweig, H.; Dewhurst, R. D.; Hupp, F.; Nutz, M.; Radacki, K.; Tate, C. W.; Vargas, A.; Ye, Q. Multiple Complexation of CO and Related Ligands to a Main-Group Element. *Nature* **2015**, *522*, 327–330.

(52) Braunschweig, H.; Krummenacher, I.; Legare, M. A.; Matler, A.; Radacki, K.; Ye, Q. Main-Group Metallomimetics: Transition Metal-like Photolytic CO Substitution at Boron. *J. Am. Chem. Soc.* **2017**, *139*, 1802–1805.

(53) Peng, J. B.; Geng, H. Q.; Wu, X. F. The Chemistry of CO: Carbonylation. *Chem* **2019**, *5*, 526–552.

(54) Jazzar, R.; Bourg, J. B.; Dewhurst, R. D.; Donnadieu, B.; Bertrand, G. Intramolecular "Hydroiminiumation and -Amidiniumation" of Alkenes: A Convenient, Flexible, and Scalable Route to Cyclic Iminium and Imidazolinium Salts. *J. Org. Chem.* **2007**, *72*, 3492–3499.

(55) Hudnall, T. W.; Moerdyk, J. P.; Bielawski, C. W. Ammonia N-H Activation by a N,N′-Diamidocarbene. *Chem. Commun.* **2010**, *46*, 4288–4290.

(56) Jazzar, R.; Dewhurst, R. D.; Bourg, J.-B.; Donnadieu, B.; Canac, Y.; Bertrand, G. Intramolecular "Hydroiminiumation" of Alkenes: Application to the Synthesis of Conjugate Acids of Cyclic Alkyl Amino Carbenes (CAACs). *Angew. Chem. Int. Ed.* **2007**, *46*, 2899–2902.

(57) O. V. Dolomanov, L. J. Bourhis, R. J. Gildea, J. A. K. Howard, H. P. Olex2: A Complete Structure Solution, Refinement and Analysis Program. *J. Appl. Cryst.* **2009**, *42*, 339–341.

(58) G. M. Sheldrick. A Short History of SHELX. *Acta Crystallogr. A* **2008**, *64*, 112–122.

(59) Frisch, M. J.; Trucks, G. W.; Schlegel, H. B.; Scuseria, G. E.; Robb, M. A.; Cheeseman, J. R.; Scalmani, G.; Barone, V.; Petersson, G. A.; Nakatsuji, H.; Li, X.; Caricato, M.; Marenich, A. V.; Bloino, J.; Janesko, B. G.; Gomperts, R.; Mennucci, B.; Hratchian, H. P.; Ortiz, J. V.; Izmaylov, A. F.; Sonnenberg, J. L.; Williams-Young, D.; Ding, F.; Lipparini, F.; Egidi, F.; Goings, J.; Peng, B.; Petrone, A.; Henderson, T.; Ranasinghe,D.; Zakrzewski, V. G.; J. Gao, N. R.; Zheng, G.; Liang, W.; Hada, M.; Ehara, M.; Toyota, K.; Fukuda, R.; Hasegawa, J.; Ishida, M.; Nakajima, T.; Honda, Y.; Kitao, O.; Nakai, H.; Vreven, T.; Throssell, K.; Montgomery, J. A.; Jr., J. E. P.; Ogliaro, F.; Bearpark, M. J.; Heyd, J. J.; Brothers, E. N.; Kudin, K. N.; Staroverov, V. N.; Keith, T. A.; Kobayashi, R.; Normand, J.; Raghavachari, K.; A. P. Rendell; J. C. Burant; S. S. Iyengar; J. Tomasi; M. Cossi; J. M. Millam; M. Klene; C. Adamo; R. Cammi; J. W. Ochterski; R. L. Martin; K. Morokuma; O. Farkas; J. B. Foresman; Fox, D. J. *Gaussian 16, Revision A.03.* Gaussian, Inc.: Wallingford CT 2016.

(60) Hohenberg, P.; Kohn, W. Inhomogeneous Electron Gas. *Phys. Rev.* **1964**, *136*, B864–B871.

(61) Kohn, W.; Sham, L. J. Self-Consistent Equations Including Exchange and Correlation Effects. *Phys. Rev.* **1965**, *140*, A1133–A1138.

(62) Grimme, S.; Antony, J.; Ehrlich, S.; Krieg, H. A Consistent and Accurate Ab Initio Parametrization of Density Functional Dispersion Correction (DFT-D) for the 94 Elements H-Pu. *J. Chem. Phys.* **2010**, *132*, 154104.

(63)   Grimme, S.; Ehrlich, S.; Goerigk, L. Effect of the Damping Function in Dispersion Corrected Density Functional Theory. *J. Comput. Chem.* **2011**, *32*, 1456–1465.

(64)   Legault, C. Y. *CYLview, 1.0b.* Université de Sherbrooke 2009.

Chapter 3 – Eliminating Nonradiative Decay in Cu(I) Emitters: >99% Quantum Efficiency & Microsecond Lifetime

3.1   Introduction

In the 1950's, André Bernanose *et al.* discovered a process known as electroluminescence, an optical and electrical phenomenon in which a current engenders emission, in organic materials, more specifically, organic dyes (Figure 3.1).[1,2] Afterwards, in 1987, Van Slyke *et al.* at Eastman Kodak developed the first electroluminescent device based on exploiting a thin multilayered structure with an organic material as the source of emission, nominally an organic light emitting diode (OLED).[3] Because of their high emissive efficiency and greater contrast-ratio, with the ability to produce "true black," OLEDs have been extensively used in a range of devices that rely on light emitting displays (*e.g.*, mobile phones, TVs, and laptops).[4,5]

Bernanose, 1953
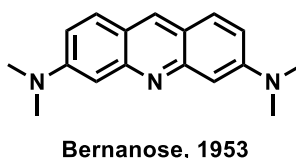
Figure 3.1: One of the first electroluminescent compounds discovered, acridine orange, by applying an alternating voltage.

3.1.1   Heavy Metal Phosphorescence.

Despite this technology's more organic beginnings, in a seminal report, Forrest *et al.* were able to demonstrate that phosphorescent dyes coordinated to platinum, a heavy transition metal, achieved high-efficiency energy transfer from both singlet and triplet states to produce an electroluminescent device with saturated red emission (Figure 3.2, left).[6] The slow phosphorescence, a typically highly spin forbidden process, however, led to problems associated with the saturation of emissive sites and a decrease in efficiency at high drive currents.[7] Therefore, subsequent development of organometallic species led to the design of several iridium based complexes such as the green emitting facial tris(2-phenylpyridine) iridium complex[7] (Figure 3.2, middle) and even a rare example of a high energy deep blue emitting iridium tris(1-phenyl-3-methylbenzimidazolin-2-ylidene.[8] Unlike small organic emissive compounds which tend to operate through fluorescence and therefore can only achieve a maximum quantum efficiency of 25% due

to spin statistics, heavy transition metal complexes can achieve 100% efficiency thereby harvesting all excitons.[6,9,10] The reason for this enhanced efficiency extends from rapid intersystem crossing (ISC) and triplet emission facilitated by augmented spin-orbit coupling (SOC) which scales with the effective nuclear charge and the principal quantum number of the valence electrons, nominally the "heavy atom effect."[11] As a result, these heavy metal complexes typically feature long-lived triplet states and high luminescent efficiencies which have led to a range of applications (*e.g.*, photocatalysis,[12,13] chemo- and biosensing,[14–16] dye-sensitized solar cells[17,18] and organic electronics[19,20]).
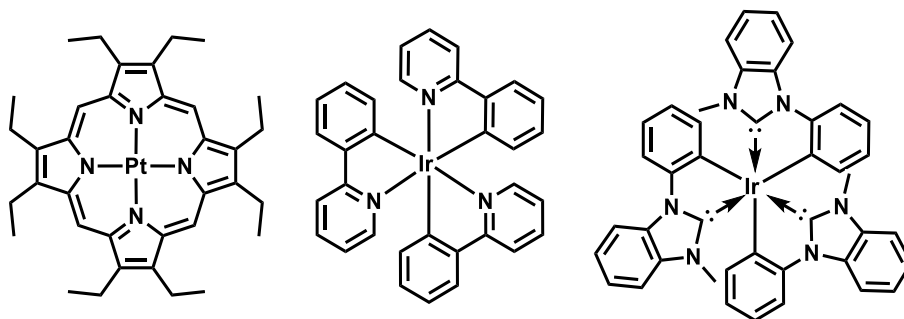
Figure 3.2: The heavy atom effect leads to highly efficient organometallic species for OLEDs: (left) The seminal phosphorescent dye 2,3,7,8,12,13,17,18-octaethyl-21H,23H-porphine platinum(II) complex initially demonstrated the power of the heavy atom effect; (middle) faster phosphorescence discovered in a green emitting facial tris(2-phenylpyridine) iridium; (right) a rare example of a deep blue emitting iridium tris(1-phenyl-3-methylbenzimidazolin-2-ylidene.

While these advancements led to several highly efficient complexes capable of spanning the visible spectrum,[21] the sparse supply and expensiveness of these heavy elements coupled with an ever-growing demand for luminescent displays have led to real concerns about potential shortages in the near future.[22] To address these concerns, there has been a paradigm shift towards the development of d^{10}-coinage metal alternatives, especially copper, which is inexpensive and for the most part, innocuous.[22] Furthermore, the photophysical benefit of completely occupied d-orbitals precludes internal quenching of the excited states by typical d*−d transitions.

3.1.2   Copper Phosphorescence.

As opposed to heavy transition metals, phosphorescence of typical copper complexes, a 1st row transition metal, is plagued by inefficient processes.[23] A large component of the problem with copper stems from the SOC parameter (ξ): for typical heavy metals such as iridium and platinum ($\xi = 3909$ cm^{-1} and 4481 cm^{-1}, respectively), the ξ is quite substantial whereas for the much lighter copper nucleus, the value is significantly smaller (ξ of 857 cm^{-1}).[24] Inherently, this leads to much slower rates in spin forbidden transitions such as ISC from the lowest excited singlet (S_1) to the lowest excited triplet (T_1)[25,26] and ISC from the lowest excited triplet (T_1) to the ground state (S_0).[19,27] These problems are exacerbated by the many copper complexes that rely on metal-to-ligand charge transfers (MLCT) for their lowest energy transitions. The reason is because d^{10} complexes experience large reorganization energies from Jahn-Teller distortions in the excited state thereby leading to low Φ_{PL} from both the higher rates of nonradiative decay and the more sluggish ISC rates.[28,29]

Given the clear struggles of copper complexes in phosphorescence based emission, a way to still harvest both singlet and triplet excitons involves taking advantage of Thermally Activated Delayed Fluorescence (TADF) (Figure 3.3, blue).[30] Typically, phosphorescent compounds exploit an equilibrium that is shifted towards a significantly lower energy T_1 state with strong spin orbit coupling for fast emission (Figure 3.3, red), but for copper complexes this leads to weak emission. Fluorescence (S_1 to S_0), on the other hand, is a much faster a spin allowed transition which is exploited in the excited state TADF manifold. A TADF systems hinges on being able to undergo up-intersystem crossing (up-ISC) from the triplet state back to the singlet state for rapid emission. An effective system involves a small enough energy splitting between the lowest excited states, $\Delta E(S_1 - T_1)$, so that they can be thermally funneled into the S_1 state thereby capturing all of the T_1 and S_1 excitons while enabling rapid, efficient emission. To minimize $\Delta E(S_1 - T_1)$, the key is to also minimize frontier orbital overlap and maximize their separation distance.[31]
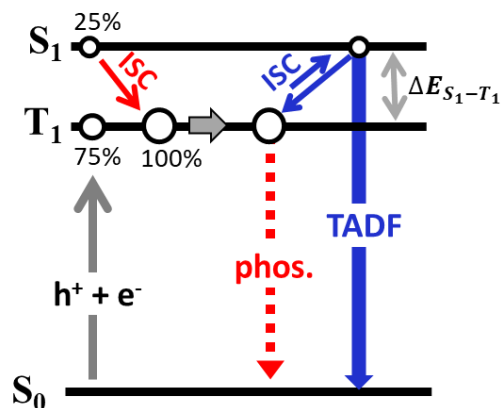
Figure 3.3: Radiative processes in an OLEDs featuring phosphorescence (in red) versus TADF (in blue).

When TADF behavior was first discovered, towards the end of the 1970's, McMillin initially described it for copper(I) phenanthroline compounds that were emitting from two different excited states, fast emission at room temperature that significantly slowed down at cryogenic temperatures.[32,33] These seminal reports led to increased interest in copper based luminescence with TADF as the predominant mechanism exploited for several categories of mononuclear complexes.[30] Many complexes that have been investigated were ligated by phenanthroline, pyridyl, phosphine, pyrazolyl, and recently NHC type ligands and comprise three major categories: cationic tetrahedral, neutral tetrahedral, and tricoordinate coordination complexes (Figure 3.4).[34–37] As can be seen, these complexes have experienced the typical low photoluminescence quantum yields (Φ_{PL}) for copper in fluid which is reflected in their poor performance in polymeric matrices and by extension, OLEDs. However, they have led to the enhancement of design principles such as the benefit of neutral species which are not prone to degradation pathways resulting from the counterion that would decompose under high current densities in electroluminescent devices. Furthermore, the Φ_{PL} was still competitive even with lower coordination numbers such as the trigonal species with Φ_{PL} of 15% (Figure 3.4). As previously mentioned, these problems are further complicated by Jahn Teller effects in the excited state for copper. The drawback of these systems, therefore, is that they are characterized by high rates of non-radiative decay especially observed in non-rigid steric environments due to significant distortions in the excited state.[38,39]
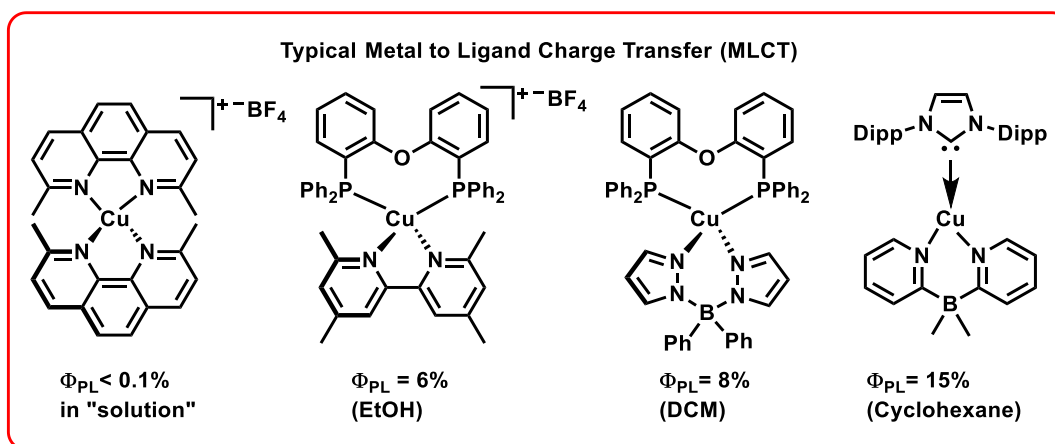
Figure 3.4: 4- and 3-coordinate tetrahedral and trigonal copper(I) TADF complexes displaying the typical low photoluminescence quantum yields (Φ_{PL}) in fluid and polymeric matrices: below each of the complexes is the solution phase Φ_{PL}.

Another problem associated with these and many other copper complexes is that they depend on metal to ligand charge transfer (MLCT) for emission. Historically, emission involves a HOMO that is metal-based and a LUMO comprised of the ligand's π^* orbitals. As opposed to organic TADFs,[40] typical copper TADF complexes, which have a much higher ξ value, experience forward ISC to the T_1 state that is sped up enough to depopulate the S_1 state before fluorescent decay relaxes the system. This results in mono-exponential emission decay at all temperatures. For example, a highly emissive copper complex with the smallest $\Delta E(S_1 - T_1)$ rate of emission is still a full order of magnitude slower than its calculated rate of fluorescence because its waiting on up-ISC.[36] Therefore, traditionally, even the best copper TADF systems experience a rate limiting factor from the endothermic transition of T_1 to S_1.

Peters *et al.*, however, described an often overlooked feature in that their system relied on interligand charge transfer (ICT) with minimal participation of copper in the excited state.[41] The result was that it significantly slowed the rate of nonradiative decay (k_{nr}) and led to an exceptionally high Φ_{PL} for a copper complex of 70% in DCM (Figure 3.5).[41] Although this highlighted an important strategy to advance copper luminescence by ICT, these complexes still could not match the efficiency of state-of-the-art 3rd row transition metals.

Interligand Charge Transfer (ICT)

Ph−N P(*i*Pr)$_2$

Cu

Ph$_3$P PPh$_3$

Φ_{PL} = 70%
(DCM)
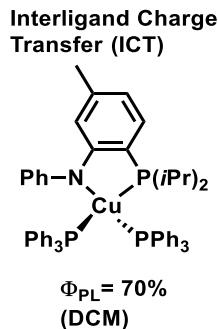
Figure 3.5: Interligand charge transfer (ICT) results in highly efficient Φ_{PL} in solution as compared to previous MLCT copper complexes.

3.1.3 Dicoordinate Copper TADFs.

Recently, a trend towards linear dicoordinate copper species began and featured an L/X ligand manifold. In 2016, Bochmann *et al.* described the first use of the ambiphilic CAAC based ligand for photoluminescent copper complexes, (^{Ad}CAAC)CuCl which achieved a Φ_{PL} of 96% in the solid state but was not reported in solution (Figure 3.6, top row, left).[42] Interestingly, soon after, a report by Steffen *et al.* found that while a (^{Me}CAAC)CuCl led to a Φ_{PL} of 60% in the solid state (Figure 3.6, top row, right), the related NHC complex was barely emissive.[43] Clearly, the CAAC ligand's strong π-acceptor properties leading to a low lying LUMO and the strong σ-donation to destabilize the metal based d-orbitals of the HOMO are essential in these photoluminescent copper systems.[44] Moreover, the comparison between the significantly less hindered ^{Me}CAAC and the bulkier, rigid ^{Ad}CAAC highlighted the importance of rigid sterics in shutting down k_{nr}. Further developments in these systems featured an array of X type ligands that supported the requirement of a rigid steric environment and dicoordinate species for higher Φ_{PL} (Figure 3.6).[45,46] These results served to cement the idea that linear copper complexes with low coordination numbers limit excited state reorganization with narrower emission profiles and lower reorganization energy energies (low k_{nr} in the solid state~$10^3\,s^{-1}$)[45] but their luminescent efficiency was still inhibited by the typical MLCT radiative transitions that suffer from longer excited state lifetimes (τ ~ 20 μs) and low k_r values (~$10^4\,s^{-1}$).[43,45]

(AdCAAC)CuCl

Φ_{PL} = 96%
k_r = 3.3 x 10^4 s^{-1}
τ = 29 μs

(EtCAAC)CuCl

Φ_{PL} = 86%
k_r = 3.9 x 10^4 s^{-1}
τ = 32 μs

(MeCAAC)CuCl

Φ_{PL} = 60%
k_r = 2.3 x 10^4 s^{-1}
τ = 26 μs

(AdCAAC)CuTp

Φ_{PL} = 2%
k_r = 2.6 x 10^4 s^{-1}
τ = 0.4 (40%), 1.0 (60%) μs

(EtCAAC)CuTp

Φ_{PL} = 46%
k_r = 3.9 x 10^4 s^{-1}
τ = 12 μs
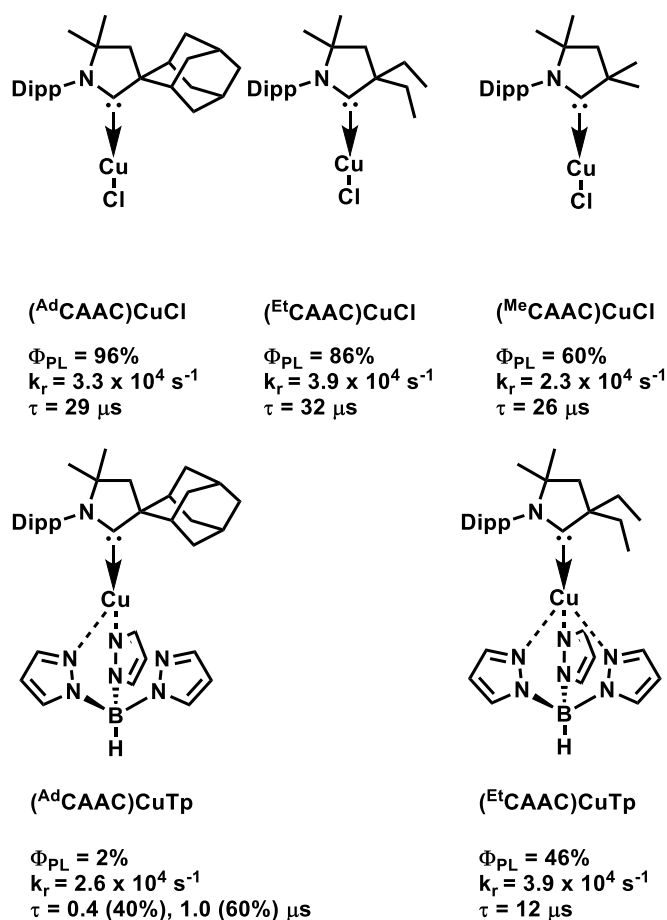
Figure 3.6: (Top row) while excited state lifetimes (τ) and k_r (τ and k_r for (AdCAAC)CuCl are from a different study[45]) appear to be unaffected by sterics, the more bulky CAAC ligands enhance solid state Φ_{PL}; (bottom row) despite much shorter τ and similar k_r values compared to the top row, 3- and 4- coordinate complexes experience much lower solid state Φ_{PL}.

As opposed to these systems that rely on MLCT, herein, we developed 2-coordinate, neutral CAAC copper(I) amide complexes that were significantly enhanced by the rigidity and sterics of the menthyl moiety. Furthermore, upon exploiting this (MenthCAAC)Cu-C$_6$F$_5$ (**3.1**), a complex that was the origin of this project, we were able to make the first example, to the best of my knowledge, of an all copper based emissive layer. Through the MenthylCAAC, we achieved Φ_{PL} >99% and short emission lifetimes (τ = 2–3 μs) in both fluid and polymeric media. Electrochemical, photophysical and computational analyses reveal the true nature for the mechanisms behind the impressive emissive properties. Furthermore, we demonstrate that too much bulk can lead to the deviation from a coplanar ligand arrangement which demonstrated that

optimized sterics are critical to maintaining high Φ_{PL} in solution and in the solid state. Finally, one of the complexes is employed in a functioning rare light blue OLED device.

3.2   Results & Discussion

Amid the burgeoning investigation into dicoordinate copper photoluminescent species, my foray into copper luminescence had peculiar origins because it was not my objective at the outset. Initially, I investigated a cationic copper complex for Lewis acid catalysis. To generate this complex, I abstracted a methyl in a copper alkyl complex with $B(C_6F_5)_3$ (BCF) (Scheme 3.1). Interestingly, this attempted abstraction led to a decomposition product over time which involved a σ-bond metathesis with BCF to engender **3.1** as confirmed by an X-ray diffraction study. At first glance, **3.1** doesn't seem unusual; however, upon scratching the surface of the glassware to collect the powder, I noticed the emission of blue light in a process known as triboluminescence.[47] Under the impression that this was indicative of a well-defined band gap and with the knowledge that high energy blue emissive materials are rare, I investigated this complex further.
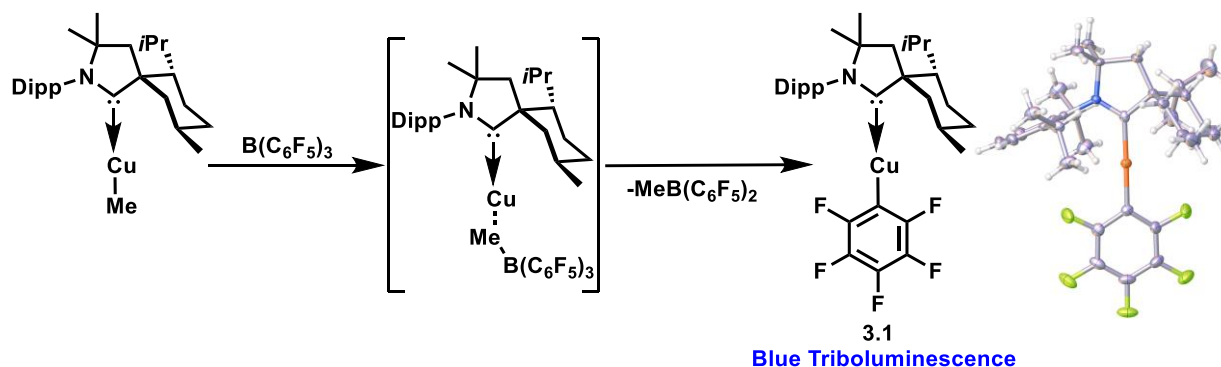
Scheme 3.1: Cationic copper complex generated by $B(C_6F_5)_3$ (BCF) with an accessible vacant coordination site undergoes a σ-bond metathesis BCF to engender a triboluminescent (^{Menth}CAAC)Cu-C$_6$F$_5$ (**3.1**).

To determine if this complex was interesting beyond triboluminescence, I screened its emissive properties by shining a UV lamp on the material in the solid state and in a pentane solution (Figure 3.7). Gratifyingly, it led to an intense blue emission. I hypothesized that the bright luminescent properties were

the result of the menthyl moiety which is extremely rigid and represents the bulkiest five membered-CAAC that is readily available. This idea was cemented in my mind since I had extensive experience in synthesizing CAAC copper complexes, but I had never observed this phenomenon in the less hindered moieties. Therefore, I optimized the synthesis by doing a salt metathesis between LiC_6F_5 and $(^{Et}CAAC)CuCl$ to afford **3.1** in 78% yield (Scheme 3.2).

Figure 3.7: **3.1** displays bright blue emission with a UV lamp: (left) in the solid state; (right) in a saturated pentane solution under argon.
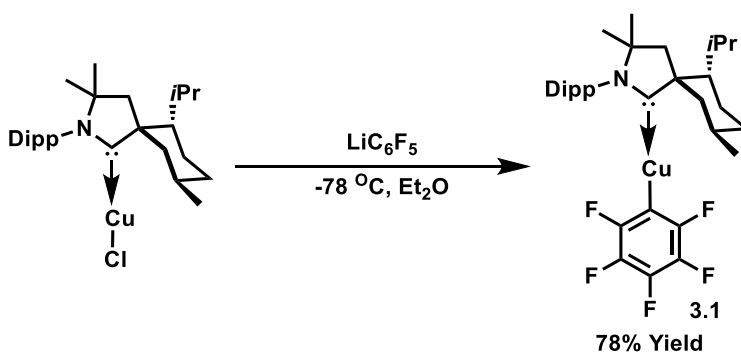
Scheme 3.2: $(^{Menth}CAAC)CuCl$ reacts with in-situ generated LiC_6F_5 (from nBuLi and C_6F_5Br) to afford **3.1**.

After making this discovery, I collaborated with the Thompson group (based on my synthetic and their photophysical expertise) at the University of Southern California where Dr. Rasha Hamze (who collected and analyzed the photophysical data for the complexes in this chapter) gave me first-hand experience in exploring the photophysical properties of **3.1**. Notably, the Φ_{PL} in the solid state (SS) was 92% and the τ of 15 μs was much shorter than previous dicoordinate complexes, but the λ_{max} was a very high energy 424 nm. We became interested in this blue emitting complex and sought to make a rare blue

91

OLED. However, the high energy emission of **3.1** was too intense to be tamed as a dopant for an OLED device because not that many hosts are readily available that feature a lower HOMO and a higher LUMO. We therefore decided to exploit it as the host instead of the dopant because its frontier energetics would form an ideal pair with a lower energy emitting dopant. This led to the idea of fabricating the first all copper based emissive layer.

Interestingly, **3.1** did not display strong TADF behavior as the excited state lifetime barely shifted from 15 μs at room temperature to 14 μs at 77 K. We therefore crystallized this species which revealed a large dihedral angle of 21.6° which is known to increase the $\Delta E(S_1 - T_1)$[29,48] leading to phosphorescent based emission. Then, we turned our attention towards a carbazole (Cz) based X ligand which would act as a π-donor that is trans to a π-accepting CAAC ligand which would favor coplanarity and lead to stronger TADF properties. While still relying on the ideal sterics of a menthyl substituent on the CAAC, we synthesized (^{Menth}CAAC)CuCz, **3.1.A** (Scheme 3.3, left). Additionally, because of the carbazole moiety, which features a planar nitrogen with a filled p orbital, the compound's HOMO raises in energy. Upon raising the HOMO, of course, the emission redshifted and the metal contribution to the HOMO is attenuated to a greater extent. Gratifyingly, **3.1.A** featured a λ_{max} with a bathochromic shift to 492 nm opening the possibility for a diversity of potential hosts in an OLED device. Also, τ was an incredible 2.5 μs, a full order of magnitude less than previous dicoordinate copper species, and strikingly, the Φ_{PL} in the extremely challenging fluid phase (dissolved in 2-MeTHF) was at unity.

During our investigation, similar findings were reported by Di and co-workers. Notably, they described the photoluminescent activity of redox active two coordinate (^{Ad}CAAC)M(carbazole) (M = Cu, Au) with a maximum external efficiency (EQE$_{max}$) of 26.3% for the gold and 9.7% for the copper.[49] In their report, they proposed that this system involves a rotationally assisted spin-state inversion (RASI) mechanism leading to the triplet state going below that of the singlet state; however, a subsequent computational study found no such point of intersection between the two states based on ligand rotation.[50] Moreover, another computational investigation found that these systems were strong TADFs from the structural reorganization that involves bending and not rotation.[51]

3.2.1   Investigation into the Steric Profile of the Ligands.

To investigate the true mechanism of these species and because our system exploited idealized sterics and rigidity from a menthyl substituent, we continued our investigation into this ligand manifold. At this juncture, we were interested in elucidating the importance of the sterics. Therefore, we synthesized a variety of (CAAC)CuCz complexes with different steric profiles for the CAAC ligand. Through a simple salt metathesis between (CAAC)CuCl and an *in-situ* deprotonated carbazole, the desired compounds were formed (**3.1.A**-**3.4.A**) in great yields (80-90%) (Scheme 3.3). Given that the previous report used **3.2.A**,[49] which we found had a Φ_{PL} of 68% in 2-MeTHF, we compared it to our optimized sterics of **3.1.A.** Based on the quantum yield at unity for **3.1.A**, it became clear just how profound the impact of the menthyl substituent had on the photophysical properties. Unsurprisingly, the Φ_{PL} drops off precipitously upon decreasing the steric bulk until finally reaching $^{Me}CAAC$ in **3.4.A** with a meager 11% quantum yield in solution. Despite the low Φ_{PL}, the fast τ observed for **3.1.A** remains exceptional throughout the series and decreases very slightly with a smaller steric profile in solution. Moreover, the rate of radiative decay remained nearly constant across the entire series (k_r = 2.0–4.3 x 10^5 s^{-1}). In contrast, the $^{Menth}CAAC$ effectively shut down k_{nr} (< 8.0 x 10^3 s^{-1}) as opposed to the other CAAC based ligands (k_{nr} between 10^5-10^6 s^{-1}) in solution. All these complexes featured broad and featureless emission profiles indicative of the ICT origins of these transitions. Additionally, they led to very fast k_r compared to previous dicoordinate copper complexes in solution highlighting the prowess of the combination of the redox active Cz and CAAC moieties.
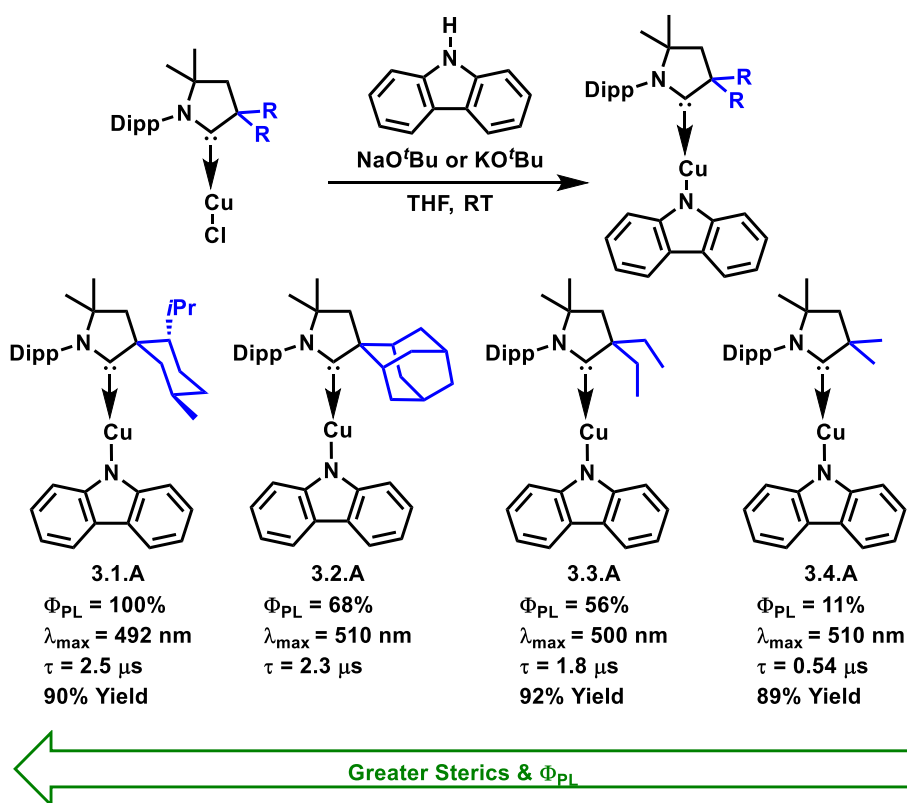
Scheme 3.3: While there is little variation in the λ_{max} for different steric profiles, Φ_{PL} in solution (dissolved in 2-MeTHF at a concentration of 10^{-5} M) attenuates quickly upon reduced steric bulk at the quaternary carbon of the CAAC.

We then investigated the conformations responsible for the TADF behavior. Initially, we synthesized, through the deprotonation method, (^{Menthyl}CAAC)Cu-^{Me}Cz (**3.1.B**) featuring the bulkier ^{Me}Cz with methyl groups ortho to the nitrogen, but the immense steric bulk of the system led to the pyramidalization of the nitrogen as observed by an X-ray diffraction study (Scheme 3.4, left). The complex was also extremely air sensitive complicating photophysical analysis, but the subtle change in bulk leading to drastically different conformations of the carbazole between **3.1.A** and **3.1.B** highlighted that our system in **3.1.A** is optimized at nearly the maximum amount of steric protection for a coplanar arrangement. Therefore, we switched to investigating (^{Ad}CAAC)Cu-^{Me}Cz (**3.2.B**) (Scheme 3.4, right). X-ray diffraction revealed that the carbazole was nearly orthogonal to the **3.2.A** (dihedral angle of 83.2° versus 7.8° respectively). While **3.2.B** had a significantly reduced absorption extinction coefficient by a factor of over

94

3 with respect to **3.2.A**, the Φ_{PL} and k_r dropped significantly (12% and 1.1 x 10^5 s^{-1}, respectively) in relation

to the nearly coplanar **3.2.A**. Unlike the mechanism described by Di *et al.* of rotationally assisted spin state

inversion,[49] the decrease in k_r and the photophysical properties for the nearly orthogonal **3.2.B** highlights

the requirement for a coplanar ligand conformation in maintaining the strongly-allowed ICT transitions in

absorption and emission as noted by Marian *et al.* and Penfold *et al.*[50,52] Furthermore, the RASI mechanism

by Di *et al.* is not supported by fundamental quantum mechanical considerations because exchange energy

stabilizes the T_1 state with respect to the S_1 state.[53]

3.1.B
97% Yield

3.2.B
Φ_{PL} = 12%
k_r = 1.1 x 10^5 s^{-1}
93% Yield
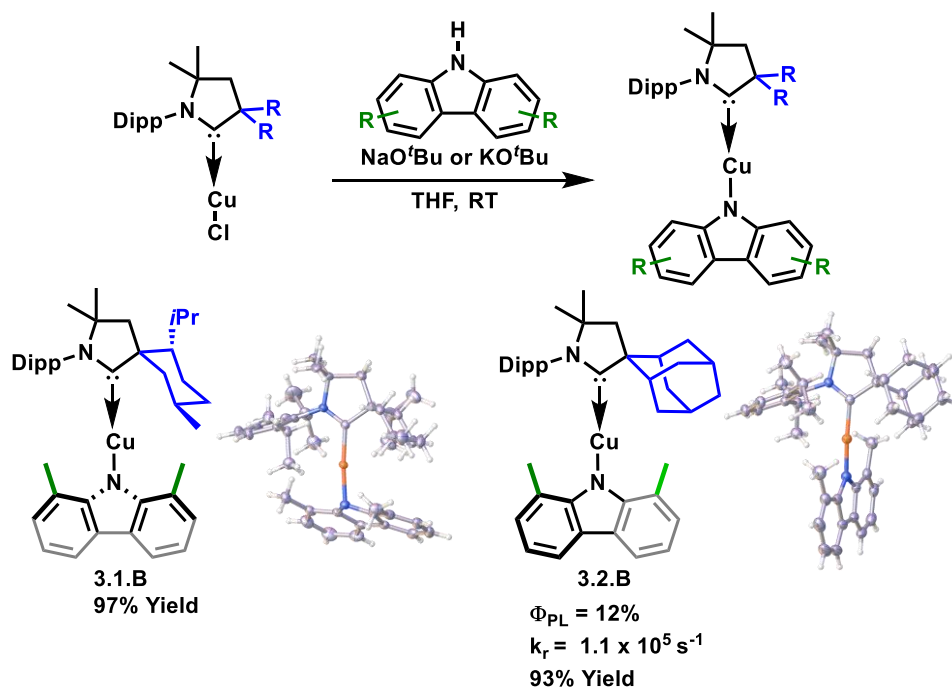
Scheme 3.4: ^{Menthyl}CAAC sterics are too large to be used in tandem with a bulkier ^{Me}Cz carbazole leading to a pyramidalized nitrogen (**3.1.B**), but the ^{Ad}CAAC leads to a nearly orthogonal confirmation (**3.2.B**) with poor photophysical properties in 2-MeTHF which highlights the significance of coplanarity.

3.2.2   Color Tuning the Emission.

After determining the importance of coplanarity, we focused on tuning the color using the previous

synthetic approach to incorporate a variety of the readily modifiable amide type ligands. A range of

^{Menth}CAAC copper complexes were synthesized featuring 3,6-dicyanocarbazolide (**3.1.C**), 3,6-

dimethoxycarbazolide (**3.1.D**), and diphenylamide, NPh$_2$, (**3.1.E**) (Figure 3.8). Interestingly, as opposed to

3.1.A which led to a Φ_{PL} at unity in solution, the new complexes **3.1.C**, **3.1.D**, and **3.1.E** had poor Φ_{PL} in the range of 11 to 25% in 2-MeTHF. This coupled with the presence of additional peaks indicated that these new complexes are prone to aggregation and excimer formation in solution. Therefore, we turned towards doping them into thin films (1 wt% in polystyrene, PS) which would essentially remove the possibility for excimer formation and aggregation. This effect was corroborated by the suppressed rates of k_{nr} which went from 10^6 to $<10^4\,s^{-1}$ in the thin films and by the observation that additional excimer peaks were not present in the emission spectra for the polymeric matrices (Figure 3.8). After being doped into PS, the complexes **3.1.A-3.1.D** retained their broad featureless emission spectra, but had good to excellent Φ_{PL} in the range of 78-100% and displayed a λ_{max}: 426 nm for **3.1.C**, 474 nm for **3.1.A**, 518 nm for **3.1.D**, and 532 nm for **3.1.E** (Figure 3.8). Thin films of **3.1.A**, **3.1.D** and **3.1.E** had a $k_r \sim 10^5\,s^{-1}$ and a τ of 2.3 to 2.8 μs which makes them competitive with state-of-the-art heavy metal phosphors such as iridium and platinum. However, the thin film of complex **3.1.C** led to narrow, structured emission at room temperature with bi-exponential decay lifetimes of 240 μs and 1.3 ms and a slow radiative rate of $1.5 \times 10^3\,s^{-1}$. Given the more difficult ICT if **3.1.C** because of a lower lying HOMO from the electron withdrawing cyano groups on the carbazole, this emission tracks with a ^{3}Cz based emission, where the lowest triplet is localized on the carbazolide. This observation was further corroborated by Time Dependent Density Functional Theory (TDDFT, B3LYP/LACVP**) which was used to model the main electronic transitions of the excited states in these complexes. We found that the ^{3}Cz state is only 0.03 to 0.1 eV higher in energy than the triplet interligand charge transfer (^{3}ICT) state in all the carbazolide-based complexes except for **3.1.C**, where ^{3}Cz is the lowest triplet state. As for the diphenylamide, **3.1.E**, the ^{3}ICT state was 0.5 eV more stable than the triplet state localized on the amide moiety, ^{3}NPh$_2$.
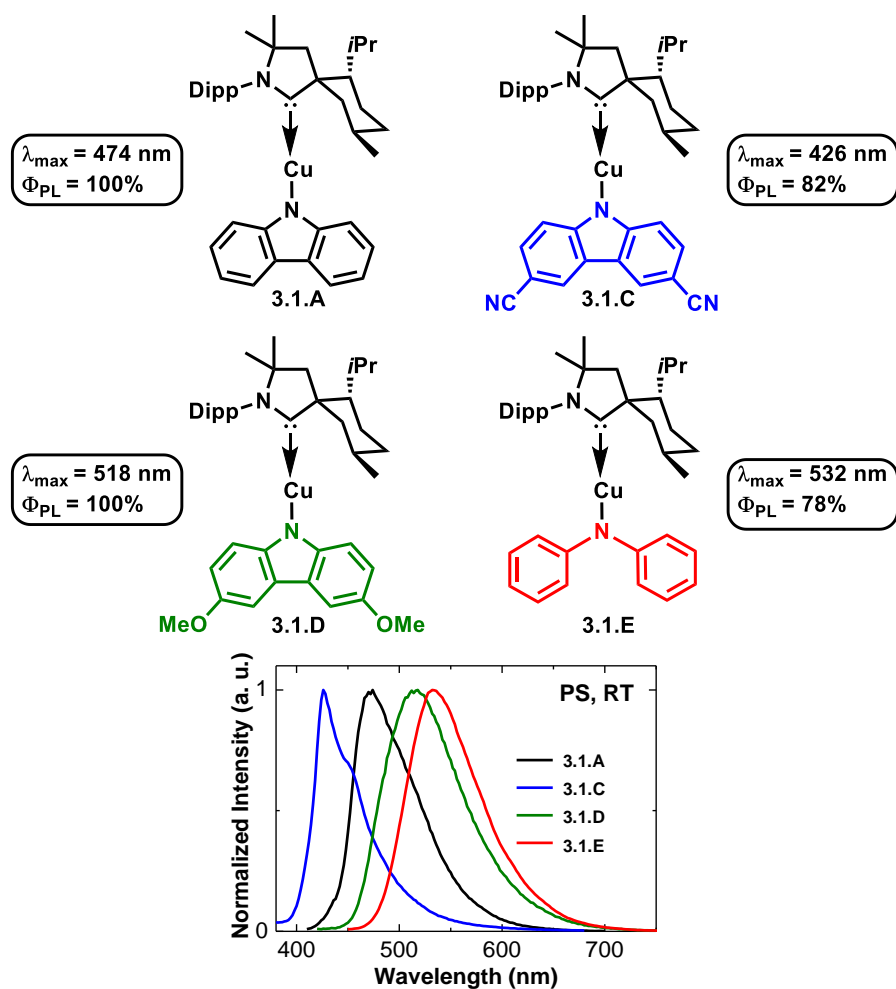
Figure 3.8: (Top) Color tunability by changing the π-donor ability of the carbazole gives rise to a broad range of λ_{max} and high quantum yields when doped into thin films (1 wt% in polystyrene, PS) (**3.1.A**, **3.1.C**, **3.1.D**, and **3.1.E**); (bottom) emission spectra highlighting the range of emissions in PS thin films.

3.2.3 Understanding the Nature of our TADF Mechanism

Absorption spectra of complexes **3.1.A**, **3.1.C**, **3.1.D**, and **3.1.E** show high-energy bands ($\lambda <$ 350 nm) corresponding to π-π* transitions of the ligands. Therefore, these bands are assigned to singlet interligand charge transfer (^{1}ICT) from the filled p orbital of the amide to the empty p orbital of the CAAC. This is demonstrated by cyclic voltammetry (CV) experiments: first, the CAAC copper complexes undergo irreversible oxidation (HOMO) that depends on the donor strength of the amide ligand, and second, reduction potentials (LUMO) are quasi-reversible and do not deviate from (^{Menth}CAAC)CuCl. The CV data

97

therefore shows that the redox potentials are independently controlled by the ligands with oxidation at the amide, and reduction at the π-acidic CAAC. Strikingly, despite the distance between the two ligands of ~3.7 Å as exemplified by their crystal structures, the complexes feature high extinction coefficients ($>10^3$ $M^{-1}cm^{-1}$) in the absorption spectra. Therefore, these strongly allowed CT transitions from the donor to the acceptor are occurring because of the coplanar arrangement of the ligands which enables long-range orbital overlap and is enhanced by the participation of the copper d-orbitals which are acting as an effective electronic bridge (Figure 3.9).

The importance of the d-orbitals in acting as a conduit between the frustrated π-pair, is also captured by Density Functional Theory (DFT at the B3LYP/LACVP** level). As expected, the HOMO is amide-based in the filled p-orbital of the nitrogen on the Cz and the lowest unoccupied molecular orbital (LUMO) is localized predominantly on the empty p-orbital of the $C_{carbene}$. The donor-bridge-acceptor linear system features weak participation of the metal d-orbitals that align with the carbazole in the HOMO and the CAAC LUMO, thereby enhancing the ability for long-range π-interactions.[54,55]
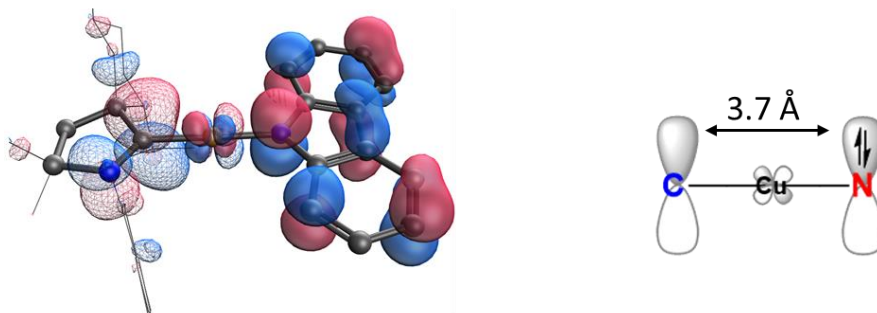
Figure 3.9: (Left) HOMO (solid) and LUMO (mesh) surfaces of complex **3.1.A**; (right) simplified picture of the HOMO and LUMO for this complex along with highlighting the long-range interaction occurring over 3.7 Å with participation from a copper d orbital.

This ICT behavior is reflected in the negative solvatochromism displayed where upon increasing solvent polarity, there is a hypsochromic shift in the absorption spectra. For example, **3.1.A** undergoes a blue shift in the ICT band of 2400 cm^{-1} upon increasing solvent polarity which reflects a strong change in the electronic dipole moment upon excitation. Due to the long-range interactions between the polarized

empty LUMO from the CAAC p orbital and the filled HOMO on the carbazole's nitrogen p orbital, the ground state dipole is significant which is partially quenched by sharing one of the carbazole's electrons with the CAAC after excitation. Therefore, the direction of the shift is a consequence of the ground-state dipole being much larger in magnitude and opposite in orientation relative to its excited-state counterpart.[56]

To understand the TADF behavior of the system, the photoluminescent properties were investigated upon cooling to 77 K. A vibronic, longer lived emission was observed in frozen glasses of 2-MeTHF and MeCy (τ = ms to seconds with $k_r < 10^3$ s^{-1}). This emission can be assigned to low-lying ^{3}Cz. The reason is because the TADF excited state manifold is destabilized by the frozen solvent molecules that cannot reorient from the large dipole in the ground state to the excited state (Figure 3.10, middle to left). This destabilization of ICT tracks with the hypsochromic shifts in both the emission and absorption spectra at 77 K. Furthermore, the new emission based on ^{3}Cz was experimentally demonstrated by comparing the emission of **3.1.A** to the phosphorescence of potassium carbazolide (KCz) which shares the same profile.

Solvent effects were modeled on the excited states of complex **3.1.A** at 77 K and 300 K using a multi-scale hybrid approach that employed Molecular Dynamics (MD) simulations in conjunction with TDDFT. At room temperature, the ^{3}ICT state is the lowest triplet state in all cases due to stabilization by the solvent dipoles. A similar procedure was followed to study the effect of solvation at 77 K, where single point TDDFT calculations were performed on a frozen equilibrated cell using the hybrid scheme. At lower temperatures, the ^{3}Cz state became the lowest lying triplet, in accordance with the experimental observation of ^{3}Cz emission in 2-Me-THF at 77 K. The destabilization of the ^{3}ICT state can be attributed to its associated dipole (4.25 D), which is opposite in direction to the large dipole in the ground (11.8 D) and ^{3}Cz states (11.27 D). Hence, solvent molecules in a frozen matrix are ordered to stabilize the large dipole in the ground state but destabilize the ^{3}CT state. This also explains the negative solvatochromic effects observed in absorption which stabilize the ground state in a more polar medium.

Therefore, to remove complications from the solvent leading to ^{3}Cz based emission and to further understand the properties of the TADF manifold experimentally, as in ^{3}ICT-based phosphorescence when ^{1}CT is no longer thermally accessible, temperature-dependent emission was investigated with PS thin films

to reveal a highly efficient TADF system (Figure 3.10, right). For example, a temperature-dependent photoluminescent decay curve fitted to a Boltzmann distribution[36] gave $\Delta E(^1CT - {}^3CT) = 0.063$ eV (510 cm^{-1}) for **3.1.A.** When coupled to the τ of ^1CT (150±15 ns) and ^3ICT (64±6 μs) for **3.1.A**, it showcased a TADF system that is on par with the fastest copper(I) TADF emitters, by Yersin *et al.* and Bräse *et al.*, reported at this time.[30,57]
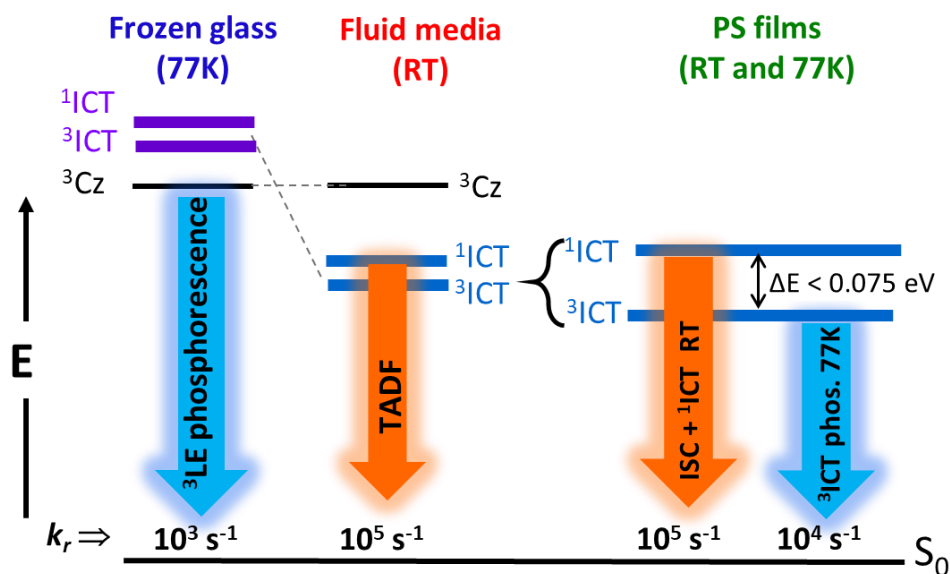
Figure 3.10: Jablonski diagram depicting the different processes operating in various media at room temperature and 77 K.

3.2.4 Exploration of (CAAC)Cu-Amides as Emitters in Blue OLEDs.

With a clear understanding of the photophysics that led to our efficient luminescent complexes, we targeted incorporating **3.1.A** as an emitter through vapor deposition as a proof of principle. To optimize the OLED device, we screened different wide bandgap host materials in the emissive layer (**3.1**, 1,3-bis(triphenylsilyl)benzene, UGH3; 3,3′-bis(carbazol-9-yl)biphenyl, mCBP; and dicarbazolyl-3,5-benzene, mCP). Interestingly, **3.1** as a host displays high EQE_{max} (external quantum efficiency) of ~10% at low charge densities, but experiences rapid roll-off in device efficiency with higher current densities presumably due to the susceptibility of the C-F bond to degradation in OLED devices.[58,59] UGH3 on the other hand is more resistant to degradation at higher current densities and can achieve a EQE_{max} of 9.0% and 16 cd/A at

2 mA/cm^2 whereas the low EQE$_{max}$ of the mCBP and mCP devices can be explained by their low triplet energy as hosts for blue OLEDs. Notably, while the EQE values for green and yellow/orange emitting copper-based OLEDs have been reported to be > 20%,[60,61] the highest efficiencies previously reported for the more challenging blue emitting (λ_{max} < 500 nm) copper based OLEDs are < 6%.[62,63] Therefore, our copper blue OLED device was the most efficient which is made more prominent by the fact that an iridium-based emitter using UGH3 also experiences the same roll off.[64] All devices with varying hosts exhibited blue electroluminescence like what was observed for **3.1.A** in a PS film with minor shifts due differences in the host matrices (Figure 3.11, top, right). Interestingly, the polyvinylcarbazole host used with the similar **3.1.B** by Di *et al.* led to green emission in their OLED as opposed to our light blue emission.[49] Given the limitations in the options for stable, high triplet energy host materials for blue OLEDs, the design of new host materials should significantly impact both the efficiency and device stability for the high energy emitting **3.1.A**.
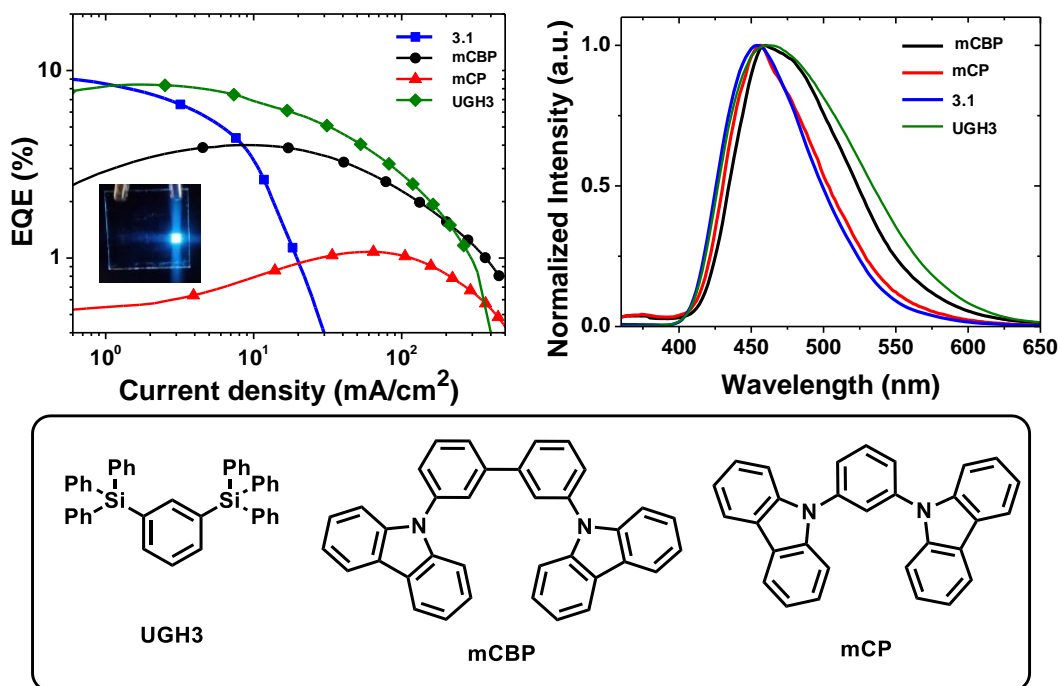
Figure 3.11: (Top, left) External Quantum Efficiency (EQE) traces of devices employing different hosts with **3.1.A** doped into the emissive layer at 20% volume; the inset is a photograph of a working blue emitting device of **3.1.A**; (top, right) electroluminescence (EL) spectra of devices employing different hosts; (bottom) different commonly used host materials screened for our OLED devices.

3.3　Conclusion

2-coordinate copper species without a doubt show marked increase in photoluminescent properties over the higher coordination numbers leading to a paradigm shift in copper-based luminescence. This behavior is especially pronounced when using a strong π-donor, carbazole, and strong π-acid, CAAC, which leads to a frustrated π-pair type system with a high dipole moment in the ground state. Furthermore, this combination causes ligand-to-ligand charge transfer (LLCT) by shifting the HOMO to the carbazole ligand. By exploiting LLCT, the copper d-orbitals enable more rapid spin flipping from the ξ of copper which enhances ISC events, but the contribution is small enough to avoid the high reorganization in typical MLCT type luminescent copper complexes. The metal in these systems acts as a conduit between the extremely redox active ligands which was further described for the coinage metal series in a follow-up report.[65] Due to the SOC from the metal, TADFs in these types of organometallic complexes are not aptly described in terms of spin-pure emissions[66] but rather thermally enhanced luminescence (TEL) from the significant mixing between ^{3}ICT and ^{1}ICT. This is apparent from the slower than expected rate of fluorescence (lifetimes as typically on the order of 0.2 μs) which signifies a sizable contribution from the triplet state.[66,67]

The initially observed triboluminescence in **3.1** led to our investigation of dicoordinate copper species and the rigidity coupled with the ideal sterics of $^{\text{Menth}}$CAAC proved invaluable in shutting down nonradiative decay. Moreover, the idea of using the high energy emitting **3.1** laid the foundation for how to achieve an all copper emissive layer and especially emphasized the necessity of avoiding fluorine for a more durable host. From this investigation, the key to using an ideal copper host for this series of 2-coordinate (CAAC)Cu-amide complexes would be to choose a related highly efficient dicoordinate analogue which would feature a less π-acidic carbene for a higher LUMO, and a more donating amide type ligand for a lower HOMO. This would effectively sandwich the electronics of the dopant.

In summary, we have prepared a series of 2-coordinate CAAC-Cu-amide complexes with emission tunable across the visible spectrum, high Φ_{PL} (up to unity) in non-rigid media, and $k_r > 10^5$ s^{-1}. Emission stems from a strongly allowed amide to carbene ICT transition, with the coplanar ligand conformation and

coupling through the metal d-orbitals ensuring strong ε_{ICT} and resultant k_r. In contrast, a near-orthogonal arrangement of ligands leads to both low ε_{ICT} and a decrease in k_r due to poor orbital overlap which overrides the RASI mechanism. In the copper-carbazolide complexes, there exists a closely-lying ^{3}Cz-centered state that dominates emission in frozen solvent glasses, due to the destabilization of the ICT manifold in such media. Therefore, we have designed copper(I) complexes with photophysical properties akin to their heavy metal counterparts *e.g.*, iridium and platinum. These results open the door to investigation of these complexes in fields where traditional heavy metal-based phosphors have been used, *e. g.*, optical sensing, photoredox catalysis and solar fuel generation, to name a few.

3.4 Appendix

3.4.1 General Methods & Materials.

All reactions were performed under nitrogen atmosphere in oven dried glassware. Carbazole (Cz), diphenylamine (NPh2), and polystyrene beads (PS, average Mw~192,000) were purchased from Sigma-Aldrich. 3,5-dimethoxy-9-H-carbazole (CzOMe) was purchased from Ark Pharm. 3,5-dicyano-9-H-carbazole (CzCN)[68] and 1,8-dimethyl-9-H-carbazole (MeCz)[69] were prepared following literature procedures. CAAC-CuCl precursors and complex **3.1.B**[49] were synthesized following published reports.[42,70–72] Dry, air-free methylcyclohexane (MeCy) and 2-methyltetrahydrofuran (2-MeTHF) were purchased from Sigma-Aldrich. MeCy was used without further purification. Dichloromethane (CH_2Cl_2), and toluene (tol.) were purified by Glass Contour solvent system by SG Water USA, LLC. Tetrahydrofuran (THF) and 2-MeTHF were distilled over Na/benzophenone under an argon atmosphere for use with complexes **3.2.B** and **3.1.E** that are ultrasensitive to trace moisture. Drisolv acetonitrile (AcN) and dimethylformamide (DMF) were purchased from EMD Millipore. ^{1}H and ^{13}C NMR spectra were recorded on a Varian Mercury 400, a Bruker Advance 300 (**3.2.B**), and a Varian Inova 500 (**3.1**). ^{19}F NMR spectrum for **3.1** was recorded on a Bruker Avance 300 MHz. The chemical shifts are given in units of ppm and referenced to the residual proton resonances of acetone ((CD3)2CO) at 2.05 ppm, chloroform (CDCl3) at

7.26 ppm., or dichloromethane CD2Cl2 at 5.32 ppm. Elemental analyses were performed at the University of Southern California, CA.

3.4.2   Experimental Procedures & Characterization Data.

(^{Menth}CAAC)Cu-C$_6$F$_5$ (3.1).
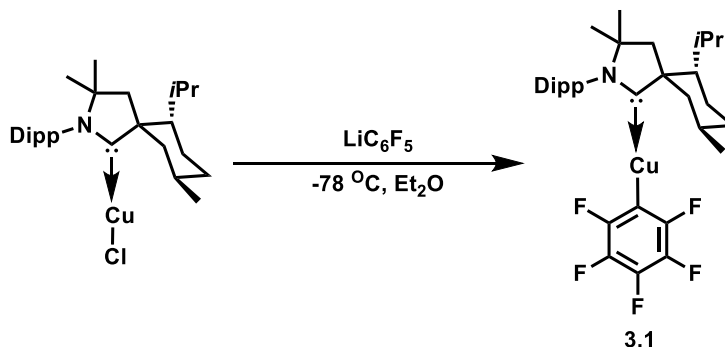
Scheme 3.5: *In-situ* deprotonation and metalation of pentafluorobenzene to engender (CAAC)Cu-C$_6$F$_5$ (**3.1**).

LiC$_6$F$_5$ was prepared by the addition of nBuLi (1.05 mmol, 2.5 M in hexanes) to bromopentafluorobenzene (131 μL, 1.05 mmol) in ether (30 mL) at -78 °C for 45 minutes (Caution: LiC$_6$F$_5$ is known to explode at temperatures above -40 °C). To the crude solution of LiC$_6$F$_5$, an ether solution of (^{Menth}CAAC)CuCl (500 mg, 1.04 mmol, 0.017 M) was slowly added at -78 °C over 30 minutes. The reaction mixture was then stirred for one hour and slowly warmed to room temperature for another 12 hours. Subsequently, the mixture was filtered through celite, and the volatiles were removed under vacuum to afford a pale yellow solid. Afterwards, the solid was washed with pentane (3x2 mL) to obtain a white powder (497 mg, 78% yield). Crystals suitable for an X-ray diffraction study were grown from a saturated solution of benzene layered with pentane. **Characterization data**: ^{1}**H NMR** (C$_6$D$_6$, 500 MHz): δ = 7.18 (t, J = 7.80 Hz, 1H), 7.06 (d, J = 7.80 Hz, 1H), 7.04 (d, J = 7.80 Hz, 1H), 3.01-2.93 (m, 2H), 2.83 (sept, J = 6.10 Hz, 2H), 2.18 (br d, J = 12.42 Hz, 1H), 1.92 (d, J = 12.42 Hz), 1.84-1.76 (m, 3H), 1.38 (d, J = 6.59 Hz, 3H), 1.29 (d, 13.16 Hz, 1H), 1.20 (d, J = 12.42 Hz, 1H), 1.14-1.08 (m, 7H), 1.05-0.99 (m, 1H), 0.98 (d,

J = 4.1 Hz, 6H), 0.94 (d, J = 6.23 Hz, 3H) 0.90 (d, J = 6.43 Hz, 3H) ppm; ^{13}C{^{1}H} **NMR** (C_6D_6, 125 MHz): 254.6, 150.2 (d, JF = 222.5 Hz), 150.0 (d, JF = 222.5 Hz), 145.8, 145.3, 139.1 (d, JF = 243.3 Hz), 136.6 (d, JF = 252.3 Hz), 135.8, 130.0, 125.8 (t, 2JF = 74.2 Hz), 125.2, 125.0, 77.7, 65.9, 53.1, 51.6, 48.0, 36.1, 31.4, 29.6, 29.5, 29.2, 29.0, 28.0, 27.5, 26.6, 25.2, 24.2, 23.1, 22.8, 22.6, 20.0 ppm; ^{19}**F NMR** (C_6D_6, 282 MHz): δ = -111.9 – -112.2 (m), -160.4 (t, J = 19.8 Hz), -162.9 – -163.2 (m) ppm; **HRMS ESI** (m/z): Despite several attempts, we were not able to obtain HRMS data.

General procedure for (CAAC)Cu-Carbazolide complexes.
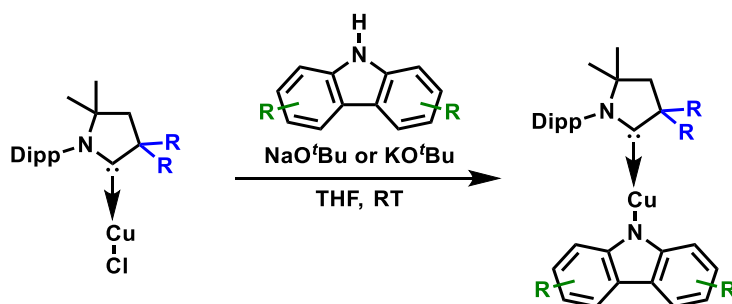
Scheme 3.6: *In-situ* deprotonation and metalation of carbazole to engender (CAAC)Cu-Cz.

(CAAC)CuCl, a carbazole ligand, and sodium or potassium *tert*-butoxide (NaO^{t}Bu or KO^{t}Bu) were dissolved in THF and stirred overnight at room temperature. The resulting mixture was filtered through Celite and the solvent was removed under reduced pressure to afford a solid. The solid was washed copiously with cold pentane and filtered. The filtrate was dried under vacuum for 24 hours.

(^{Menth}CAAC)Cu-Cz (3.1.A).

The complex was prepared from (^{Menth}CAAC)CuCl (200 mg, 0.42 mmol), Cz (73 mg, 0.44 mmol) and NaO^{t}Bu (42 mg, 0.44 mmol) and isolated as a yellowish microcrystalline solid. Yield: 228 mg (90%). Crystals suitable for an X-ray diffraction study were grown from a saturated solution of CH_2Cl_2 layered with pentane. **Characterization data**: $T_{sublimation}$ = 250 °C at 2 x 10^{-6} Torr. ^{1}**H NMR** (400 MHz,
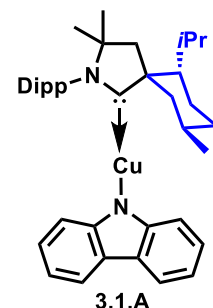
CDCl$_3$): δ = 7.96 (d, J = 7.7 Hz, 2H), 7.68 (t, J = 8.5 Hz, 1H), 7.46 (dd, J = 16.2, 7.8 Hz, 2H), 7.05 (t, J = 7.6 Hz, 2H), 6.92 (t, J = 7.7 Hz, 2H), 6.42 (d, J = 8.2 Hz, 2H), 3.19 – 2.86 (m, 5H), 2.41 (d, J = 13.5 Hz, 2H), 2.19 – 1.96 (m, 4H), 1.87 (d, J = 14.4 Hz, 1H), 1.51 (dd, J = 26.1, 2.5 Hz, 11H), 1.34 (t, J = 7.2 Hz, 7H), 1.16 (dd, J = 14.5, 6.1 Hz, 6H), 1.07 (t, J = 6.0 Hz, 6H), 0.93 (d, J = 6.4 Hz, 3H) ppm; **^{13}C{^{1}H} NMR** (101 MHz, CDCl$_3$): δ = 252.22, 150.14, 146.51, 146.03, 136.26, 129.73, 125.57, 125.49, 124.48, 123.22, 119.39, 115.26, 114.45, 77.91, 65.73, 35.99, 31.60, 30.10, 29.76, 29.59, 29.41, 28.00, 27.64, 26.44, 25.63, 24.43, 23.12, 22.95, 22.86, 19.90 ppm; **Elemental Analysis**: Anal. Cacld. for C$_{39}$H$_{51}$CuN$_2$: C, 76.62%; H, 8.41%; N, 4.58%. Found: C, 76.77%; H, 9.26%; N, 4.70%.

(^{Et}CAAC)Cu-Cz (3.3.A).

The complex was prepared from (^{Et}CAAC)CuCl (150 mg, 0.36 mmol), carbazole (64 mg, 0.38 mmol) and NaO^{t}Bu (37 mg, 0.38 mmol) and isolated as an off-white microcrystalline solid. Yield: 182 mg (92%). Crystals suitable for an X-ray diffraction study were grown by slow evaporation of a saturated solution of acetone. **Characterization data**: **^{1}H NMR** (400 MHz, CDCl$_3$): δ = 7.97 (d, J = 7.6 Hz, 2H), 7.64 (t, J = 7.8 Hz, 1H), 7.44 (d, J = 7.8 Hz, 2H), 7.09 (t, J = 8.2 Hz, 2H), 6.93 (t, J = 7.3 Hz, 2H), 6.65 (d, J = 8.1 Hz, 2H), 2.98 (hept, J = 6.8 Hz, 3H), 2.20 – 1.92 (m, 7H), 1.34 (d, J = 6.8 Hz, 7H), 1.27 – 1.18 (m, 12H) ppm; **^{13}C{^{1}H} NMR** (101 MHz, CDCl$_3$): δ = 252.56, 149.91, 145.80, 135.45, 129.65, 125.16, 124.29, 123.11, 119.37, 115.18, 114.37, 80.54, 62.59, 43.40, 31.50, 29.34, 26.78, 22.60, 9.77 ppm; **Elemental Analysis**: Anal. Cacld. for C$_{37}$H$_{43}$CuN$_2$ + 2 H$_2$O: C, 70.49%; H, 8.18%; N, 4.84%. Found: C, 70.26%; H, 7.80%; N, 4.84%.
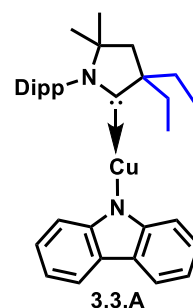
(^{Me}CAAC)Cu-Cz (3.4.A).

The complex was prepared from (^{Me}CAAC)CuCl (250 mg, 0.65 mmol), carbazole (114 mg, 0.68 mmol) and NaO^tBu (66 mg, 0.68 mmol) and isolated as a beige microcystalline solid. Crystals suitable for an X-ray diffraction study were grown by slow evaporation of a saturated solution of Et$_2$O. Yield: 317 mg (89%). **Characterization data**: **^{1}H NMR** (400 MHz, Chloroform-d): δ = 7.92 (d, J = 7.4 Hz, 2H), 7.57 (t, J = 7.8 Hz, 1H), 7.37 (d, J = 7.8 Hz, 2H), 7.04 (t, J = 8.2 Hz, 2H), 6.87 (t, J = 7.7 Hz, 2H), 6.65 (d, J = 8.1 Hz, 2H), 2.88 (hept, J = 6.8 Hz, 2H), 2.10 (s, 2H), 1.60 (s, 6H), 1.40 (s, 6H), 1.28 (d, J = 6.8 Hz, 6H), 1.18 (d, J = 6.7 Hz, 6H) ppm; **^{13}C{^{1}H} NMR** (101 MHz, CDCl$_3$): δ = 250.62, 149.89, 145.75, 134.80, 129.74, 125.13, 124.29, 123.14, 119.40, 115.22, 114.37, 110.55, 81.22, 77.20, 54.25, 49.84, 29.28, 28.89, 26.79, 22.67 ppm; **Elemental Analysis**: Anal. Cacld. for C$_{32}$H$_{39}$CuN$_2$: C, 69.72%; H, 7.08%; N, 5.08%. Found: C, 69.35%; H, 7.08%; N, 4.87%.
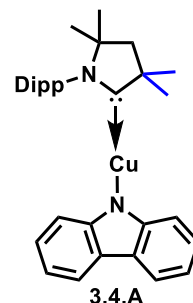
(^{Menth}CAAC)Cu-^{Me}Cz (3.1.B).

A mixture of (^{Menth}CAAC)CuCl (250 mg, 0.52mmol), potassium *tert*-butoxide (59 mg, 0.53 mmol), and ^{Me}Cz (102 mg, 0.52 mmol) were dissolved in dry THF (15 mL) under an argon atmosphere. After stirring for 3 hours, the volatiles were removed under vacuum, and the pale-yellow solid was washed with ether (3x3 mL). Extraction with toluene (20 mL) followed by washing with pentane (3x3 mL), and subsequent evaporation of the volatiles afforded the product as a tannish white powder (323 mg, 97 % yield). Crystals suitable for an X-ray diffraction study were grown from a saturated solution of THF layered with TMS$_2$O. **Characterization data**: **^{1}H NMR** (CD$_2$Cl$_2$, 500 MHz): δ = 7.76 (d, *J* = 7.47 Hz, 2H), 7.48 (t, *J* = 7.66 Hz, 1H), 7.35 (d, *J* = 7.66 Hz, 2H), 6.92-6.82 (m, 4H), 2.95-2.74 (m, 2H), 2.27 (s, 6H), 2.17 (d, *J* = 13.76 Hz, 1H), 2.15-2.03 (br m, 1H), 1.85-1.70 (m, 2H), 1.65 (d, *J* = 13.76 Hz, 1H), 1.56-1.47 (m, 1H), 1.34-1.30 (m, 15H), 1.25 (d, *J* = 6.64 Hz, 3H), 1.18-1.14 (m, 2H), 1.10 (d, *J* = 6.64 Hz, 3H), 0.85 (d, *J* = 6.84 Hz, 3H),
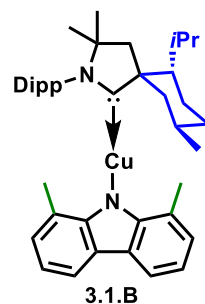
0.72 (d, J = 6.37 Hz, 3H), 0.43 (d, J = 6.84 Hz, 3H) ppm; $^{13}C\{^1H\}$ **NMR** (CD$_2$Cl$_2$, 125 MHz): δ = 251.5, 151.4, 145.9, 145.5, 136.3, 129.9, 126.3, 125.7, 125.6, 124.4, 124.0, 117.0, 116.4, 78.6, 66.1, 52.9, 52.0, 49.3, 35.6, 31.2, 30.4, 29.8, 29.6, 29.5, 27.6, 27.6, 27.5, 24.7, 24.1, 23.4, 23.3, 22.7, 19.7, 19.5 ppm; **HRMS ESI** (m/z): Despite several attempts, we were not able to obtain HRMS data.

(^{Ad}CAAC)Cu-^{Me}Cz (3.2.B).

A mixture of (^{Ad}CAAC)CuCl (250 mg, 0.52mmol), potassium *tert*-butoxide (KO^{t}Bu, 59 mg, 0.53 mmol), and ^{Me}Cz (102 mg, 0.52 mmol) was dissolved in dry THF (15 mL) under an argon atmosphere. After stirring for 3 hours, the volatiles were removed under vacuum, and the light-yellow solid was washed with ether (3x3 mL). Extraction with toluene (20 mL) followed by washing with pentane (3x3 mL), and
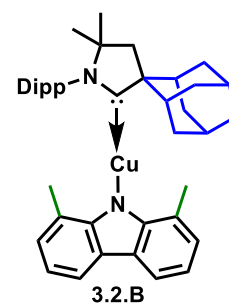
subsequent evaporation of the volatiles afforded the product as a pale-yellow powder (311 mg, 93 % yield). Crystals suitable for an X-ray diffraction study were grown from a saturated solution of THF layered with TMS$_2$O. **Characterization data**: ^{1}**H NMR** (CD$_2$Cl$_2$, 500 MHz): δ = 7.84 (d, J = 7.4 Hz, 2H), 7.42 (t, J = 7.7 Hz, 1H), 7.30 (d, J = 7.7 Hz, 2H), 7.02 (d, J = 7.4 Hz, 2H), 6.89 (t, J = 7.4 Hz, 2H), 3.50 (br d, J = 12.2 Hz, 2H), 3.06 (sept, J = 6.7 Hz, 2H) 2.56 (s, 6H), 2.34 (s, 2H), 2.10-1.78 (m, 12H), 1.46 (s, 6H), 1.34 (d, J = 6.7, 6H), 1.24 (d, J = 6.7 Hz, 6H) ppm; $^{13}C\{^1H\}$ **NMR** (CD$_2$Cl$_2$, 125 MHz): δ = 257.4, 149.7, 145.5, 136.6, 129.8, 125.8, 125.2, 124.6, 122.6, 117.2, 115.7, 79.3, 66.5, 47.5, 38.5, 37.7, 36.4, 34.6, 30.3, 29.4, 28.2, 27.5, 26.8, 24.0, 21.1 ppm; **Elemental Analysis**: Anal. Cacld. for C$_{40}$H$_{47}$CuN$_2$ + H$_2$O: C, 75.14%; H, 8.04%; N, 4.38%. Found: C, 74.99%; H, 7.92%; N, 4.04%.

(^{Menth}CAAC)Cu-CN₂Cz (3.1.C).

The complex was prepared from (^{Menth}CAAC)CuCl (130 mg, 0.27 mmol), CN₂Cz (62 mg, 0.28 mmol) and NaO^tBu (27 mg, 0.28 mmol) and isolated as a white solid. Crystals suitable for an X-ray diffraction study were grown by slow evaporation of a saturated solution of toluene. Yield: 158 mg (88%). **Characterization data**: **¹H NMR** (400 MHz, CDCl₃): δ = 8.25 (d, J = 1.2 Hz, 2H), 7.71 (t, J = 7.8 Hz, 1H), 7.47 (dd, J = 12.9, 8.5 Hz, 2H), 7.33 (dd, J = 8.5, 1.7 Hz, 2H), 6.36 (d, J = 8.5 Hz, 2H), 3.03 – 2.88 (m, 4H), 2.79 (bs, 1H), 2.43 (d, J = 13.5 Hz, 1H), 2.35 (d, J = 13.2 Hz, 1H), 2.21 – 2.12 (m, 1H), 2.09 – 1.96 (m, 3H), 1.90 (d, J = 13.6 Hz, 1H), 1.61 – 1.46 (m, 10H), 1.36 (t, J = 6.8 Hz, 8H), 1.15 – 1.04 (m, 10H), 1.02 (d, J = 6.9 Hz, 3H), 0.95 (d, J = 6.4 Hz, 3H) ppm; **¹³C{¹H} NMR** (101 MHz, CDCl₃): δ = 251.25, 152.76, 146.47, 146.02, 136.29, 129.99, 127.94, 125.77, 125.63, 125.04, 123.95, 121.69, 115.34, 99.15, 78.53, 65.74, 52.87, 51.36, 48.43, 35.86, 32.06, 30.14, 29.72, 29.58, 29.40, 27.91, 27.65, 26.47, 25.85, 24.29, 23.03, 22.89, 22.77, 19.84 ppm; **Elemental Analysis**: Anal. Cacld. for $C_{41}H_{49}CuN_4$ + H_2O: C, 72.48%; H, 7.57%; N, 8.25%. Found: C, 72.29%; H, 7.60%; N, 7.91%.
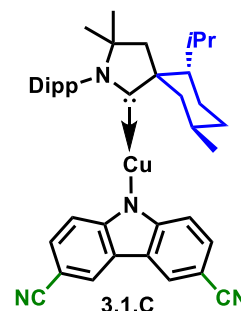
(^{Menth}CAAC)Cu-OMe₂Cz (3.1.D).

The complex was prepared from (^{Menth}CAAC)CuCl (200 mg, 0.42 mmol), OMe₂Cz (95 mg, 0.42 mmol) and NaO^tBu (44 mg, 0.46 mmol) and isolated as a microcrystalline yellow solid; bright green luminescent. Crystals suitable for an X-ray diffraction study were grown by slow evaporation of a saturated solution of Et₂O. Yield: 305 mg (109%) due to residual THF. The powder was further dried under vacuum for 4 days. **Characterization data**: **¹H NMR** (400 MHz, CDCl₃): δ = 7.65 (t, J = 7.8 Hz, 2H), 7.47 – 7.42 (m, 4H), 7.41 (d, J = 2.6 Hz, 5H), 6.72 (dd, J = 8.8, 2.6 Hz, 4H), 6.28 (d, J = 8.8 Hz, 4H), 3.88 (s, 11H), 3.13 – 2.90 (m, 5H), 2.39 (d, J = 13.5 Hz, 3H), 2.17 – 1.95 (m, 2H), 1.84 (d, J = 3.8 Hz, 2H), 1.52 (dd, J = 13.7, 4.4 Hz, 4H), 1.46 (d, J = 4.6 Hz, 14H), 1.38 – 1.28 (m, 10H), 1.15 (dd, J = 15.9, 6.7
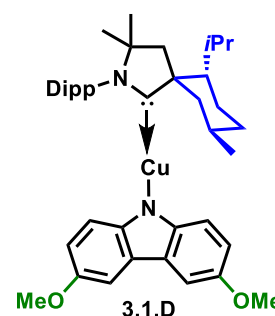
Hz, 11H), 1.07 (t, J = 7.3 Hz, 12H), 0.92 (d, J = 6.4 Hz, 6H) ppm; ^{13}C{^{1}H} NMR (101 MHz, CDCl$_3$): δ = 252.22, 151.04, 146.52, 146.02, 136.30, 129.69, 125.58, 125.48, 123.92, 115.20, 113.37, 101.70, 68.12, 65.67, 56.41, 53.00, 51.51, 48.62, 35.98, 31.59, 30.07, 29.71, 29.56, 29.39, 27.97, 27.60, 26.43, 25.76, 25.66, 24.42, 23.09, 22.93, 22.84, 19.88 ppm; **Elemental Analysis**: Anal. Cacld. for C$_{41}$H$_{55}$CuN$_2$O$_2$ + H$_2$O: C, 71.43%; H, 8.33%; N, 4.06%. Found: C, 71.69%; H, 8.69%; N, 4.12%.

(^{Menth}CAAC)Cu-NPh$_2$ (3.1.E).
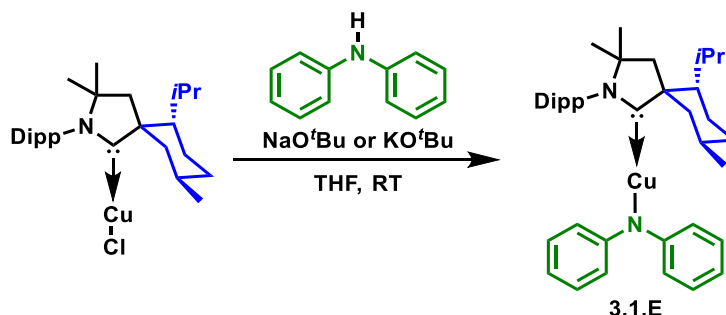
Figure 3.12: *In-situ* deprotonation and metalation of diphenyl amine to engender (^{Menth}CAAC)Cu-NPh$_2$.

The complex was made from (^{Menth}CAAC)CuCl (950 mg, 1.98 mmol), NPh$_2$ (351 mg, 2.08 mmol) and NaO^{t}Bu (200 mg, 2.08 mmol) as a bright yellow solid. Yield: 1.1 g (93%). The complex is exceedingly sensitive to moisture, especially in solution. Single crystals suited for structural determination were grown by vacuum sublimation. **Characterization data**: T$_{sub}$ = 175 °C, P = 1.8 x 10^{-6} mTorr. ^{1}H NMR (400 MHz, CDCl$_3$): δ = 7.56 (t, J = 7.8 Hz, 1H), 7.44 – 7.31 (m, 3H), 7.31 – 7.21 (m, 3H), 7.08 (dd, J = 8.6, 1.1 Hz, 1H), 6.94 (dt, J = 7.3, 1.2 Hz, 1H), 6.92 – 6.83 (m, 4H), 6.47 (t, J = 7.2 Hz, 2H), 6.33 (dd, J = 8.5, 1.1 Hz, 3H), 2.98 – 2.78 (m, 4H), 2.68 (dd, J = 13.3, 9.6 Hz, 1H), 2.53 (bs, 1H), 2.34 – 2.20 (m, 3H), 2.13 (d, J = 11.4 Hz, 1H), 1.99 – 1.63 (m, 7H), 1.51 (dd, J = 14.0, 3.5 Hz, 1H), 1.43 – 1.18 (m, 29H), 1.04 (dd, J = 11.2, 6.9 Hz, 4H), 0.94 (d, J = 6.9 Hz, 3H), 0.89 (dd, J = 6.7, 3.1 Hz, 5H), 0.76 (d, J = 6.5 Hz, 3H) ppm; ^{13}C{^{1}H} NMR (101 MHz, CDCl$_3$): δ = 252.00, 156.13, 146.23, 145.72, 145.25, 136.23, 129.84, 129.49, 128.61, 125.31, 124.90, 121.40, 117.96, 115.97, 65.39, 52.82, 51.43, 51.24, 48.97, 48.63, 36.88, 35.66, 31.23, 30.97, 30.08, 29.70, 29.48, 29.33, 29.18, 27.89, 27.31, 27.13, 26.11, 24.65, 24.43, 23.19, 23.08, 22.81,

22.73, 22.60, 20.18, 19.72, 2.95, 2.92, 2.89, 2.88, 2.82, 2.81, 2.79, 2.68 ppm; **Elemental Analysis**: Anal. Cacld. for $C_{39}H_{53}CuN_2$ + 0.75 H_2O: C, 74.72%; H, 8.76%; N, 4.47%. Found: C, 74.83%; H, 8.48%; N, 4.18%.

3.4.3   X-Ray Crystal Structure Determination.

The single-crystal X-ray diffraction data for compounds **3.1.A-3.1.E**, **3.3.A**, and **3.4.A** were collected on a Bruker SMART APEX DUO three-circle platform diffractometer with the χ axis fixed at 54.745° and using Mo Kα radiation (λ = 0.710 73 Å) monochromated by a TRIUMPH curved-crystal monochromator. The crystals were mounted in Cryo-Loops using Paratone oil. Data were corrected for absorption effects using the multiscan method (SADABS). The structures were solved by direct methods and refined on F2 using the Bruker SHELXTL software package.[73] All non-hydrogen atoms were refined anisotropically. The single crystal X-ray diffraction study for **3.2.B** was carried out on a Bruker D8 diffractometer equipped with a Dectris Eiger R 1M HPAD detector and Cu Ka radiation (l = 1.5478). For **3.1**, X-ray diffraction analysis was carried out on a Bruker Kappa APEX-II CCD diffractometer equipped with Mo Ka radiation (l = 0.71073 Å). In both complexes, crystals were selected under Fomblin oil, mounted on a Cryoloop, and then immediately placed in a cold stream of nitrogen. The data was integrated using the Bruker SAINT software program and scaled using the SADABS software program. Solution by direct methods (SHELXT) produced a complete phasing model consistent with the proposed structure. The structure was refined with SHELXL[73] using Olex2 software.[74] All nonhydrogen atoms were refined anisotropically by full-matrix least-squares (SHELXL). All hydrogen atoms were placed using a riding model. Their positions were constrained relative to their parent atom using the appropriate HFIX command in SHELXL.

X-Ray data and structure for 3.1.

Table 3.1: Crystal data and structure refinement for **3.1**.

Identification code	**3.1**
Empirical formula	$C_{33}H_{43}CuF_5N$
Formula weight	612.22
Temperature/K	296.15
Crystal system	monoclinic
Space group	$P2_1$
a/Å	9.427(3)
b/Å	17.163(6)
c/Å	10.043(3)
α/°	90
β/°	102.780(9)
γ/°	90
Volume/Å^3	1584.6(9)
Z	2
ρ_{calc}g/cm^3	1.283
μ/mm^{-1}	0.740
F(000)	644.0
Crystal size/mm^3	$0.14 \times 0.1 \times 0.02$
Radiation	MoKα (λ = 0.71073)
2Θ range for data collection/°	4.43 to 51.41
Index ranges	$-11 \leq h \leq 10, -20 \leq k \leq 20, -12 \leq l \leq 8$
Reflections collected	11727
Independent reflections	5931 [R_{int} = 0.0293, R_{sigma} = 0.0661]
Data/restraints/parameters	5931/1/370
Goodness-of-fit on F^2	1.008
Final R indexes [I>=2σ (I)]	R_1 = 0.0336, wR_2 = 0.0660
Final R indexes [all data]	R_1 = 0.0450, wR_2 = 0.0702
Largest diff. peak/hole / e Å^{-3}	0.38/-0.35
Flack parameter	0.009(7)
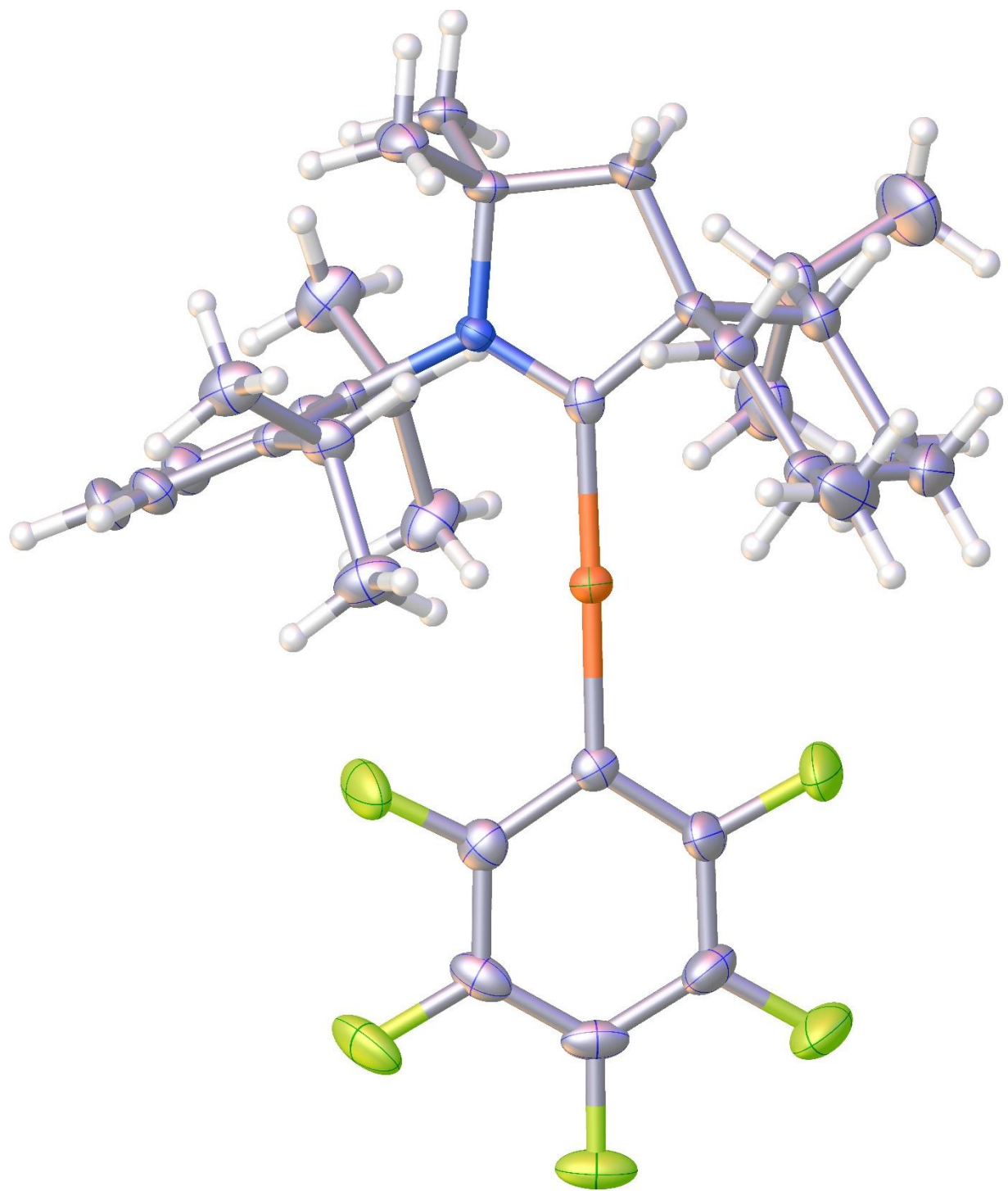
Figure 3.13: X-ray structure of **3.1** (ellipsoid shown at 30% probability).

X-Ray data and structure for 3.1.A.

Table 3.2: Crystal data and structure refinement for **3.1.A**.

Identification code	**3.1.A**
Empirical formula	$C_{39}H_{51}CuN_2$
Formula weight	611.35
Temperature/K	100.(2)
Crystal system	monoclinic
Space group	$P2_1/c$
a/Å	9.767(3)
b/Å	18.347(6)
c/Å	19.157(7)
α/°	90
β/°	92.041(5)
γ/°	90
Volume/Å^3	3431.(2)
Z	4
ρ_{calc}g/cm^3	1.184
μ/mm^{-1}	0.665
F(000)	1312.0
Crystal size/mm^3	$0.436 \times 0.341 \times 0.238$
Radiation	MoKα ($\lambda = 0.71073$)
2Θ range for data collection/°	3.08 to 61.08
Index ranges	$-13 \leq h \leq 13, -26 \leq k \leq 26, -27 \leq l \leq 27$
Reflections collected	89234
Independent reflections	10314 [$R_{int} = 0.0428$, $R_{sigma} = 0.0224$]
Data/restraints/parameters	10314/19/479
Goodness-of-fit on F^2	1.186
Final R indexes [I>=2σ (I)]	$R_1 = 0.0532$, $wR_2 = 0.1179$
Final R indexes [all data]	$R_1 = 0.0583$, $wR_2 = 0.1197$
Largest diff. peak/hole / e Å^{-3}	0.67/-0.46
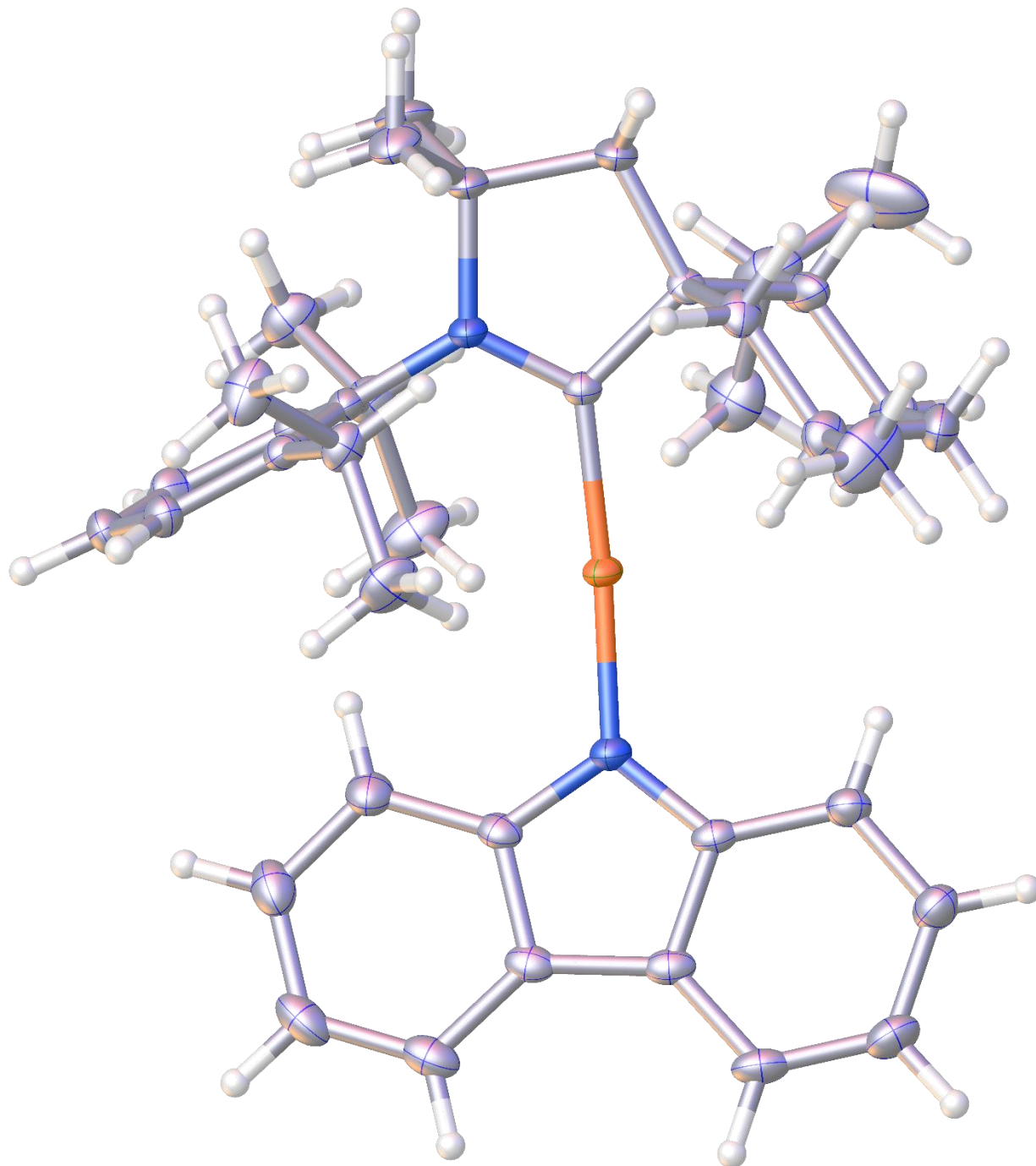
Figure 3.14: X-ray structure of **3.1.A** (ellipsoid shown at 30% probability).

X-Ray data and structure for 3.3.A.

Table 3.3: Crystal data and structure refinement for **3.3.A**.

Identification code	**3.3.A**
Empirical formula	$C_{34}H_{43}CuN_2$
Formula weight	543.24
Temperature/K	100.(2)
Crystal system	monoclinic
Space group	$P2_1/c$
a/Å	9.6428(13)
b/Å	18.251(2)
c/Å	17.048(2)
α/°	90
β/°	95.077(2)
γ/°	90
Volume/Å^3	2988.5(7)
Z	4
ρ_{calc}g/cm^3	1.207
μ/mm^{-1}	0.755
F(000)	1160.0
Crystal size/mm^3	$0.180 \times 0.110 \times 0.040$
Radiation	MoKα ($\lambda = 0.71073$)
2Θ range for data collection/°	4.24 to 56.66
Index ranges	$-12 \leq h \leq 12$, $-24 \leq k \leq 22$, $-21 \leq l \leq 22$
Reflections collected	23724
Independent reflections	7429 [$R_{int} = 0.0624$, $R_{sigma} = 0.0709$]
Data/restraints/parameters	7429/0/342
Goodness-of-fit on F^2	1.003
Final R indexes [I>=2σ (I)]	$R_1 = 0.0426$, $wR_2 = 0.0809$
Final R indexes [all data]	$R_1 = 0.0776$, $wR_2 = 0.0923$
Largest diff. peak/hole / e Å^{-3}	0.38/-0.47
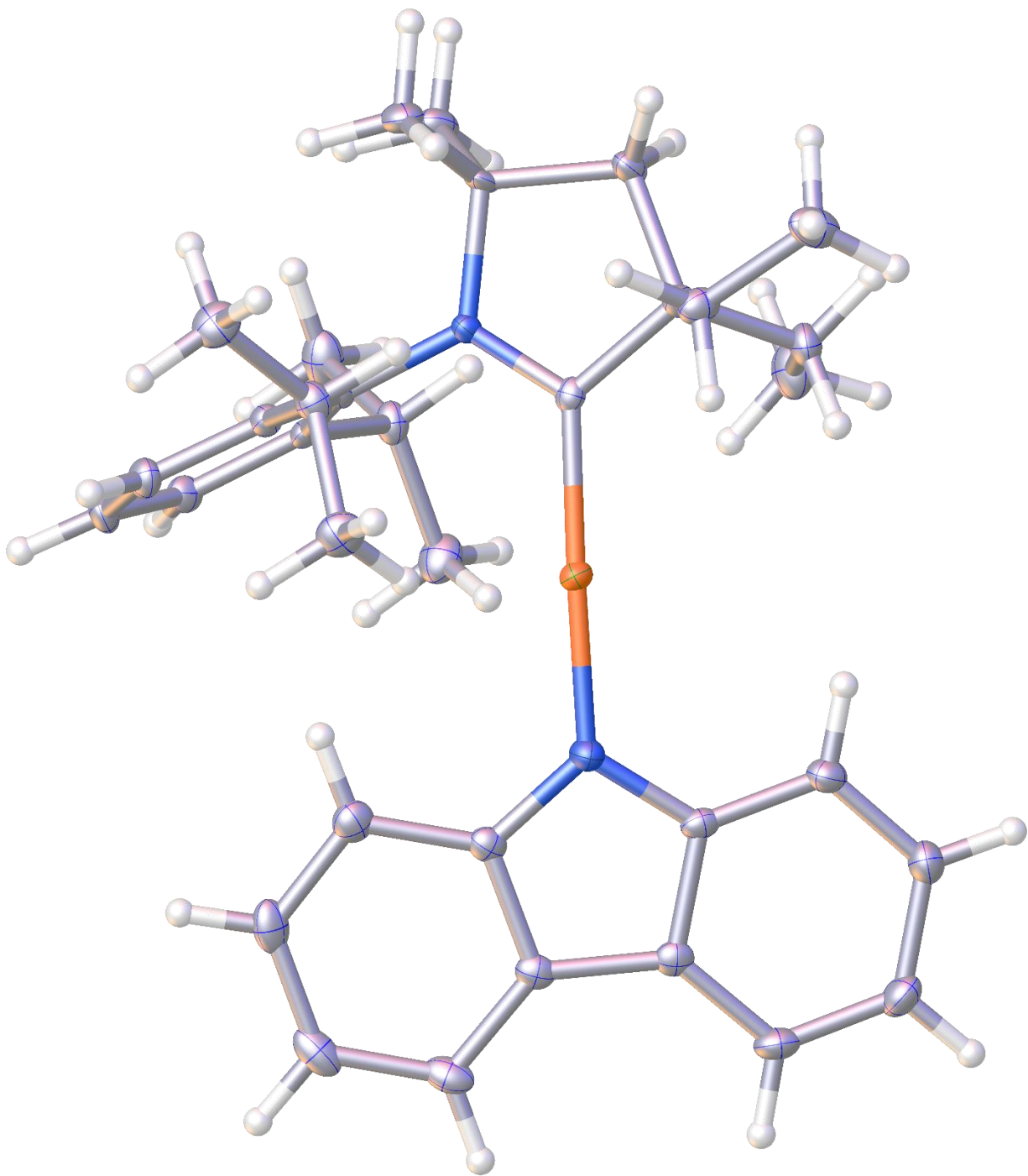
Figure 3.15: X-ray structure of **3.3.A** (ellipsoids shown at 30% probability).

X-Ray data and structure for 3.4.A.

Table 3.4: Crystal data and structure refinement for **3.4.A**.

Identification code	**3.4.A**
Empirical formula	$C_{32}CuN_2H_{39}$
Formula weight	515.19
Temperature/K	100.02
Crystal system	monoclinic
Space group	$P2_1/c$
a/Å	23.8847(18)
b/Å	12.6804(9)
c/Å	18.3937(13)
α/°	90
β/°	92.9495(12)
γ/°	90
Volume/Å^3	5563.5(7)
Z	8
ρ_{calc}g/cm^3	1.230
μ/mm^{-1}	0.807
F(000)	2192.0
Crystal size/mm^3	$0.18 \times 0.12 \times 0.08$
Radiation	MoKα ($\lambda = 0.71073$)
2Θ range for data collection/°	3.414 to 61.154
Index ranges	$-33 \leq h \leq 33$, $-17 \leq k \leq 18$, $-25 \leq l \leq 26$
Reflections collected	137227
Independent reflections	17004 [$R_{int} = 0.0446$, $R_{sigma} = 0.0241$]
Data/restraints/parameters	17004/8/691
Goodness-of-fit on F^2	1.031
Final R indexes [I>=2σ (I)]	$R_1 = 0.0283$, $wR_2 = 0.0721$
Final R indexes [all data]	$R_1 = 0.0372$, $wR_2 = 0.0766$
Largest diff. peak/hole / e Å^{-3}	0.44/-0.42
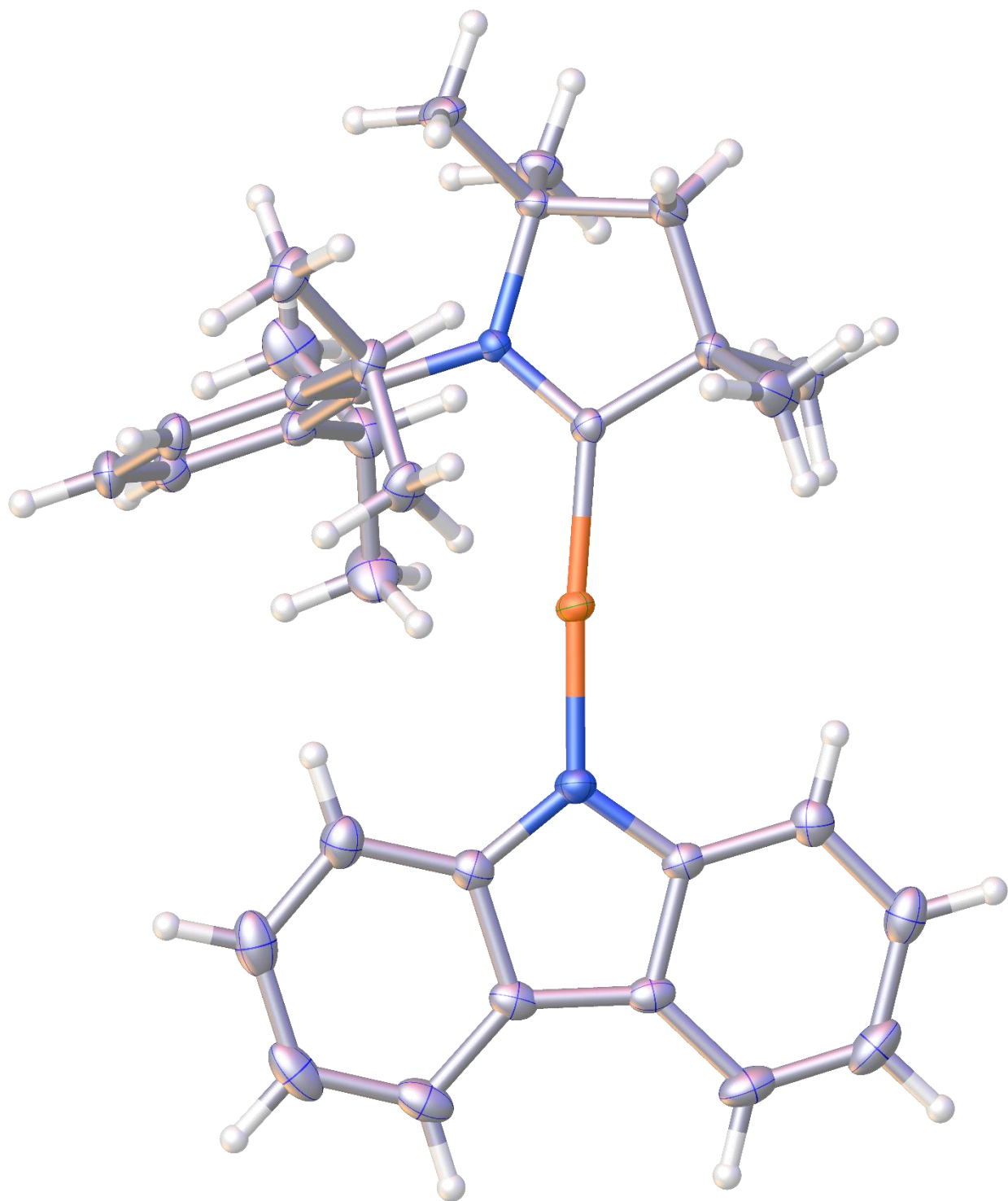
Figure 3.16: X-ray structure of **3.4.A** (ellipsoids shown at 30% probability).

X-Ray data and structure for 3.1.B.

Table 3.5: Crystal data and structure refinement for **3.1.B**.

Identification code	**3.1.B**
Empirical formula	$C_{41}H_{55}CuN_2$
Formula weight	639.41
Temperature/K	100.0
Crystal system	orthorhombic
Space group	$P2_12_12_1$
a/Å	9.8926(4)
b/Å	18.4354(7)
c/Å	19.6061(7)
α/°	90
β/°	90
γ/°	90
Volume/Å^3	3575.6(2)
Z	4
ρ_{calc}g/cm^3	1.188
μ/mm^{-1}	1.067
F(000)	1376.0
Crystal size/mm^3	$0.16 \times 0.12 \times 0.11$
Radiation	CuKα ($\lambda = 1.54178$)
2Θ range for data collection/°	6.58 to 140.266
Index ranges	$-12 \leq h \leq 12, -21 \leq k \leq 22, -22 \leq l \leq 23$
Reflections collected	27387
Independent reflections	6782 [$R_{int} = 0.0510$, $R_{sigma} = 0.0368$]
Data/restraints/parameters	6782/0/408
Goodness-of-fit on F^2	1.044
Final R indexes [I>=2σ (I)]	$R_1 = 0.0325$, $wR_2 = 0.0882$
Final R indexes [all data]	$R_1 = 0.0331$, $wR_2 = 0.0891$
Largest diff. peak/hole / e Å^{-3}	0.36/-0.28
Flack parameter	-0.018(9)
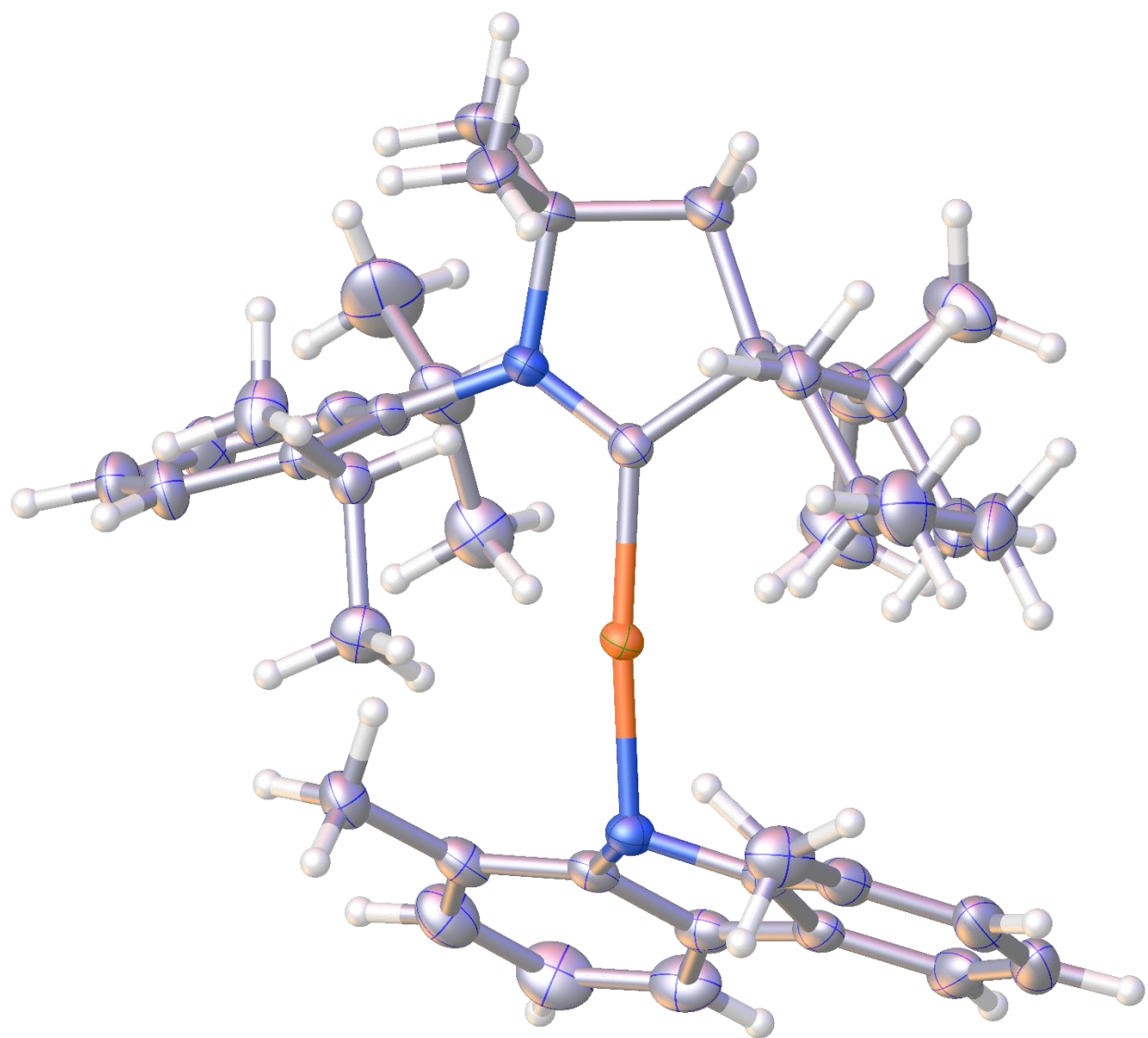
Figure 3.17: X-ray structure of **3.1.B** (ellipsoids shown at 30% probability).

X-Ray data and structure for 3.2.B.

Table 3.6: Crystal data and structure refinement for **3.2.B**.

Identification code	**3.2.B**
Empirical formula	$C_{41}H_{51}CuN_2$
Formula weight	635.37
Temperature/K	273(2)
Crystal system	monoclinic
Space group	$P2_1/c$
a/Å	10.5958(9)
b/Å	16.4793(14)
c/Å	24.023(2)
α/°	90
β/°	90.755(2)
γ/°	90
Volume/Å^3	4194.3(6)
Z	4
ρ_{calc}g/cm^3	1.006
μ/mm^{-1}	0.909
F(000)	1360.0
Crystal size/mm^3	$0.14 \times 0.12 \times 0.11$
Radiation	CuKα (λ = 1.54178)
2Θ range for data collection/°	6.504 to 144.406
Index ranges	$-13 \leq h \leq 13$, $-20 \leq k \leq 20$, $-29 \leq l \leq 29$
Reflections collected	89310
Independent reflections	8244 [R_{int} = 0.0329, R_{sigma} = 0.0147]
Data/restraints/parameters	8244/0/405
Goodness-of-fit on F^2	1.046
Final R indexes [I>=2σ (I)]	R_1 = 0.0329, wR_2 = 0.0934
Final R indexes [all data]	R_1 = 0.0354, wR_2 = 0.0949
Largest diff. peak/hole / e Å^{-3}	0.27/-0.32
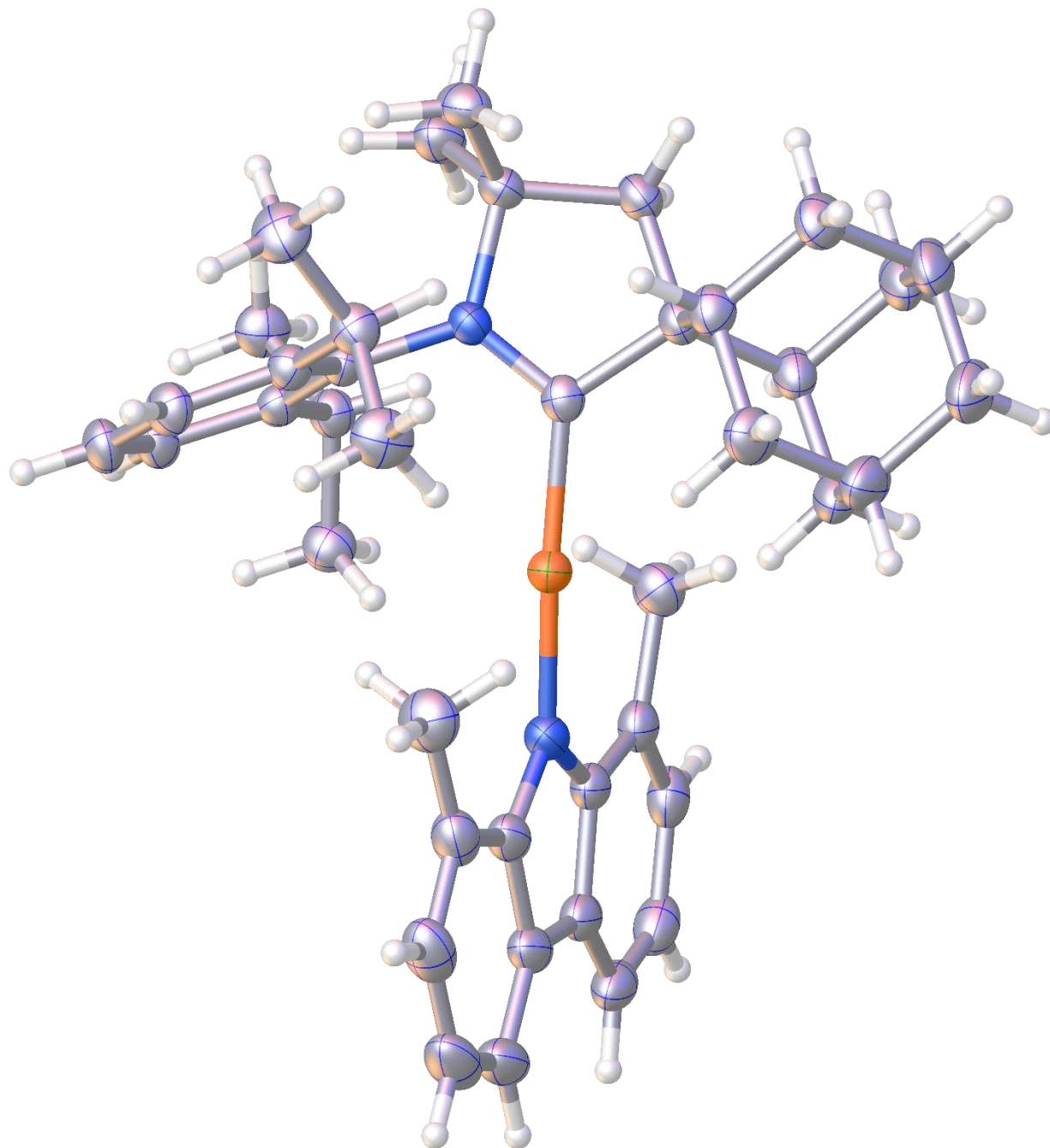
Figure 3.18: X-ray structure of **3.2.B** (ellipsoids shown at 30% probability). N.B. for a comparison with the unsubstituted carbazole see Di *et al.*[49]

X-Ray data and structure for 3.1.C.

Table 3.7: Crystal data and structure refinement for **3.1.C**.

Identification code	**3.1.C**
Empirical formula	$C_{48}H_{57}CuN_4$
Formula weight	753.51
Temperature/K	100.(2)
Crystal system	orthorhombic
Space group	$P2_12_12_1$
a/Å	14.452(4)
b/Å	19.993(6)
c/Å	28.992(8)
α/°	90
β/°	90
γ/°	90
Volume/Å^3	8377.(4)
Z	8
ρ_{calc}g/cm^3	1.195
μ/mm^{-1}	0.558
F(000)	3216.0
Crystal size/mm^3	$0.570 \times 0.373 \times 0.283$
Radiation	MoKα (λ = 0.71073)
2Θ range for data collection/°	2.48 to 61.04
Index ranges	$-20 \leq h \leq 20, -28 \leq k \leq 28, -40 \leq l \leq 41$
Reflections collected	203099
Independent reflections	25466 [R_{int} = 0.0751, R_{sigma} = 0.0425]
Data/restraints/parameters	25466/174/1095
Goodness-of-fit on F^2	1.022
Final R indexes [I>=2σ (I)]	R_1 = 0.0350, wR_2 = 0.0866
Final R indexes [all data]	R_1 = 0.0425, wR_2 = 0.0908
Largest diff. peak/hole / e Å^{-3}	0.51/-0.60
Flack parameter	0.008(7)
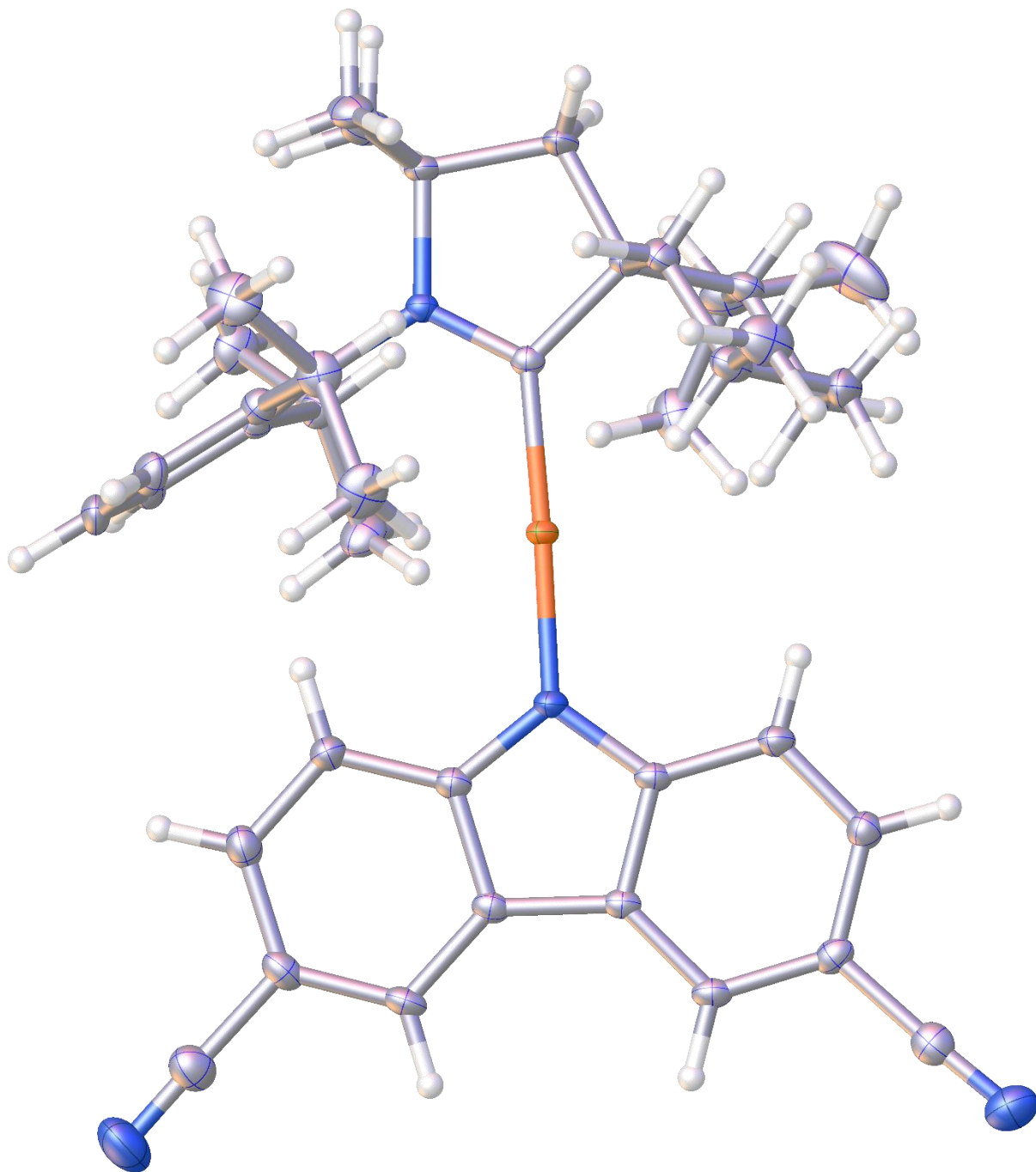
Figure 3.19: X-ray structure of **3.1.C** (ellipsoids shown at 30% probability with toluene omitted for clarity).

X-Ray data and structure for 3.1.D.

Table 3.8: Crystal data and structure refinement for **3.1.D**.

Identification code	**3.1.D**
Empirical formula	$C_{41}H_{55}CuN_2O_2$
Formula weight	671.41
Temperature/K	100.(2)
Crystal system	hexagonal
Space group	$P6_5$
a/Å	17.566(4)
b/Å	17.566(4)
c/Å	25.527(6)
α/°	90
β/°	90
γ/°	120
Volume/Å^3	6821.(4)
Z	6
ρ_{calc}g/cm^3	0.981
μ/mm^{-1}	0.509
F(000)	2160.0
Crystal size/mm^3	$0.499 \times 0.278 \times 0.244$
Radiation	MoKα (λ = 0.71073)
2Θ range for data collection/°	2.68 to 61
Index ranges	$-25 \leq h \leq 24, -24 \leq k \leq 24, -36 \leq l \leq 35$
Reflections collected	161171
Independent reflections	13692 [R_{int} = 0.0364, R_{sigma} = 0.0234]
Data/restraints/parameters	13692/1/426
Goodness-of-fit on F^2	1.026
Final R indexes [I>=2σ (I)]	R_1 = 0.0284, wR_2 = 0.0704
Final R indexes [all data]	R_1 = 0.0332, wR_2 = 0.0729
Largest diff. peak/hole / e Å^{-3}	0.24/-0.19
Flack parameter	0.001(2)
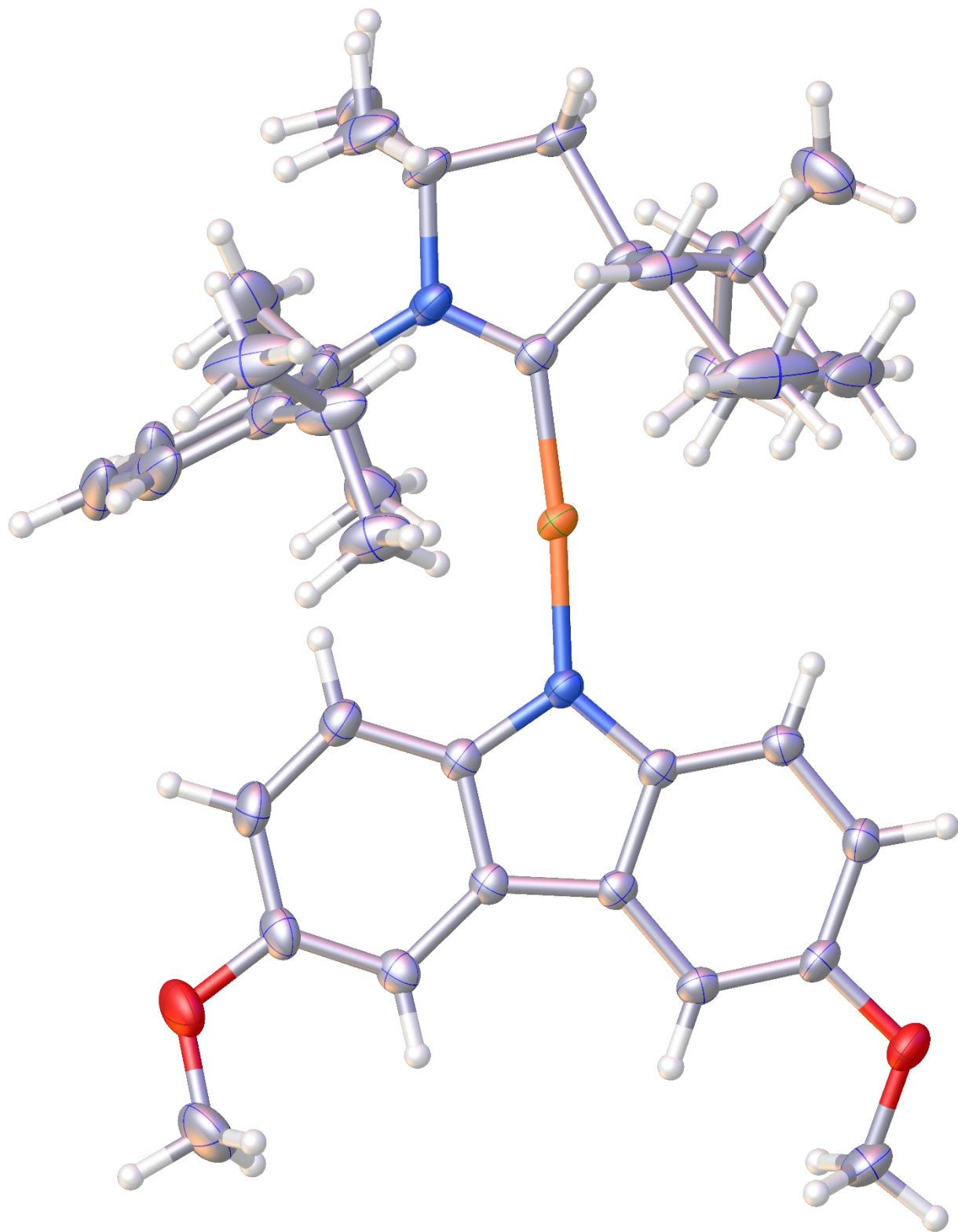
Figure 3.20: X-ray structure of **3.1.D** (ellipsoids shown at 30% probability).

X-Ray data and structure for 3.1.E.

Table 3.9: Crystal data and structure refinement for **3.1.E**.

Identification code	**3.1.E**
Empirical formula	$C_{39}H_{53}CuN_2$
Formula weight	613.37
Temperature/K	100.(2)
Crystal system	orthorhombic
Space group	$P2_12_12_1$
a/Å	9.4863(4)
b/Å	18.4245(8)
c/Å	39.6911(15)
α/°	90
β/°	90
γ/°	90
Volume/Å^3	6937.2(5)
Z	8
$\rho_{calc}g/cm^3$	1.175
μ/mm^{-1}	1.079
F(000)	2640.0
Crystal size/mm^3	$0.090 \times 0.080 \times 0.020$
Radiation	CuKα ($\lambda = 1.54178$)
2Θ range for data collection/°	5.28 to 144.04
Index ranges	$-11 \leq h \leq 11$, $-22 \leq k \leq 22$, $-40 \leq l \leq 47$
Reflections collected	33063
Independent reflections	12879 [$R_{int} = 0.0542$, $R_{sigma} = 0.0614$]
Data/restraints/parameters	12879/24/813
Goodness-of-fit on F^2	1.048
Final R indexes [I>=2σ (I)]	$R_1 = 0.0536$, $wR_2 = 0.1345$
Final R indexes [all data]	$R_1 = 0.0632$, $wR_2 = 0.1406$
Largest diff. peak/hole / e Å^{-3}	0.65/-0.56
Flack parameter	0.013(15)
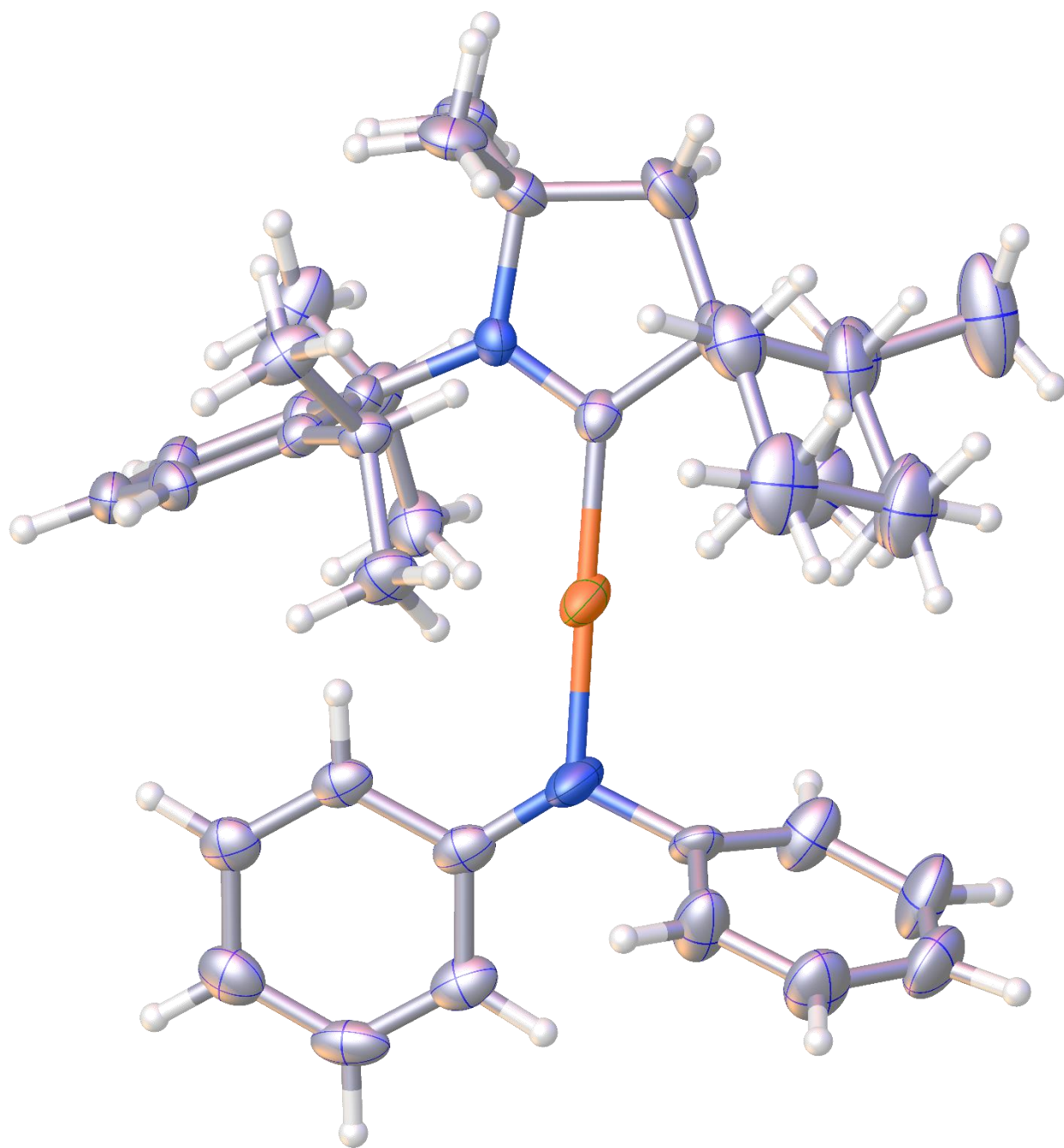
Figure 3.21: X-ray structure of **3.1.E** (ellipsoids shown at 30% probability).

3.4.4 Electrochemical Characterization.

Table 3.10: Redox potentials of complexes **3.1**, **3.1.A**, **3.1.C**-**3.1.E** as well as KCz, the parent amines, and (^{Menth}CAAC)CuCl precursor.

	E^{ox} (V)	E^{red} (V)	ΔE_{redox} (V)
3.1.A	0.24 (ir)	-2.84 (q)	3.08
3.1.C^a	0.69 (ir)	-2.79 (q)	3.48
3.1.D	-0.20 (ir)	-2.85 (q)	2.65
3.1.E	-0.29 (ir)	-2.89 (q)	2.60
KCz	0.42 (ir)	---	---
Cz^a	0.84 (ir)	---	---
4,4'-CN$_2$Cz^a	1.38	---	---
4,4'-OMe$_2$Cz	0.44	---	---
HNPh$_2$	0.45	---	---
3.1	0.90	-2.7	3.6
(^{Menth}CAAC)CuCl	> 1.5^b	-2.85	---
Potentials versus ferrocenium/ferrocene obtained in DMF with 0.1 M TBAPF$_6$. ^{a}Potentials obtained in acetonitrile. ^{b}Oxidation not observed in the DMF solvent window. *ir* = irreversibie, *q* = quasi-reversible.			

3.4.5 Photophysical Characterization.

The UV-visible spectra were recorded on a Hewlett-Packard 4853 diode array spectrometer. Steady state emission measurements were performed using a QuantaMaster Photon Technology International spectrofluoremeter. All reported spectra are corrected for photomultiplier response. Phosphorescence lifetime measurements were performed using an IBH Fluorocube instrument equipped with 331 nm LED and 405 nm laser excitation sources using time-correlated single photon counting method. Long-lived phosphorescence decays (> 30 μs) were measured using a QuantaMaster Photon Technology International spectrofluoremeter equipped with a Xe flash lamp. Quantum yields at room temperature were measured using a Hamamatsu C9920 system equipped with a xenon lamp, calibrated integrating sphere and model C10027 photonic multichannel analyzer (PMA). All samples were deoxygenated by bubbling N$_2$ in a glass cuvette fitted with a Teflon stopcock. Samples of complexes **3.2.B** and **3.1.E** were prepared under N$_2$ in an airtight Schlenk flask connected to a quartz cuvette via a glass bridge.

Table 3.11: Photophysical properties of **3.1** in MeCy and in the microcrystalline powder form at RT and 77 K.

	Emission at room temperature					Emission at 77 K	
	λ_{max} (nm)	τ (μs)	Φ_{PL}	k_r (s^{-1})	k_{nr} (s^{-1})	λ_{max} (nm)	τ (μs)
MeCy	440	3.6	0.17	4.7 x 10^4	2.3 x 10^5	422	14
SS	424	15	0.92	3.9 x 10^4	5.3 x 10^3	418	14

Table 3.12: Photophysical data for complexes (**3.1.A-3.4.A**, **3.2.B**, **3.1.B**, **3.1.C**, and **3.1.D**) dissolved in 2-MeTHF at a concentration of 10^{-5} M.

	Emission at room temperature					Emission at 77 K	
Compound	λ_{max} (nm)	τ (μs)	Φ_{PL}	k_r (s^{-1})	k_{nr} (s^{-1})	λ_{max} (nm)	τ (μs)
3.1.A	492	2.5	1.0	3.9 x 10^5	< 8.0 x 10^3	430	7300
3.2.A	510	2.3	0.68	3.0 x 10^5	1.7 x 10^5	430	430 nm: 3000; 500 nm: 48
3.3.A	500	1.8	0.56	3.1 x 10^5	2.4 x 10^5	430	7000
3.4.A	510	0.54	0.11	2.0 x 10^5	1.6 x 10^6	430	5000
3.2.B	542	0.86 (79%); 2.3 (21%)	0.12	1.1 x 10^5	8.0 x 10^{5*}	438	430 nm: 2400; 500 nm: 37
3.1.C	428; 590†	450 nm: 8.3; 600 nm: 8.0	0.11	–	–	422	12000
3.1.D	558	0.28	0.25	8.9 x 10^5	2.7 x 10^6	470	seconds
3.1.E	580	0.87	0.26	1.8 x 10^5	9.7 x 10^6	500	215

*Calculated from a weighted average of two contributions of τ. †Excimer peak.

Table 3.13: Photophysical data for complexes (**3.1.A, 3.1.C-3.1.E**) doped 1% by weight into PS thin films.

Emission at room temperature						Emission at 77 K	
Compound	λ_{max} (nm)	τ (μs)	Φ_{PL}	k_r (s^{-1})	k_{nr} (s^{-1})	λ_{max} (nm)	τ (μs)
3.1.A	474	2.8	1.0	3.5×10^5	3.6×10^3	480	64
3.1.C	426	240 (70%); 1300 (30%)	0.82	1.5×10^3	3.2×10^2	424	6900
3.1.D	518	2.3	1.0	4.3×10^5	$<4.4 \times 10^3$	490	550
3.1.E	532	2.6	0.78	3.0×10^5	8.5×10^4	536	264

Table 3.14: Photophysical properties of complex **3.1.A** in solvents of increasing polarity as well as in neat thin film form. [a]Non-Gaussian emission.

	Emission at room temperature					Emission at 77 K	
	λ_{max} (nm)	τ (μs)	Φ_{PL}	k_r (s^{-1})	k_{nr} (s^{-1})	λ_{max} (nm)	τ (μs)
MeCy	486; 468[a]	2.3	0.92	4.0×10^5	3.5×10^4	430	6700
Toluene	488	2.5	1.0	4.0×10^5	$< 4.0 \times 10^3$	---	---
2-MeTHF	492	2.5	1.0	3.9×10^5	$< 8.0 \times 10^3$	430	7300
CH$_2$Cl$_2$	482	1.6	0.4	2.5×10^5	3.8×10^5	---	---
Neat thin film	474	1.3	0.65	4.9×10^5	2.6×10^5	482	70.4

Table 3.15: Photophysical properties of microcrystalline powders (or solid state, SS) of complex **3.2.B** at RT and 77 K. [a]calculated from weighted average.

	Emission at room temperature					Emission at 77 K	
	λ_{max} (nm)	τ (μs)	Φ_{PL}	k_r (s^{-1})[a]	k_{nr} (s^{-1})[a]	λ_{max} (nm)	τ (μs)
SS	492	2 (30%); 11.2 (70%)	0.61	7.2×10^4	4.6×10^4	508	34 (at 550 nm)

Table 3.16: Photophysical properties of complex **3.1.E** in solvents of increasing polarity as well as in the microcrystalline solid form (SS) at RT and 77 K.

	Emission at room temperature					Emission at 77 K	
	λ_{max} (nm)	τ (μs)	Φ_{PL}	k_r (s^{-1})	k_{nr} (s^{-1})	λ_{max} (nm)	τ (μs)
MeCy	556	2.38	0.55	2.3 x 10^5	1.9 x 10^5	556	193
Toluene	468	1.43	0.41	2.9 x 10^5	4.1 x 10^5	---	---
2-MeTHF	580	0.87	0.16	1.8 x 10^5	9.7 x 10^5	498	215
CH$_2$Cl$_2$	568	0.88	0.24	2.7 x 10^5	8.6 x 10^5	---	---
AcN	584	0.47	0.11	2.3 x 10^5	1.9 x 10^5	---	---
SS	496	4.1	1.0	2.4 x 10^5	< 2.4 x 10^3	518	87

Table 3.17: Photophysical properties of complexes **3.1.A**, **3.1.C** – **3.1.E** in MeCy at RT and 77 K. [a]excimer emisssion.

	Emission at room temperature					Emission at 77 K	
	λ_{max} (nm)	τ (μs)	Φ_{PL}	k_r (s^{-1})	k_{nr} (s^{-1})	λ_{max} (nm)	τ (μs)
3.1.A	486	2.3	0.92	4.0 x 10^5	3.5 x 10^4	430	6700
3.1.C	482; 586[a]	450 nm: 5.9 600 nm[a]: 2.3 (-7%); 20.5 (107%)	0.19	---	---	422	5300
3.1.D	542	1.12	0.62	5.5 x 10^5	3.4 x 10^5	472	Seconds
3.1.E	556	2.38	0.55	2.3 x 10^5	1.9 x 10^5	530	193

3.4.6 OLED Optimization.

OLED devices were fabricated on pre-patterned ITO-coated glass substrates (20 ± 5 Ω cm-2, Thin Film Devices, Inc.). Prior to deposition, the substrates were cleaned with soap, rinsed with deionized water and sonicated for 15 minutes. Afterwards, two subsequent rinses and 12-minute sonication baths were performed in acetone and isopropyl alcohol sequentially. All organic layers as well as the Al cathode were deposited in a vacuum thermal evaporator, EVO Vac 800 deposition system from Angstrom Engineering, at 6 x 10-7 Torr.

Current-voltage-luminescence (J-V-L) curves were using a Keithley power source meter model 2400 and a Newport multifunction optical model 1835-C, PIN-220DP/SB blue-enhanced silicon photodiodes (OSI optoelectronics Ltd.). The sensor was set to measure power at an energy of 520 nm, followed by correcting to the average electroluminescence wavelength for each individual device during data process. Electroluminescence (EL) spectra of OLEDs were measured using the fluorimeter (model C-60 Photon Technology International QuantaMaster) at several voltages.

Table 3.18: Summary of device optimization where the following parameters in the EML were varied: the host (**3.1**, UGH3, mCBP, and mCP), EML thickness (40 nm), and doping concentration (5%, 10%, 20% and 25%). The compounds 4,4'-Cyclohexylidenebis[N,N-bis(4-methylphenyl)benzenamine] (TAPC), and 2,2',2"-(1,3,5-Benzinetriyl)-tris(1-phenyl-1-H-benzimidazole) (TPBi) are used in the electron transport layer and the hole transport layer respectively. The device architectures are: (40)nm/EML(20, 40nm)/TPBI(40nm, 50nm)/LiF(1nm)/Al(100nm). [a]Turn on voltage was determined as the voltage at 1cd/m$_2$.

Host	EML thickness (nm)	Doping concentration (vol%)	EQE$_{max}$ (%)	Current density at EQE$_{max}$ (mA/cm^2)	[a]V turn on (V)	Max cd/A	Max cd/m^2
3.1	20	5	4.2	0.008	3.5	3.1	123.2
	20	10	3.2	0.1	3.2	3.5	196.5
	20	20	2.6	1.9	3.1	3.4	296.9
	40	5	0.8	0.009	4.5	0.8	15.4
	40	10	1.1	0.02	4.1	1.2	44.7
			9.2	0.3	4.4	10.3	391.7
	40	20	9.5 (ETL = 50nm)	0.2	4.4	12.5	433.8
	40	30	1.2	10.6	3.1	1.8	515.7
UGH3	40	5	7.4	0.1	4.2	10.8	976.1
	40	10	5	2.6	3.6	7.6	2396
	40	20 (ETL = 50nm)	8.4	1.8	4.0	15.6	3797
	40	25	2.6	35.3	3.1	4.3	4517
mCBP	20	5	0.7	11.7	3.1	1.2	845.7
	20	10	0.6	25.9	2.8	1.1	1281
	20	20	4	10.3	2.8	1.7	2365
mCP	20	5	0.5	11.5	3.5	0.4	418.9
	20	10	0.4	17.7	3.4	0.3	286.6
	40	20	1.1	69.1	3.3	1.6	1304

3.4.7 **Computational Details**.

All DFT and TDDFT calculations reported in this work were performed using the Q-Chem 5.0 package.[75] Common hybrid functionals, such as B3LYP and PBE0, have been reported to severely underestimate the energies of charge transfer states,[76–78] whereas long-range corrected functionals, such as CAM-B3LYP, ωPBE and ωB97xD, better match the observed energies.[79–82] In this work, TDDFT calculations performed using the CAM-B3LYP functional were found to offer good agreement with

experimental values. For all (CAAC)Cu-amide complexes, the first two singlet excited states can be characterized as interligand charge-transfer, from the amide to the carbene ligand, *i.e.*[1]ICT from the amide to the carbene ligand. These states are characterized by high oscillator strengths (f > 0.1).

Gas phase geometry optimization for all complexes was performed at the B3LYP/LACVP** level in Jaguar. Geometric parameters obtained from XRD analyses were used as a starting point for single point calculations on the ground state and geometry optimization was performed on the triplet state. Single point TDDFT calculations were performed on the ground state optimized structures at the CAM-B3LYP/LACVP** level to compute excited state properties. The electrostatic potential-fitted (esp) atomic charges for 2-MeTHF and complex 1a used to replace the partial charges of the OPLS2005 forcefield for the MD simulations, were computed at the B3LYP/6-31G** and ωPBEh($\omega = 0.263$ bohr^{-1}) /6-31G** levels respectively. The esp charges of the triplet (^{3}ICT) state of **3.1.A** was computed using the unrestricted DFT scheme (UDFT). TDDFT calculations on the solvated clusters derived from the snapshots of the MD simulations were performed at the ωPBEh($\omega = 0.263$ bohr^{-1}) /6-31G** level by replacing the atoms of all solvent molecules with their corresponding esp charges to act as a polarizing influence on the complex. The value of the range separation parameter (ω) in the ωPBEh functional was tuned to satisfy the global density-dependent (GDD) criterion to get a balanced description of CT and LE states and in the case of complex **3.1.A**, the tuned value was found to be 0.263 bohr^{-1}.[83]

Molecular Dynamics. All MD simulations reported here were performed using the Desmond program available within Schrödinger's Materials Science Suite.[84] A simulation cell was built by populating 128 2-MeTHF solvent molecules around the complex following which a 200ns NPT MD simulation (P = 1 atm, T = 300 K) was performed using the OPLS2005 forcefield.[85] The atomic charges of the forcefield for the complex were replaced by esp-fitted (electrostatic potential) point charges of the ^{3}CT state derived from UDFT (ωPBEh/6-31G** with ω=0.263 bohr^{-1} tuned to satisfy the GDD criterion[83] to get a balanced description of CT and LE states) while those of the 2-MeTHF molecules were replaced by ground state esp-fitted point charges calculated at the B3LYP/6-31G** level. This was done to approximate the response of

136

the solvent molecules to the ^{3}CT excited state at 300 K. 50 snapshots were extracted from the last 100ns of the MD run, and TDDFT (ωPBEh/6-31G**) calculations were performed on each snapshot where all the atoms of the 2-MeTHF molecules were replaced with the corresponding esp-fitted point charges to serve as a polarizing influence on the complex which was treated at the TDDFT level. To model the phenomena occurring at 77 K, a series of 10 ns NVT runs were performed on the 300 K equilibrated cell in steps of decreasing temperatures (300-200-100-77 K) followed by a 200 ns NPT simulation (P = 1 atm, T = 77 K). In this case, the atomic charges of the OPLS2005 forcefield were replaced by the ground state esp-fitted charges for both the complex and the solvent molecules computed at the ωPBEh/6-31G** and B3LYP/6-31G** levels respectively. The simulation resulted in a frozen rigid equilibrated cell which was used to perform a single point TDDFT calculation, as done in the previous case. Under these conditions, it was found that the ^{3}Cz state becomes the lowest lying triplet (2.90 eV) in accordance with the experimental observation of ^{3}Cz emission in 2-MeTHF at 77 K.

Table 3.19: Calculated singlet and triplet excited state energies for the complexes in this paper obtained through TDDFT performed at the CAM-B3LYP/LACVP** level. Also reported are $\Delta E_{^1CT\text{-}^3ICT}$, the energy gap between the closest-lying ligand localized state (^{3}LE) and interligand charge transfer (^{3}ICT), $\Delta E_{^3LE\text{-}^3ICT}$, the S_1 oscillator strength f_{S_1}, and the excited state dipole moment, μ_{ES}. The character of the states was assigned based on the largest MO contributions associated with the transition. The ^{3}LE state in complexes **3.1.A**-**3.4.A**, **3.2.B**, **3.1.C**, and **3.1.D** is carbazolide-centered (referred to as ^{3}Cz) and **3.1.E** is diphenyl-amide centered in the complex (referred to as ^{3}NPh$_2$).

	E (eV)						ΔE^1CT-^3CT	ΔE^3LE-^3CT	f_{S_1}
	T_1	T_2	T_3	S_1	S_2	S_3			
3.1.A	2.99 (CT)	3.02 (LE)	3.23 (LE)	3.25 (CT)	3.89 (CT)	4.11 (LE)	0.26	0.03	0.123
3.2.A	2.99 (CT)	3.12 (LE)	3.19 (CT)	3.23 (CT)	3.66 (CT)	4.18 (CT)	0.24	0.13	0.112
3.3.A	2.91 (CT)	3.02 (LE)	3.23 (LE)	3.17 (CT)	3.87 (CT)	4.04 (CT)	0.26	0.11	0.128
3.4.A	2.97 (CT)	3.02 (LE)	3.22 (LE)	3.23 (CT)	3.90 (CT)	4.20 (CT)	0.26	0.05	0.125
3.2.B	2.98 (CT)	3.04 (LE)	3.09 (CT)	3.06 (CT)	3.57 (CT)	4.06 (CT)	0.08	0.06	0.005
3.1.C	2.91 (LE)	3.14 (LE)	3.38 (LE)	3.79 (CT)	4.06 (CT)	4.11 (LE)	---	< -0.47	0.144
3.1.D	2.67 (CT)	2.80 (LE)	2.95 (LE)	2.94 (CT)	3.70 (LE)	4.02 (CT)	0.27	0.13	0.129
3.1.E	2.68 (CT)	3.04 (LE)	3.33 (CT)	2.96 (CT)	3.75 (CT)	4.09 (CT)	0.28	0.36	0.102
3.1	3.27 (CT)	3.38 * (LE)	3.48 (LE)	3.78 (CT)	4.75 (CT)	4.82 (CT)	0.51	0.11	0.011

Table 3.20: Dipole moments (μ) computed at the CAM-B3LYP/LACVP** level.

	μ (D)		
	GS	**³CT**	**³LE**
3.1.A	11.80	4.25	11.27
3.2.A	11.76	5.47	11.18
3.3.A	12.18	5.11	11.62
3.4.A	12.01	4.50	11.45
3.2.B	11.58	2.46	13.80
3.1.C	20.41	15.70	20.37
3.1.D	13.25	0.99	12.64
3.1.E	10.01	6.66	10.43
3.1	11.21	6.80	10.29
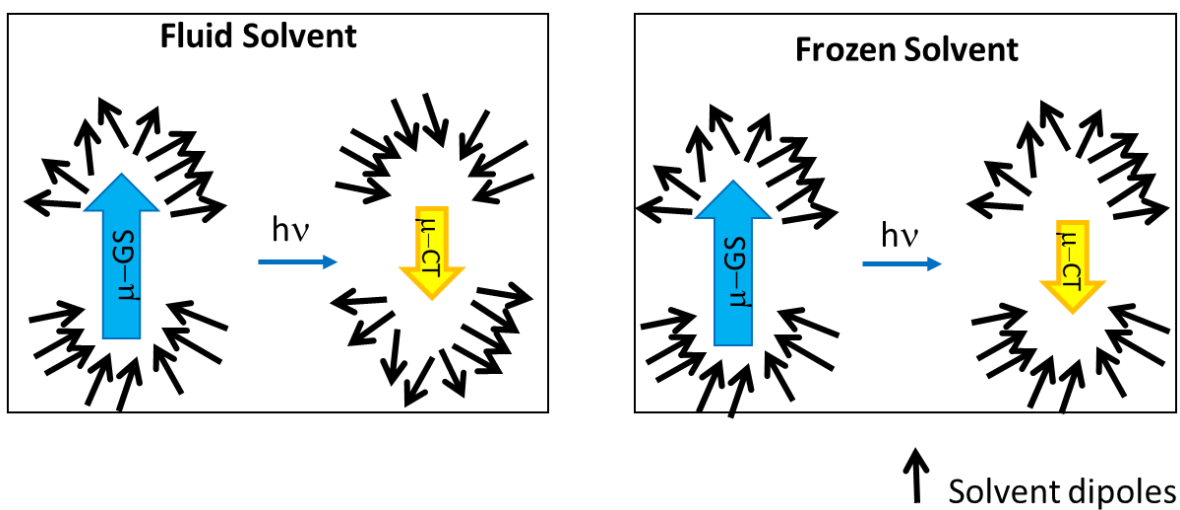
Figure 3.22: Solvation effects operating in a polar medium, 2-MeTHF, on the ground and the ICT excited state dipoles (μ-GS and μ-CT respectively) at room temperature (fluid medium) and 77 K (frozen glass).
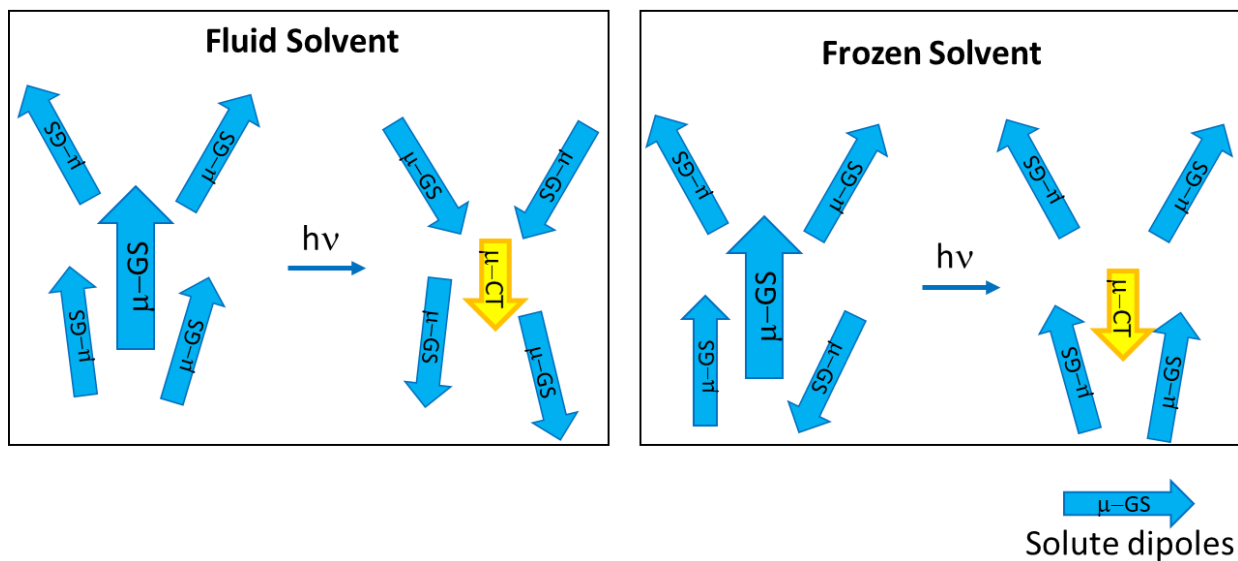
Figure 3.23: Solute-solute interactions operating in a non-polar fluid and a frozen media that lead to the observed destabilization in the ICT state at low temperatures.

3.5 Acknowledgements

3.6 References

(1)   Bernanose, A.; Comte, M.; Vouaux, P. A New Method of Light Emission by Certain Organic Compounds. *J. Chim. Phys. Phys.-Chim.Biol* **1953**, *50*, 64−68.

(2)   Bernanose, A.; Vouaux, P. Organic Electroluminescence Type of Emission. *J. Chim. Phys. Phys.-Chim. Biol* **1953**, *50*, 261−263.

(3)   Tang, C. W.; Vanslyke, S. A. Organic Electroluminescent Diodes. *Appl. Phys. Lett.* **1987**, *51*, 913–

915.

(4)   Coffey, V. C. The Age of OLED Displays. *Opt. Photonics News* **2017**, *28*, 34–41.

(5)   Khazanchi, A.; Kanwar, A.; Saluja, L.; Damra, A.; Damara, V. OLED: A New Display Technology. *Int. Jouranal Eng. Comput. Sci.* **2012**, *1*, 75–84.

(6)   Baldo, M. A.; an dY. You, D. F. O.; Shoustikov, A.; Sibley, S.; Thompson, M. E.; Forrest, S. R. Highly Efficient Phosphorescent Emission from Organic Electroluminescent Devices. *Nature* **1998**, *395*, 151–154.

(7)   Baldo, M. A.; Lamansky, S.; Burrows, P. E.; Thompson, M. E.; Forrest, S. R. Very High-Efficiency Green Organic Light-Emitting Devices Based on Electrophosphorescence. *Appl. Phys. Lett.* **1999**, *75*, 4–6.

(8)   Sajoto, T.; Djurovich, P. I.; Tamayo, A.; Yousufuddin, M.; Bau, R.; Thompson, M. E.; Holmes, R. J.; Forrest, S. R. Blue and Near-UV Phosphorescence from Iridium Complexes with Cyclometalated Pyrazolyl or N-Heterocyclic Carbene Ligands. *Inorg. Chem.* **2005**, *44*, 7992–8003.

(9)   Kawamura, Y.; Goushi, K.; Brooks, J.; Brown, J. J.; Sasabe, H.; Adachi, C. 100% Phosphorescence Quantum Efficiency of Ir (III) Complexes in Organic Semiconductor Films. *Appl. Phys. Lett.* **2005**, *86*, 1–3.

(10)   Yersin, H.; Rausch, A. F.; Czerwieniec, R.; Hofbeck, T.; Fischer, T. The Triplet State of Organo-Transition Metal Compounds. Triplet Harvesting and Singlet Harvesting for Efficient OLEDs. *Coord. Chem. Rev.* **2011**, *255*, 2622–2652.

(11)   Yu-Tzu Li, E.; Jiang, T. Y.; Chi, Y.; Chou, P. T. Semi-Quantitative Assessment of the Intersystem Crossing Rate: An Extension of the El-Sayed Rule to the Emissive Transition Metal Complexes. *Phys. Chem. Chem. Phys.* **2014**, *16*, 26184–26192.

(12)   Kalyanasundaram, K. Photophysics, Photochemistry and Solar Energy Conversion with Tris(Bipyridyl)Ruthenium(II) and Its Analogues. *Coord. Chem. Rev.* **1982**, *46*, 159–244.

(13)   Kuramochi, Y.; Ishitani, O. Iridium(III) 1-Phenylisoquinoline Complexes as a Photosensitizer for Photocatalytic CO2 Reduction: A Mixed System with a Re(I) Catalyst and a Supramolecular Photocatalyst. *Inorg. Chem.* **2016**, *55*, 5702–5709.

(14)   Keefe, M. H.; Benkstein, K. D.; Hupp, J. T. Luminescent Sensor Molecules Based on Coordinated Metals: A Review of Recent Developments. *Coord. Chem. Rev.* **2000**, *205*, 201–228.

(15)   Lo, K. K. W.; Louie, M. W.; Zhang, K. Y. Design of Luminescent Iridium(III) and Rhenium(I) Polypyridine Complexes as in Vitro and in Vivo Ion, Molecular and Biological Probes. *Coord. Chem. Rev.* **2010**, *254*, 2603–2622.

(16)   Ma, D. L.; Lin, S.; Wang, W.; Yang, C.; Leung, C. H. Luminescent Chemosensors by Using Cyclometalated Iridium(III) Complexes and Their Applications. *Chem. Sci.* **2017**, *8*, 878–889.

(17)   Grätzel, M. Solar Energy Conversion by Dye-Sensitized Photovoltaic Cells. *Inorg. Chem.* **2005**, *44*, 6841–6851.

(18)   Kuciauskas, D.; Freund, M. S.; Gray, H. B.; Winkler, J. R.; Lewis, N. S. Electron Transfer Dynamics in Nanocrystalline Titanium Dioxide Solar Cells Sensitized with Ruthenium or Osmium Polypyridyl Complexes. *J. Phys. Chem. B* **2001**, *105*, 392–403.

(19)   Lamansky, S.; Djurovich, P.; Murphy, D.; Abdel-Razzaq, F.; Lee, H. E.; Adachi, C.; Burrows, P. E.; Forrest, S. R.; Thompson, M. E. Highly Phosphorescent Bis-Cyclometalated Iridium Complexes: Synthesis, Photophysical Characterization, and Use in Organic Light Emitting Diodes. *J. Am. Chem. Soc.* **2001**, *123*, 4304–4312.

(20)   Bolink, H. J.; Coronado, E.; Costa, R. D.; Lardiés, N.; Ortí, E. Near-Quantitative Internal Quantum Efficiency in a Light-Emitting Electrochemical Cell. *Inorg. Chem.* **2008**, *47*, 9149–9151.

(21)   Li, T. Y.; Wu, J.; Wu, Z. G.; Zheng, Y. X.; Zuo, J. L.; Pan, Y. Rational Design of Phosphorescent Iridium(III) Complexes for Emission Color Tunability and Their Applications in OLEDs. *Coord. Chem. Rev.* **2018**, *374*, 55–92.

(22)   Bizzarri, C.; Spuling, E.; Knoll, D. M.; Volz, D.; Bräse, S. Sustainable Metal Complexes for Organic Light-Emitting Diodes (OLEDs). *Coord. Chem. Rev.* **2018**, *373*, 49–82.

(23)   Ford, P. C.; Vogler, A. Photochemical and Photophysical Properties of Tetranuclear and Hexanuclear Clusters of Metals with D10 and S2 Electronic Configurations. *Acc. Chem. Res.* **1993**, *26*, 220–226.

(24)   Fraga, S.; Karwowski, J.; Saxena, K. M. S. *Handbook of Atomic Data*; Elsevier Scientific Publishing Company: New York, NY, 1976; Vol. 5.

(25)   Bergmann, L.; Hedley, G. J.; Baumann, T.; Bräse, S.; Samuel, I. D. W. Direct Observation of Intersystem Crossing in a Thermally Activated Delayed Fluorescence Copper Complex in the Solid State. *Sci. Adv.* **2016**, *2*, 2–7.

(26)   Penfold, T. J.; Gindensperger, E.; Daniel, C.; Marian, C. M. Spin-Vibronic Mechanism for Intersystem Crossing. *Chem. Rev.* **2018**, *118*, 6975–7025.

(27)   Brooks, J.; Babayan, Y.; Lamansky, S.; Djurovich, P. I.; Tsyba, I.; Bau, R.; Thompson, M. E. Synthesis and Characterization of Phosphorescent Cyclometalated Platinum Complexes. *Inorg. Chem.* **2002**, *41*, 3055–3066.

(28)   Lamansky, S.; Kwong, R. C.; Nugent, M.; Djurovich, P. I.; Thompson, M. E. Molecularly Doped Polymer Light Emitting Diodes Utilizing Phosphorescent Pt(II) and Ir(III) Dopants. *Org. Electron.* **2001**, *2*, 53–62.

(29)   Siddique, Z. A.; Yamamoto, Y.; Ohno, T.; Nozaki, K. Structure-Dependent Photophysical Properties of Singlet and Triplet Metal-to-Ligand Charge Transfer States in Copper(I) Bis(Diimine) Compounds. *Inorg. Chem.* **2003**, *42*, 6366–6378.

(30)   Leitl, M. J.; Zink, D. M.; Schinabeck, A.; Baumann, T.; Volz, D.; Yersin, H. Copper(I) Complexes for Thermally Activated Delayed Fluorescence: From Photophysical to Device Properties. *Top. Curr. Chem.* **2016**, *374*, 1–34.

(31)   Chen, T.; Zheng, L.; Yuan, J.; An, Z.; Chen, R.; Tao, Y.; Li, H. Understanding the Control of Singlet-Triplet Splitting for Organic Exciton Manipulating : A Combined Theoretical and

Experimental Approach. *Nat. Publ. Gr.* **2015**, 1–11.

(32)   Blasse, G.; McMillin, D. R. On the Luminescence of Bis (Triphenylphosphine) Phenanthroline Copper (I). *Chem. Phys. Lett.* **1980**, *70*, 1–3.

(33)   Kirchhoff, J. R.; Gamache, R. E.; Blaskie, M. W.; Paggio, A. A. D.; Lengel, R. K.; Mcmillin, D. R. Temperature Dependence of Luminescence from Cu(NN)2+ Systems in Fluid Solution. Evidence for the Participation of Two Excited States. *Inorg. Chem.* **1983**, *22*, 2380–2384.

(34)   Blasse, G.; Breddels, P. A.; McMillin, D. R. The Luminescence of Solid Bis(2,9-Diphenyl-1,10-Phenanthroline) Copper(I). *Chem. Phys. Lett.* **1984**, *109*, 24–26.

(35)   Linfoot, C. L.; Leitl, M. J.; Richardson, P.; Rausch, A. F.; Chepelin, O.; White, F. J.; Yersin, H.; Robertson, N. Thermally Activated Delayed Fluorescence (TADF) and Enhancing Photoluminescence Quantum Yields of [CuI(Diimine)(Diphosphine)]+ Complexes - Photophysical, Structural, and Computational Studies. *Inorg. Chem.* **2014**, *53*, 10854–10861.

(36)   Czerwieniec, R.; Yu, J.; Yersin, H. Blue-Light Emission of Cu(I) Complexes and Singlet Harvesting. *Inorg. Chem.* **2011**, *50*, 8293–8301.

(37)   Krylova, V. A.; Djurovich, P. I.; Conley, B. L.; Haiges, R.; Whited, M. T.; Williams, T. J.; Thompson, M. E. Control of Emission Colour with N-Heterocyclic Carbene (NHC) Ligands in Phosphorescent Three-Coordinate Cu(I) Complexes. *Chem. Commun.* **2014**, *50*, 7176–7179.

(38)   McCusker, C. E.; Castellano, F. N. Design of a Long-Lifetime, Earth-Abundant, Aqueous Compatible Cu(I) Photosensitizer Using Cooperative Steric Effects. *Inorg. Chem.* **2013**, *52*, 8114–8120.

(39)   Iwamura, M.; Watanabe, H.; Ishii, K.; Takeuchi, S.; Tahara, T. Coherent Nuclear Dynamics in Ultrafast Photoinduced Structural Change of Bis(Diimine)Copper(I) Complex. *J. Am. Chem. Soc.* **2011**, *133*, 7728–7736.

(40)   Czerwieniec, R.; Leitl, M. J.; Homeier, H. H. H.; Yersin, H. Cu(I) Complexes – Thermally Activated Delayed Fluorescence. Photophysical Approach and Material Design. *Coord. Chem. Rev.* **2016**, *325*, 2–28.

(41)   Miller, A. J. M.; Dempsey, J. L.; Peters, J. C. Long-Lived and Efficient Emission from Mononuclear Amidophosphine Complexes of Copper. *Inorg. Chem.* **2007**, *46*, 7244–7246.

(42)   Romanov, A. S.; Di, D.; Yang, L.; Fernandez-Cestau, J.; Becker, C. R.; James, C. E.; Zhu, B.; Linnolahti, M.; Credgington, D.; Bochmann, M. Highly Photoluminescent Copper Carbene Complexes Based on Prompt Rather than Delayed Fluorescence. *Chem. Commun.* **2016**, *52*, 6379–6382.

(43)   Gernert, M.; Müller, U.; Haehnel, M.; Pflaum, J.; Steffen, A. A Cyclic Alkyl(Amino)Carbene as Two-Atom π-Chromophore Leading to the First Phosphorescent Linear CuIComplexes. *Chem. Eur. J.* **2017**, *23*, 2206–2216.

(44)   Visbal, R.; Gimeno, M. C. N-Heterocyclic Carbene Metal Complexes: Photoluminescence and Applications. *Chem. Soc. Rev.* **2014**, *43*, 3551–3574.

(45)   Hamze, R.; Jazzar, R.; Soleilhavoup, M.; Djurovich, P. I.; Bertrand, G.; Thompson, M. E. Phosphorescent 2-, 3- and 4-Coordinate Cyclic (Alkyl)(Amino)Carbene (CAAC) Cu(I) Complexes. *Chem. Commun.* **2017**, *53*, 9008–9011.

(46)   Romanov, A. S.; Becker, C. R.; James, C. E.; Di, D.; Credgington, D.; Linnolahti, M.; Bochmann, M. Copper and Gold Cyclic (Alkyl)(Amino)Carbene Complexes with Sub-Microsecond Photoemissions: Structure and Substituent Effects on Redox and Luminescent Properties. *Chem. Eur. J.* **2017**, *23*, 4625–4637.

(47)   Xie, Y.; Li, Z. Triboluminescence: Recalling Interest and New Aspects. *Chem* **2018**, *4*, 943–971.

(48)   Oh, C. S.; Pereira, D. D. S.; Han, S. H.; Park, H. J.; Higginbotham, H. F.; Monkman, A. P.; Lee, J. Y. Dihedral Angle Control of Blue Thermally Activated Delayed Fluorescent Emitters through Donor Substitution Position for Efficient Reverse Intersystem Crossing. *ACS Appl. Mater. Interfaces* **2018**, *10*, 35420–35429.

(49)   Di, D.; Romanov, A. S.; Yang, L.; Richter, J. M.; Rivett, J. P. H.; Jones, S.; Thomas, T. H.; Jalebi, M. A.; Friend, R. H.; Linnolahti, M.; Bochmann, M.; Credgington, D. High-Performance Light-Emitting Diodes Based on Carbene-Metal-Amides. *Science* **2017**, *356*, 159–163.

(50)   Föller, J.; Marian, C. M. Rotationally Assisted Spin-State Inversion in Carbene-Metal-Amides Is an Artifact. *J. Phys. Chem. Lett.* **2017**, *8*, 5643–5647.

(51)   Taffet, E. J.; Olivier, Y.; Lam, F.; Beljonne, D.; Scholes, G. D. Carbene-Metal-Amide Bond Deformation, Rather Than Ligand Rotation, Drives Delayed Fluorescence. *J. Phys. Chem. Lett.* **2018**, *9*, 1620–1626.

(52)   Thompson, S.; Eng, J.; Penfold, T. J. The Intersystem Crossing of a Cyclic (Alkyl)(Amino) Carbene Gold (i) Complex. *J. Chem. Phys.* **2018**, *149*, 014304.

(53)   McGlynn, S. P.; Azumi, T.; Kinoshita, M. *Molecular Spectroscopy of the Triplet State*; Prentice-Hall, Inc., 1969.

(54)   Hansmann, M. M.; Melaimi, M.; Munz, D.; Bertrand, G. Modular Approach to Kekulé Diradicaloids Derived from Cyclic (Alkyl)(Amino)Carbenes. *J. Am. Chem. Soc.* **2018**, *140*, 2546–2554.

(55)   Rosenfeld, D. C.; Wolczanski, P. T.; Barakat, K. A.; Buda, C.; Cundari, T. R. 3-Center-4-Electron Bonding in [(Silox)2Mo=NtBu] 2(μ-Hg) Controls Reactivity While Frontier Orbitals Permit a Dimolybdenum π-Bond Energy Estimate. *J. Am. Chem. Soc.* **2005**, *127*, 8262–8263.

(56)   Reichardt, C. Solvatochromic Dyes as Solvent Polarity Indicators. *Chem. Rev.* **1994**, *94*, 2319–2358.

(57)   Volz, D.; Zink, D. M.; Bocksrocker, T.; Friedrichs, J.; Nieger, M.; Baumann, T.; Lemmer, U.; Bräse, S. Molecular Construction Kit for Tuning Solubility, Stability and Luminescence Properties: Heteroleptic MePyrPHOS-Copper Iodide-Complexes and Their Application in Organic Light-Emitting Diodes. *Chem. Mater.* **2013**, *25*, 3414–3426.

(58)   Scholz, S.; Kondakov, D.; Leo, K. Degradation Mechanisms and Reactions in Organic Light-Emitting Devices. *Chem. Rev.* **2015**, *115*, 8449−8503.

(59)   Sivasubramaniam, V.; Brodkorb, F.; Hanning, S.; Peter, H.; Elsbergen, V. Van; Boerner, H.; Scherf,

U.; Kreyenschmidt, M. Fluorine Cleavage of the Light Blue Heteroleptic Triplet Emitter FIrpic. **2009**, *130*, 640–649.

(60)   Liu, Y.; Yiu, S. C.; Ho, C. L.; Wong, W. Y. Recent Advances in Copper Complexes for Electrical/Light Energy Conversion. *Coord. Chem. Rev.* **2018**, *375*, 514–557.

(61)   Wallesch, M.; Volz, D.; Fléchon, C.; Zink, D. M. Bright Coppertunities : Efficient OLED Devices with Copper (I) Iodide- NHetPHOS-Emitters. **2014**, *9183*, 1–11.

(62)   Liang, D.; Chen, X. L.; Liao, J. Z.; Hu, J. Y.; Jia, J. H.; Lu, C. Z. Highly Efficient Cuprous Complexes with Thermally Activated Delayed Fluorescence for Solution-Processed Organic Light-Emitting Devices. *Inorg. Chem.* **2016**, *55*, 7467–7475.

(63)   Chen, X. L.; Yu, R.; Zhang, Q. K.; Zhou, L. J.; Wu, X. Y.; Zhang, Q.; Lu, C. Z. Rational Design of Strongly Blue-Emitting Cuprous Complexes with Thermally Activated Delayed Fluorescence and Application in Solution-Processed OLEDS. *Chem. Mater.* **2013**, *25*, 3910–3920.

(64)   Ren, X.; Li, J.; Holmes, R. J.; Djurovich, P. I.; Forrest, S. R.; Thompson, M. E. Ultrahigh Energy Gap Hosts in Deep Blue Organic Electrophosphorescent Devices. *Chem. Mater.* **2004**, *16*, 4743–4747.

(65)   Hamze, R.; Shi, S.; Kapper, S. C.; Ravinson, D. S. M.; Estergreen, L.; Jung, M.-C.; Tadle, A. C.; Haiges, R.; Djurovich, P. I.; Peltier, J. L.; Jazzar, R.; Bertrand, G.; Bradforth, S. E.; Thompson, M. E. "Quick-Silver" from a Systematic Study of Highly Luminescent, Two-Coordinate, D10 Coinage Metal Complexes. *J. Am. Chem. Soc.* **2019**, *141*, 8616–8626.

(66)   Baková, R.; Chergui, M.; Daniel, C.; Vlček Jr., A.; Záliš, S. Relativistic Effects in Spectroscopy and Photophysics of Heavy-Metal Complexes Illustrated by Spin–Orbit Calculations of [Re(Imidazole)(CO)3(Phen)]+. *Coord. Chem. Rev.* **2011**, *255*, 975–989.

(67)   Turro, N. J. *Modern Molecular Photochemistry*; University Science Books, 1991.

(68)   Yang, Y.; Xue, M.; Marshall, L. J.; De Mendoza, J. Hydrogen-Bonded Cyclic Tetramers Based on Ureidopyrimidinones Attached to a 3,6-Carbazolyl Spacer. *Org. Lett.* **2011**, *13*, 3186–3189.

(69)   Bedford, R. B.; Betham, M. N-H Carbazole Synthesis from 2-Chloroanilines via Consecutive Amination and C-H Activation. *J. Org. Chem.* **2006**, *71*, 9403–9410.

(70)   Frey, G. D.; Dewhurst, R. D.; Kousar, S.; Donnadieu, B.; Bertrand, G. Cyclic (Alkyl)(Amino)Carbene Gold(I) Complexes: A Synthetic and Structural Investigation. *J. Organomet. Chem.* **2008**, *693*, 1674–1682.

(71)   Hu, X.; Soleilhavoup, M.; Melaimi, M.; Chu, J.; Bertrand, G. Air-Stable (CAAC)CuCl and (CAAC)CuBH4 Complexes as Catalysts for the Hydrolytic Dehydrogenation of BH3NH3. *Angew. Chem. Int. Ed.* **2015**, *54*, 6008–6011.

(72)   Lavallo, V.; Canac, Y.; Prasang, C.; Donnadieu, B.; Bertrand, G. Stable Cyclic (Alkyl)(Amino)Carbenes as Rigid or Flexible, Bulky, Electron-Rich Ligands for Transition-Metal Catalysts: A Quaternary Carbon Atom Makes the Difference. *Angew. Chem. Int. Ed.* **2005**, *44*, 5705–5709.

(73)   G. M. Sheldrick. A Short History of SHELX. *Acta Crystallogr. A* **2008**, *64*, 112–122.

(74)   O. V. Dolomanov, L. J. Bourhis, R. J. Gildea, J. A. K. Howard, H. P. OLEX2: A Complete Structure Solution, Refinement and Analysis Program. *J. Appl. Cryst.* **2009**, *42*, 339–341.

(75)   Shao, Y.; Gan, Z.; Epifanovsky, E.; Gilbert, A. T. B.; Wormit, M.; Kussmann, J.; Lange, A. W.; Behn, A.; Deng, J.; Feng, X.; Ghosh, D.; Goldey, M.; Horn, P. R.; Jacobson, L. D.; Kaliman, I.; Khaliullin, R. Z.; Kuš, T.; Landau, A.; Liu, J.; Proynov, E. I.; Rhee, Y. M.; Richard, R. M.; Rohrdanz, M. A.; Steele, R. P.; Sundstrom, E. J.; Woodcock, H. L.; Zimmerman, P. M.; Zuev, D.; Albrecht, B.; Alguire, E.; Austin, B.; Beran, G. J. O.; Bernard, Y. A.; Berquist, E.; Brandhorst, K.; Bravaya, K. B.; Brown, S. T.; Casanova, D.; Chang, C. M.; Chen, Y.; Chien, S. H.; Closser, K. D.; Crittenden, D. L.; Diedenhofen, M.; Distasio, R. A.; Do, H.; Dutoi, A. D.; Edgar, R. G.; Fatehi, S.; Fusti-Molnar, L.; Ghysels, A.; Golubeva-Zadorozhnaya, A.; Gomes, J.; Hanson-Heine, M. W. D.; Harbach, P. H. P.; Hauser, A. W.; Hohenstein, E. G.; Holden, Z. C.; Jagau, T. C.; Ji, H.; Kaduk, B.; Khistyaev, K.; Kim, J.; Kim, J.; King, R. A.; Klunzinger, P.; Kosenkov, D.; Kowalczyk, T.; Krauter, C. M.; Lao, K. U.; Laurent, A. D.; Lawler, K. V.; Levchenko, S. V.; Lin, C. Y.; Liu, F.; Livshits, E.; Lochan, R. C.; Luenser, A.; Manohar, P.; Manzer, S. F.; Mao, S. P.; Mardirossian, N.; Marenich, A. V.; Maurer, S. A.; Mayhall, N. J.; Neuscamman, E.; Oana, C. M.; Olivares-Amaya, R.; Oneill, D. P.; Parkhill, J. A.; Perrine, T. M.; Peverati, R.; Prociuk, A.; Rehn, D. R.; Rosta, E.; Russ, N. J.; Sharada, S. M.; Sharma, S.; Small, D. W.; Sodt, A.; Stein, T.; Stück, D.; Su, Y. C.; Thom, A. J. W.; Tsuchimochi, T.; Vanovschi, V.; Vogt, L.; Vydrov, O.; Wang, T.; Watson, M. A.; Wenzel, J.; White, A.; Williams, C. F.; Yang, J.; Yeganeh, S.; Yost, S. R.; You, Z. Q.; Zhang, I. Y.; Zhang, X.; Zhao, Y.; Brooks, B. R.; Chan, G. K. L.; Chipman, D. M.; Cramer, C. J.; Goddard, W. A.; Gordon, M. S.; Hehre, W. J.; Klamt, A.; Schaefer, H. F.; Schmidt, M. W.; Sherrill, C. D.; Truhlar, D. G.; Warshel, A.; Xu, X.; Aspuru-Guzik, A.; Baer, R.; Bell, A. T.; Besley, N. A.; Chai, J. Da; Dreuw, A.; Dunietz, B. D.; Furlani, T. R.; Gwaltney, S. R.; Hsu, C. P.; Jung, Y.; Kong, J.; Lambrecht, D. S.; Liang, W.; Ochsenfeld, C.; Rassolov, V. A.; Slipchenko, L. V.; Subotnik, J. E.; Van Voorhis, T.; Herbert, J. M.; Krylov, A. I.; Gill, P. M. W.; Head-Gordon, M. Advances in Molecular Quantum Chemistry Contained in the Q-Chem 4 Program Package. *Mol. Phys.* **2015**, *113*, 184–215.

(76)   Dreuw, A.; Weisman, J. L.; Head-Gordon, M. Long-Range Charge-Transfer Excited States in Time-Dependent Density Functional Theory Require Non-Local Exchange. *J. Chem. Phys.* **2003**, *119*, 2943–2946.

(77)   Dreuw, A.; Head-Gordon, M. Failure of Time-Dependent Density Functional Theory for Long-Range Charge-Transfer Excited States: The Zincbacteriochlorin-Bacteriochlorin and Bacteriochlorophyll-Spheroidene Complexes. *J. Am. Chem. Soc.* **2004**, *126*, 4007–4016.

(78)   Tozer, D. J.; Amos, R. D.; Handy, N. C.; Roos, B. O.; Serrano-ANDRES, L. Does Density Functional Theory Contribute to the Understanding of Excited States of Unsaturated Organic Compounds? *Mol. Phys.* **1999**, *97*, 859–868.

(79)   Chai, J. Da; Head-Gordon, M. Long-Range Corrected Double-Hybrid Density Functionals. *J. Chem. Phys.* **2009**, *131*, 174105.

(80)   Jacquemin, D.; Perpète, E. A.; Scuseria, G. E.; Ciofini, I.; Adamo, C. TD-DFT Performance for the Visible Absorption Spectra of Organic Dyes: Conventional versus Long-Range Hybrids. *J. Chem. Theory Comput.* **2008**, *4*, 123–135.

(81)   Jacquemin, D.; Wathelet, V.; Perpète, E. A.; Adamo, C. Extensive TD-DFT Benchmark: Singlet-Excited States of Organic Molecules. *J. Chem. Theory Comput.* **2009**, *5*, 2420–2435.

146

(82)   Tsuneda, T.; Hirao, K. Long-Range Correction for Density Functional Theory. *Wiley Interdiscip. Rev. Comput. Mol. Sci.* **2014**, *4*, 375–390.

(83)   Modrzejewski, M.; Rajchel, Ł.; Chalasinski, G.; Szczesniak, M. M. Density-Dependent Onset of the Long-Range Exchange: A Key to Donor-Acceptor Properties. *J. Phys. Chem. A* **2013**, *117*, 11580–11586.

(84)   Materials Suite. Schrödinger, LLC: New York 2018.

(85)   Banks, J. L.; Beard, H. S.; Cao, Y.; Cho, A. E.; Damm, W.; Farid, R.; Felts, A. K.; Halgren, T. A.; Mainz, D. T.; Maple, J. R.; Murphy, R.; Philipp, D. M.; Repasky, M. P.; Zhang, L. Y.; Berne, B. J.; Friesner, R. A.; Gallicchio, E.; Levy, R. M. Integrated Modeling Program, Applied Chemical Theory (IMPACT). *J. Comput. Chem.* **2005**, *26*, 1752–1780.

Chapter 4 – Absolute Templating of M(111) Cluster Surrogates by Galvanic Exchange

4.1   Introduction

The Moche civilization (200 AD, Peru) achieved the plating of gold onto copper artefacts by immersing copper objects in a solution of chloroauric acid,[1] yet unbeknownst to them, this process was governed by the electrochemical differences in these metals. The overall metal replacement involves a metal in a material that reduces another more noble metal additive that acts as an oxidizing agent. When the oxidizing metal interacts with the reducing metal in the material, the metals are exchanged and the newly oxidized metal is released from the material, dissolved and then removed with the solution. While metal replacement by electrochemical differences have been invoked in describing geological processes such as metasomatism,[2] in 1993, Girolami *et al.* first used this approach on thin film copper surfaces.[3]   In their approach, they described chemical vapor deposition that occurred in tandem with redox processes that led to exchange of the copper for the more noble palladium or silver (Figure 4.1). However, the synthetic utility of this electrochemical replacement for nanomaterials was truly realized upon synthesizing new nanostructures.
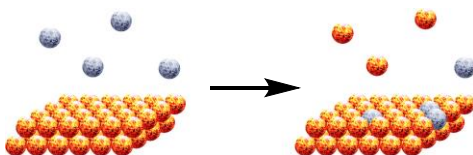
Figure 4.1: A simplified diagram depicting the galvanic exchange on a thin film metal surface involving the electrochemical replacement of a more active metal such as copper (orange dot) for a more noble one such as palladium or silver (grey dot) which demonstrates the difficulty in predicting the extent of exchange *a priori*.

In 2002, Xia *et al.* discovered a technique for silver nanocubes that involved the electrochemical replacement, galvanic exchange, of silver atoms on the surface by gold atoms from a solution of high oxidation state $HAuCl_4$ (Scheme 4.1).[4] After replacing the more reducing silver atoms on the surface of the material, they were able to selectively remove the silver interior which led to hollow gold polyherdra. Markedly, this route led to an incomplete gold shell, but the shell was able to fill in the gaps upon heating

in the presence of excess $HAuCl_4$ thus leading to a highly crystalline structure.[4] Building upon these results, galvanic replacement methodologies were developed that enabled multiple walled tubes of gold and silver alloy.[5] Additionally, techniques were discovered that allowed the voids and wall thicknesses to be controlled by varying the nanomaterial precursor.[6] Interestingly, Mirkin *et al.* was able to demonstrate that the use of a mild reducing agent, ascorbic acid, could engender gold-silver alloy triangular nanoframes.[7] Notably, galvanic exchange used in combination with the Kirkendall effect, differences in the rate of diffusion between two metals at their interface, opened up the synthetic route for the production of polymetallic hollow nanoparticles and displayed that more reactive matter leads to the enhancement of diffusive processes.[8]

$$3Ag(s) \quad + \quad HAuCl_4 \text{ (aq)} \quad \longrightarrow \quad Au(s) \quad + \quad 3AgCl \text{ (aq)} + \quad HCl \text{ (aq)}$$

Scheme 4.1: Overall chemical equation showcasing the electrochemical reaction responsible for switching a silver surface with gold. The standard reduction potential to consider for the exchange involves $Ag+/Ag$ (0.80 V vs SHE) and $AuCl_4^-/Au$ (0.99 V vs SHE).

From these seminal studies, galvanic exchange, has emerged as a powerful tool to control the metal composition, structure, and size of nanomaterials.[9,10] For these materials, the ability to manipulate these physicochemical properties has led to the design of innovative applications such as nanoplasmonics,[11] nanomedicine,[12] electronics,[13] and catalysis.[14] However, these heterogenous observations have led to a poorly understood mechanism by which these processes transpire. Inherently, this lack of mechanistic understanding limits both the ability to predict the outcome beforehand and this technique's broad utility. Therefore, viewing this technology through the lens of atomically precise clusters, a bridge between materials and molecular systems,[15–17] homogenous techniques can be exploited to enable a transition from an observation-driven to a design-driven approach.

4.1.1 Galvanic Exchange in Nanoclusters.

In the 1950s and 1960s,[18] mass spectrometry ions led to the first observable clusters by superatomic expansion at low temperatures.[19] Early work on cluster technology by Chini in 1958 and into the 1960s

involved the formation of higher nuclearity metal carbonyls because of their purported importance in leading to an unexplained product distribution observed in the hydroformylation at low pressures of carbon monoxide.[20] Afterwards, a "gold rush" in clusters came from a discovery by Haruta *et al.* in the late 1980s where gold, often considered an inert metal in catalysis, in combination with metal oxides led to pronounced activity in the oxidation of carbon monoxide and hydrogen.[21,22] While this and relativistic effects have led to a focus on gold nanoclusters, the preparation and isolation of atomically precise nanoclusters have been described for a number of metals featuring structural modularity, uniformity and scalability. Because direct reduction methods are difficult to control and predict *a priori*, the use of well-defined structures of clusters (often confirmed by X-ray crystallography) leads to ideal building blocks and desirable templates for galvanic exchange.

Interestingly, as opposed to nanomaterials such as nanoparticles,[23–29] nanoclusters initially led to anti-galvanic replacement (AGR) — the opposite of galvanic exchange — wherein the more noble nanocluster reduces a more active metal ion based on the electrochemical series. As discovered by Murray *et al.* in 2010, $[Au_{25}(SCH_2CH_2Ph)_{18}]^-$ was found to exchange one to a few atoms of Ag^+, Cu^{2+}, or Pb^{2+} ions in solution.[30] In 2012, Wu showcased and proposed the general concept of AGR in that it hinged on having nanoclusters smaller than 3 nm.[31] This phenomenon was attributed to quantum confinement,[32] the formation of discrete frontier energy levels as opposed to a continuous bandgap, which leads to a decrease in the reducing ability upon smaller metal sizes. Because of the resulting decrease in reducing ability, these nanoclusters could undergo AGR as opposed to larger nanoparticles. Surprisingly, another Au_{25} cluster was incapable of undergoing AGR with the less active Ni, Pd, and Pt but reacted readily with the more active cadmium to generate $Cd_1Au_{24}(SR)_{18}$.[33] This highlights the difficulty in predicting the outcome based on AGR alone. Despite the development and advancement of AGR, the clusters only feature mild reducing capabilities limiting the range of metals that can be exchanged, and typically results in only a few metal atoms that can be exchanged at a time.[34] Furthermore, several different alloying modes are known and new ones are continually being discovered to help explain new reactions outcomes,[35] thus frustrating rational design.

Galvanic exchange, on the other hand, follows the electrochemical series and enables the potential for a greater degree of exchange from a stronger driving force. Additionally, it broadens the variety of metals that can be doped into the nanocluster. While this technique has been well known to occur in nanomaterials, recently it was found to also apply to nanoclusters. This is unsurprising, however, given the dearth of stable active, reducing nanoclusters. In fact, in 2016, immediately following the rare discovery of an active silver nanocluster, $[Ag_{25}(SPhMe_2)_{18}]^-$,[36] Bakr *et al.* used post-synthetic galvanic replacement to exchange one silver atom for gold in the low-valent silver cluster to afford $[Ag_{24}Au(SPhMe_2)_{18}]^-$ which featured enhanced stability over the mother nanocluster (Figure 4.2).[37] This strategy, however, still suffers from several disadvantages.
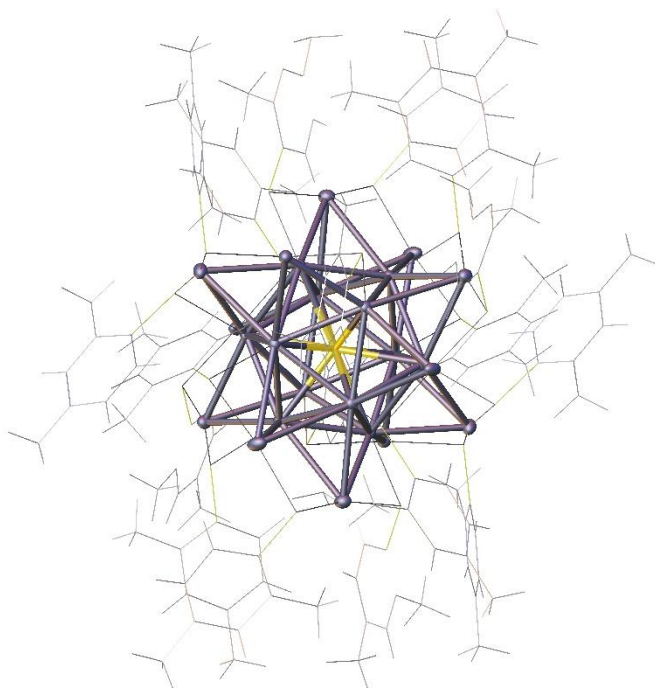
Figure 4.2: The highly active low-valent $[Ag_{25}(SPhMe_2)_{18}]^{-}$[36] was exploited by Baker *et al.* in 2016 to demonstrate galvanic exchange in nanoclusters for the first time to afford $[Ag_{24}Au(SPhMe_2)_{18}]^-$ (X-ray structure above: ligands with a wire frame and cation omitted for clarity).[37]

Aside from rare examples (Scheme 4.2),[38] it is generally accepted that exchanging more than one atom in a nanocluster template is unpredictable *a priori*, and often leads to polydisperse mixtures through scrambling or aggregation.[39,40] To complicate the matter further, the mechanism remains poorly understood,

152

which inherently impairs future developments. Furthermore, a constraint on the use of this process for nanoclusters involves the significant challenge of synthesizing and stabilizing more active metal nanoclusters with M^0 character. Because of the serious limitations of AGR on replacement, we sought to investigate galvanic exchange to help further elucidate the mechanism and expand the scope of this process in nanoclusters. Therefore, we targeted the stabilization of a rare example of an active metal cluster, *i.e.*, copper.

Ultra-small nanoparticles   *Partial templating*

$[Ag_{44}(SR)_{30}]^{4-}$ $[Au_{12}Ag_{32}(SR)_{30}]^{4-}$
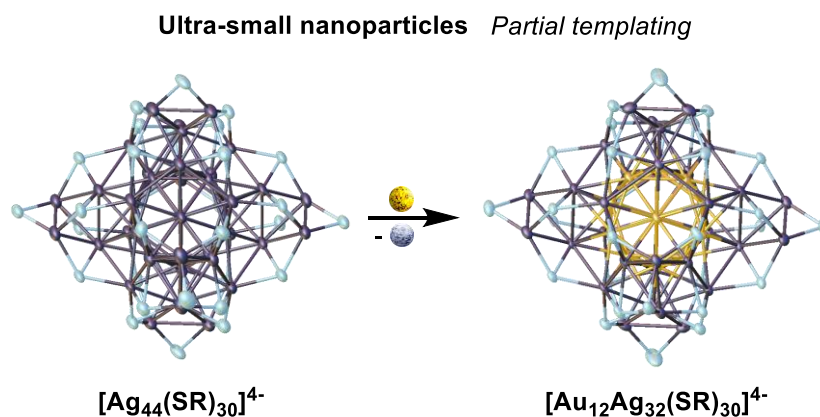
Scheme 4.2: A rare example of multiple atom galvanic exchange in nanoclusters without loss of structural integrity.[38]

4.1.2   Carbenes for the Stabilization of Low Valent Copper Clusters.

As opposed to the well-established field of mixed-valent gold clusters,[41] the lighter congener, copper, is still in its infancy. This stems in part from the low half-cell potential of copper (0.52 V) making it difficult to reduce and stabilize strong Cu^0 character. This challenge is particularly pronounced when compared to the other coinage metal congeners such as silver (0.80 V), and gold (1.69 V).[42] From the difficulty of reduction, the incorporation of Cu^0 into nanoclusters tends to produce ill-defined, polydisperse mixtures. Therefore, the synthesis of copper clusters with Cu^0 character represents a serious synthetic challenge. In a seminal report, Hayton *et al.* synthesized the first copper nanocluster with partial Cu^0 character (Figure 4.3, left).[43] While this copper cluster only featured two Cu^0 centers out of 25 total Cu atoms, the result demonstrated that these clusters are in fact isolable. Subsequently, a handful of other

copper based super atoms that feature the incorporation of Cu^0 centers into clusters has been achieved for variety of sizes (Figure 4.3, middle[44] and right[45]).[46–49] However, the field has been limited to clusters with only minimal Cu^0 character and a sizable amount of Cu^I to stabilize the moieties. The lack of stabilizing ligands has most assuredly stymied progress in incorporating large amounts of Cu^0 character.

$[Cu_{25}H_{22}(PPh_3)_{12}]Cl$ $\qquad$ $[Cu_{13}(S_2CNnBu_2)_6(C_3O_2Me)_4][PF_6]$ $\qquad$ $[Cu_{53}(CF_3COO)_{10}(C=CtBu)_{20}Cl_2H_{18}]^+$
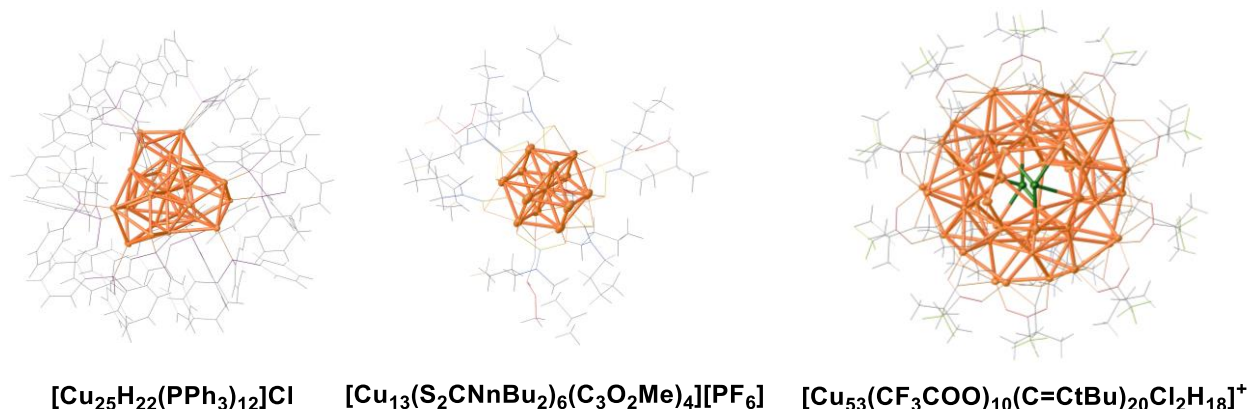
Figure 4.3: (Left) X-ray structure of the first partial Cu^0 nanocluster by Hayton *et al.* in 2015;[43] (middle) the smallest Cu nanocluster with partial (0) character;[44] (right) one of the largest Cu^0 clusters known[45] (all X-ray structures' ligands are with a wire-frame and the anions have been removed for clarity).

Close examination of the literature reveals that thiolate and phosphine type ligands, weakly coordinating ligands prone to undergo redistribution, dominate cluster technology,[50–53] thus making it more difficult to isolate active metal nanoclusters. Recently, carbenes have been shown to strongly bind to metal surfaces and impart significant stabilizing power in materials chemistry.[54–68] In terms of clusters, advances have been predominantly focused on NHCs in stabilizing coordination (*i.e.*, all metals in M^I or greater oxidation state) and metallic (*i.e.*, incorporation of M^0 character) clusters.[69–72] However, the drawback of NHCs extends from their poor Lewis acidity which prevents them from taming more active metallic clusters with larger amounts of M^0 character.

In contrast, CAACs, with strong π-acidity, have led to the stabilization of a slew of transition metals in their formally M^0 (*e.g.*, Fe, Cu, Au, and Mn)[73,74] oxidation state for the first time. Previously, Bertrand *et al.* first demonstrated that CAACs could stabilize metallic nanoclusters upon isolating an air stable trinuclear gold species (**4.1.A**) in 91% yield.[75] This was achieved by reducing the corresponding μ_3-

oxonium (**4.1**) with carbon monoxide, a mild reducing agent, to produce carbon dioxide as a byproduct (Scheme 4.3). Furthermore, as gold typically does not engage in redox catalytic cycles, they demonstrated that the stability imparted from the CAAC ligands enabled an unprecedented Au^0/Au^I catalytic cycle in the carbonylation of cyclohexylamine to the corresponding urea. Therefore, we aimed to exploit CAACs to stabilize a more active metallic cluster, namely copper, to engage in galvanic exchange.
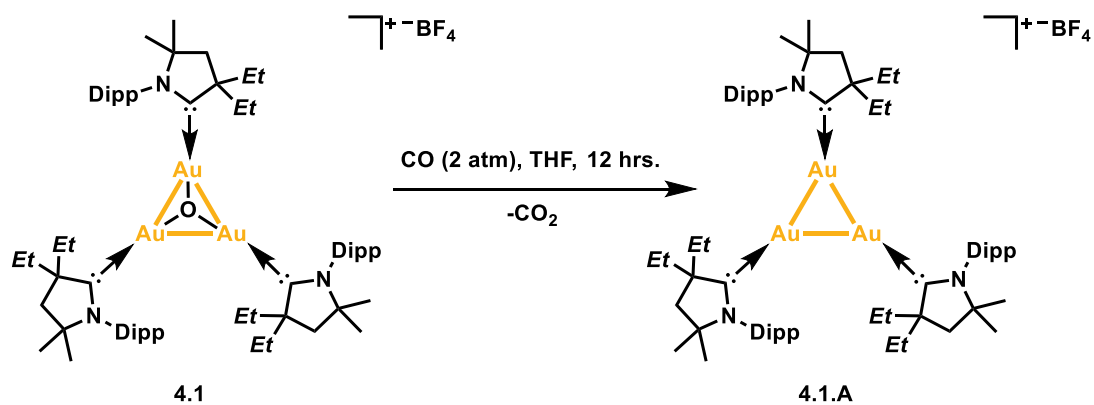
Scheme 4.3: Bertrand *et al.* used the CAAC for the first time to afford an air- and moisture-stable trinuclear mixed-valence Au^0/Au^I cluster.[75]

In this chapter, we report the formation of a mixed valent $Cu^0_2Cu^I$ cluster that features pure Cu-Cu interactions (previous clusters were decorated with X type ligands throughout causing them to be a far cry from the larger nanomaterials and surface chemistry) and predominantly Cu^0 character. We then exploited this high Cu^0 character to achieve the absolute templating — the complete exchange of metals — of group 11 clusters by means of galvanic exchange. This strategy enabled the synthesis of trinuclear mixed-valent $M^0_2M^I$ coinage metal clusters for the entire coinage metal series (Figure 4.4). Upon analyzing these structures *in silico*, we discovered their striking resemblance to M(111) surfaces. Therefore, to further delineate the use of clusters as intermediates between homo- and hetero-geneous systems, we show that these species provide a molecular model for better understanding the reduction of CO_2 at the surface of metals.

155
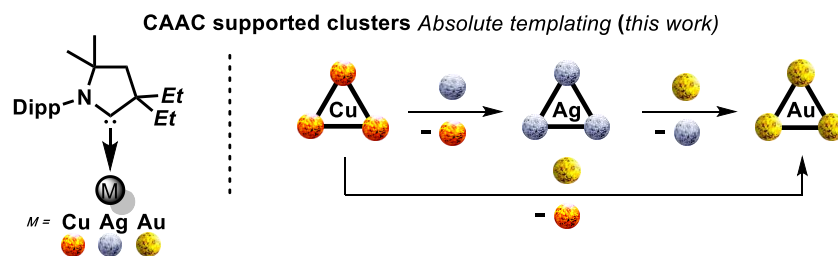
Figure 4.4: Stabilization provided by cyclic (alkyl)(amino)carbenes (CAACs) allows for the absolute templating of trinuclear clusters by galvanic exchange.

4.2   Results & Discussion

Copper, the most reducing out of the coinage metals, should provide an ideal template. To gauge the feasibility of this hypothesis, we evaluated the thermodynamics of exchanging copper for gold in a trinuclear $M^0_2M^I$ clusters with DFT at the M06[76]/def2-tzvpp[77,78] level. From a truncated model, this sequential exchange was confirmed to be exergonic by 27.6 kcal.mol^{-1} (Figure 4.5).
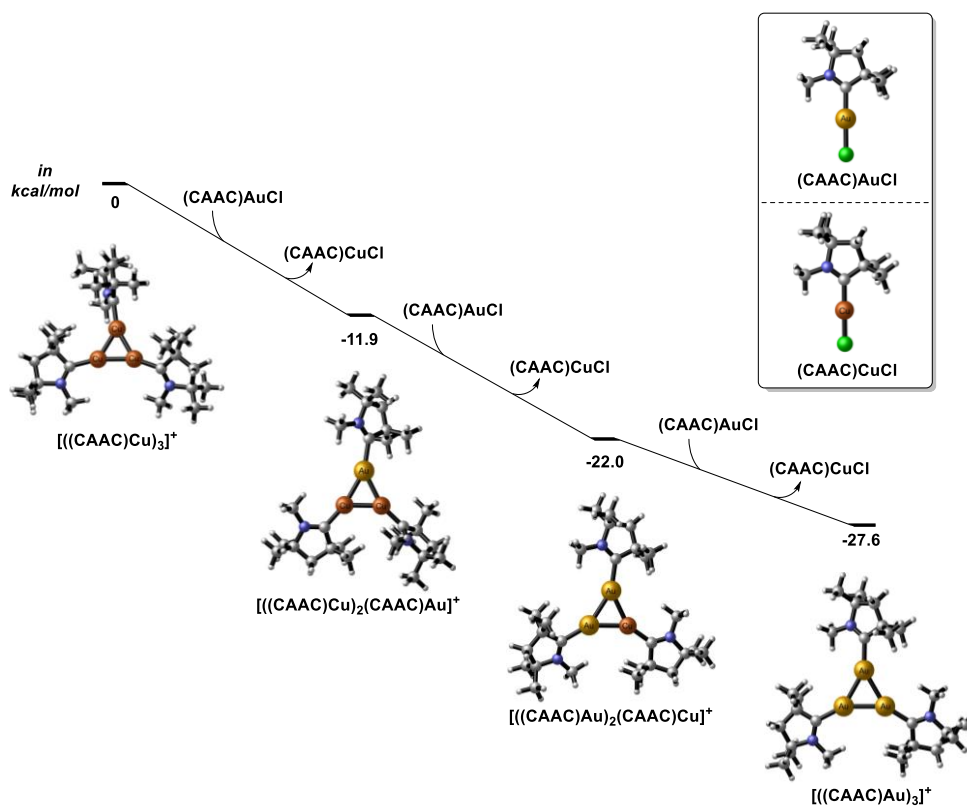
Figure 4.5: Reaction Profile for the exchange between truncated **4.2.A** and (CAAC)AuCl to form **4.1.A**.

156

Encouraged by these results, we set out to prepare the desired $Cu^0_2Cu^I$ cluster, **4.2.A**. Although our group was able to access **4.1** in the past through a salt metathesis with Ag_2O and $NaBF_4$,[75] this pathway was not amenable to access the analogous μ_3-oxo-[Cu(^{Et}CAAC)]$_3$[BF$_4$], **4.2**. Given that *tris*-(triphenylphosphinegold)oxonium salts were accessible from the double deprotonation of water,[79] we sought to exploit a similar strategy but with an easily accessible copper aryl species (*i.e.*, (^{Et}CAAC)CuPh) to act as the metal-base. After abstracting one-third of the phenyl from (^{Et}CAAC)CuPh with triphenyl carbenium tetrafluoroborate to generate the required cationic copper species, the remaining two-thirds of (^{Et}CAAC)CuPh deprotonated water twice to afford the desired **4.2** in 93% yield (Scheme 4.4).
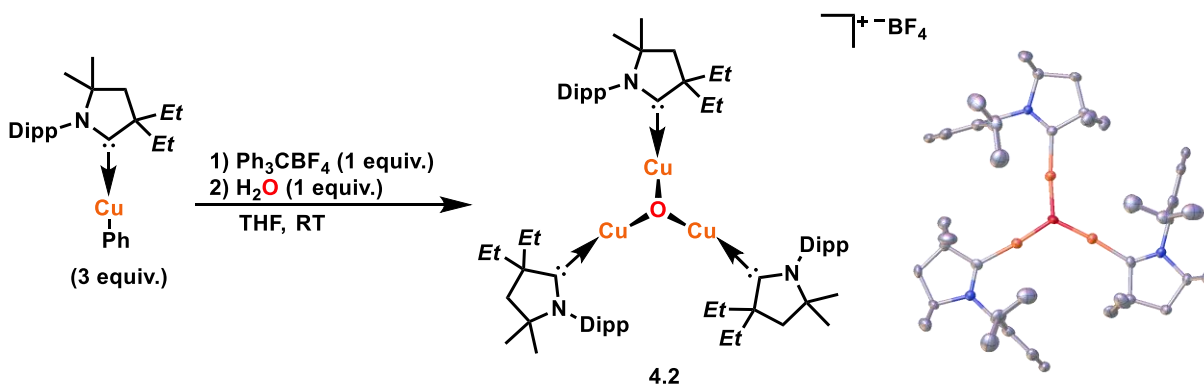
Scheme 4.4: Synthesis of **4.2** (X-ray structure with protons and anion omitted for clarity) from a phenyl abstraction followed by a double deprotonation of water.

With the coordination cluster **4.2** in hand, we then explored the reduction to the mixed-valent $Cu^0_2Cu^I$ metallic cluster. While our previous report highlighted that **4.1** could be reduced in the presence of carbon monoxide, unsurprisingly, the more challenging **4.2** proved immune to this method. Because isocyanide is isolobal but more electron rich than carbon monoxide, presumably, it should have a greater propensity towards acting as a reductant. We tried cyclohexyl isocyanide, but it also did not function as a reducing agent for our system even at elevated temperatures. Additionally, strong reducing agents such as KC_8 gave intractable mixtures. At this point, we had to revise our synthetic strategy. Thus, we turned our attention to boron which forms incredibly strong covalent bonds with oxygen and has been known to act as a reducing agent for oxygen based compounds.[80–82]

We first tried the reduction with pinacol borane, HBPin, in THF at room temperature. After allowing the reaction to occur overnight, brownish-red crystals had formed from the mother liquor. Upon X-ray analysis, these crystals revealed the first example of a carbene copper hydride cluster, [(^{Et}CAAC)$_6$Cu$_{14}$H$_{12}$][BF$_4$]$_2$, **4.2.B** which was isolated in 18% yield (Scheme 4.5). The geometry with respect to copper is a tetrakisdodecahedron and features μ_3-hydrides. This result was particularly surprising given the propensity for carbenes to engender lower nuclearity dimeric copper hydride complexes.[83–88] Interestingly, this cluster is very similar to the previously reported [Cu$_{14}$H$_{12}$(phen)$_6$(PPh$_3$)$_4$][Cl]$_2$ by Hayton *et al.* [89] which will allow for direct comparison of the stability imparted by CAAC ligands.
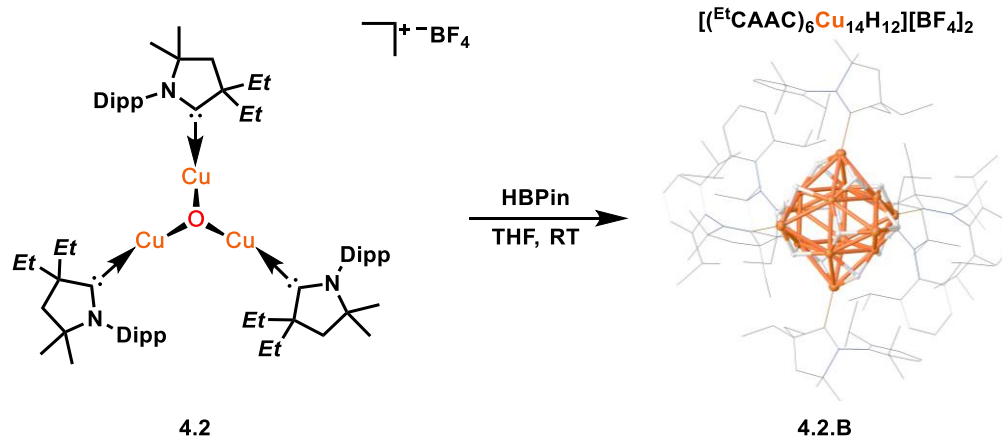
Scheme 4.5: The reduction of **4.2** with HBPin results in the formation of the first (carbene)copper-hydride nanocluster **4.2.B** (X-ray: anions and protons removed for clarity. ^{Et}CAAC ligands in a wireframe).

Since the formation of one B-O bond from HBPin proved to be an insufficient thermodynamic sink for the difficult reduction to Cu$^0_2$Cu^I, we tried bis(neopentyl-glycolato)diboron, B$_2$(Neop)$_2$. Gratifyingly, this diboron reagent at -40 °C reduced **4.2** to afford the Cu$^0_2$Cu^I trinuclear cluster **4.2.A** in excellent yield (72%) (Scheme 4.6). X-ray quality crystals obtained from a THF solution layered with diethyl ether confirmed the structure of **4.2.A** (Figure 4.6, right). Notably, this is the first predominant Cu^0 mixed-valent cluster known and it does not feature any X type ligands stabilizing the cluster such as the typical hydride observed at the center for almost all of the previously reported partial Cu^0 clusters.[49]
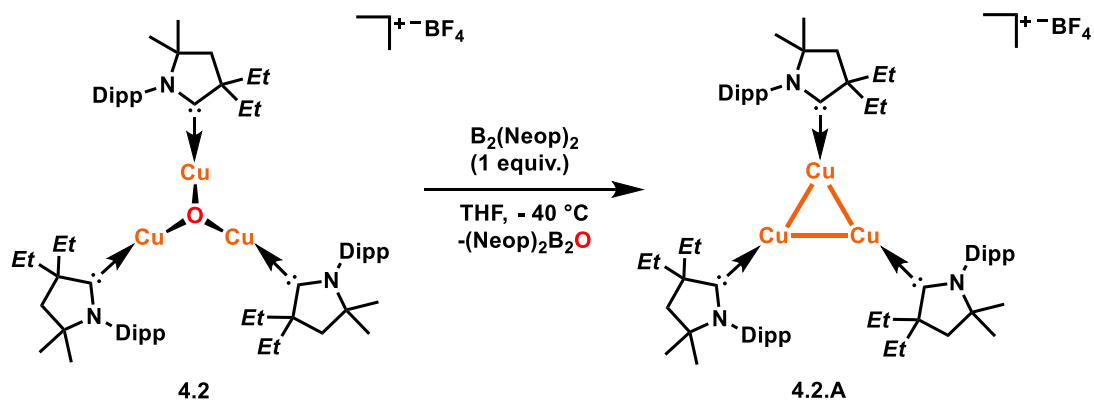
Scheme 4.6: Reduction of **4.2** affords the first predominantly mixed-valent Cu^0 cluster **4.2.A**.

To test our overarching hypothesis that an active cluster such as **4.2.A** can engage in absolute templating, we targeted the previously reported **4.1.A**.[75] Upon reacting three equivalents of (^{Et}CAAC)AuCl, as an electrochemical partner, with **4.2.A**, we observed clean formation of the $Au^0_2Au^I$ trinuclear cluster **4.1.A** which had a characteristic $^{13}C\{^1H\}$ NMR signal for the carbene at 265.8 ppm in THF-d_8. Furthermore, we confirmed the extrusion of (^{Et}CAAC)CuCl by $^{13}C\{^1H\}$ NMR spectroscopy which was removed by washing the solid with diethyl ether thereby leading to the isolation of **4.1.A** in 92% yield. Because of the possibility for a higher order aggregate, we confirmed the formation of **4.1.A** after growing crystals from THF layered with diethyl ether which were characterized by X-ray crystallography (Figure 4.6, left).
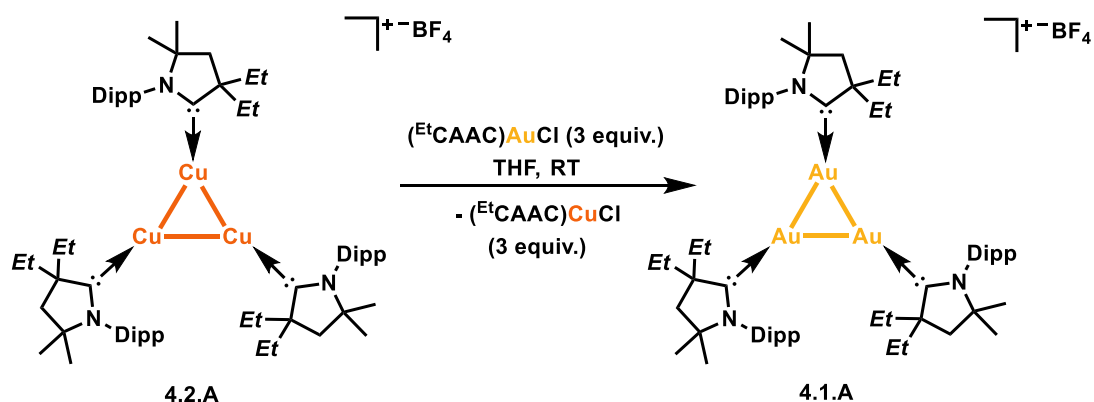
Scheme 4.7: **4.2.A** undergoes galvanic exchange with (^{Et}CAAC)AuCl to afford **4.1.A**.

After successfully confirming this was a viable strategy, we aimed for the electrochemical templating of copper by silver to access the last unknown cluster of the coinage metal series. Unexpectedly, reaction of **4.2.A** with three equivalents of (^{Et}CAAC)AgCl led to rapid plating of silver and the formation of a dark grey precipitate in the reaction vessel. Unfortunately, at -40°C the reaction did not occur at an appreciable rate. To circumvent this problem, we envisaged exploiting the stronger oxophilicity of copper versus silver as a driving force. **4.2.A** cleanly reacted with (^{Et}CAAC)AgOPh to engender **4.3.A** (Scheme 4.8). The new product had two sets of doublets for the carbene carbon in $^{13}C\{^1H\}$ NMR at 258.5 [$^1J(^{107}Ag-^{13}C) = 182.6$ Hz and $^1J(^{109}Ag-^{13}C) = 159.9$ Hz] suggesting the formation of a new silver compound. Of course, we also confirmed the exchange occurred by observing the formation of (^{Et}CAAC)CuOPh by its $^{13}C\{^1H\}$ NMR signals.[90] **4.3.A** was purified by washing with cold diethyl ether and isolated in 63% yield. Due to the subtle variations observed by $^{13}C\{^1H\}$ NMR for the carbene carbon signal for silver complexes, we indisputably confirmed the desired trinuclear **4.3.A** by X-ray crystallography (Figure 4.6, middle).
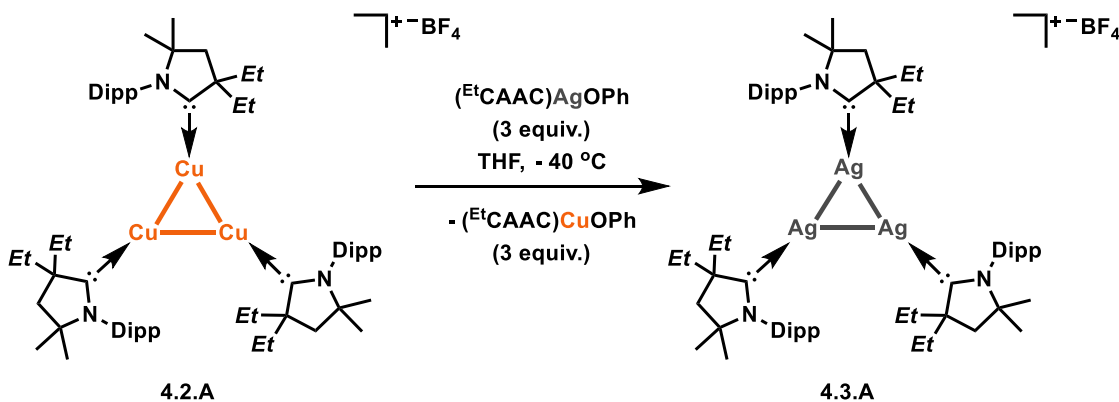
Scheme 4.8: **4.2.A** reacts with (^{Et}CAAC)AgOPh to afford **4.3.A** the last trinuclear mix-valent cluster of the coinage metal series.

Since **4.3.A** represents a rare example of a silver nanocluster with Ag^0 character,[36,45,91–94] a more active metal than gold, we wondered if this cluster could exchange with gold similar to the more active **4.2.A**. Upon reacting **4.3.A** with (^{Et}CAAC)AuCl, we achieved the electrochemical templating from the trinuclear silver to the trinuclear gold **4.1.A** in 39% yield (Scheme 4.9). As opposed to the prevailing

reactivity observed for nanoclusters in participating in AGR, these small trinuclear clusters with high proportions of M^0 exhibit absolute galvanic exchange.
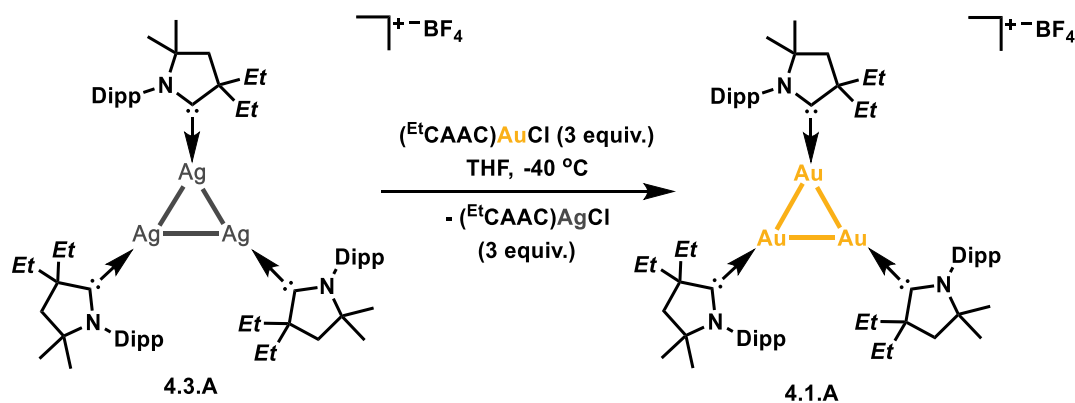
Scheme 4.9: **4.3.A** exchanges with (^{Et}CAAC)AuCl to afford **4.1.A** thus demonstrating that galvanic exchange occurs downstream following the electrochemical series.

In the trinuclear series, only the $Au^0_2Au^1$ has been isolated[69,75] whereas the copper and silver analogues were only studied *in silico*.[95] Structurally, the main difference between the three clusters **4.1.A-4.3.A** lies in the M–M bond distance which follows the order Cu < Au < Ag (Figure 4.6). Although at first glance, the smaller metal-metal bonds for gold, a 3rd row transition metal, over silver, a 2nd row transition metal, seems surprising, but the reduced bond length is the result of the larger relativistic effect for gold compared to that of silver.[96]
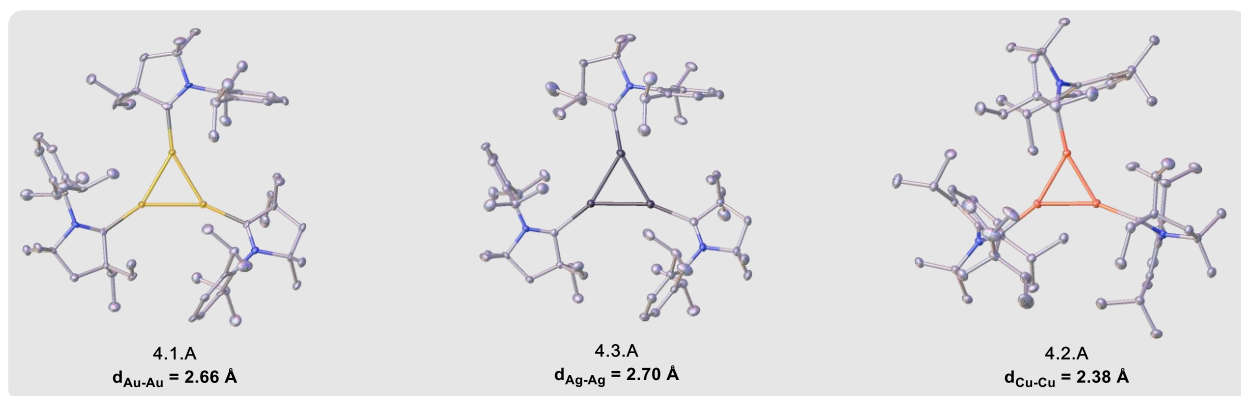
Figure 4.6: X-ray structures of **4.1.A**-**4.3.A** (anions and hydrogens have been omitted for clarity).

At this juncture, we wanted to compare the electronic properties for the trinuclear coinage metal clusters. As noted by Sadighi *et al.*, $Au^0_2Au^I$ clusters, comparable to the H_3^+ ions, are rare examples of σ-aromatic compounds.[69] We confirmed that this is also the case with the trinuclear coinage metal series **4.1.A**-**4.3.A**, and that CAAC ligands do not significantly perturb the electronic structure in these systems. Indeed, topological analysis of the Electron Localization Function (ELF),[97] revealed the typical trisynaptic basin for a three-center two-electron cycle at the orthocenter of the trinuclear metal clusters (Figure 4.7).
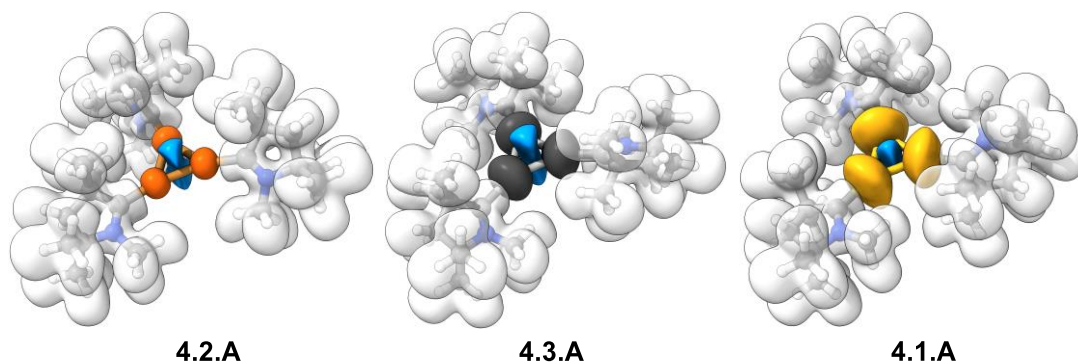
Figure 4.7: The electron localization function (ELF) in **4.1.A-4.3.A** highlights a trisynaptic basin (light blue) of a three-center two-electron cycle.

Additionally, strongly negative values for computed Nuclear Independent Chemical Shift Scan (NICS-Scan)[98] were found at the vicinity of the center and began to approach zero with greater r values from the center (Figure 4.8). Given the negative values, this supports the notion of σ-aromaticity in these species.[95]
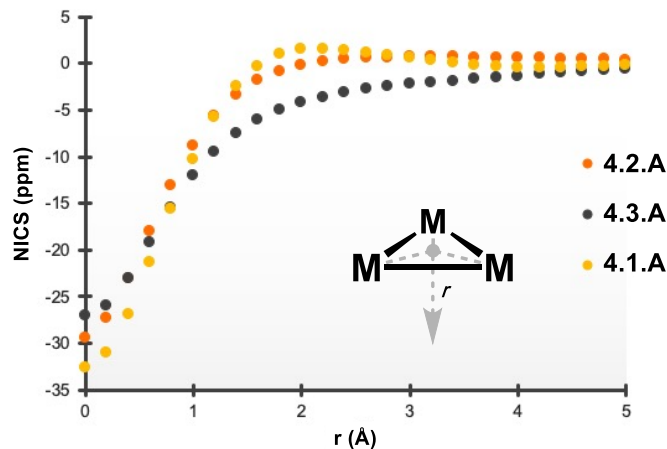
Figure 4.8: The σ-aromaticity in trinuclear **4.1.A** to **4.3.A** is indicated by the NICS scan plots showing large negative values at the ring center, gradually increasing to zero moving away from the ring center.

162

We were also curious to gauge the redox properties of these clusters to compare their reducing capabilities and to better understand the galvanic process. Interestingly, cyclic voltammetry studies of **4.1.A-4.3.A** indicated irreversible reductions at very low potentials (< -2V) and irreversible oxidations above 0.5 V. This suggested that the galvanic replacement is unlikely to occur through an outer sphere reduction pathway, but rather involves an associative addition-elimination type mechanism. This behavior has precedent as trinuclear cationic σ-aromatic clusters have been shown to behave as Lewis bases where the delocalized metal–metal bonds mimic π-aromatics interactions and are thus capable of forming tetranuclear 4-center-2e⁻ clusters with Lewis acidic metal complexes.[99] Through this mechanistic lens, the ambiphilicty of the cluster is essential. The lone pair of the trinuclear cluster, as highlighted in the ELF, nucleophilically attacks a monomeric metal complex which forms a transient, high energy tetranuclear dication. This dication features repulsion between the positively charged centers. Upon eliminating the least electronegative metal center, which is not as strongly tethered to the M^0 character, the cluster relieves the electronic repulsion. Taken together, these considerations support that galvanic templating is presumably occurring incrementally via a transient tetranuclear dicationic alloy cluster, where the least electronegative metal is replaced, and the intermediate trinuclear alloys are formed (Figure 4.9).
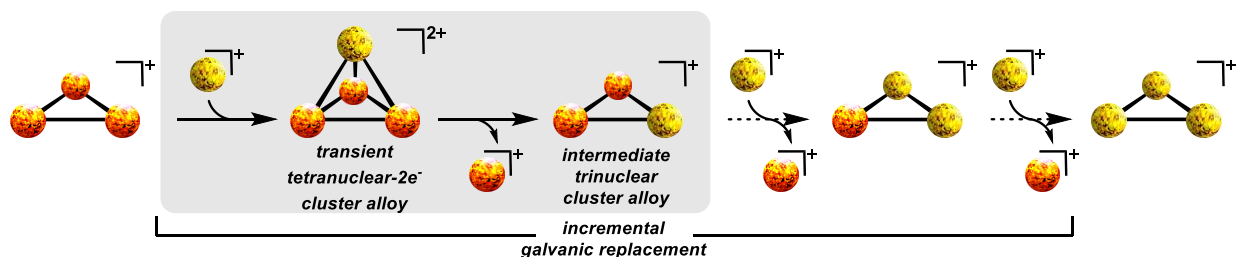
Figure 4.9: The galvanic templating is proposed to involve sequential and incremental galvanic replacement via transient tetranuclear 4-center-2e− clusters.

Since the trinuclear clusters **4.1.A-4.3.A** feature predominantly M^0 character and a triangular geometric arrangement of metals that is reminiscent of a M(111) metal surface, we were curious to compare the two systems. This connection is strengthened by the experimental M-M bond distances and ELF topology in these clusters which closely mirrors those observed in free-standing 2D monolayers (Figure

4.10).[100] Consequently, we were under the impression that these species might provide a molecular platform for understanding the interaction of small molecules with M(111) metal surfaces.[101]
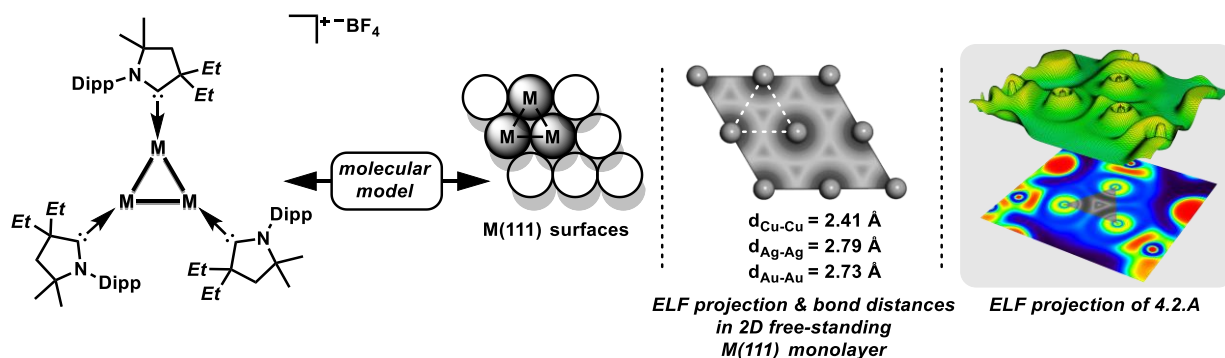
Figure 4.10: M-M bond distances and ELF topology suggest similarities between trinuclear **4.1.A**-**4.3.A** clusters and free standing M(111) monolayers.[100,102,103]

Amongst the various possible small molecules, carbon dioxide was deemed ideal for our comparison because coinage metal nanomaterials in various forms have been well-established to behave as heterogeneous electrocatalysts for the reduction of CO_2 to commodity chemicals and fuels.[104–109] While systems like these have been thoroughly examined, the mechanism of CO_2 electroreduction at these surfaces is still controversial. It has been postulated that charge transfer from the surface to the π^* orbital of CO_2 induces the formation of a bent radical anion ($CO_2^{\bullet-}$), which leads to one of several possibilities: (i) CO_2 dissociation, especially with strong charge transfer ($CO_2 \rightarrow CO + O$), (ii) a transient carboxyl (COOH), or (iii) a formate (HCOO) intermediate.[110,111] To parse out the mechanism for copper, a study that used X-ray photoelectron spectroscopy (APXPS) and high-pressure scanning tunneling microscopy (HPSTM) revealed that there is gradual coverage of atomically adsorbed oxygen on Cu(111) surfaces when under a $CO_{2(g)}$ atmosphere.[112] Notably, a computational study by Han *et al.* highlighted that Cu(111) surfaces facilitated the CO_2 dissociation, but Ag(111) and Au(111) required a higher E_a.[113] To determine if $M^0_2M^I$ (M = Cu, Ag, Au) clusters are molecular surrogates for M(111) surfaces, we screened the reaction of CO_2 (1 atm) with **4.1.A**-**4.3.A**. Strikingly, our results for the coinage metal clusters mirrored the proposed reactivity of coinage metal surfaces based on the previously mentioned computational investigation:[113] no reaction was

observed for gold **4.1.A** nor silver **4.3.A** clusters with CO_2 (Scheme 4.10, bottom). In marked contrast, the copper cluster, **4.2.A**, akin to the Cu(111) surfaces, reacted with 1 equivalent of CO_2 to abstract an oxygen and afforded **4.2** which suggested the formation of carbon monoxide (Scheme 4.10, top). We turned towards ^{13}C labeled carbon dioxide ($^{13}CO_2$) to confirm the formation of carbon monoxide and we were pleased to observe a characteristic signal for ^{13}CO at 185.1 ppm by $^{13}C\{^1H\}$ NMR. Since **4.2** is reduced to **4.2.A** in the presence of a diboron, we investigated a catalytic reduction of CO_2 to CO that relied on $B_2(Neop)_2$ as a stoichiometric reductant for **4.2**. We were pleased to obtain up to 1000 TON (Scheme 4.10, top) at room temperature and confirmed that no reaction occurs between CO_2 and $B_2(Neop)_2$ alone.
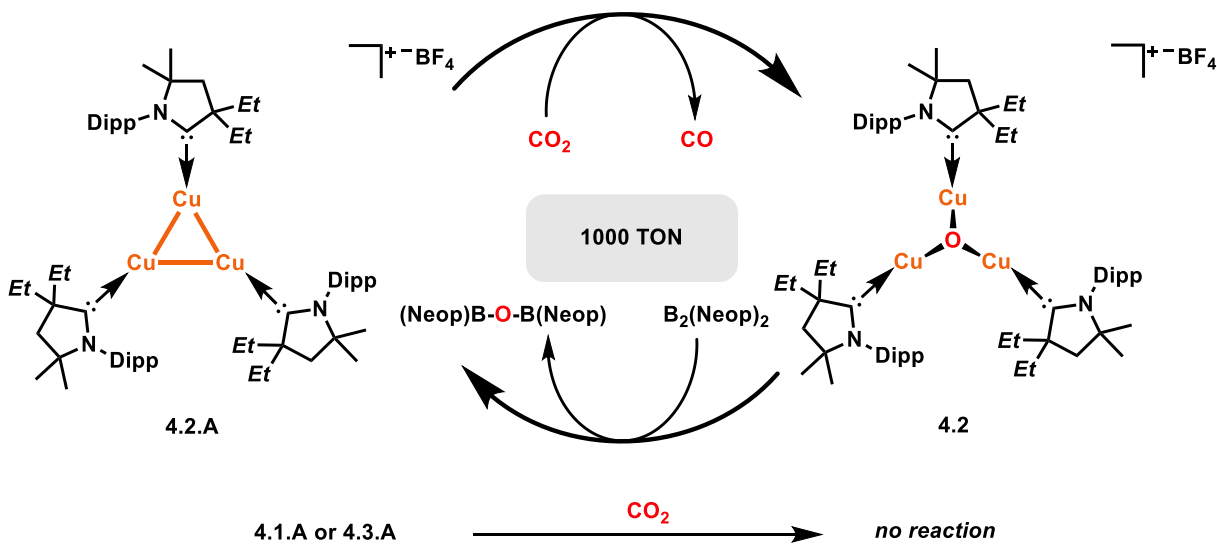
Scheme 4.10: In contrast to the gold and silver equivalent, the trinuclear **4.2.A** promotes the dissociative reduction of CO_2 thereby affording **4.2**. Using bis(neopentyl-glycolato)diboron to regenerate **4.2.A**, up to 1000 TON could be obtained in the reduction of CO_2 to CO.

Our experimental evidence at the molecular level corroborates the existence of a reductive CO_2 dissociation mechanism ($CO_2 \rightarrow CO + O$) by copper surfaces. This process is likely at play in Cu electrodes which are unique in their ability to convert CO_2 into small hydrocarbons (*e.g.*, CH_4, C_2H_4),[114,115] but are known to degrade under catalytic conditions.

4.3 Conclusion

Although anti-galvanic exchange has been the typical route for nanoclusters, we have demonstrated that galvanic exchange is possible for active clusters with a large degree of M^0 character. While galvanic exchange is commonly employed throughout materials chemistry, it often results in major structural changes including differences in metal nuclearity. In contrast, we have systematically applied galvanic exchange to trinuclear complexes of the coinage metals with maintenance of metal nuclearity throughout the series, but by demonstrating the possibility for this metal replacement, we have advanced a connection between homogenous and heterogenous systems. As a result, we were able to isolate exceedingly rare examples of silver and copper clusters with predominantly M^0 character. These clusters have been synthesized in high yields using standard air-free techniques and thus provide a good platform for further study. Additionally, they feature metals in the predominantly zero oxidation state and in triangular arrangements, making them reminiscent of M(111) surfaces. To further the connection between materials and clusters, we showed that the copper cluster **4.2.A** promotes CO_2 reduction, a process commonly observed for Cu(111) surfaces. Additionally, the small size of these clusters allowed for the isolation and characterization of the μ_3-oxo copper complex **4.2**, which has the potential to be occurring on Cu(111) surfaces.[104–109] Our results highlight the mounting impact of π-acidic carbene ligands in materials science and demonstrate that they can remedy the typical drawbacks associated with galvanic replacement.

4.4 Appendix

4.4.1 General Methods & Materials.

All manipulations were performed — unless otherwise noted — under an atmosphere of dry argon using standard Schlenk and glovebox techniques. Benzene, tetrahydrofuran, diethyl ether, n-pentane, and toluene were freshly distilled over Na metal under an atmosphere of argon. Hexanes, dichloromethane, and chloroform were freshly distilled over CaH_2 under an atmosphere of argon. ^{1}H, ^{13}C, ^{19}F, ^{31}P and ^{11}B NMR spectra were recorded on a Varian VX 500 MHz equipped with a 5mm X-Sens cold probe or a Bruker 300

MHz spectrometer. Chemical shifts (δ) are reported in ppm and are referenced to SiMe$_4$ (^{1}H, ^{13}C), CFCl$_3$ (^{19}F), H$_3$PO$_4$ (^{31}P), or BF$_3$·Et$_2$O (^{11}B). Coupling constants J are given in Hertz as positive values regardless of their real individual signs. NMR multiplicities are abbreviated as follows: s = singlet, d = doublet, t = triplet, q = quartet, sept = septet, m = multiplet, br = broad signal. All spectra were obtained at 298 K in the solvent indicated—unless otherwise noted. Electrochemical experiments were carried out with a Biologic SP-300 potentiostat. Ferrocene was used as standard, and all reduction potentials are reported with respect to the E$_{1/2}$ of the Fc/Fc$^+$ redox couple. The UV-Vis spectra were recorded on a Shimadzu UV–3600 UV/vis/NIR spectrometer. Solvent peaks were digitally subtracted from all solution UV-Vis spectra by comparison with an authentic solvent spectrum obtained prior to that of the sample. Melting points were measured with an electrothermal MEL-TEMP apparatus and Mass spectra were performed at the UC San Diego Mass Spectrometry Laboratory on an Agilent 6230 Accurate-Mass TOFMS spectrometer. Single crystal X-ray diffraction data were collected on Bruker Apex diffractometers using Mo-Kα radiation (λ = 0.71073 Å) or Cu-Kα radiation (λ = 1.54178 Å) at the UC San Diego Crystallography Facility. (^{Et}CAAC)CuCl,[116] (^{Et}CAAC)AgCl,[117] and (^{Et}CAAC)AuCl[118] were prepared as reported in the literature, while all other starting materials were either used as received from commercial sources or purified by standard procedures.[119]

4.4.2   Experimental Procedures & Characterization Data.

Reaction of (^{Et}CAAC)CuCl with PhLi to afford (^{Et}CAAC)CuPh.
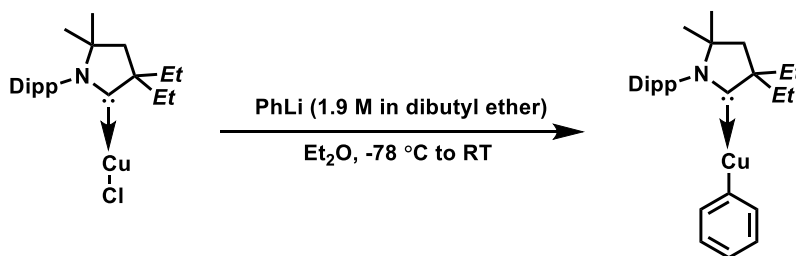
Scheme 4.11: Synthesis of (^{Et}CAAC)CuPh from a salt metathesis of (^{Et}CAAC)CuCl with PhLi.

(^{Et}CAAC)CuCl (5.0 grams, 12.1 mmol) was partially dissolved in diethyl ether (15 mL), stirred, and cooled to -78 °C. Phenyl lithium (6.5 mL, 12.4 mmol, 1.9 M in dibutyl ether) was added dropwise to the stirring solution, and the mixture was warmed to room temperature. After one hour of stirring, the solvent was concentrated to 5 mL under vacuum, filtered off, and the yellow solid was washed with diethyl ether (2x5 mL). Then, any remaining solvent was completely removed under vacuum. The resulting solid was dissolved in dichloromethane (30 mL) and filtered through dry celite to completely remove LiCl. A pale white solid was obtained (4.94 grams, 10.88 mmol, 89.7% yield). **Characterization data: M.P.**: 106-109 °C; **^{1}H NMR** (C$_6$D$_6$, 500 MHz, 298K): δ 7.90 (dd, J = 7.7, 1.5 Hz, 2H), 7.37 (t, J = 7.5 Hz, 2H), 7.23 (tt, J = 7.3, 1.5 Hz, 1H), 7.15 (t, J = 7.8 Hz, 1H), 7.03 (d, J = 7.7 Hz, 2H), 2.83 (sept, J = 6.7 Hz, 2H), 1.77-1.69 (m, 2H), 1.67-1.60 (m, 2H), 1.46 (d, J = 6.7 Hz, 6H), 1.38 (s, 2H), 1.11 (d, J = 6.7 Hz, 6H), 0.99 (t, J = 7.5 Hz, 6H), 0.87 (s, 6H) ppm; **^{13}C{^{1}H} NMR** (C$_6$D$_6$, 125.7 MHz, 298K): δ 256.8, 166.0, 145.5, 141.0, 135.3, 129.7, 126.5, 124.8, 124.5, 79.7, 62.7, 43.4, 31.3, 29.4, 28.8, 27.0, 22.4, 9.8 ppm.

Reaction of (^{Et}CAAC)AgCl with KOPh to afford (^{Et}CAAC)AgOPh.
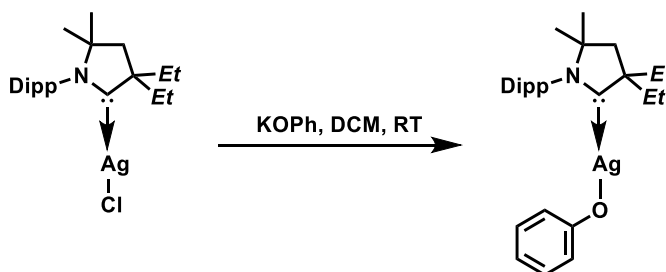
Scheme 4.12: Synthesis of (^{Et}CAAC)AgOPh from a salt metathesis of (^{Et}CAAC)AgCl with KOPh.

(^{Et}CAAC)AgCl (200 mg, 0.438 mmol) and KOPh (61 mg, 0.461 mmol) were dissolved in dichloromethane (5 mL) and stirred for 1 hour. Afterwards, the solution with the precipitate was filtered through dry celite, the solvent was removed under vacuum, and the solid was washed with pentane (3x1 mL) to afford a white solid (212 mg, 93.9% yield). **Characterization data: M.P.**: 137-139 °C; **^{1}H NMR** (THF-d$_8$, 500 MHz, 298K): δ 7.27 (t, J = 7.8 Hz, 2H), 7.20 (d, J = 7.8 Hz, 1H), 7.01 (d, J = 7.8 Hz, 2H), 6.78-6.73 (m, 3H) 2.63 (sept, J = 6.8 Hz, 2H), 1.43-1.35 (m, 2H), 1.33-1.29 (m, 4H), 1.26 (d, J = 6.8 Hz,

6H), 1.04 (d, J = 6.8 Hz, 6H), 0.81 (s, 6H), 0.71 (t, J = 7.5 Hz, 6H) ppm; ^{13}C{^{1}H} NMR (THF-d$_8$, 125.7

MHz, 298K): δ 258.2 (pseudo-dd, $J(^{13}C\text{-}^{107}Ag)$ = 236.2 Hz, $J(^{13}C\text{-}^{109}Ag)$ = 204.1 Hz, C$_{Carbene}$), 171.2, 145.3

(C$_q$), 135.7 (^{107}Ag, C$_q$), 135.6 (^{109}Ag, C$_q$), 130.1 (CH$_{Ar}$), 129.4, 125.4 (CH$_{Ar}$), 120.2, 112.8, 81.8 (^{107}Ag, C$_q$),

81.7 (^{109}Ag, C$_q$), 62.5 (^{107}Ag, C$_q$), 62.5 (^{109}Ag, C$_q$), 41.3 (^{107}Ag, CH$_2$), 41.2 (^{109}Ag, CH$_2$), 30.9 (CH$_2$), 29.3

(CH), 28.9 (CH$_3$), 27.0 (CH$_3$), 22.6 (CH$_3$), 9.5 (CH$_3$) ppm.

Reaction of (^{Et}CAAC)CuPh with trityl $^-$BF$_4$ and H$_2$O to afford 4.2.
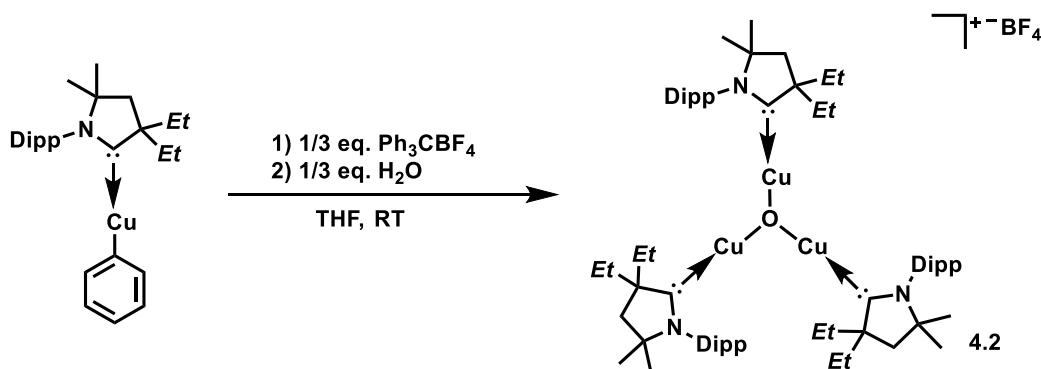
Scheme 4.13: Synthesis of **4.2** from a phenyl abstraction followed by a double deprotonation of water.

(^{Et}CAAC)CuPh (2 grams, 4.40 mmol) and triphenylcarbenium tetrafluoroborate (0.485 g, 1.47

mmol) were added to THF (20 mL) at 0 ℃, warmed to room temperature, and stirred for 30 minutes. Then,

distilled water (26.4 µL, 0.026 g, 1.47 mmol) was added to the mixture and the solution was stirred for 12

hours. Afterwards, the solvent was removed under vacuum and the solid was washed with diethyl ether

(3x20 mL) to give a white powder (1.68 g, 92.7% yield). Crystals for X-ray diffraction were grown at room

temperature from a THF solution layered with diethyl ether. **Characterization data: M.P.**: 207-209 ℃; **^{1}H**

NMR (THF-d$_8$, 500 MHz, 298K): δ 7.43 (t, J = 7.7 Hz, 3H), 7.30 (d, J = 7.8 Hz, 6H), 2.78 (sept, J = 6.5

Hz, 6H), 1.94 (s, 6H), 1.67-1.60 (m, 6H), 1.46-1.39 (m, 6H), 1.27–1.24 (m, 36H), 1.11 (d, J = 6.6 Hz, 18H),

0.95 (t, J = 7.3 Hz, 18H) ppm; ^{13}C{^{1}H} NMR (THF-d$_8$, 125.7 MHz, 298K): δ 251.9 (C$_{Carbene}$), 145.8 (C$_q$),

135.7 (C$_q$), 130.4 (CH$_{Ar}$), 125.3 (CH$_{Ar}$), 82.2 (C$_q$), 63.6 (C$_q$), 41.0 (CH$_2$), 32.4 (CH$_2$), 29.8 (CH), 29.2 (CH$_3$),

28.1 (CH$_3$), 22.3 (CH$_3$), 10.1 (CH$_3$) ppm; ^{19}F NMR (THF-d$_8$, 282 MHz, 298K): δ -154.4 (^{10}B), -154.5 (^{11}B)

ppm; ^{11}B{^{1}H} NMR (THF-d$_8$, 160 MHz, 298K): δ -1.1 ppm; **HRMS (ESI-TOFMS)**: m/z calc. for [C$_{66}$ H$_{105}$Cu$_3$ N$_3$O]$^+$, [M]$^+$, 1144.6140, found 1144.6134.

Attempted Reduction of A with HBpin to afford 4.2.B.
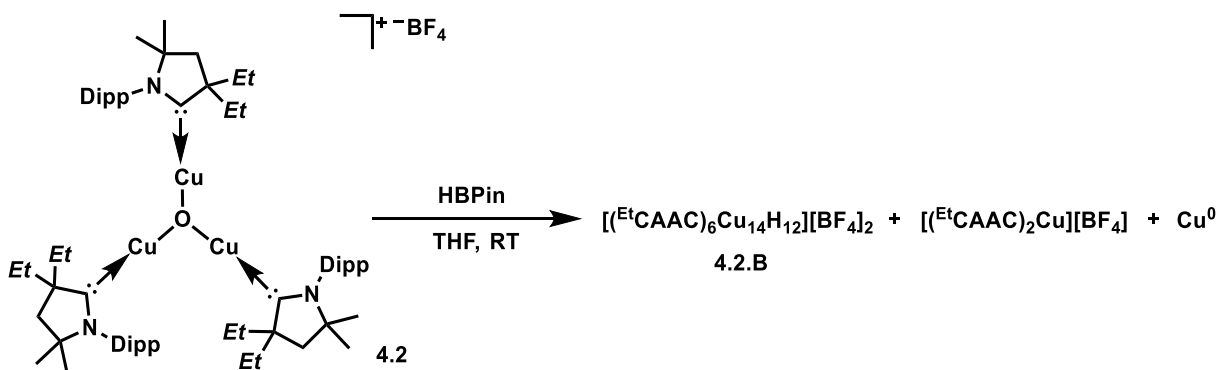
Scheme 4.14: Reduction of **4.2** with HBPin leads to a CAAC copper hydride nanocluster, **4.2.B**.

μ_3-oxo-[Cu(^{Et}CAAC)]$_3$ (0.5 grams, 0.405 mmol) and HBPin were dissolved in THF (2 mL) and left in a standing solution overnight. Afterwards, brownish-red crystals were found at the bottom of the vessel and used for X-ray diffraction. Subsequent purification involved decanting the dark mother liquor and washing the crystals with THF (3x3 mL) to give a dark reddish brown crystalline solid (0.065 grams, 17.6 % yield). **Characterization data: ^{1}H NMR** (CD$_2$Cl$_2$, 300 MHz, 298K): δ 7.39 (t, *J* = 7.5 Hz, 6H), 7.21 (d, *J* = 7.5 Hz, 12H), 2.74 (br m, 12H), 2.48 (br s, 12 H, Cu-H), 1.98–1.82 (br m, 12H), 1.57 (br m, 24H), 1.27 (br m, 36H), 1.18 (br s, 36H), 1.10-0.75 (br m, 72H) ppm; ^{13}C{^{1}H} NMR (CD$_2$Cl$_2$, 125.7 MHz, 298K): δ 260.2 (C$_{Carbene}$), 145.5 (C$_q$), 135.5 (C$_q$), 129.9 (CH$_{Ar}$), 124.6 (CH$_{Ar}$), 82.6 (C$_q$), 66.1 (C$_q$), 39.8 (CH$_2$), 33.1 (CH$_2$), 29.9 (CH), 29.4 (CH$_3$), 29.3 (CH$_3$), 22.3 (CH$_3$), 10.9 (CH$_3$) ppm; ^{19}F NMR (CD$_2$Cl$_2$, 282 MHz, 298K): δ -154.5 (^{10}B), -154.6 (^{11}B) ppm; ^{11}B{^{1}H} NMR (CD$_2$Cl$_2$, 160 MHz, 298K): δ -1.1 ppm.

170

Absolute Galvanic exchange of 4.2 with diboron to afford 4.2.A.
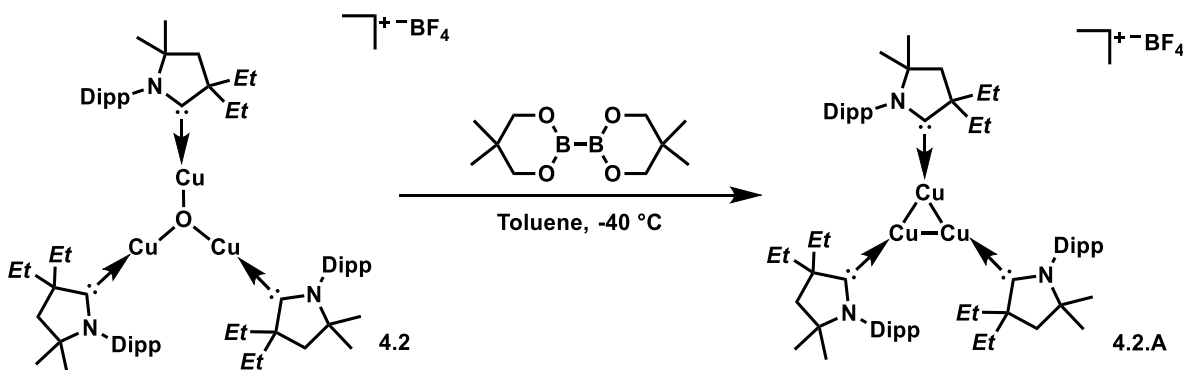
Scheme 4.15: Synthesis of **4.2.A** from the reduction of **4.2** with bis(neopentyl glycolato)diboron.

μ_3-oxo-[Cu(^{Et}CAAC)]$_3$ (5.0 grams, 4.05 mmol) was dissolved in toluene (30 mL) (note reaction works in THF, but not as cleanly) and cooled to -40 °C. Bis(neopentyl glycolato)diboron (0.915 grams, 4.05 mmol) was added to the solution and kept at -40 °C for 12 hours. Afterwards, the solution was warmed to room temperature, the dark mother liquor was filtered off, and the crystals were washed with toluene (3x3 mL). The crystals were then collected, dissolved in THF (5 mL) at -40 °C, and layered with toluene to recrystallize again at -40 °C. The resulting solid was washed with toluene (3x3 mL) to give a dark yellow crystalline solid (3.55 grams, 71.9% yield). Crystals for X-ray diffraction were grown at room temperature from a THF solution layered with diethyl ether. **Characterization data: M.P.**: 98-100 °C (Dec. to brown solid); **^{1}H NMR** (THF-d$_8$, 300 MHz, 298K): δ 7.35 (t, J = 7.5 Hz, 3H), 7.21 (d, J = 7.5 Hz, 6H), 2.67 (sept, J = 6.6 Hz, 6H), 2.02–1.95 (m, 6H), 1.90 (s, 6H), 1.66–1.58 (m, 6H), 1.23–1.20 (m, 36H), 1.09 (t, J = 7.4 Hz, 18H), 0.77 (d, J = 6.6 Hz, 18H) ppm; **^{13}C{^{1}H} NMR** (THF-d$_8$, 125.7 MHz, 298K): δ 252.7 (C$_{Carbene}$), 146.1 (C$_q$), 135.4 (C$_q$), 130.1 (CH$_{Ar}$), 125.1 (CH$_{Ar}$), 81.8 (C$_q$), 64.4 (C$_q$), 43.0 (CH$_2$), 31.9 (CH$_2$), 29.9 (CH), 29.2 (CH$_3$), 28.6 (CH$_3$), 22.0 (CH$_3$), 9.9 (CH$_3$) ppm; **^{19}F NMR** (THF-d$_8$, 282 MHz, 298K): δ -154.5 (^{10}B), -154.6 (^{11}B) ppm; **^{11}B{^{1}H} NMR** (THF-d$_8$, 160 MHz, 298K): δ -1.1 ppm.

Absolute Galvanic exchange of 4.2.A with (^{Et}CAAC)AuCl to afford 4.1.A.
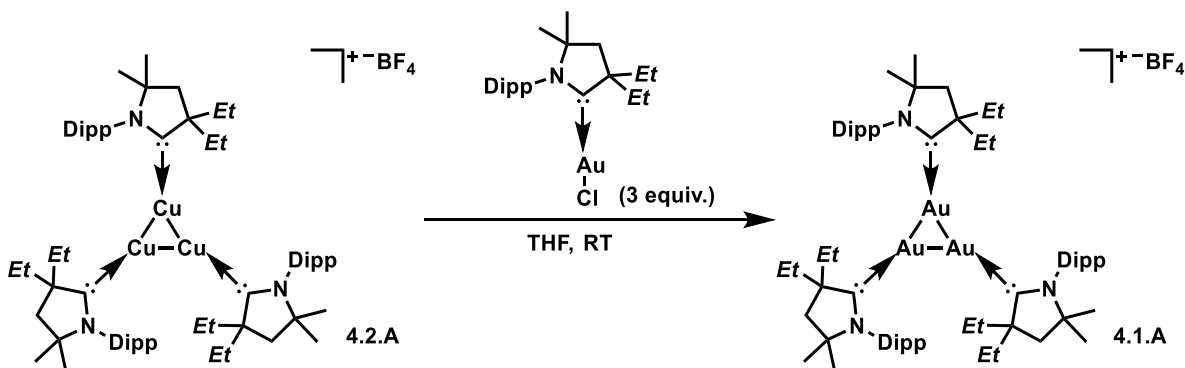
Scheme 4.16: Synthesis of **4.1.A** from the galvanic exchange of **4.2.A** with (^{Et}CAAC)AuCl.

(^{Et}CAAC)AuCl (270 mg, 0.493 mmol) and [((^{Et}CAAC)Cu)$_3$][BF$_4$] (200 mg, 0.164 mmol) were dissolved in THF (5 mL) and stirred for 2 hour. Afterwards, the solvent was completely removed under vacuum and the solid was washed with diethyl ether (3x10 mL) to give a pale white precipitate (245 mg, 92.2 % yield). To definitively confirm **4.1.A** beyond NMR analysis,[75] crystals were grown from THF layered with diethyl ether. **Characterization data: ^{1}H NMR** (THF-d$_8$, 500 MHz, 298K): δ 7.42 (t, J = 7.8 Hz, 3H), 7.28 (d, J = 7.8 Hz, 6H), 2.78 (sept, J = 6.6 Hz, 6H), 1.99 (s, 6H), 1.62-1.57 (m, 6H), 1.46-1.40 (m, 6H), 1.27–1.25 (m, 36H), 1.19 (d, J = 6.6 Hz, 18H), 0.93 (t, J = 7.3 Hz, 18H) ppm; ^{13}C{^{1}H} **NMR** (THF-d$_8$, 125.7 MHz, 298K): δ 265.8 (C$_{Carbene}$), 145.8 (C$_q$), 135.0 (C$_q$), 130.4 (CH$_{Ar}$), 125.4 (CH$_{Ar}$), 82.7 (C$_q$), 64.4 (C$_q$), 42.0 (CH$_2$), 32.4 (CH$_2$), 30.0 (CH), 29.1 (CH$_3$), 28.5 (CH$_3$), 22.6 (CH$_3$), 10.1 (CH$_3$) ppm; ^{19}**F NMR** (THF-d$_8$, 282 MHz, 298K): δ -154.6 (^{10}B), -154.6 (^{11}B) ppm; ^{11}**B{^{1}H} NMR** (THF-d$_8$, 160 MHz, 298K): δ -1.1 ppm.

Absolute Galvanic exchange of 4.2.A with (EtCAAC)AgOPh to afford 4.3.A.
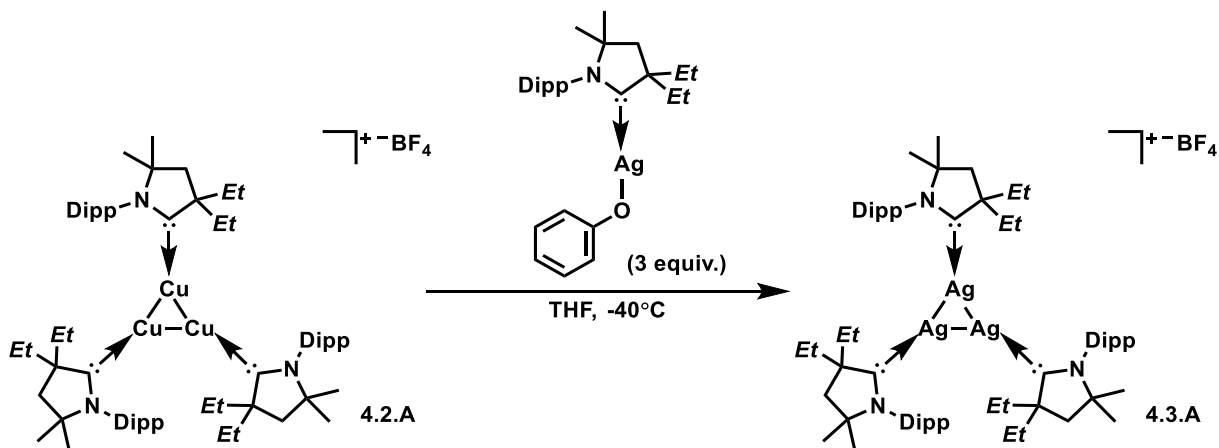
Scheme 4.17: Synthesis of **4.3.A** from the galvanic exchange of **4.2.A** with (EtCAAC)AgOPh.

(EtCAAC)AgOPh (200 mg, 0.389 mmol) and [((EtCAAC)Cu)$_3$][BF$_4$] (156 mg, 0.128 mmol) were dissolved in THF (2 mL) at -40 °C and stirred for 12 hours at this temperature. Afterwards, the solution was layered with hexanes and left at -40 °C. Upon crystallization, the solvent was decanted, and the crystals were washed with diethyl ether (3x5mL) at -40 °C to give a pale white powder (109 mg, 63.0 % yield). Crystals for X-ray diffraction were grown from a THF solution layered with hexanes at -40 °C. (N.B. **4.3.A** decomposes rapidly in solution at room temperature). **Characterization data: ^{1}H NMR** (THF-d$_8$, 500 MHz, 278K): δ 7.41 (t, J = 7.7 Hz, 3H), 7.30 (d, J = 7.7 Hz, 6H), 2.77 (sept, J = 6.6 Hz, 6H), 2.08 (s, 6H), 1.78-1.70 (m, 6H), 1.59-1.53 (m, 6H), 1.37 (s, 18H), 1.25 (d, J = 6.7 Hz 18H), 0.96 (t, J = 7.4 Hz, 18H), 0.87 (br, 18H) ppm; **^{13}C{^{1}H} NMR** (THF-d$_8$, 125.7 MHz, 278K): δ 258.5 (pseudo-dd, $J(^{13}C\text{-}^{107}Ag)$ = 182.6 Hz, $J(^{13}C\text{-}^{109}Ag)$ = 159.9 Hz, C$_{\text{Carbene}}$), 145.6 (C$_q$), 136.0 (C$_q$), 130.8 (CH$_{\text{Ar}}$), 126.0 (CH$_{\text{Ar}}$), 85.1 (^{107}Ag, C$_q$), 85.0 (^{109}Ag, C$_q$), 64.6 (^{107}Ag, C$_q$), (64.5 (^{109}Ag, C$_q$), 40.5 (CH$_2$), 32.1 (CH$_2$), 29.8 (CH), 29.4 (CH$_3$), 28.0 (CH$_3$), 22.6 (CH$_3$), 10.0 (CH$_3$) ppm; **^{19}F NMR** (THF-d$_8$, 282 MHz, 278K): δ -153.3 (^{10}B), -153.4 (^{11}B) ppm; **^{11}B{^{1}H} NMR** (THF-d$_8$, 160 MHz, 278K): δ -1.2 ppm.

Absolute Galvanic exchange of 4.3.A with (ᴱᵗCAAC)AuCl to afford 4.1.A.
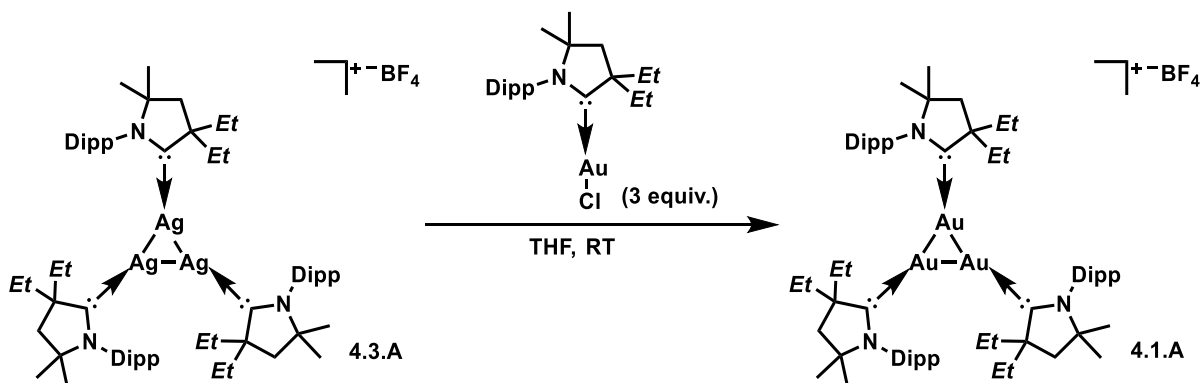
Scheme 4.18: Synthesis of **4.1.A** from the galvanic exchange of **4.3.A** with (ᴱᵗCAAC)AuCl.

(ᴱᵗCAAC)AuCl (122 mg, 0.223mmol) and [(((ᴱᵗCAAC)Ag)₃][BF₄] (100 mg, 0.0740 mmol) were dissolved in THF (mL) at -40 °C, stirred for 15 minutes, warmed to room temperature, and stirred for 1 hour. Afterwards, the solvent was removed under vacuum and the solid was washed with diethyl ether (3x5 mL) to give a pale white precipitate (47 mg, 39.2% yield). **Characterization data:** *Vide Supra.*

Exploration of coinage metal cluster's reactivity with carbon dioxide.
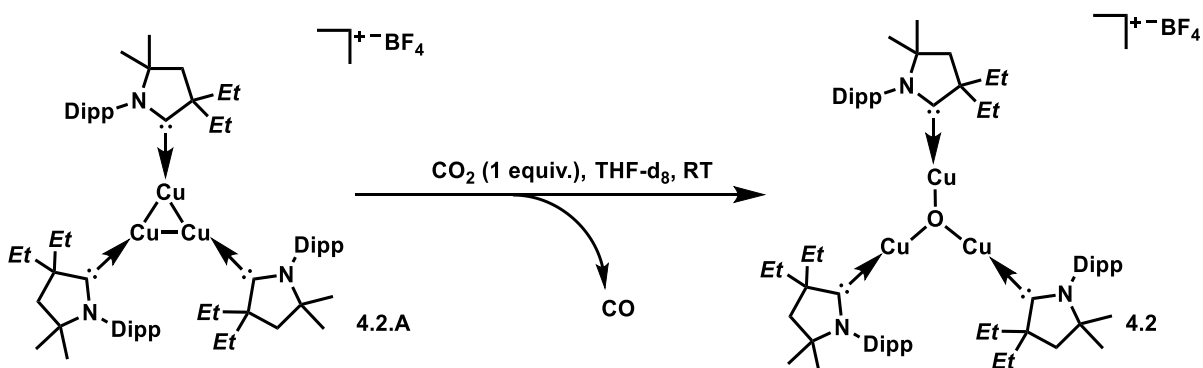
Scheme 4.19: Reaction of **4.2.A** with CO_2 affords **4.2** and CO.

In a J. Young tube, **4.2.A** (50 mg, 0.0246 mmol) was dissolved in THF-d$_8$. Subsequently, CO_2 (1 equiv.) was slowly bubbled through the solution. After 12 hours, the mixture was analyzed by $^{13}C\{^1H\}$ NMR.
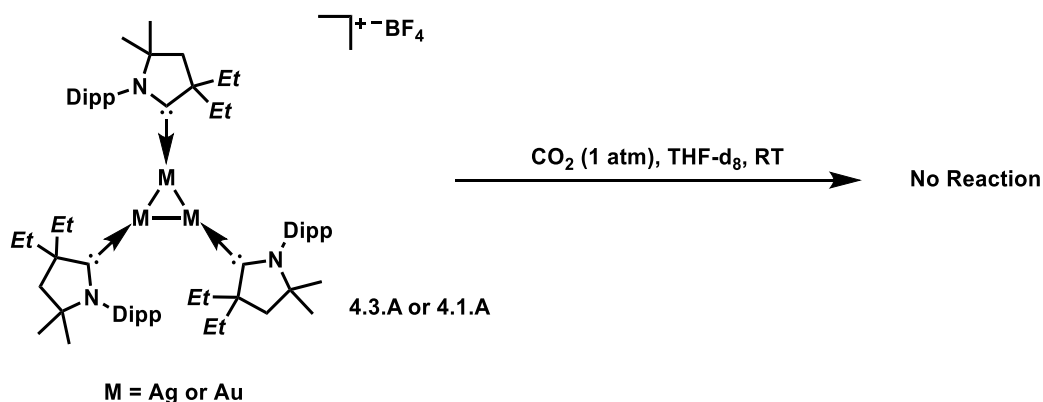
Scheme 4.20: No reaction was observed with **4.3.A** or **4.1.A** under CO_2 (1 atm).

In a J. Young tube, **4.3.A** or **4.1.A** (0.0246 mmol) was dissolved in THF-d_8 at -40 °C. Subsequently, the mixture underwent 3 cycles of freeze-pump-thaw, and CO_2 (1 atm.) was introduced into the tube while still cold. Afterwards, the solution was warmed to room temperature and despite being monitored for 24 hours by $^{13}C\{^1H\}$ NMR, still no reaction was observed for either complex (N.B. **4.3.A** begins to decompose when warmed to room temperature).

Isotopic labeling study (^{13}C) to elucidate products from reduction of $^{13}CO_2$.
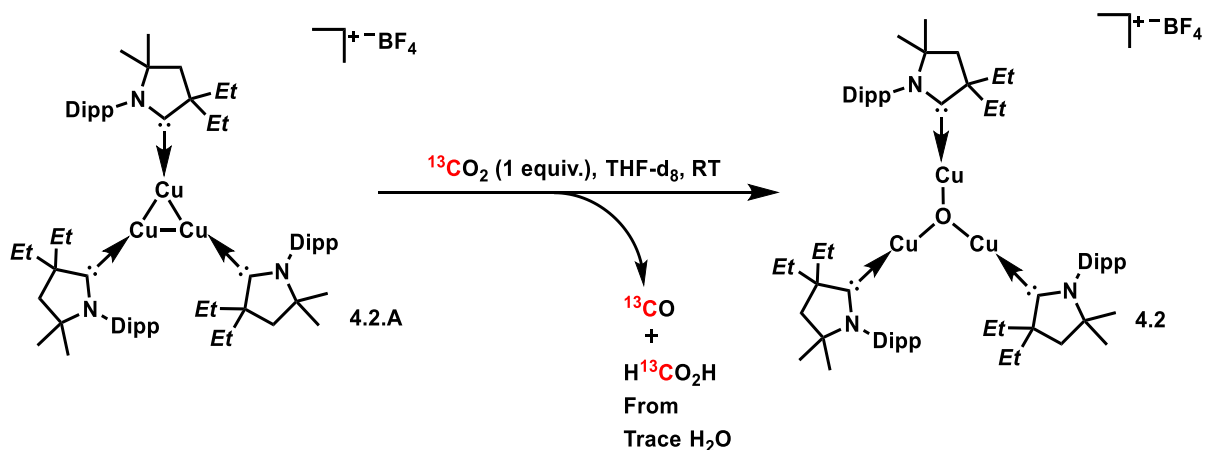
Scheme 4.21: Elucidation of products formed from $^{13}CO_2$ reduction with **4.2.A**.

In a J. Young tube, [((^{Et}CAAC)Cu)$_3$][BF$_4$] (50 mg, 0.0246 mmol) was dissolved in THF-d$_8$ (1 mL). After 3 cycles of freeze-pump-thaw, the degassed solution was then sealed under ^{13}CO$_2$ (1 atm) at room temperature. After sitting for 12 hours, a ^{13}C{^{1}H} NMR was taken to conclusively reveal the products of the reaction. **Characterization data for Important Products: ^{13}C{^{1}H} NMR** (THF-d$_8$, 125.7 MHz, 298K): 185.1 (^{13}CO), 166.8 (H^{13}CO$_2$H from adventitious water) ppm.

Catalytic reduction of CO$_2$
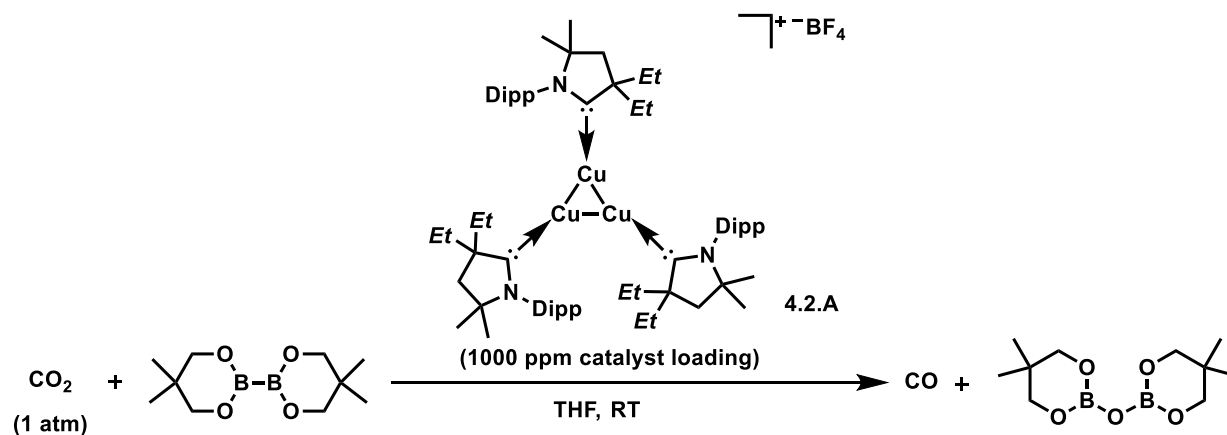
Scheme 4.22: Catalytic reduction of CO$_2$ with **4.2.A** and diboron to engender CO.

Procedure A: To confirm the generation of CO under catalytic conditions, we conducted the catalysis in a heavy wall J. Young tube. **4.2.A** (10 mg, 8.2 μmol) and bis(neopentyl glycolato)diboron (185.5 mg, 0.82 mmol) were added to the tube and dissolved in THF-d$_8$ (0.5 mL). Then, the tube underwent 3 cycles of freeze-pump-thaw, CO$_2$ (1 atm) was introduced at room temperature, and the tube was sealed. After 72 hours transpired, the production of CO was confirmed by ^{13}C{^{1}H} NMR analysis. **Characterization data for important products: ^{13}C{^{1}H} NMR** (THF-d$_8$, 125.7 MHz, 298K): 185.1 (CO) ppm.

Procedure B: In a 250 mL Pressure Schlenk, **4.2.A** (20 mg, 16.4 μmol) and bis(neopentyl glycolato)diboron (371 mg, 1.64 mmol) were partially dissolved in THF (2 mL). The pressure Schlenk then underwent 3 cycles of freeze-pump-thaw and was sealed under CO$_2$ (1 atm) atmosphere at room temperature. After stirring for 5 days, the tube was degassed and a ^{11}B{^{1}H} NMR was taken of the THF

solution (N.B. bis(neopentyl glycolato)diboron starting material appears at 28.4 ppm in $^{11}B\{^1H\}$ NMR)[120] to confirm the completion of the reaction. Afterwards, the solvent was removed under vacuum and the solid material was then completely dissolved in $CDCl_3$ (3 mL). The yield was determined by ^1H NMR through the integration of the bis(neopentyl glycolato)diboron starting material[120] vs. the 2,2'-oxybis[5,5-dimethyl-1,3,2-dioxaborinane] product. **Isolation of 2,2'-oxybis[5,5-dimethyl-1,3,2-dioxaborinane]**: After conducting Procedure B, the solvent was completely removed under vacuum. Subsequently, the oxidized diboron species was extracted with pentane (3x30 mL). After removing the solvent under vacuum, a white powder was obtained (386 mg, 97.2% yield). **Characterization data: ^1H NMR** ($CDCl_3$, 300 MHz, 278K): δ 3.65 (s, 8H), 0.98 (s, 12H) ppm; **$^{13}C\{^1H\}$ NMR** ($CDCl_3$, 125.7 MHz, 298K): δ 73.1, 31.8, 21.7 ppm; **$^{11}B\{^1H\}$ NMR** ($CDCl_3$, 160 MHz, 298K): δ 17.5 ppm.
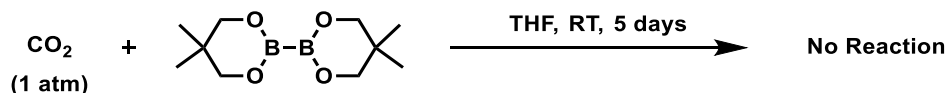
Scheme 4.23: Control experiment of bis(neopentyl glycolato)diboron in the presence of CO2.

Control Experiment: Although tetraalkoxydiboron based reagents have not been reported to reduce CO_2 without the presence of a catalyst,[82] we confirmed that bis(neopentyl glycolato)diboron does not react. In a J. Young tube, bis(neopentyl glycolato)diboron (50 mg, 0.221 mmol) was dissolved in THF-d_8. After a $^{13}C\{^1H\}$ NMR was taken, the tube underwent 3 cycles of freeze-pump-thaw. Subsequently, CO_2 (1 atm) was introduced into the tube at room temperature. Even after 5 days at room temperature, there was still no reaction.

4.4.3 Crystallographic Structure Determinations.

Single-crystal X-ray structure determinations were carried out at low temperature on a Bruker P4 Platform, or a Kappa diffractometer equipped with a Mo (λ = 0.71073 Å) radiation source and a Bruker APEX detector. Crystals were selected under oil, mounted on nylon loops, then immediately placed in a cold stream of nitrogen. All structures were solved by direct methods with SIR 2004 or SHELXS and

refined by full-matrix least-squares procedures utilizing SHELXL[121] within the Olex 2 small-molecule solution, refinement, and analysis software package.[122]

Crystallographic data for 4.2.

Table 4.1: Crystal data and structure refinement for **4.2**.

CCDC identification code	**4.2**
Empirical formula	$C_{66}H_{105}BCu_3F_4N_3O$
Formula weight	1233.95
Temperature/K	100.0
Crystal system	monoclinic
Space group	$P2_1/c$
a/Å	9.721(3)
b/Å	26.661(9)
c/Å	25.627(8)
α/°	90
β/°	99.950(10)
γ/°	90
Volume/Å^3	6542(4)
Z	4
$\rho_{calc}g/cm^3$	1.253
μ/mm^{-1}	1.019
F(000)	2632.0
Crystal size/mm^3	$0.26 \times 0.23 \times 0.1$
Radiation	MoKα (λ = 0.71073)
2Θ range for data collection/°	2.222 to 50.752
Index ranges	-11 ≤ h ≤ 11, -27 ≤ k ≤ 32, -26 ≤ l ≤ 30
Reflections collected	22462
Independent reflections	11619 [R_{int} = 0.0284, R_{sigma} = 0.0494]
Data/restraints/parameters	11619/79/773
Goodness-of-fit on F^2	1.038
Final R indexes [I>=2σ (I)]	R_1 = 0.0523, wR_2 = 0.1125
Final R indexes [all data]	R_1 = 0.0728, wR_2 = 0.1206
Largest diff. peak/hole / e Å^{-3}	1.56/-0.52
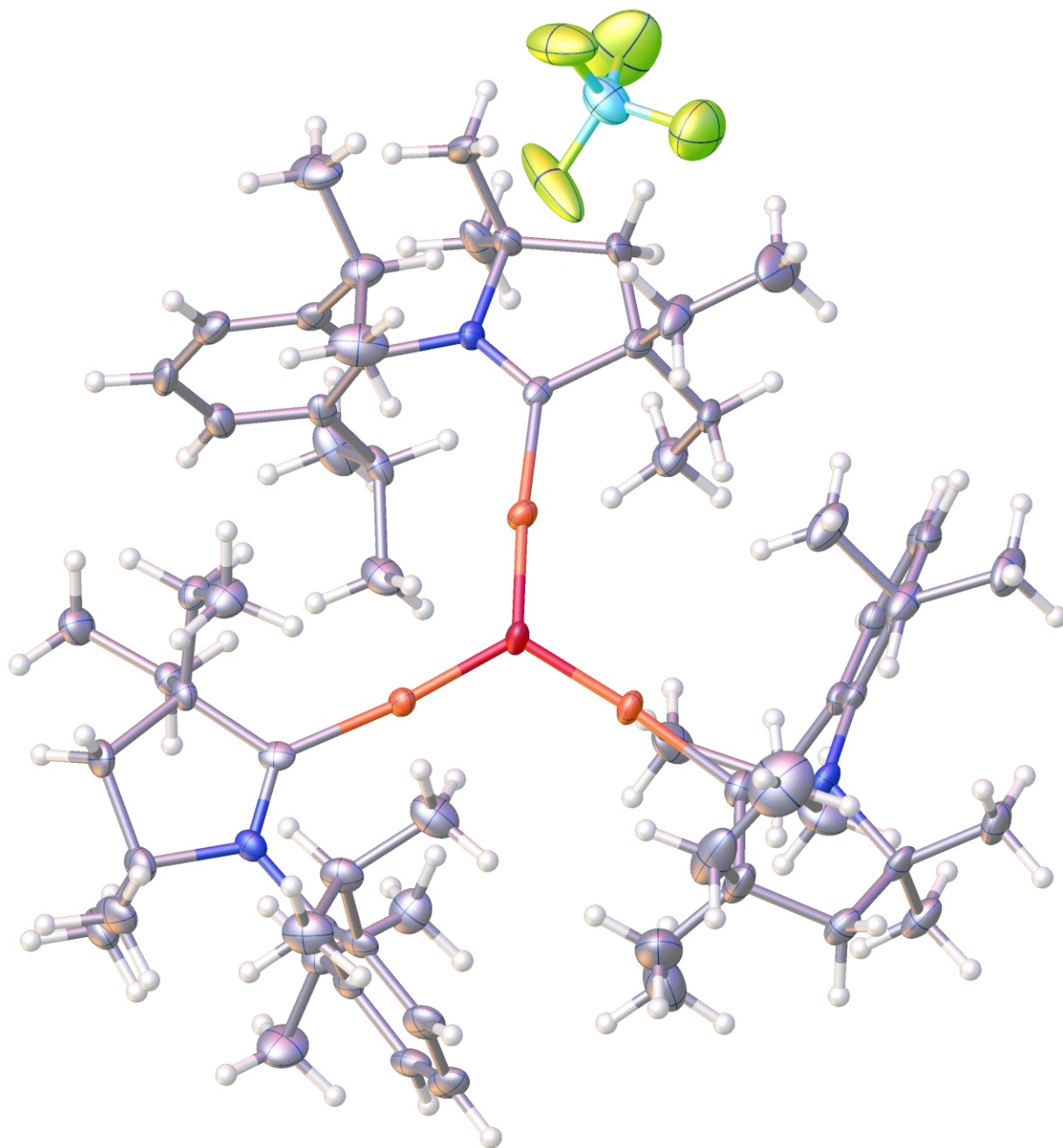
Figure 4.11: X-ray structure of **4.2** (ellipsoids shown at 30% probability).

Crystallographic data for 4.2.B.

Table 4.2: Crystal data and structure refinement for **4.2.B**.

Identification code	**4.2.B**
Empirical formula	$C_{132}H_{222}B_2Cu_{14}F_8N_6$
Formula weight	2956.26
Temperature/K	100.15
Crystal system	cubic
Space group	Pa-3
a/Å	24.6551(4)
b/Å	24.6551(4)
c/Å	24.6551(4)
$\alpha/°$	90
$\beta/°$	90
$\gamma/°$	90
Volume/Å^3	14987.2(7)
Z	4.00008
$\rho_{calc}g/cm^3$	1.310
μ/mm^{-1}	2.501
F(000)	6176.0
Crystal size/mm^3	$0.23 \times 0.27 \times 0.11$
Radiation	CuKα ($\lambda = 1.54178$)
2Θ range for data collection/°	6.208 to 108.768
Index ranges	$-25 \le h \le 16, -25 \le k \le 22, -24 \le l \le 25$
Reflections collected	38702
Independent reflections	3071 [$R_{int} = 0.1102, R_{sigma} = 0.0432$]
Data/restraints/parameters	3071/0/260
Goodness-of-fit on F^2	1.096
Final R indexes [I>=2σ (I)]	$R_1 = 0.0557, wR_2 = 0.1361$
Final R indexes [all data]	$R_1 = 0.1040, wR_2 = 0.1757$
Largest diff. peak/hole / e Å^{-3}	0.73/-0.50
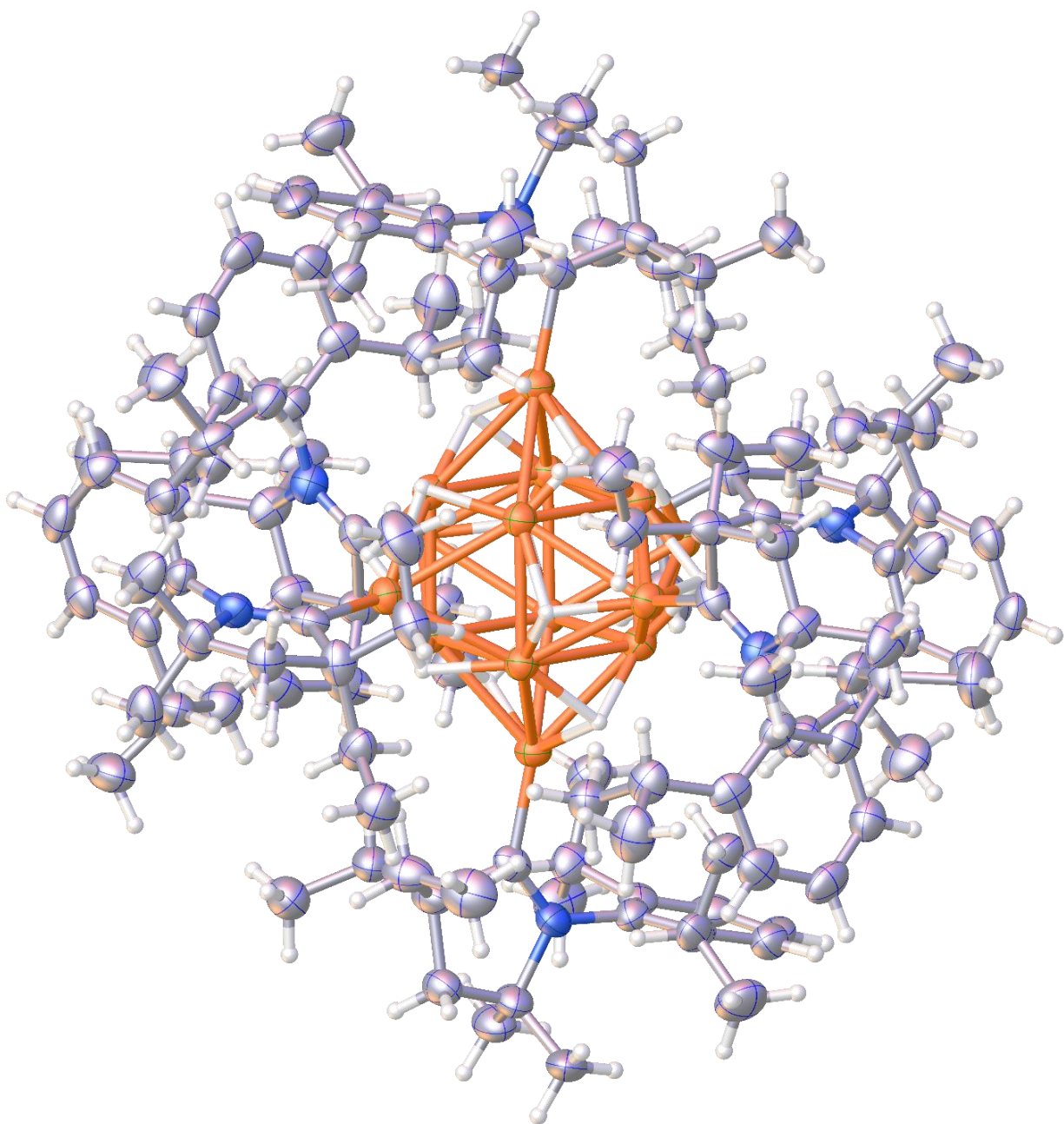
Figure 4.12: X-ray structure of **4.2.B** (ellipsoids shown at 30% probability and anions are removed for clarity).
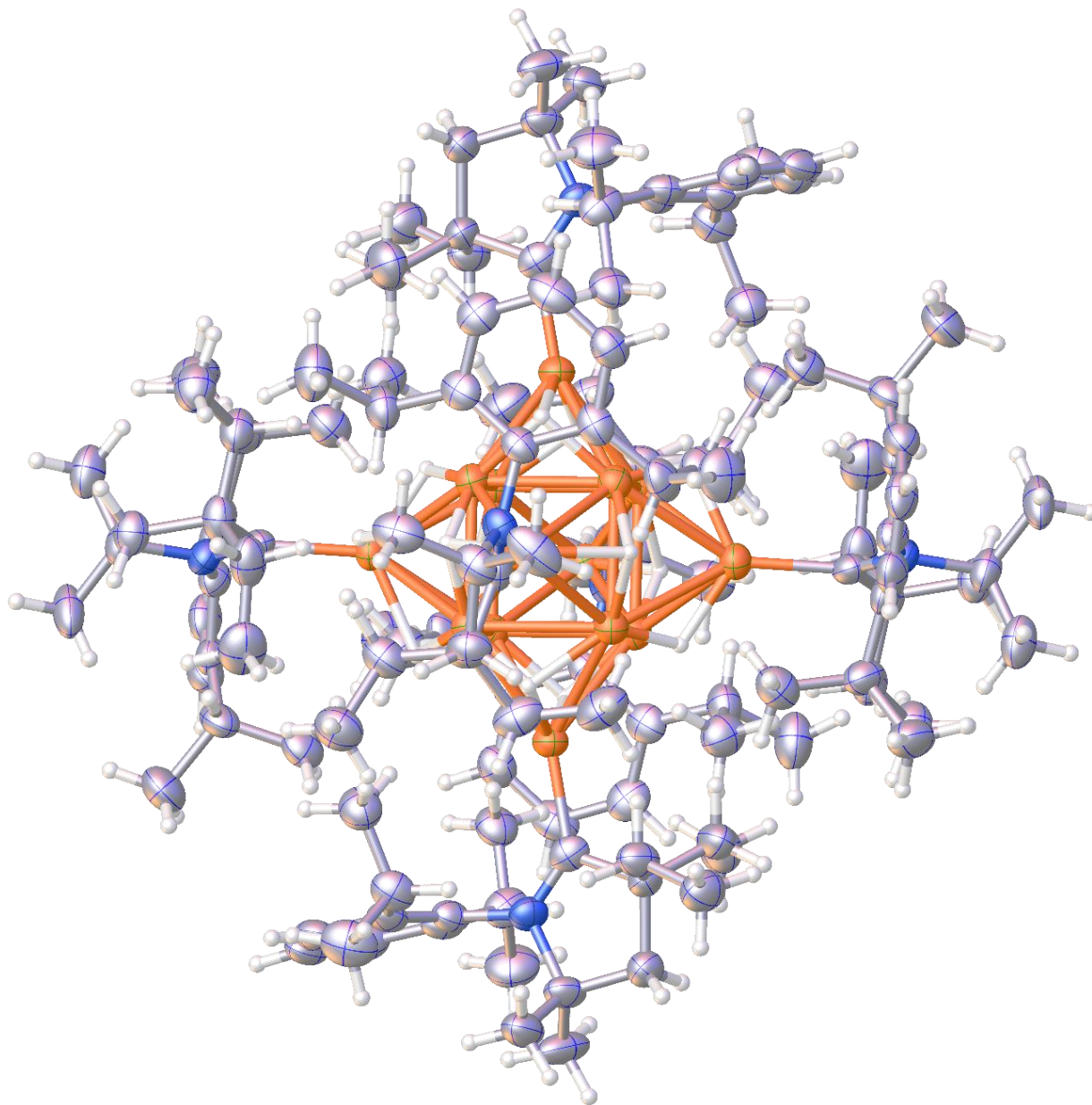
Figure 4.13: Another perspective for the X-ray structure of **4.2.B** (ellipsoids shown at 30% probability and anions removed for clarity).

Crystallographic data for 4.2.A.

Table 4.3: Crystal data and structure refinement for **4.2.A**.

CCDC identification code	**4.2.A**
Empirical formula	$C_{66}H_{105}BCu_3F_4N_3$
Formula weight	1217.95
Temperature/K	100.0
Crystal system	monoclinic
Space group	$P2_1/c$
a/Å	13.7060(6)
b/Å	17.3577(7)
c/Å	28.2431(12)
α/°	90
β/°	103.0520(10)
γ/°	90
Volume/Å^3	6545.6(5)
Z	4
ρ_{calc}g/cm^3	1.236
μ/mm^{-1}	1.017
F(000)	2600.0
Crystal size/mm^3	$0.2 \times 0.2 \times 0.1$
Radiation	MoKα (λ = 0.71073)
2Θ range for data collection/°	2.774 to 50.782
Index ranges	$-11 \leq h \leq 16, -20 \leq k \leq 20, -34 \leq l \leq 34$
Reflections collected	104416
Independent reflections	12020 [R_{int} = 0.0358, R_{sigma} = 0.0202]
Data/restraints/parameters	12020/0/729
Goodness-of-fit on F^2	1.029
Final R indexes [I>=2σ (I)]	R_1 = 0.0251, wR_2 = 0.0594
Final R indexes [all data]	R_1 = 0.0324, wR_2 = 0.0630
Largest diff. peak/hole / e Å^{-3}	0.34/-0.29

      Note: Three *Level A PLAT308_ALERT_2_A* errors were detected by the IUCR checkcif software for **4.2.A**.[123] Those originate from the inability of the current version of the IUCr checkCIF software algorithm to process Cu··Cu to be seen as a bond or short contact. The structure has been thoroughly checked by our crystallographer Dr. Milan Gembicky who confirmed the quality of the data and notified the problem to Prof. Dr. A.L. Spek and the IUCR. The reported issue will be addressed on the IUCr server with the next update."
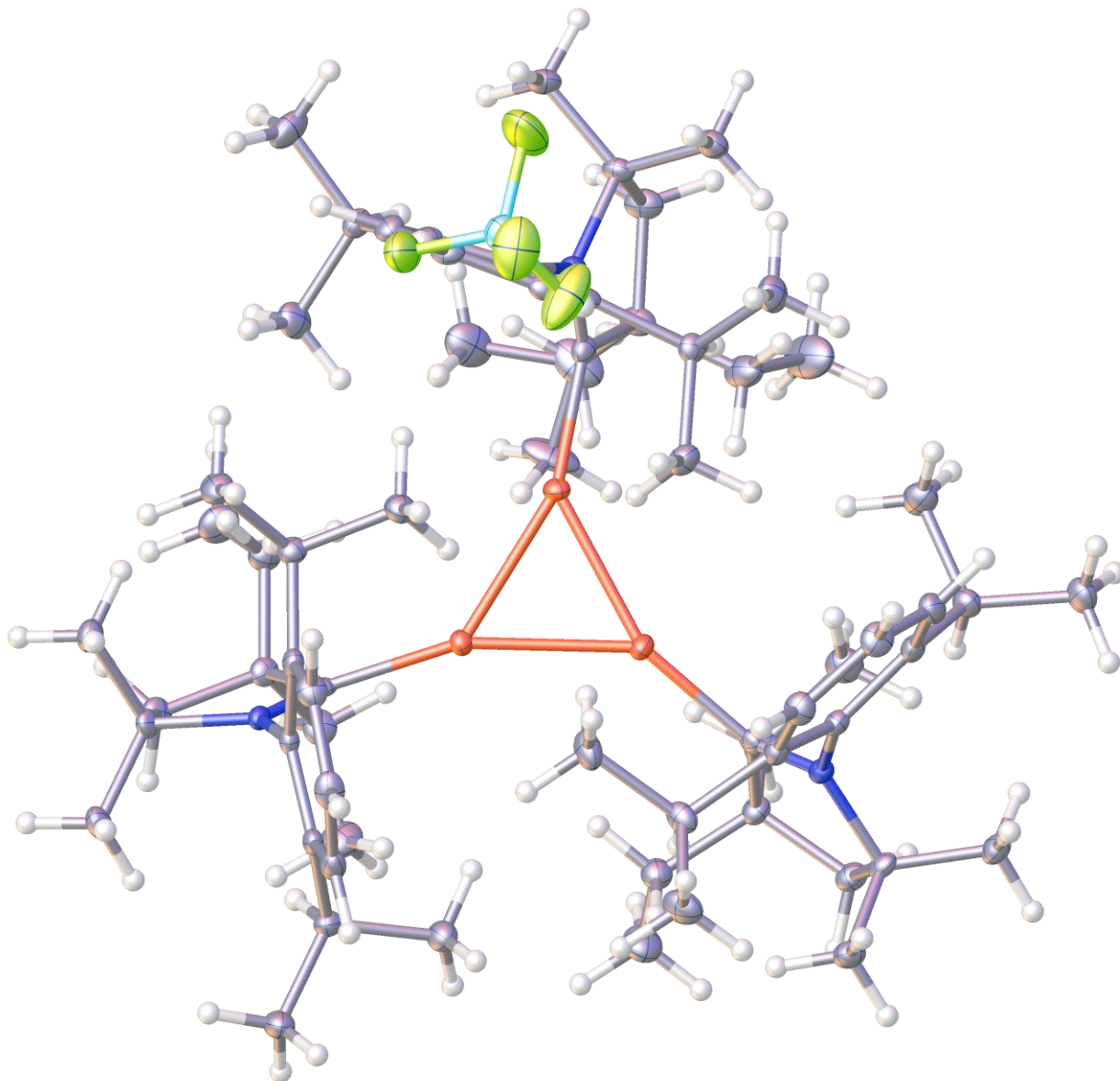
Figure 4.14: X-ray structure of **4.2.A** (ellipsoids shown at 30% probability).

Crystallographic data for 4.1.A.

Table 4.4: Crystal data and structure refinement for **4.1.A**.

CCDC identification code	**4.1.A**
Empirical formula	$C_{66}H_{105}Au_3BF_4N_3$
Formula weight	1618.23
Temperature/K	100.0
Crystal system	orthorhombic
Space group	Fdd2
a/Å	50.481(6)
b/Å	52.026(6)
c/Å	9.7297(11)
α/°	90
β/°	90
γ/°	90
Volume/Å^3	25553(5)
Z	16
ρ_{calc}g/cm^3	1.683
μ/mm^{-1}	6.925
F(000)	12800.0
Crystal size/mm^3	$0.13 \times 0.12 \times 0.09$
Radiation	MoKα (λ = 0.71073)
2Θ range for data collection/°	2.248 to 51.41
Index ranges	$-61 \le h \le 61, -63 \le k \le 49, -11 \le l \le 11$
Reflections collected	52445
Independent reflections	12156 [R_{int} = 0.0463, R_{sigma} = 0.0457]
Data/restraints/parameters	12156/1/718
Goodness-of-fit on F^2	1.010
Final R indexes [I>=2σ (I)]	R_1 = 0.0241, wR_2 = 0.0498
Final R indexes [all data]	R_1 = 0.0289, wR_2 = 0.0513
Largest diff. peak/hole / e Å^{-3}	1.10/-0.73
Flack parameter	0.000(5)
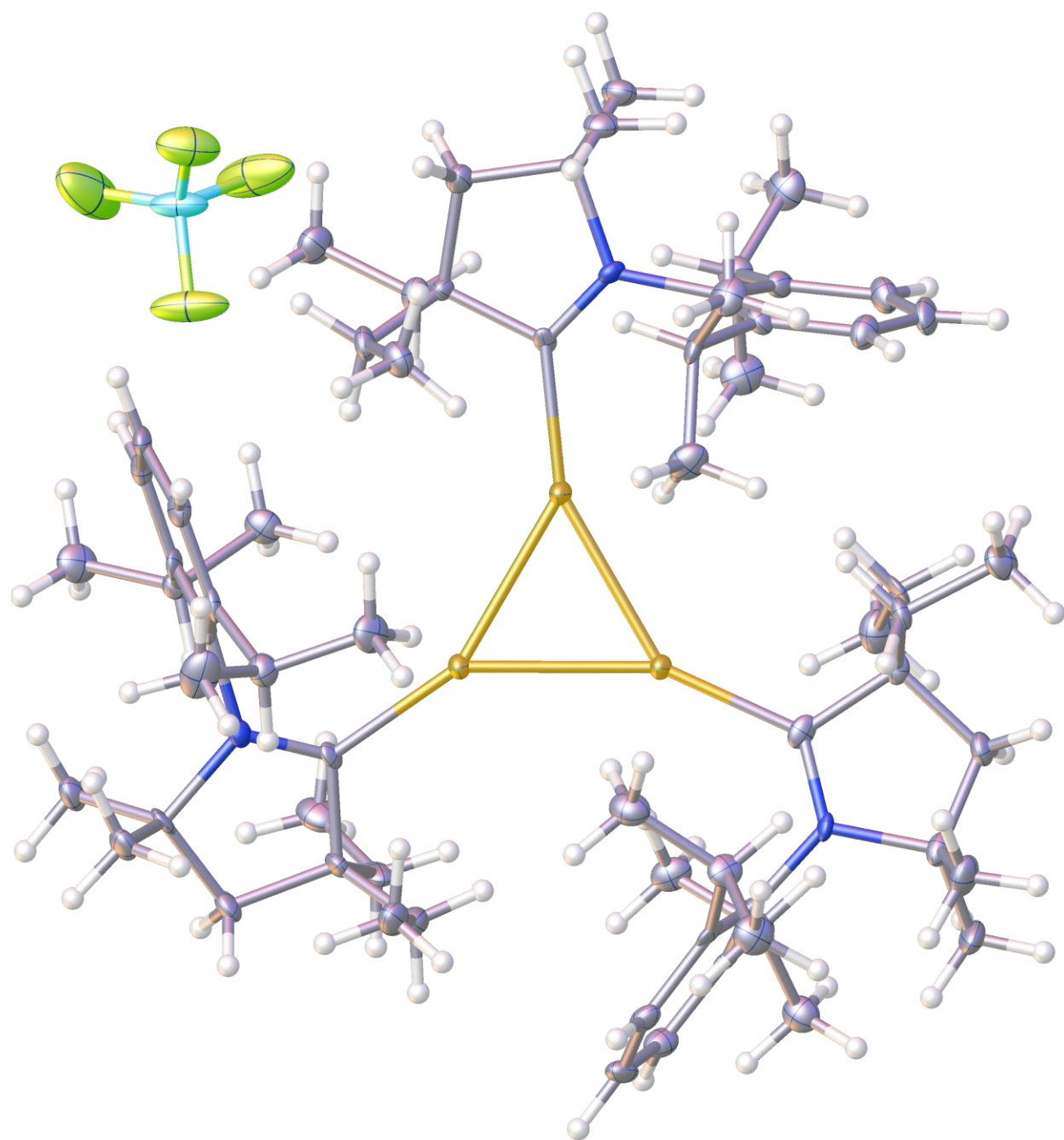
Figure 4.15: X-ray structure of **4.1.A** (ellipsoids shown at 30% probability).

Crystallographic data for 4.3.A.

Table 4.5: Crystal data and structure refinement for **4.3.A**.

CCDC identification code	***4.3.A***
Empirical formula	$C_{66}H_{105}Ag_3BF_4N_3$
Formula weight	1350.94
Temperature/K	296.15
Crystal system	monoclinic
Space group	$P2_1/n$
a/Å	9.7140(10)
b/Å	26.116(3)
c/Å	27.649(3)
$\alpha/°$	90
$\beta/°$	91.690(2)
$\gamma/°$	90
Volume/Å^3	7011.3(12)
Z	4
$\rho_{calc}g/cm^3$	1.280
μ/mm^{-1}	0.877
F(000)	2816.0
Crystal size/mm^3	$0.96 \times 0.79 \times 0.1$
Radiation	MoKα ($\lambda = 0.71073$)
2Θ range for data collection/°	2.948 to 51.388
Index ranges	$-6 \leq h \leq 11, -31 \leq k \leq 31, -32 \leq l \leq 33$
Reflections collected	48744
Independent reflections	13308 [$R_{int} = 0.0177$, $R_{sigma} = 0.0165$]
Data/restraints/parameters	13308/0/718
Goodness-of-fit on F^2	1.064
Final R indexes [I>=2σ (I)]	$R_1 = 0.0287$, $wR_2 = 0.0744$
Final R indexes [all data]	$R_1 = 0.0314$, $wR_2 = 0.0760$
Largest diff. peak/hole / e Å^{-3}	1.19/-0.52

Note: One disordered molecule of THF was squeezed from the solution.
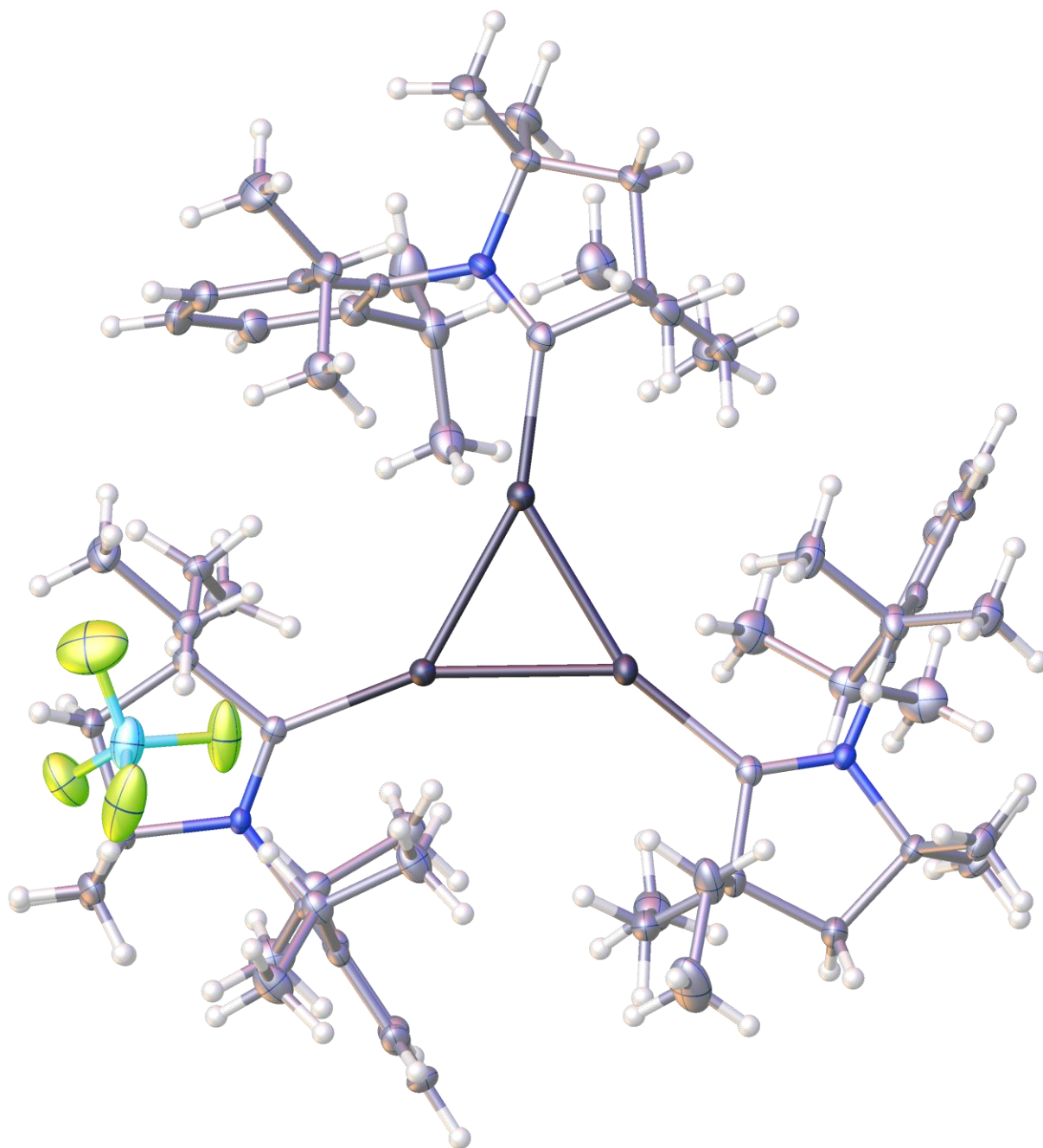
Figure 4.16: X-ray structure of **4.3.A** (ellipsoids shown at 30% probability).

4.4.4 Computational Details.

All calculations were used based on the Gaussian09 program suite[124] with ultrafine (99,590) integration grids.[125] The theoretical approach is based on the framework of density functional theory (DFT).[126,127] To probe the energetics of intermediates in the galvanic exchange as well as for population analysis, NICS Scan, and ELF, all compounds and calculation were done at the M06[76]/def2-TZVPP[77,78] level of theory with a pseudo potential applied for Au and Ag atoms.[128] For all calculations (except NICS-Scan), a truncated model was used for the ^{Et}CAAC wherein the 2,6-diisopropylphenyl (Dipp) substituent on the nitrogen and the ethyl groups on the quaternary carbon adjacent to the carbene center were replaced by methyl substituents. Ground states were fully optimized without constraints and the minima were verified by making sure there were no imaginary frequencies at the same level of theory. Gibbs free reaction energies were calculated for standard conditions ($p = 1$ atm, $T = 298$ K) and are unscaled. All NICS-Scans[98] (bq, NICS probe, were used from 0 to 5 Å with 0.2 Å intervals) were conducted on the crystal structures without additional optimization. Optimized structures were illustrated using CYLview.[129] All results (.chk, .fchk, .log, and .wfn files) are made available for download from UCSD Library Digital Collections (https://doi.org/10.6075/J0T15256).[130]

NICS Scan Results.

The NICS-Scan[98] method was used on each of the structures at the M06[76]/def2-TZVPP[77,78] level and involved the use of several NICS probes (*i.e.*, bq ghost atoms) starting at the center of each of the coinage metal trinuclear rings and placing a bq ghost atom sequentially over a range of distances (*i.e.*, bq's from 0 to 5 Å with 0.2 Å intervals) orthogonal to the plane of the ring. The NICS values, the isotropic chemical shifts of each of the bq atoms, obtained were then plotted versus their distance from the center of the ring.

Electron Localization Function.

The analyses of molecular orbitals and ELF were completed using Multiwfn 3.4.1,[131] which is a multifunctional wavefunction analysis program. The 3-dimensional ELF plots were rendered using ChimeraX[132] based on the outputs of Multiwfn. The shaded surface map with projection of electron localization function (ELF) was generated by Multiwfn 3.4.1.
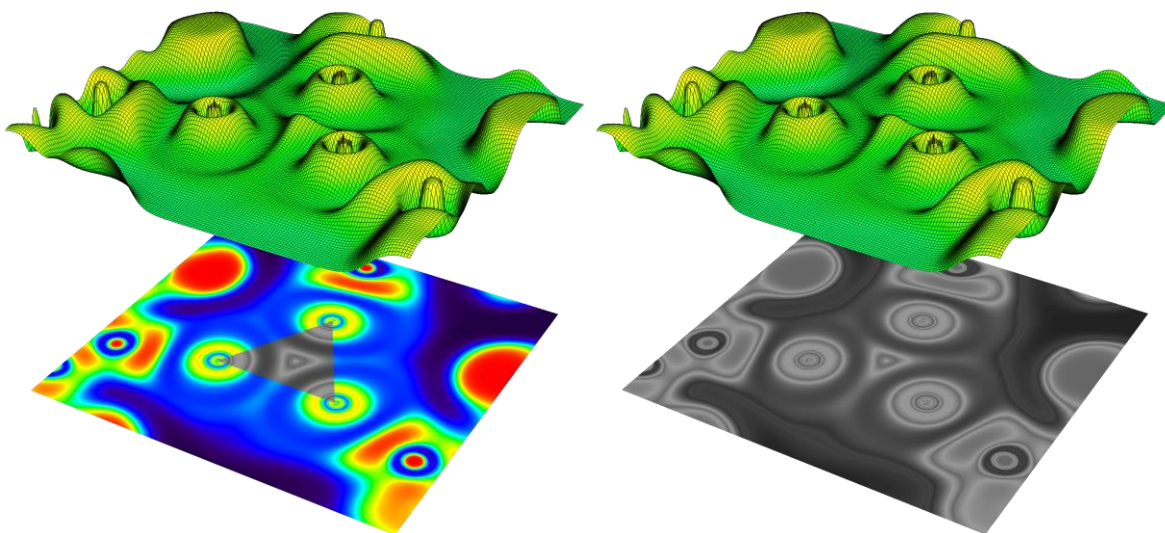
Figure 4.17: The shaded surface map with projection (colored "left" and grey-scale "right") of the electron localization function (ELF) in **4.2.A** suggest similarities free standing M(111) monolayers.

Similarities between **4.1.A-4.3.A** and free standing M(111) were illustrated upon considering the electron localization function (ELF) obtained for free standing M(111) monolayers published by Li-Ming Yang *et al.*[100,102,103] Note that the latter were obtained using CASTEP.[133] As an example for this manuscript, we reproduced, with modification, the Cu(111) monolayer depicted in Figure 4.17 and Figure 4.10.[100,102,103]

$d_{Cu-Cu} = 2.41$ Å
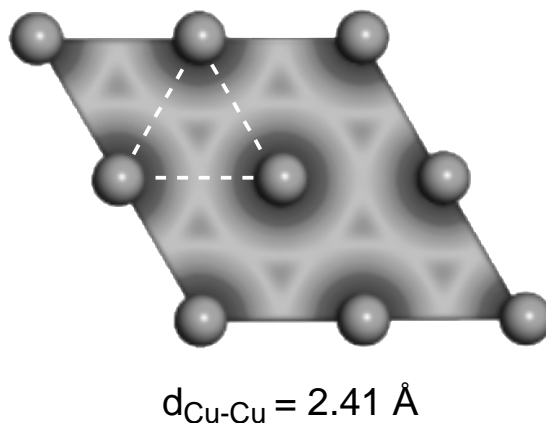
Figure 4.18: Electron localization function (ELF) of a free standing Cu(111) monolayers.

Population Analysis.
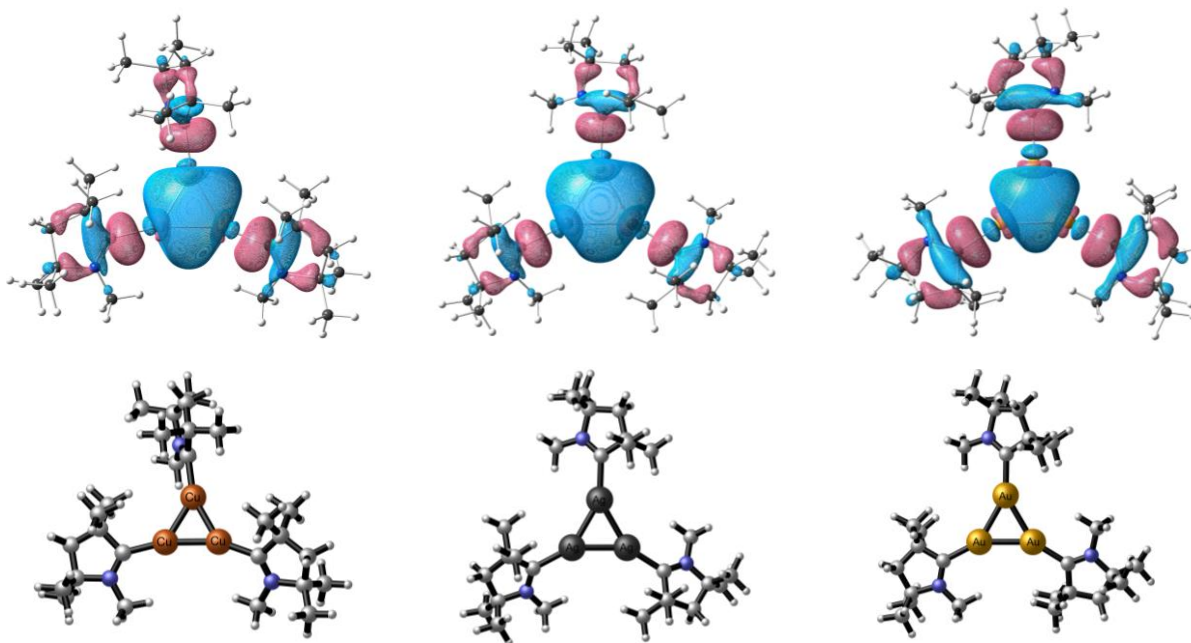
Figure 4.19: Population Analysis showing the HOMO for truncated **4.2.A**, **4.3.A** and **4.1.A** (left to right) that highlights subtle differences between each 3-center 2-electron bond.

4.4.5 UV-Vis.

The UV-Vis spectra were recorded on a Shimadzu UV–3600 UV/vis/NIR spectrometer. Each of the samples were prepared in a solution of THF under argon and transferred to an air-tight cuvette (l=1.0 mm).
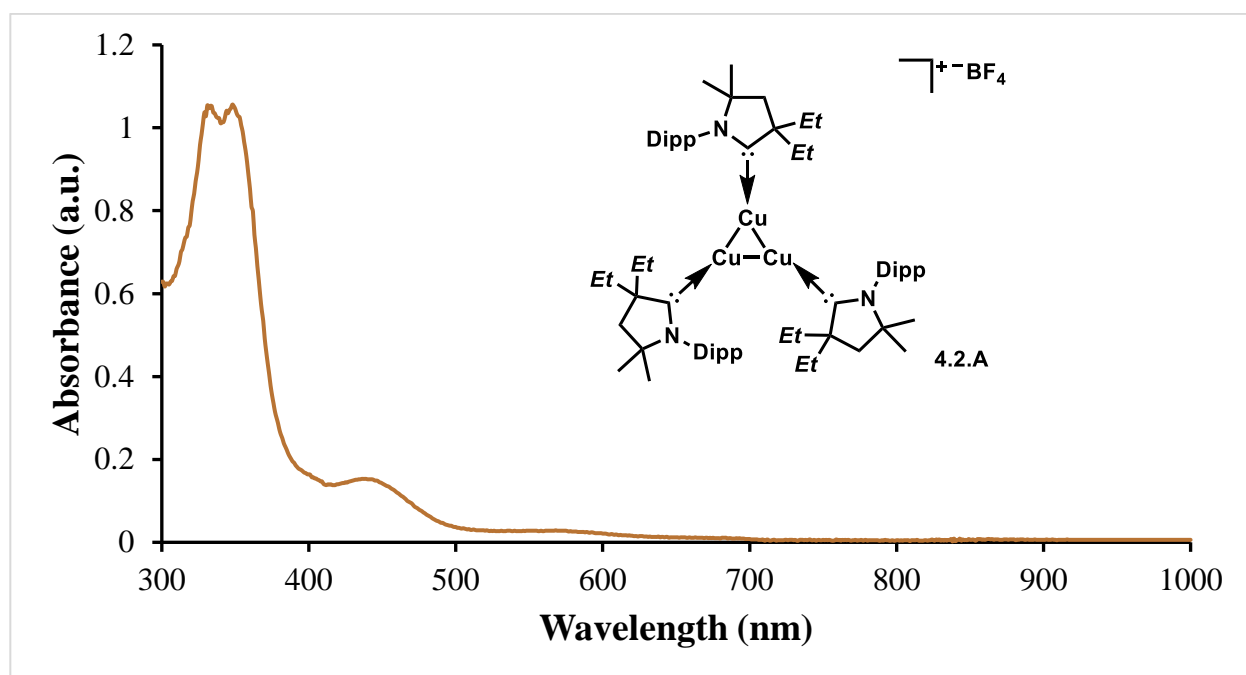
Figure 4.20: UV-Vis of **4.2.A** in THF at 298 K.
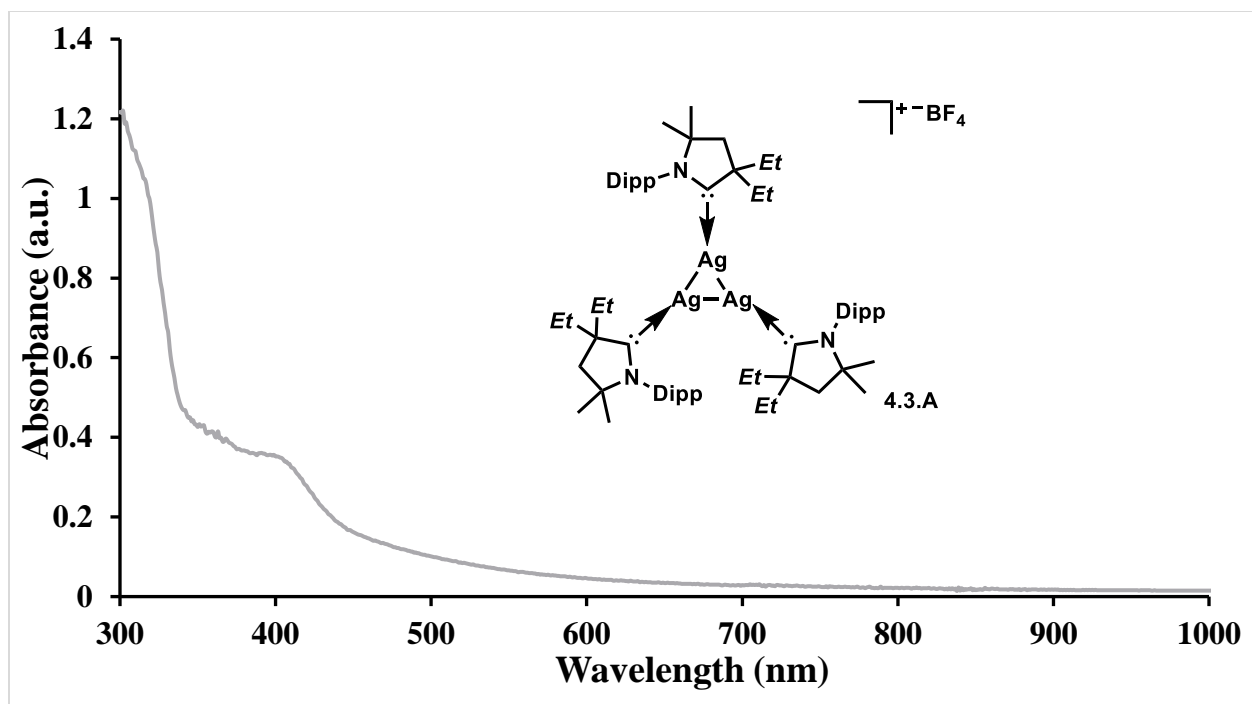
Figure 4.21: UV-Vis of **4.3.A** in THF at 298 K.
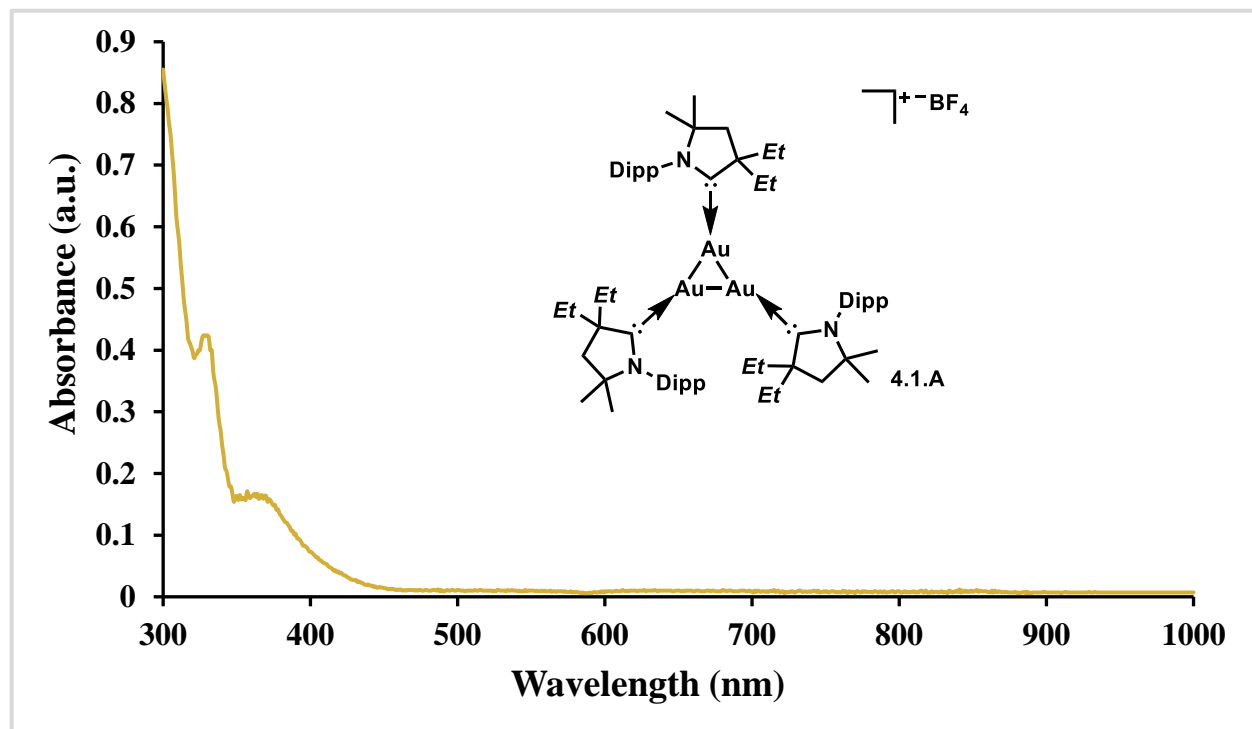
Figure 4.22: UV-Vis of **4.1.A** in THF at 298 K.
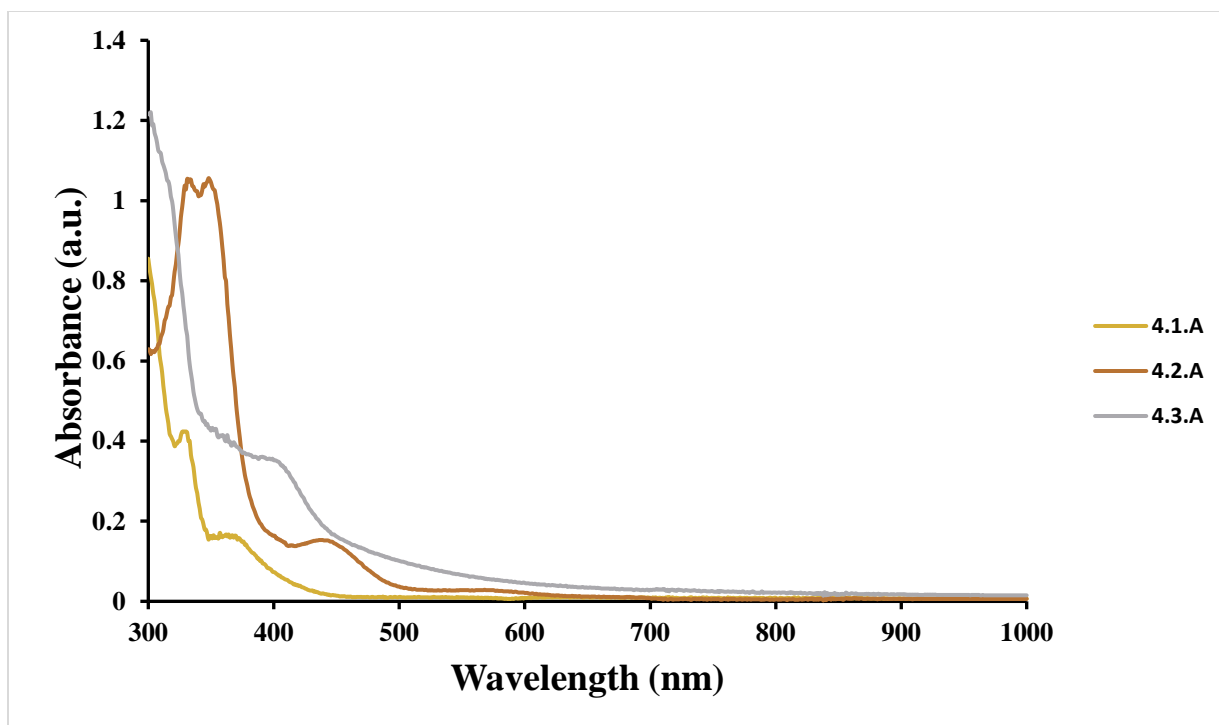
Figure 4.23: Comparison of UV-Vis of **4.1.A**, **4.2.A**, and **4.3.A** in THF at 298 K.

4.4.6 Cyclic Voltammetry.

Electrochemical experiments were carried out with a Biologic SP-300 potentiostat. A silver reference electrode (0.01 M $AgNO_3$ in 0.1 M $[nBu_4N][PF_6]$ in CH_3CN) was used. Cyclic voltammetry experiments were performed in 0.1 M $[nBu_4N][PF_6]$ THF solution. A vitreous carbon disk (3 mm in diameter) and a platinum wire were employed as a working electrode and an auxiliary electrode, respectively.
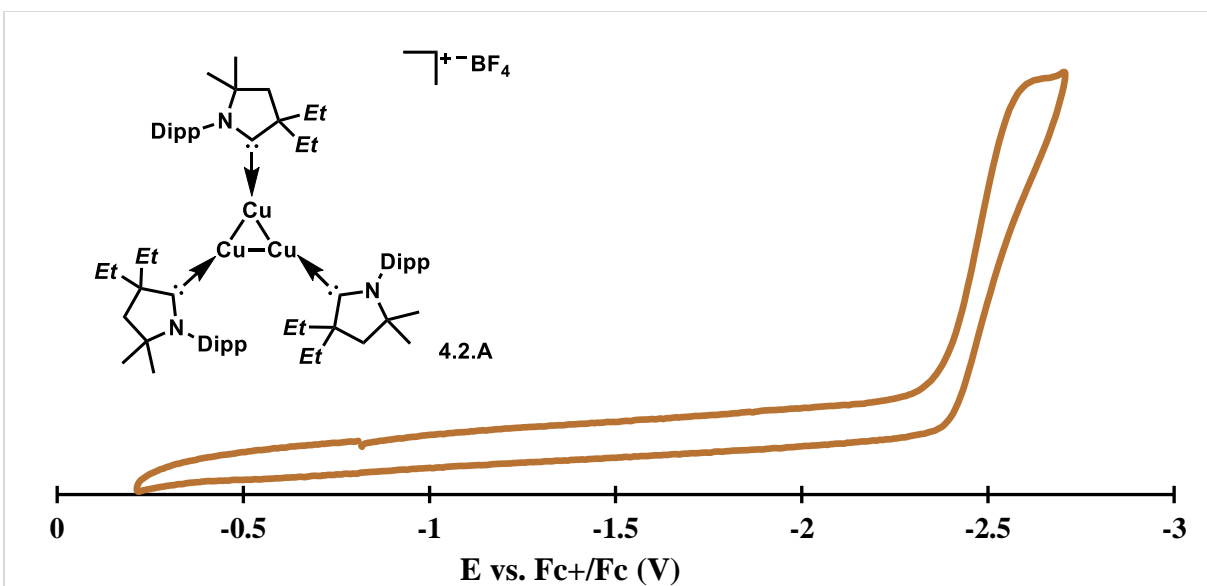
Figure 4.24: Cyclic voltammetry of **4.2.A** under reducing conditions in THF at 298 K at 100 mV/S.
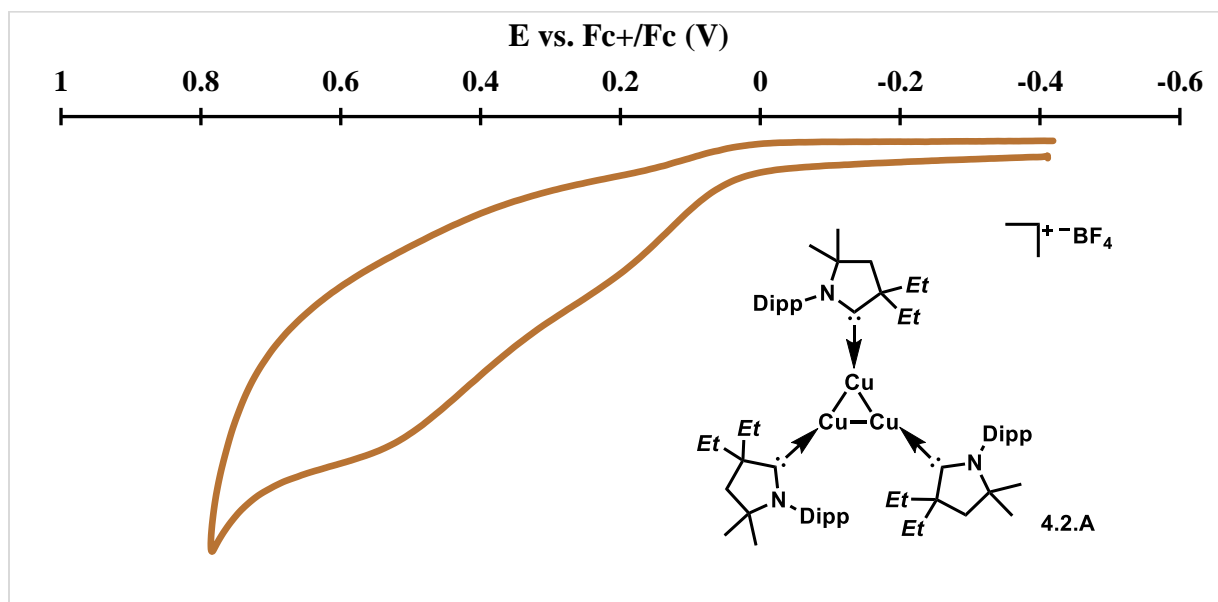
Figure 4.25: Cyclic voltammetry of **4.2.A** under oxidizing conditions in THF at 298 K at 100 mV/S.
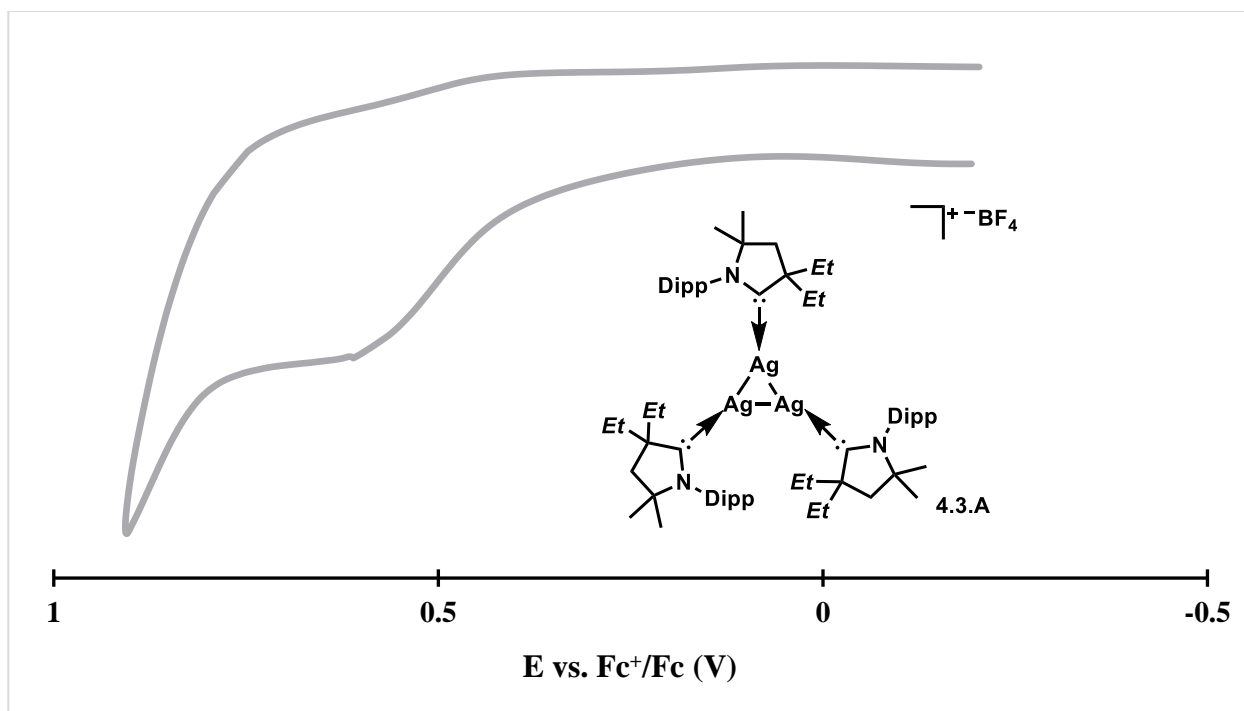
Figure 4.26: Cyclic voltammetry of **4.3.A** under reducing conditions in THF at 298 K at 100 mV/S.
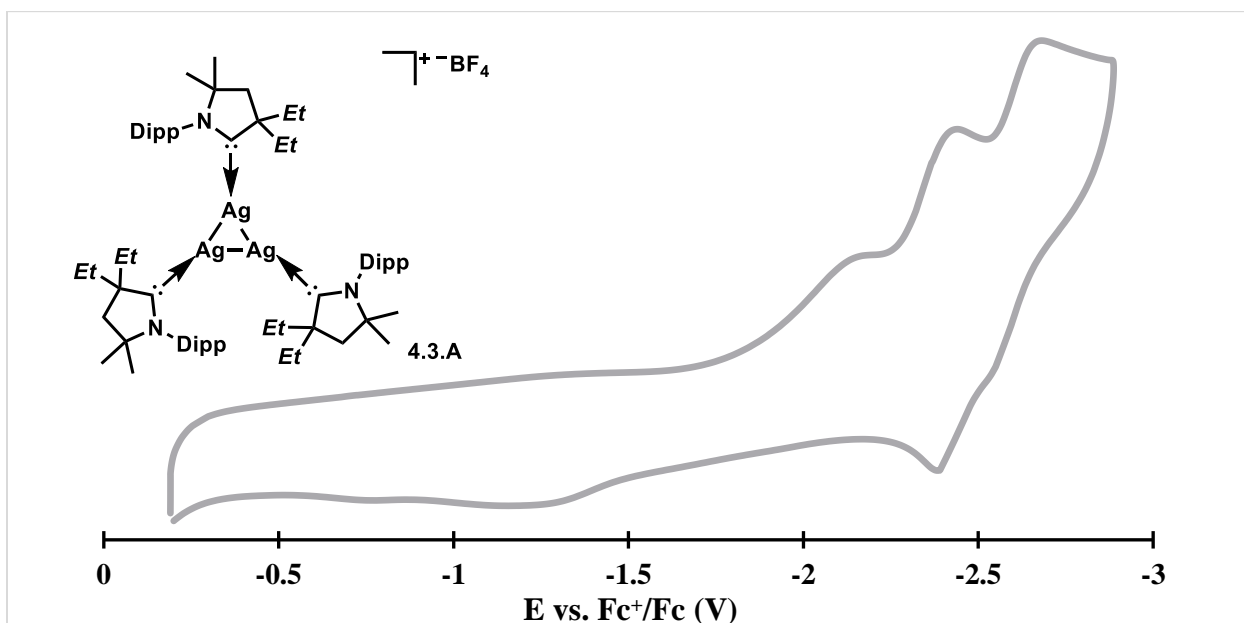
Figure 4.27: Cyclic voltammetry of **4.3.A** under oxidizing conditions in THF at 298 K at 100 mV/S.

Figure 4.28: Cyclic voltammetry of **4.1.A** under reducing conditions in THF at 298 K at 100 mV/S.

Figure 4.29: Cyclic voltammetry of **4.1.A** under oxidizing conditions in THF at 298 K at 100 mV/S.

197

4.5   Acknowledgements

4.6   References

(1)   Lechtman, H. A Pre-Columbian Technique for Electrochemical Replacement Plating of Gold and Silver on Copper Objects. *JOM* **1979**, *31*, 154–160.

(2)   Douglas, G. V.; Goodman, N. R.; Milligan, G. C. On the Nature of Replacement. *Econ. Geol.* **1946**, *41*, 546–553.

(3)   Lin, W.; Warren, T. H.; Nuzzo, R. G.; Girolami, G. S. Surface-Selective Deposition of Palladium and Silver Films from Metal-Organic Precursors: A Novel Metal-Organic Chemical Vapor Deposition Redox Transmetalation Process. *J. Am. Chem. Soc.* **1993**, *115*, 11644–11645.

(4)   Sun, Y.; Xia, Y. Shape-Controlled Synthesis of Gold and Silver Nanoparticles. *Science* **2002**, *298*, 2176–2179.

(5)   Sun, Y.; Xia, Y. Multiple-Walled Nanotubes Made of Metals. *Adv. Mater.* **2004**, *16*, 264–268.

(6)   Sun, Y.; Mayers, B. T.; Xia, Y. Template-Engaged Replacement Reaction: A One-Step Approach to the Large-Scale Synthesis of Metal Nanostructures with Hollow Interiors. *Nano Lett.* **2002**, *2*, 481–485.

(7)   Métraux, G. S.; Cao, Y. C.; Jin, R.; Mirkin, C. A. Triangular Nanoframes Made of Gold and Silver. *Nano Lett.* **2003**, *3*, 519–522.

(8)   González, E.; Arbiol, J.; Puntes, V. F. Carving at the Nanoscale : Sequential Galvanic Exchange and Kirkendall Growth at Room Temperature. *Science* **2011**, *334*, 1377–1380.

(9)   Gilroy, K. D.; Ruditskiy, A.; Peng, H. C.; Qin, D.; Xia, Y. Bimetallic Nanocrystals: Syntheses, Properties, and Applications. *Chem. Rev.* **2016**, *116*, 10414–10472.

(10)   Wang, X.; Feng, J.; Bai, Y.; Zhang, Q.; Yin, Y. Synthesis, Properties, and Applications of Hollow Micro-/Nanostructures. *Chem. Rev.* **2016**, *116*, 10983–11060.

(11)   Baffou, G.; Quidant, R. Nanoplasmonics for Chemistry. *Chem. Soc. Rev.* **2014**, *43*, 3898–3907.

(12)   Pang, B.; Yang, X.; Xia, Y. Putting Gold Nanocages to Work for Optical Imaging , Controlled

Release and Cancer Theranostics. *Nanomedicine* **2016**, *11*, 1715–1728.

(13)   Kamyshny, A.; Magdassi, S. Conductive Nanomaterials for Printed Electronics. *Small* **2014**, *10*, 3515–3535.

(14)   Da Silva, A. G. M.; Rodrigues, T. S.; Haigh, S. J.; Camargo, P. H. C. Galvanic Replacement Reaction: Recent Developments for Engineering Metal Nanostructures towards Catalytic Applications. *Chem. Commun.* **2017**, *53*, 7135–7148.

(15)   Du, Y.; Sheng, H.; Astruc, D.; Zhu, M. Atomically Precise Noble Metal Nanoclusters as Efficient Catalysts : A Bridge between Structure and Properties. *Chem. Rev.* **2020**, *120*, 526–622.

(16)   Higaki, T.; Li, Q.; Zhou, M.; Zhao, S.; Li, Y.; Li, S.; Jin, R. Toward the Tailoring Chemistry of Metal Nanoclusters for Enhancing Functionalities. *Acc. Chem. Res.* **2018**, *51*, 2764–2773.

(17)   Astruc, D. Introduction: Nanoparticles in Catalysis. *Chem. Rev.* **2020**, *120*, 461–463.

(18)   Jena, P.; Castleman, A. W. J. *Nanoclusters: A Bridge across Disciplines*; Elsevier: Amsterdam, 2010.

(19)   Becker, E. W.; Bier, K.; Henkes, W. Strahlen Aus Kondensierten Atomen Und Molekeln Im Hochvakuum. *Zeitschrift für Phys.* **1956**, *146*, 333–338.

(20)   Chini, P. Large Metal Carbonyl Clusters (LMCC). *J. Organomet. Chem.* **1980**, *200*, 37–61.

(21)   Haruta, M.; Kobayashi, T.; Sano, H.; Yamada, N. Novel Gold Catalysts for the Oxidation of Carbon Monoxide at a Temperature Far Below 0 °C. *Chem. Lett.* **1987**, *16*, 405–408.

(22)   Haruta, M.; Yamada, N.; Kobayashi, T.; Iijima, S. Gold Catalysts Prepared by Coprecipitation for Low-Temperature Oxidation of Hydrogen and of Carbon Monoxide. *J. Catal.* **1989**, *115*, 301–309.

(23)   Guo, S.; Dong, S.; Wang, E. A General Method for the Rapid Synthesis of Hollow Metallic or Bimetallic Nanoelectrocatalysts with Urchinlike Morphology. *Chem. Eur. J.* **2008**, *14*, 4689–4695.

(24)   Fang, J.; Ma, X.; Cai, H.; Song, X.; Ding, B. Nanoparticle-Aggregated 3D Monocrystalline Gold Dendritic Nanostructures. *Nanotechnology* **2006**, *17*, 5841–5845.

(25)   Au, L.; Lu, X.; Xia, Y. A Comparative Study of Galvanic Replacement Reactions Involving Ag Nanocubes and AuCl2- or AuCl4-. *Adv. Mater.* **2008**, *20*, 2517–2522.

(26)   Liu, Y.; Hight Walker, A. R. Preferential Outward Diffusion of Cu during Unconventional Galvanic Replacement Reactions between HAuCl4 and Surface-Limited Cu Nanocrystals. *ACS Nano* **2011**, *5*, 6843–6854.

(27)   Zhang, Q.; Xie, J.; Liang, J.; Lee, J. Y. Synthesis of Monodisperse Ag-Au Alloy Nanoparticles with Independently Tunable Morphology, Composition, Size, and Surface Chemistry and Their 3-D Superlattices. *Adv. Funct. Mater.* **2009**, *19*, 1387–1398.

(28)   Aherne, D.; Cara, M.; Kelly, J. M.; Gun'Ko, Y. K. From Ag Nanoprisms to Triangular Auag Nanoboxes. *Adv. Funct. Mater.* **2010**, *20*, 1329–1338.

(29)   Skrabalak, S. E.; Au, L.; Li, X.; Xia, Y. Facile Synthesis of Ag Nanocubes and Au Nanocages. *Nat.*

Protoc. **2007**, *2*, 2182–2190.

(30) Choi, J. P.; Fields-Zinna, C. A.; Stiles, R. L.; Balasubramanian, R.; Douglas, A. D.; Crowe, M. C.; Murray, R. W. Reactivity of [Au25(SCH2CH2Ph) 18]1- Nanoparticles with Metal Ions. *J. Phys. Chem. C* **2010**, *114*, 15890–15896.

(31) Wu, Z. Anti-Galvanic Reduction of Thiolate-Protected Gold and Silver Nanoparticles. *Angew. Chem. Int. Ed.* **2012**, *51*, 2934–2938.

(32) Varnavski, O.; Ramakrishna, G.; Kim, J.; Lee, D.; Goodson, T. Critical Size for the Observation of Quantum Confinement in Optically Excited Gold Clusters. *J. Am. Chem. Soc.* **2010**, *132*, 16–17.

(33) Wang, S.; Song, Y.; Jin, S.; Liu, X.; Zhang, J.; Pei, Y.; Meng, X.; Chen, M.; Li, P.; Zhu, M. Metal Exchange Method Using Au25 Nanoclusters as Templates for Alloy Nanoclusters with Atomic Precision. *J. Am. Chem. Soc.* **2015**, *137*, 4018–4021.

(34) Gan, Z.; Xia, N.; Wu, Z. Discovery, Mechanism, and Application of Antigalvanic Reaction. *Acc. Chem. Res.* **2018**, *51*, 2774–2783.

(35) Zhu, M.; Wang, P.; Yan, N.; Chai, X.; He, L.; Zhao, Y.; Xia, N.; Yao, C.; Li, J.; Deng, H.; Zhu, Y.; Pei, Y.; Wu, Z. The Fourth Alloying Mode by Way of Anti-Galvanic Reaction. *Angew. Chem. Int. Ed.* **2018**, *57*, 4500–4504.

(36) Joshi, C. P.; Bootharaju, M. S.; Alhilaly, M. J.; Bakr, O. M. [Ag25(SR)18]-: The "Golden"Silver Nanoparticle Silver Nanoparticle. *J. Am. Chem. Soc.* **2015**, *137*, 11578–11581.

(37) Bootharaju, M. S.; Joshi, C. P.; Parida, M. R.; Mohammed, O. F.; Bakr, O. M. Templated Atom-Precise Galvanic Synthesis and Structure Elucidation of a [Ag24Au(SR)18]- Nanocluster. *Angew. Chem. Int. Ed.* **2016**, *55*, 922–926.

(38) Yao, Q.; Feng, Y.; Fung, V.; Yu, Y.; Jiang, D. E.; Yang, J.; Xie, J. Precise Control of Alloying Sites of Bimetallic Nanoclusters via Surface Motif Exchange Reaction. *Nat. Commun.* **2017**, *8*, 1555.

(39) Kang, X.; Li, Y.; Zhu, M.; Jin, R. Atomically Precise Alloy Nanoclusters: Syntheses, Structures, and Properties. *Chem. Soc. Rev.* **2020**. https://doi.org/10.1039/C9CS00633H.

(40) Wang, S.; Li, Q.; Kang, X.; Zhu, M. Customizing the Structure, Composition, and Properties of Alloy Nanoclusters by Metal Exchange. *Acc. Chem. Res.* **2018**, *51*, 2784–2792.

(41) Jin, R.; Zeng, C.; Zhou, M.; Chen, Y. Atomically Precise Colloidal Metal Nanoclusters and Nanoparticles: Fundamentals and Opportunities. *Chem. Rev.* **2016**, *116*, 10346–10413.

(42) Bratsch, S. G. Standard Electrode Potentials and Temperature Coefficients in Water at 298.15 K. *J. Phys. Chem. Ref. Data* **1989**, *18*, 1–21.

(43) Nguyen, T. A. D.; Jones, Z. R.; Goldsmith, B. R.; Buratto, W. R.; Wu, G.; Scott, S. L.; Hayton, T. W. A Cu25 Nanocluster with Partial Cu(0) Character. *J. Am. Chem. Soc.* **2015**, *137*, 13319–13324.

(44) Chakrahari, K. K.; Liao, J. H.; Kahlal, S.; Liu, Y. C.; Chiang, M. H.; Saillard, J. Y.; Liu, C. W. [Cu13{S2CNnBu2}6(Acetylide)4]+: A Two-Electron Superatom. *Angew. Chem. Int. Ed.* **2016**, *128*, 14924–14928.

(45) Yuan, P.; Chen, R.; Zhang, X.; Chen, F.; Yan, J.; Sun, C.; Ou, D.; Peng, J.; Lin, S.; Tang, Z.; Teo, B. K.; Zheng, L. S.; Zheng, N. Ether-Soluble Cu 53 Nanoclusters as an Effective Precursor of High-Quality CuI Films for Optoelectronic Applications. *Angew. Chem. Int. Ed.* **2019**, *58*, 835–839.

(46) Nguyen, T. A. D.; Jones, Z. R.; Leto, D. F.; Wu, G.; Scott, S. L.; Hayton, T. W. Ligand-Exchange-Induced Growth of an Atomically Precise Cu29 Nanocluster from a Smaller Cluster. *Chem. Mater.* **2016**, *28*, 8385–8390.

(47) Li, Y. L.; Wang, J.; Luo, P.; Ma, X. H.; Dong, X. Y.; Wang, Z. Y.; Du, C. X.; Zang, S. Q.; Mak, T. C. W. Cu14 Cluster with Partial Cu(0) Character: Difference in Electronic Structure from Isostructural Silver Analog. *Adv. Sci.* **2019**, *6*, 6–11.

(48) Ghosh, A.; Huang, R.-W.; Alamer, B.; Abou-Hamad, E.; Hedhili, M. N.; Mohammed, O. F.; Bakr, O. M. [Cu 61 (S t Bu) 26 S 6 Cl 6 H 14] + : A Core–Shell Superatom Nanocluster with a Quasi- J 36 Cu 19 Core and an "18-Crown-6" Metal-Sulfide-like Stabilizing Belt. *ACS Mater. Lett.* **2019**, *1*, 297–302.

(49) Han, B. L.; Liu, Z.; Feng, L.; Wang, Z.; Gupta, R. K.; Aikens, C. M.; Tung, C. H.; Sun, D. Polymorphism in Atomically Precise Cu23 Nanocluster Incorporating Tetrahedral [Cu4]0 Kernel. *J. Am. Chem. Soc.* **2020**, *142*, 5834–5841.

(50) Yao, Q.; Chen, T.; Yuan, X.; Xie, J. Toward Total Synthesis of Thiolate-Protected Metal Nanoclusters. *Acc. Chem. Res.* **2018**, *51*, 1338–1348.

(51) Konishi, K.; Iwasaki, M.; Shichibu, Y. Phosphine-Ligated Gold Clusters with Core+ Exo Geometries: Unique Properties and Interactions at the Ligand-Cluster Interface. *Acc. Chem. Res.* **2018**, *51*, 3125–3133.

(52) Häkkinen, H. The Gold-Sulfur Interface at the Nanoscale. *Nat. Chem.* **2012**, *4*, 443–455.

(53) Kang, X.; Zhu, M. Transformation of Atomically Precise Nanoclusters by Ligand-Exchange. *Chem. Mater.* **2019**, *31*, 9939–9969.

(54) Bakker, A.; Freitag, M.; Kolodzeiski, E.; Bellotti, P.; Timmer, A.; Ren, J.; Schulze Lammers, B.; Moock, D.; Roesky, H. W.; Mönig, H.; Amirjalayer, S.; Fuchs, H.; Glorius, F. An Electron-Rich Cyclic (Alkyl)(Amino)Carbene on Au(111), Ag(111), and Cu(111) Surfaces. *Angew. Chem. Int. Ed.* **2020**, *59*, 13643–13646.

(55) MacLeod, M. J.; Goodman, A. J.; Ye, H. Z.; Nguyen, H. V. T.; Van Voorhis, T.; Johnson, J. A. Robust Gold Nanorods Stabilized by Bidentate N-Heterocyclic-Carbene–Thiolate Ligands. *Nat. Chem.* **2019**, *11*, 57–63.

(56) Zhukhovitskiy, A. V.; MacLeod, M. J.; Johnson, J. A. Carbene Ligands in Surface Chemistry: From Stabilization of Discrete Elemental Allotropes to Modification of Nanoscale and Bulk Substrates. *Chem. Rev.* **2015**, *115*, 11503–11532.

(57) Man, R. W. Y.; Li, C. H.; MacLean, M. W. A.; Zenkina, O. V.; Zamora, M. T.; Saunders, L. N.; Rousina-Webb, A.; Nambo, M.; Crudden, C. M. Ultrastable Gold Nanoparticles Modified by Bidentate N-Heterocyclic Carbene Ligands. *J. Am. Chem. Soc.* **2018**, *140*, 1576–1579.

(58) Wu, C. Y.; Wolf, W. J.; Levartovsky, Y.; Bechtel, H. A.; Martin, M. C.; Toste, F. D.; Gross, E.

High-Spatial-Resolution Mapping of Catalytic Reactions on Single Particles. *Nature* **2017**, *541*, 511–515.

(59)   Ernst, J. B.; Muratsugu, S.; Wang, F.; Tada, M.; Glorius, F. Tunable Heterogeneous Catalysis: N-Heterocyclic Carbenes as Ligands for Supported Heterogeneous Ru/K-Al2O3 Catalysts to Tune Reactivity and Selectivity. *J. Am. Chem. Soc.* **2016**, *138*, 10718–10721.

(60)   MacLeod, M. J.; Johnson, J. A. PEGylated N-Heterocyclic Carbene Anchors Designed to Stabilize Gold Nanoparticles in Biologically Relevant Media. *J. Am. Chem. Soc.* **2015**, *137*, 7974–7977.

(61)   Lv, A.; Freitag, M.; Chepiga, K. M.; Schäfer, A. H.; Glorius, F.; Chi, L. N-Heterocyclic-Carbene-Treated Gold Surfaces in Pentacene Organic Field-Effect Transistors: Improved Stability and Contact at the Interface. *Angew. Chem. Int. Ed.* **2018**, *57*, 4792–4796.

(62)   Doud, E. A.; Inkpen, M. S.; Lovat, G.; Montes, E.; Paley, D. W.; Steigerwald, M. L.; Vázquez, H.; Venkataraman, L.; Roy, X. In Situ Formation of N-Heterocyclic Carbene-Bound Single-Molecule Junctions. *J. Am. Chem. Soc.* **2018**, *140*, 8944–8949.

(63)   Ye, R.; Zhukhovitskiy, A. V.; Kazantsev, R. V.; Fakra, S. C.; Wickemeyer, B. B.; Toste, F. D.; Somorjai, G. A. Supported Au Nanoparticles with N -Heterocyclic Carbene Ligands as Active and Stable Heterogeneous Catalysts for Lactonization. *J. Am. Chem. Soc.* **2018**, *140*, 4144–4149.

(64)   Crudden, C. M.; Horton, J. H.; Narouz, M. R.; Li, Z.; Smith, C. A.; Munro, K.; Baddeley, C. J.; Larrea, C. R.; Drevniok, B.; Thanabalasingam, B.; McLean, A. B.; Zenkina, O. V.; Ebralidze, I. I.; She, Z.; Kraatz, H. B.; Mosey, N. J.; Saunders, L. N.; Yagi, A. Simple Direct Formation of Self-Assembled N-Heterocyclic Carbene Monolayers on Gold and Their Application in Biosensing. *Nat. Commun.* **2016**, *7*, 12654.

(65)   Wang, G.; Rühling, A.; Amirjalayer, S.; Knor, M.; Ernst, J. B.; Richter, C.; Gao, H. J.; Timmer, A.; Gao, H. Y.; Doltsinis, N. L.; Glorius, F.; Fuchs, H. Ballbot-Type Motion of N-Heterocyclic Carbenes on Gold Surfaces. *Nat. Chem.* **2017**, *9*, 152–156.

(66)   Crudden, C. M.; Horton, J. H.; Ebralidze, I. I.; Zenkina, O. V.; McLean, A. B.; Drevniok, B.; She, Z.; Kraatz, H. B.; Mosey, N. J.; Seki, T.; Keske, E. C.; Leake, J. D.; Rousina-Webb, A.; Wu, G. Ultra Stable Self-Assembled Monolayers of N-Heterocyclic Carbenes on Gold. *Nat. Chem.* **2014**, *6*, 409–414.

(67)   Zhukhovitskiy, A. V.; Mavros, M. G.; Van Voorhis, T.; Johnson, J. A. Addressable Carbene Anchors for Gold Surfaces. *J. Am. Chem. Soc.* **2013**, *135*, 7418–7421.

(68)   Baquero, E. A.; Tricard, S.; Flores, J. C.; de Jesús, E.; Chaudret, B. Highly Stable Water-Soluble Platinum Nanoparticles Stabilized by Hydrophilic N-Heterocyclic Carbenes. *Angew. Chem. Int. Ed.* **2014**, *53*, 13220–13224.

(69)   Robilotto, T. J.; Bacsa, J.; Gray, T. G.; Sadighi, J. P. Synthesis of a Trigold Monocation: An Isolobal Analogue of [H3]+. *Angew. Chem. Int. Ed.* **2012**, *51*, 12077–12080.

(70)   Khalili Najafabadi, B.; Corrigan, J. F. N-Heterocyclic Carbene Stabilized Ag-P Nanoclusters. *Chem. Commun.* **2015**, *51*, 665–667.

(71)   Narouz, M. R.; Osten, K. M.; Unsworth, P. J.; Man, R. W. Y.; Salorinne, K.; Takano, S.; Tomihara,

R.; Kaappa, S.; Malola, S.; Dinh, C. T.; Padmos, J. D.; Ayoo, K.; Garrett, P. J.; Nambo, M.; Horton, J. H.; Sargent, E. H.; Häkkinen, H.; Tsukuda, T.; Crudden, C. M. N-Heterocyclic Carbene-Functionalized Magic-Number Gold Nanoclusters. *Nat. Chem.* **2019**, *11*, 419–425.

(72)   Smith, C. A.; Narouz, M. R.; Lummis, P. A.; Singh, I.; Nazemi, A.; Li, C. H.; Crudden, C. M. N-Heterocyclic Carbenes in Materials Chemistry. *Chem. Rev.* **2019**, *119*, 4986–5056.

(73)   Roy, S.; Mondal, K. C.; Roesky, H. W. Cyclic Alkyl(Amino) Carbene Stabilized Complexes with Low Coordinate Metals of Enduring Nature. *Acc. Chem. Res.* **2016**, *49*, 357–369.

(74)   Jazzar, R.; Soleilhavoup, M.; Bertrand, G. Cyclic (Alkyl)- And (Aryl)-(Amino)Carbene Coinage Metal Complexes and Their Applications. *Chem. Rev.* **2020**, *120*, 4141–4168.

(75)   Jin, L.; Weinberger, D. S.; Melaimi, M.; Moore, C. E.; Rheingold, A. L.; Bertrand, G. Trinuclear Gold Clusters Supported by Cyclic (Alkyl)(Amino)Carbene Ligands: Mimics for Gold Heterogeneous Catalysts. *Angew. Chem. Int. Ed.* **2014**, *53*, 9059–9063.

(76)   Zhao, Y.; Truhlar, D. G. The M06 Suite of Density Functionals for Main Group Thermochemistry, Thermochemical Kinetics, Noncovalent Interactions, Excited States, and Transition Elements: Two New Functionals and Systematic Testing of Four M06-Class Functionals and 12 Other Function. *Theor. Chem. Acc.* **2008**, *120*, 215–241.

(77)   Weigend, F.; Ahlrichs, R. Balanced Basis Sets of Split Valence, Triple Zeta Valence and Quadruple Zeta Valence Quality for H to Rn: Design and Assessment of Accuracy. *Phys. Chem. Chem. Phys.* **2005**, *7*, 3297–3305.

(78)   Weigend, F. Accurate Coulomb-Fitting Basis Sets for H to Rn. *Phys. Chem. Chem. Phys.* **2006**, *8*, 1057–1065.

(79)   Nesmeyanov, A. N.; Perevalova, E. G.; Struchkov, Y. T.; Antipin, M. Y.; Grandberg, K. I.; Dyadhenko, V. P. Tris(Triphenylphosphinegold)Oxonium Salts. *J. Organomet. Chem.* **1980**, *201*, 343–349.

(80)   Romero, E. A.; Peltier, J. L.; Jazzar, R.; Bertrand, G. Catalyst-Free Dehydrocoupling of Amines, Alcohols, and Thiols with Pinacol Borane and 9-Borabicyclononane (9-BBN). *Chem. Commun.* **2016**, *52*, 10563–10565.

(81)   Hosoya, H.; Misal Castro, L. C.; Sultan, I.; Nakajima, Y.; Ohmura, T.; Sato, K.; Tsurugi, H.; Suginome, M.; Mashima, K. 4,4′-Bipyridyl-Catalyzed Reduction of Nitroarenes by Bis(Neopentylglycolato)Diboron. *Org. Lett.* **2019**, *21*, 9812–9817.

(82)   Laitar, D. S.; Müller, P.; Sadighi, J. P. Efficient Homogeneous Catalysis in the Reduction of CO2 to CO. *J. Am. Chem. Soc.* **2005**, *127*, 17196–17197.

(83)   Mankad, N. P.; Laitar, D. S.; Sadighi, J. P. Synthesis, Structure, and Alkyne Reactivity of a Dimeric (Carbene)Copper(I) Hydride. *Organometallics* **2004**, *23*, 3369–3371.

(84)   Wyss, C. M.; Tate, B. K.; Bacsa, J.; Gray, T. G.; Sadighi, J. P. Bonding and Reactivity of a μ-Hydrido Dicopper Cation. *Angew. Chem. Int. Ed.* **2013**, *52*, 12920–12923.

(85)   Frey, G. D.; Donnadieu, B.; Soleilhavoup, M.; Bertrand, G. Synthesis of a Room-Temperature-

Stable Dimeric Copper(I) Hydride. *Chem. Asian J.* **2011**, *6*, 402–405.

(86)   Jordan, A. J.; Wyss, C. M.; Bacsa, J.; Sadighi, J. P. Synthesis and Reactivity of New Copper(I) Hydride Dimers. *Organometallics* **2016**, *35*, 613–616.

(87)   Regnier, V.; Romero, E. A.; Molton, F.; Jazzar, R.; Bertrand, G.; Martin, D. What Are the Radical Intermediates in Oxidative N-Heterocyclic Carbene Organocatalysis? *J. Am. Chem. Soc.* **2019**, *141*, 1109–1117.

(88)   Romero, E. A.; Olsen, P. M.; Jazzar, R.; Soleilhavoup, M.; Gembicky, M.; Bertrand, G. Spectroscopic Evidence for a Monomeric Copper(I) Hydride and Crystallographic Characterization of a Monomeric Silver(I) Hydride. *Angew. Chem. Int. Ed.* **2017**, *56*, 4024–4027.

(89)   Nguyen, T. A. D.; Goldsmith, B. R.; Zaman, H. T.; Wu, G.; Peters, B.; Hayton, T. W. Synthesis and Characterization of a Cu14 Hydride Cluster Supported by Neutral Donor Ligands. *Chem. Eur. J.* **2015**, *21*, 5341–5344.

(90)   Romero, E. A.; Jazzar, R.; Bertrand, G. (CAAC)CuX-Catalyzed Hydroboration of Terminal Alkynes with Pinacolborane Directed by the X-Ligand. *J. Organomet. Chem.* **2017**, *829*, 11–13.

(91)   Yang, H.; Wang, Y.; Zheng, N. Stabilizing Subnanometer Ag(0) Nanoclusters by Thiolate and Diphosphine Ligands and Their Crystal Structures. *Nanoscale* **2013**, *5*, 2674–2677.

(92)   Dhayal, R. S.; Liao, J.-H.; Liu, Y.-C.; Chiang, M.-H.; Kahlal, S.; Saillard, J.-Y.; Liu, C. W. [Ag 21 {S 2 P(O i Pr) 2 } 12] + : An Eight-Electron Superatom. *Angew. Chem. Int. Ed.* **2015**, *54*, 3702 – 3706.

(93)   Wang, Z. Y.; Wang, M. Q.; Li, Y. L.; Luo, P.; Jia, T. T.; Huang, R. W.; Zang, S. Q.; Mak, T. C. W. Atomically Precise Site-Specific Tailoring and Directional Assembly of Superatomic Silver Nanoclusters. *J. Am. Chem. Soc.* **2018**, *140*, 1069–1076.

(94)   AbdulHalim, L. G.; Bootharaju, M. S.; Tang, Q.; Del Gobbo, S.; AbdulHalim, R. G.; Eddaoudi, M.; Jiang, D. E.; Bakr, O. M. Ag29(BDT)12(TPP)4: A Tetravalent Nanocluster. *J. Am. Chem. Soc.* **2015**, *137*, 11970–11975.

(95)   Pan, S.; Saha, R.; Mandal, S.; Chattaraj, P. K. σ-Aromatic Cyclic M3+ (M = Cu, Ag, Au) Clusters and Their Complexation with Dimethyl Imidazol-2-Ylidene, Pyridine, Isoxazole, Furan, Noble Gases and Carbon Monoxide. *Phys. Chem. Chem. Phys.* **2016**, *18*, 11661–11676.

(96)   Schwarz, H. Relativistic Effects in Gas-Phase Ion Chemistry: An Experimentalist's View. *Angew. Chem. Int. Ed.* **2003**, *42*, 4442–4454.

(97)   Silvi, B.; Savin, A. Classification of Chemical Bonds Based on Topological Analysis of Electron Localization Functions. *Nature* **1994**, *371*, 683–686.

(98)   Stanger, A. Nucleus-Independent Chemical Shifts (NICS): Distance Dependence and Revised Criteria for Aromaticity and Antiaromaticity. *J. Org. Chem.* **2006**, *71*, 883–893.

(99)   Wang, Y.; Monfredini, A.; Deyris, P. A.; Blanchard, F.; Derat, E.; Maestri, G.; Malacria, M. All-Metal Aromatic Cationic Palladium Triangles Can Mimic Aromatic Donor Ligands with Lewis Acidic Cations. *Chem. Sci.* **2017**, *8*, 7394–7402.

(100) Yang, L. M.; Frauenheim, T.; Ganz, E. Properties of the Free-Standing Two-Dimensional Copper Monolayer. *J. Nanomater.* **2016**, *2016*, 1-6.

(101) Chakraborty, I.; Pradeep, T. Atomically Precise Clusters of Noble Metals: Emerging Link between Atoms and Nanoparticles. *Chem. Rev.* **2017**, *117*, 8208–8271.

(102) Yang, L. M.; Dornfeld, M.; Frauenheim, T.; Ganz, E. Glitter in a 2D Monolayer. *Phys. Chem. Chem. Phys.* **2015**, *17*, 26036–26042.

(103) Yang, L. M.; Frauenheim, T.; Ganz, E. The New Dimension of Silver. *Phys. Chem. Chem. Phys.* **2015**, *17*, 19695–19699.

(104) Ringe, S.; Morales-Guio, C. G.; Chen, L. D.; Fields, M.; Jaramillo, T. F.; Hahn, C.; Chan, K. Double Layer Charging Driven Carbon Dioxide Adsorption Limits the Rate of Electrochemical Carbon Dioxide Reduction on Gold. *Nat. Commun.* **2020**, *11*, 33.

(105) Li, F.; Thevenon, A.; Rosas-Hernández, A.; Wang, Z.; Li, Y.; Gabardo, C. M.; Ozden, A.; Dinh, C. T.; Li, J.; Wang, Y.; Edwards, J. P.; Xu, Y.; McCallum, C.; Tao, L.; Liang, Z. Q.; Luo, M.; Wang, X.; Li, H.; O'Brien, C. P.; Tan, C. S.; Nam, D. H.; Quintero-Bermudez, R.; Zhuang, T. T.; Li, Y. C.; Han, Z.; Britt, R. D.; Sinton, D.; Agapie, T.; Peters, J. C.; Sargent, E. H. Molecular Tuning of CO2-to-Ethylene Conversion. *Nature* **2020**, *577*, 509–513.

(106) Xie, C.; Niu, Z.; Kim, D.; Li, M.; Yang, P. Surface and Interface Control in Nanoparticle Catalysis. *Chem. Rev.* **2020**, *120*, 1184–1249.

(107) Zhu, W.; Michalsky, R.; Metin, Ö.; Lv, H.; Guo, S.; Wright, C. J.; Sun, X.; Peterson, A. A.; Sun, S. Monodisperse Au Nanoparticles for Selective Electrocatalytic Reduction of CO2 to CO. *J. Am. Chem. Soc.* **2013**, *135*, 16833–16836.

(108) Kauffman, D. R.; Alfonso, D.; Matranga, C.; Qian, H.; Jin, R. Experimental and Computational Investigation of Au 25 Clusters and CO 2: A Unique Interaction and Enhanced Electrocatalytic Activity. *J. Am. Chem. Soc.* **2012**, *134*, 10237–10243.

(109) Hori, Y.; Murata, A.; Takahashi, R.; Suzuki, S. Electrochemical Reduction of Carbon Monoxide to Hydrocarbons at Various Metal Electrodes in Aqueous Solution. *Chem. Lett.* **1987**, *16*, 1665–1668.

(110) Wang, S. G.; Liao, X. Y.; Cao, D. B.; Huo, C. F.; Li, Y. W.; Wang, J.; Jiao, H. Factors Controlling the Interaction of CO2 with Transition Metal Surfaces. *J. Phys. Chem. C* **2007**, *111*, 16934–16940.

(111) Feaster, J. T.; Shi, C.; Cave, E. R.; Hatsukade, T.; Abram, D. N.; Kuhl, K. P.; Hahn, C.; Nørskov, J. K.; Jaramillo, T. F. Understanding Selectivity for the Electrochemical Reduction of Carbon Dioxide to Formic Acid and Carbon Monoxide on Metal Electrodes. *ACS Catal.* **2017**, *7*, 4822–4827.

(112) Eren, B.; Weatherup, R. S.; Liakakos, N.; Somorjai, G. A.; Salmeron, M. Dissociative Carbon Dioxide Adsorption and Morphological Changes on Cu(100) and Cu(111) at Ambient Pressures. *J. Am. Chem. Soc.* **2016**, *138*, 8207–8211.

(113) Ko, J.; Kim, B. K.; Han, J. W. Density Functional Theory Study for Catalytic Activation and Dissociation of CO2 on Bimetallic Alloy Surfaces. *J. Phys. Chem. C* **2016**, *120*, 3438–3447.

(114) Kuhl, K. P.; Cave, E. R.; Abram, D. N.; Jaramillo, T. F. New Insights into the Electrochemical

Reduction of Carbon Dioxide on Metallic Copper Surfaces. *Energy Environ. Sci.* **2012**, *5*, 7050–7059.

(115) Nie, X.; Esopi, M. R.; Janik, M. J.; Asthagiri, A. Selectivity of CO2 Reduction on Copper Electrodes: The Role of the Kinetics of Elementary Steps. *Angew. Chem. Int. Ed.* **2013**, *52*, 2459–2462.

(116) Jin, L.; Tolentino, D. R.; Melaimi, M.; Bertrand, G. Isolation of Bis(Copper) Key Intermediates in Cu-Catalyzed Azide-Alkyne "click Reaction. *Sci. Adv.* **2015**, *1* , e1500304.

(117) Romanov, A. S.; Bochmann, M. Synthesis, Structures and Photoluminescence Properties of Silver Complexes of Cyclic (Alkyl)(Amino)Carbenes. *J. Organomet. Chem.* **2017**, *847*, 114–120.

(118) Romanov, A. S.; Becker, C. R.; James, C. E.; Di, D.; Credgington, D.; Linnolahti, M.; Bochmann, M. Copper and Gold Cyclic (Alkyl)(Amino)Carbene Complexes with Sub-Microsecond Photoemissions: Structure and Substituent Effects on Redox and Luminescent Properties. *Chem. Eur. J.* **2017**, *23*, 4625–4637.

(119) Armarego, W. L. F.; Chai, C. L. L. *Purification of Laboratory Chemicals*, 5th ed.; Elsevier, 2003.

(120) Nguyen, P.; Lesley, G.; Taylor, N. J.; Marder, T. B.; Pickett, N. L.; Clegg, W.; Elsegood, M. R. J.; Norman, N. C. Oxidative Addition of B-B Bonds by Rhodium(I) Phosphine Complexes: Molecular Structures of B2cat2 (Cat = 1,2-O2C6H4) and Its 4-But and 3,5-But2 Analogs. *Inorg. Chem.* **1994**, *33*, 4623–4624.

(121) G. M. Sheldrick. A Short History of SHELX. *Acta Crystallogr. A* **2008**, *64*, 112–122.

(122) O. V. Dolomanov, L. J. Bourhis, R. J. Gildea, J. A. K. Howard, H. P. OLEX2: A Complete Structure Solution, Refinement and Analysis Program. *J. Appl. Cryst.* **2009**, *42*, 339–341.

(123) Spek, A. L. CheckCIF Validation ALERTS: What They Mean and How to Respond. *Acta Crystallogr. Sect. E Crystallogr. Commun.* **2020**, *76*, 1–11.

(124) Frisch, M. J.; Trucks, G. W.; Schlegel, H. B.; Scuseria, G. E.; Robb, M. A.; Cheeseman, J. R.; Scalmani, G.; Barone, V.; Mennucci, B.; Petersson, G. A.; Nakatsuji, H.; Caricato, M.; Li, X.; Hratchian, H. P.; Izmaylov, A. F.; Bloino, J.; Zheng, G.; Sonnenberg, J. L.; Hada, M.; Ehara, M.; Toyota, K.; Fukuda, R.; Hasegawa, J.; Ishida, M.; Nakajima, T.; Honda, Y.; Kitao, O.; Nakai, H.; Vreven, T.; Montgomery, J. A. Jr.; Peralta, J. E.; Ogliaro, F.; Bearpark, M.; Heyd, J. J.; Brothers, E.; Kudin, K. N.; Staroverov, V. N.; Keith, T.; Kobayashi, R.; Normand, J.; Raghavachari, K.; Rendell, A.; Burant, J. C.; Iyengar, S. S.; Tomasi, J.; Cossi, M.; Rega, N.; Millam, J. M.; Klene, M.; Knox, J. E.; Cross, J. B.; Bakken, V.; Adamo, C.; Jaramillo, J.; Gomperts, R.; Stratmann, R. E.; Yazyev, O.; Austin, A. J.; Cammi, R.; Pomelli, C.; Ochterski, J. W.; Martin, R. L.; Morokuma, K.; Zakrzewski, V. G.; Voth, G. A.; Salvador, P.; Dannenberg, J. J.; Dapprich, S.; Daniels, A. D.; Farkas, O.; Foresman, J. B.; Ortiz, J. V.; Cioslowski, J.; Fox, D. J. *Gaussian 09, Rev. D.01*. Gaussian, Inc.: Wallingford, CT 2013.

(125) Bootsma, A.; Wheeler, S. Popular Integration Grids Can Result in Large Errors in DFT-Computed Free Energies. *ChemRxiv* **2019**. https://doi.org/10.26434/chemrxiv.8864204.

(126) Hohenberg, P.; Kohn, W. Inhomogeneous Electron Gas. *Phys. Rev.* **1964**, *136*, B864–B871.

(127) Kohn, W.; Sham, L. J. Self-Consistent Equations Including Exchange and Correlation Effects. *Phys. Rev.* **1965**, *140*, A1133–A1138.

(128) Andrae, D.; Häußermann, U.; Dolg, M.; Stoll, H.; Preuß, H. Energy-Adjusted Ab Initio Pseudopotentials for the Second and Third Row Transition Elements. *Theor. Chim. Acta* **1990**, *77*, 123–141.

(129) Legault, C. Y. *CYLview, 1.0b.* Université de Sherbrooke 2009.

(130) Peltier, J. L.; Soleilhavoup, M.; Martin, D.; Jazzar, R.; Bertrand, G. All computational results are available for download free of charge from UCSD Library Digital Collections. Absolute Templating of M(111) Cluster Surrogates by Galvanic Exchange. UC San Diego Library Digital Collections: Dataset (https://doi.org/10.6075/J0T15256).

(131) Lu, T.; Chen, F. Multiwfn: A Multifunctional Wavefunction Analyzer. *J. Comput. Chem.* **2012**, *33*, 580–592.

(132) Goddard, T. D.; Huang, C. C.; Meng, E. C.; Pettersen, E. F.; Couch, G. S.; Morris, J. H.; Ferrin, T. E. UCSF ChimeraX: Meeting Modern Challenges in Visualization and Analysis. *Protein Sci.* **2018**, *27*, 14–25.

(133) Clark, S. J.; Segall, M. D.; Pickard, C. J.; Hasnip, P. J.; Probert, M. I. J.; Refson, K.; Payne, M. C. First Principles Methods Using CASTEP. *Zeitschrift fur Krist.* **2005**, *220*, 567–570.

Chapter 5 – Ancillary Ligand-free Copper-Catalyzed Hydrohydrazination of Terminal Alkynes

5.1   Introduction

Since C−N bonds are scattered throughout natural products, and pharmaceuticals, the construction of these bonds can serve as key building blocks leading to industrially and academically relevant compounds. Despite well-established and widely investigated protocols for condensation reactions between amines and carbonyls in synthesizing imines and enamines,[1,2] the hydroamination reaction, the atom economical approach of adding N-H bonds across unsaturated carbon substrates, has developed into a versatile and functional group tolerant alternative.[3–5] However, this field has had many challenges in the design of effective catalysts, especially concerning intermolecular transformations. When considering the overall thermodynamic favorability of these reactions,[5–7] this struggle is especially surprising. However, the high temperatures typically required to overcome the activation barrier of coupling two electron rich species, namely an amine and an unsaturated carbon chain, actually ends up shifting the equilibrium toward the starting materials due to the high negative entropy associated with the reaction.[8]
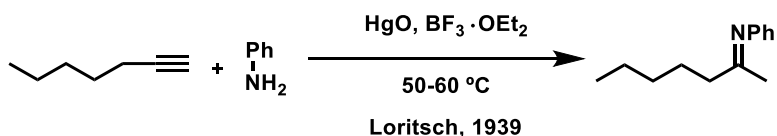
Scheme 5.1: The first transition metal catalyzed hydroamination catalysts.

Despite these challenges, one of the earliest examples of transition metal catalyzed hydroamination, in 1939 by Loritsch *et al.*, involved the use of mercury oxide to catalyze the intermolecular hydroamination of 3-octyne and 1-heptyne with aniline (Scheme 5.1).[9] Afterwards, throughout the 20th century, less toxic methodologies have been developed to circumvent the challenges of the high negative entropy, especially many intramolecular transformations.[10,11,12] In 1992, one of the earliest intermolecular early transition metal catalysts that could transform internal alkynes, Cp$_2$Zr(NHAr)$_2$, was developed by Bergman *et al.* which was able to add aniline derivatives across internal alkynes and allenes (Scheme 5.2).[13] Coincidentally, Livinghouse *et al.* was also able to exploit internal alkynes in 1992 but by an intramolecular reaction with their CpTiCl$_3$ catalyst (Scheme 5.2).[14] Furthermore, lanthanides[15] were demonstrated to catalyze

hydroamination reactions. However, early transition metals and lanthanides have a major drawback in that they are extremely oxophilic and as such, they are highly sensitive to air with low functional group tolerance.[16,17]
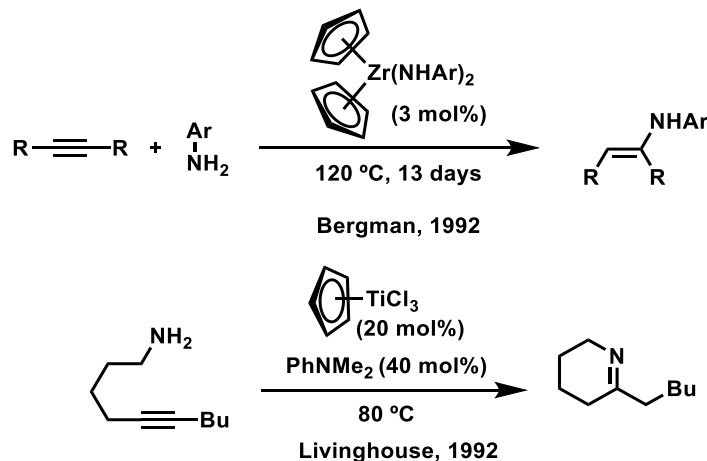
Scheme 5.2: Historical examples of early transition metals capable of hydroamination with internal alkynes.

In contrast, late transition metals have the advantage of high functional group tolerance and air stability, but they are susceptible to amine poisoning leading to catalyst degradation. Yet, a number of palladium and nickel catalyzed hydroamination reactions were discovered in the 20th century, some of which were intermolecular, albeit with relative high catalyst loadings.[12,18–21] When compared to late transition metals such as palladium, however, coinage metals, gold in particular, engender ideal catalytic systems for this transformation. This is because they have a lower propensity for β-hydride elimination which largely prevents chain walking.[22] Thus, they tend to simplify reactions with unsaturated pi bonds and give a narrower product distribution. Gold, with its strong carbophilicity from relativistic effects, also has a penchant to activate alkenes and alkynes leading to highly active catalysts.[23] As the first example of gold-catalyzed hydroamination, in 1987, Utimoto *et al.* was able to achieve the intramolecular formation of 2,3,4,5-tetrahydropyridines from 5-alkynyl-amines using a simple gold(III) salt (Scheme 5.3).[24] Because of the challenges associated with intermolecular hydroamination reactions, new gold catalysts were developed to advance this field.

$$R_1\text{---}\!\!\equiv\!\!\overset{}{\underset{\underset{H_2N}{\big|}}{}}\!\!R_2 \quad\xrightarrow[\text{CH}_3\text{CN, RT, 12 hrs.}]{\substack{\text{NaAuCl}_4\cdot\text{H}_2\text{O}\\(5\text{ mol\%})}}\quad$$

Utimoto, 1987
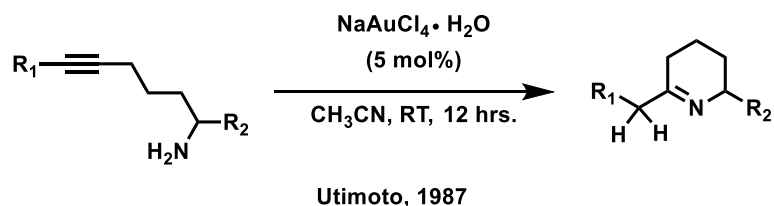
Scheme 5.3: First example of gold catalyzed intramolecular hydroamination to form 2,3,4,5-tetrahydropyridines.

5.2   Intermolecular Gold(I) Hydroamination

In 2003, a seminal report by Tanaka *et al.* demonstrated that simple cationic Au(I) complexes, starting from (PPh₃)Au-Me in the presence of an acidic promoter, underwent intermolecular hydroamination with alkynes and aniline derivatives to furnish ketimines. Since Au(I) is much less acidic than Au(III), the lesser oxophilicity leads to a lower propensity for catalyst poisoning and a higher degree of air stability.[25] Yet, given that high temperatures are normally required to effect these transformations and that these catalysts are inhibited, in part, by the presence of amines, carbenes were a natural ligand choice. Their strong σ-donating nature and ambiphilicity engender robust interactions with transition metals, stabilize proposed cationic monoligated Au(I) intermediates, and strongly labilize ligands that are *trans* to them.

$$R_1\!\!\equiv\!\!R_2 \ + \ H_2NR \quad\xrightarrow[\text{70 °C, 0.25 to 24 hrs.}]{\substack{\text{(Ph}_3\text{P)AuMe}\\(0.01\text{ to }0.2\text{ mol\%})\\\text{H}_3\text{PW}_{12}\text{O}_{40}\\(0.05\text{ to }1\text{ mol\%})}}\quad$$

Tanaka, 2003
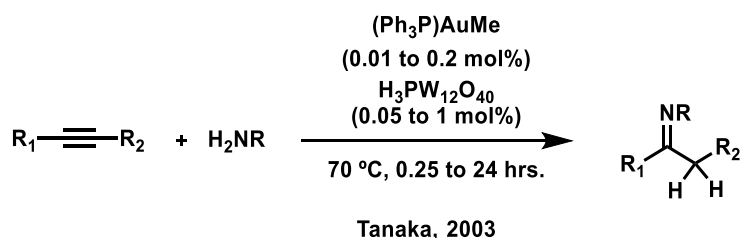
Scheme 5.4: First example of gold(I) catalyzed hydroamination to engender ketimines.

5.2.1   Ambiphilic Carbene Gold Catalyzed Hydroamination with Difficult Substrates.

The first example of carbene catalyzed hydroamination was by Widenhoefer *et al.*, in 2006, who used an in-situ formed NHC stabilized gold triflate catalyst, (IPr)AuOTf (**5.A**), to intramolecularly cyclize

211

unactivated alkenes, *N*-4-pentenyl- and *N*-5-hexenyl-urea at room temperature (Scheme 5.5, top).[26] Strikingly, Widenhoefer *et al.* had previously found that similar transformations occurred 40-80 °C higher for the phosphine stabilized version of the gold catalyst which further emphasizes the importance of carbenes in homogeneous catalysis.[27] Subsequently, by exploiting **5.A** again, two years later, Widenhoefer *et al.* was able to, under mild conditions, catalyze the regio- and stereo-selective formation of (E)-4-(benzyloxycarbonylamino)-2-pentenyl benzoate from 2,3-pentadienyl benzoate with benzyl carbamate (Scheme 5.5, bottom).[28] This system was also able to catalyze several N-unsubstituted carbamates and substituted allenes.
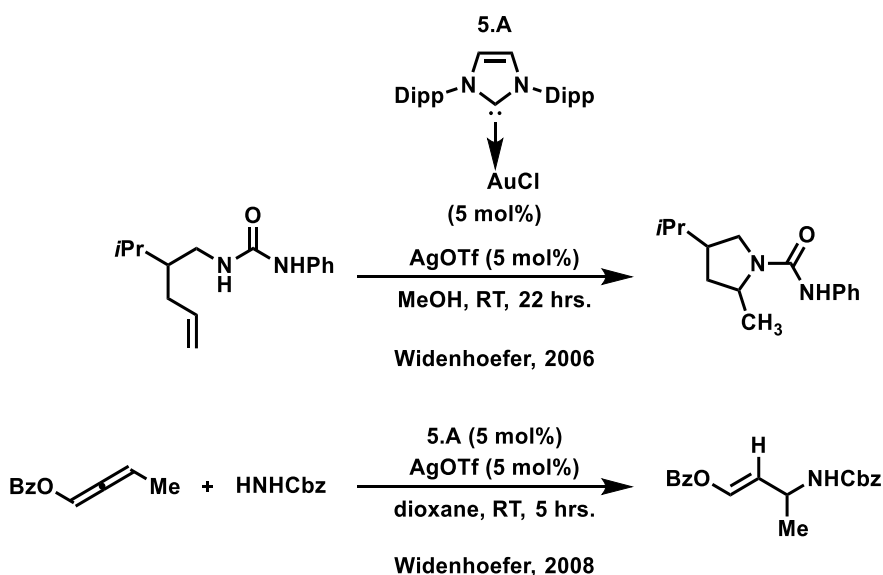
Scheme 5.5: First examples of carbene gold(I), **5.A**, catalyzed hydroamination reactions: intramolecular (top); followed by intermolecular (bottom).

A few months after the intermolecular reaction by Widenhoefer, CAACs were shown to behave as excellent ligands for hydroamination because their strong σ-donation and π-acidity for backbonding form robust bonds with metals. Therefore, it enabled the use of the formidable ammonia substrate. Previously, Bertrand *et al.* isolated the cationic gold(I) active catalyst, (^{Ad}CAAC)Au$^+$ complex (**5.B**), stabilized by η^2-coordinated toluene adduct with a BAr^F anion ($^-$B(C$_6$F$_5$)$_4$), from a halide abstraction with an extremely halophilic silylium cation, [(Tol)SiEt$_3$][BAr^F].[29] In 2008, this new species, **5.B** (note the ammonia complex

itself also catalyzes the reaction and the Bar^F complex can also be formed *in-situ* from a KBAr^F additive and the corresponding gold halide), catalyzed the hydroamination of alkynes and allenes with ammonia to form imines, enamines, and allyl amines, albeit at high temperatures (110-175 °C) (Scheme 5.6).[30] Notably, ammonia (and the parent hydrazine NH$_2$NH$_2$) is known to form extremely strong Werner complexes[31] to transition metals that are too tightly bound to the metal often rendering them inert,[32] and the N-H bond is extremely challenging to cleave even by proton transfer.[33] This, however, further highlights the prowess of CAAC ligands to bind tightly to transition metals, stabilize them at extremely high temperatures, and enable transformations with difficult substrates. Expounding upon these results, Bertand *et al.* were able to catalyze the formation of allylic amines with **5.B** from secondary amines and allenes[34] which then paved the way for a number of other carbene gold catalyzed hydroamination reactions (*e.g.*, with CAAC,[35] Acyclic Diaminocarbene,[36] ENHC,[37] NHC,[38,39] Acyclic Aminooxycarbene,[40] the extremely bulky IPr** (1,3-bis{2,6-bis[bis(4-tert-butylphenyl)methyl]-4-methylphenyl}imidazol-2-ylidene),[41] and MICs[42,43]).
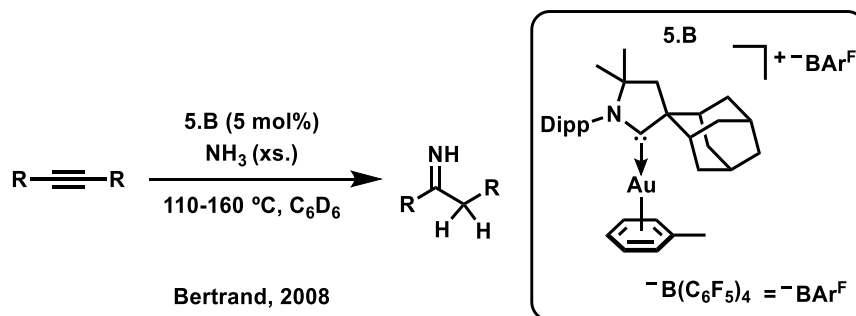
Scheme 5.6: An example of (^{Ad}CAAC)Au$^+$ and the weakly coordination BAr^F anion, **5.B**, undergoing catalysis with ammonia and an internal alkyne, 3-hexyne.

Beyond ammonia, CAACs also empower catalysis with other difficult substrates in hydroamination including the parent hydrazine in a process known as hydrohydrazination. As previously mentioned, the parent hydrazine, NH$_2$NH$_2$, has the tendency to form inert Werner complexes, but it also often reduces metals to inactive M^0 nanoparticles.[44,45] However, its transformation is highly desirable as an abundant feedstock chemical with over two hundred thousand tons produced annually.[46] Despite the economic interest, it wasn't until 2010 when the first report of a transition metal catalyzed process was able to

213

functionalize hydrazine. Upon using an electron rich, bulky phosphine type ligand, Stradiotto *et al.*, demonstrated that Palladium cross-coupling reactions could tolerate the use of hydrazine with aryl chlorides and tosylates.[47] In 2011, Bertrand *et al.* discovered that CAACs could facilitate a hydrohydrazination with the parent hydrazine on a variety of unactivated alkynes, diynes, and allenes to lead to hydrazones and *N*-heterocycles at elevated temperatures (90-110 °C).[48] Moreover, the cationic hydrazine Werner complex itself, **5.B$_1$**, was also able to efficiently catalyze the reaction which demonstrates these complexes' enhanced stability against reduction (Scheme 5.7). Yet again, highly ambiphilic carbenes, with their strong trans effect and trans influence, were able to overcome the formation of Werner complexes to still enable productive catalysis.
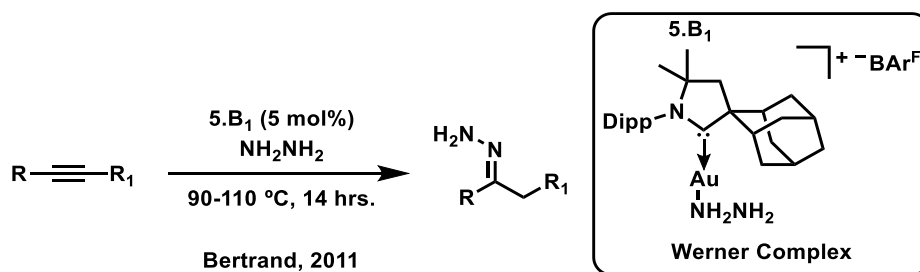
Scheme 5.7: The catalytically active Werner complex, **5.B$_1$**, can undergo this challenging hydrohydrazination.

Building upon these results, Bertrand *et al.* discovered that an anti-Bredt NHC gold complex could catalyze the hydrohydrazination of a number of terminal alkynes, but this time at room temperature (Scheme 5.8).[49] Interestingly, this NHC features a pyramidalized unhindered amino substituent adjacent to the carbene center preventing lone pair donation into the carbene thereby making it highly ambiphilic and analogous to the CAAC ligand in terms of its electronics. However, the difference with the CAAC ligand is that this sterically unencumbered carbene was better able to fit the substrates on the cationic gold center leading to the pronounced improvement in catalytic activity. Afterwards, an extremely strong σ-donating carbene (saNHC)[50] was also able to undergo hydrohydrazination of alkynes at room temperature.
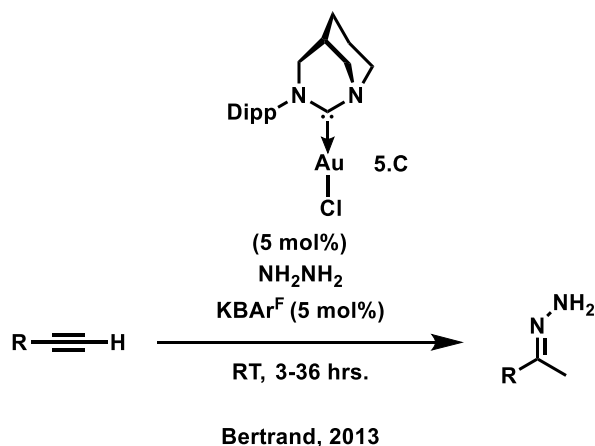
Scheme 5.8: Unhindered, ambiphilic anti-bredt NHC gold(I) (**5.C**) catalyzes the hydrohydrazination at room temperature.

The importance of carbene stabilization for the room temperature hydrohydrazination with gold complexes was further highlighted in our recent report. In contrast to the intense research effort into the design of ligands with tailored secondary interactions, we investigated the ligand-metal bond itself. By screening phosphines and a variety of carbene ligands, we provided evidence that ambiphilic carbenes, especially the BiCAAC gold complex (**5.D**), led to the most pronounced catalytic activity (Scheme 5.9).[51] Because the highly ambiphilic BiCAAC shielded the metal from catalyst degradation, stabilized the key $\pi-$alkyne gold complex intermediate, and favored a low barrier for proton transfer, high turnover numbers (TON) were obtained in the hydroamination and the hydrohydrazination of alkynes.
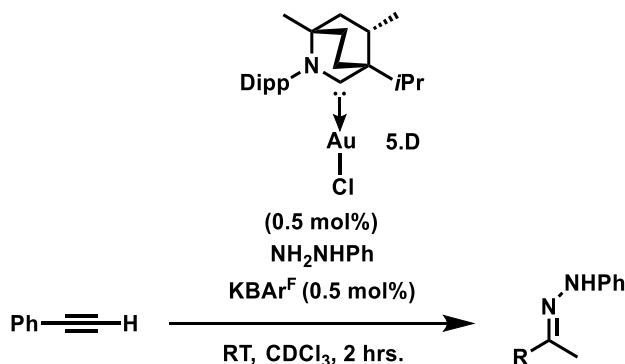
Scheme 5.9: The ambiphilic BiCAAC gold(I) (**5.D**) outcompetes many state-of-the-art gold complexes and is a highly efficient catalyst for the hydrohydrazination at room temperature. Notably, at 80 °C, neat, and with a catalyst loading of 0.0025 mol%, **5.D** can achieve an impressive TON of 36,700.

5.3   Copper Catalyzed Hydrohydrazination

Because of the expensive nature of gold complexes and their requirement for state-of-the-art stabilizing ligands, the development of new catalysts with potential industrial relevance has been hampered. Copper, gold's lighter congener, on the other hand, is an environmentally friendly and earth abundant first row transition metal. As opposed to the well-established field of gold catalyzed hydroamination, there are seldom examples of catalytic hydroamination reactions with copper. Interestingly, copper was recognized early in the history of transition metal hydroamination reactions as having potential to be a competent catalyst in the cyanoethylation of aromatic amines.[52] Despite these observations, only recently have some copper-catalyzed hydroaminations been discovered including intramolecular reactions[53–57] and to a lesser extent, intermolecular reactions.[58–61]

Given the challenges associated with the use of the parent hydrazine, and the lack of intermolecular reactions known with copper at the time, we sought to accomplish an intermolecular copper-catalyzed hydrohydrazination. Since very few examples of catalysts, beyond gold, were reported that could endure this challenging reagent, we investigated if carbene, especially ambiphilic carbene, copper complexes could also promote the hydrohydrazination of alkynes (Figure 5.1). Surprisingly, while CAACs were found to be active in this catalytic process, a selective ancillary ligand free copper-catalyzed hydrohydrazination was discovered with terminal alkynes. This methodology tolerated a broad range of functional groups, allowed for the synthesis of symmetrical and unsymmetrical azines, and could be extended to hydrazine derivatives and amines.

216

5.4   Results & Discussion
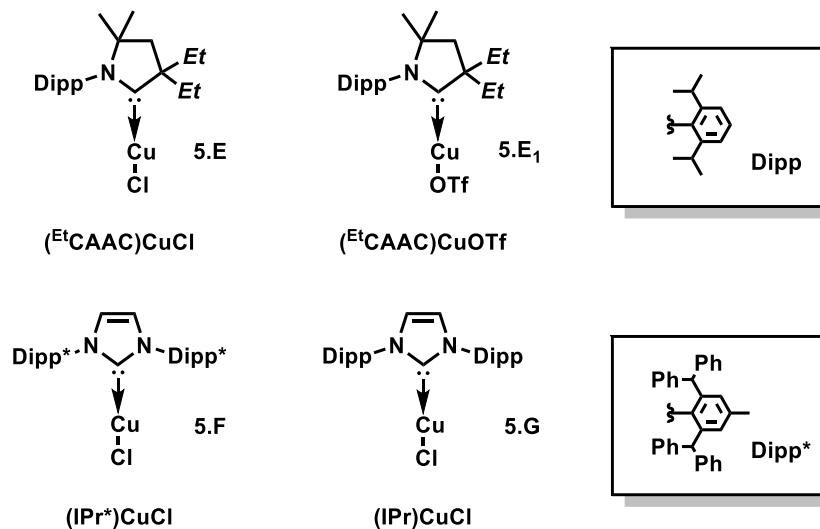
Figure 5.1: A range of carbene copper active catalyst precursors considered for hydrohydrazination.

We began our investigation by exploring the reaction between parent hydrazine and phenyl acetylene as a model substrate which would form the corresponding hydrazone **5.1.A**. Because our previously describe carbene gold catalyzed hydroaminations demonstrated pronounced activity in the presence of the weakly coordinating $^-B(C_6F_5)_4$ anion ($^-BAr^F$),[30,34,35,48,49] we began with 5 mol% KBAr^F as an additive. Additionally, we started with 5 mol% copper carbene catalysts at 100 °C for 12 hours in benzene (Table 5.1, entry 1-4). Under these conditions, **5.E** (Figure 5.1)[62] displayed modest catalytic activity (Table 5.1, entry 1). Upon switching from the $^-Bar^F$ anion to triflate, we found **5.E₁** (Figure 5.1)[62] behaves poorly in this reaction most likely due to the more coordinating triflate anion (Table 5.1, entry 2). The complex **5.F** (Figure 5.1)[63] showed a slight improvement in the yield over the CAAC complex (Table 5.1, entry 3); however, the much bulkier **5.G** featuring the IPr* ligand (Figure 5.1)[64] (buried volume 50.4%)[65] afforded complete conversion, and we were able to isolate the product in 83% yield (Table 5.1, entry 4).

Table 5.1: Optimization of copper-catalyzed hydrohydrazination of terminal alkynes.

$$\text{Ph}\!\!-\!\!\!\equiv \;+\; NH_2NH_2 \xrightarrow[\substack{\text{Additive (5 mol \%)}\\\text{Solvent, 100 °C, 12 h}}]{\text{Cat. (5 mol \%)}} \;\; \underset{\text{5.1.A}}{\overset{\displaystyle N\!\!\diagup^{NH_2}}{\underset{Ph}{\overset{\|}{\diagup}}}}$$
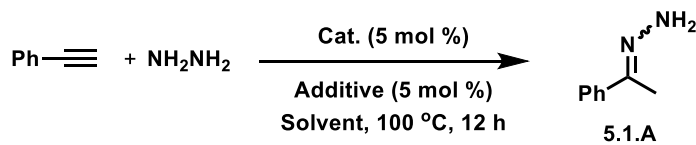
Entry	Catalyst	Additive	Solvent	Yield[a] (%)
1	(CAAC)CuCl	KBAr^F	Benzene	64
2	(CAAC)CuOTf	-	Benzene	22
3	(IPr)CuCl	KBAr^F	Benzene	66
4	(IPr*)CuCl	KBAr^F	Benzene	83[b]
5	-	KBAr^F	Benzene	0
6	CuCl	-	Benzene	0
7	(IPr*)CuCl	-	Benzene	0
8	CuCl	KBAr^F	Benzene	99
9	CuCl$_2$	KBAr^F	Benzene	86
10	CuCl	KBAr^F	THF	0
11	CuCl	KBAr^F	CHCl$_3$	0
12	CuCl	KBAr^F	Toluene	99
13	CuCl	KBPh$_4$	Benzene	< 1
14	CuCl	KSbF$_6$	Benzene	< 1
15	CuCl	AgOTf	Benzene	< 1
16	CuCl	HBAr^F	Benzene	0
17	-	HBAr^F	Benzene	0
18	CuCl	KBAr^F/Hg(0)	Benzene	99

[a]Determined by ^1H NMR spectroscopy using hexamethylbenzene as an internal standard; [b]Isolated.

At this stage, control experiments were performed to confirm the importance of the copper complex and additive. Unsurprisingly, the additive itself did not catalyze the hydrohydrazination (Table 5.1, entry 5), nor did the copper chloride, in the absence of any additive, lead to conversion with or without ligand (Table 5.1, entry 6 & 7). However, the carbene ligand free combination of copper chloride and KBAr^F proved to be an extremely effective catalyst and resulted in the quantitative formation of hydrazone (Table 5.1, entry 8). Interestingly, replacing CuCl by the more Lewis acidic CuCl$_2$ also led to a competent catalyst but resulted in a lower yield of 86% (Table 5.1, entry 9). Presumably, the stronger Lewis acidity led to a greater susceptibility to forming inert Werner complexes. Notably, the catalysis was more effective in more nonpolar solvents such as benzene and toluene (Table 5.1, entry 10-12). We then thought that it was prudent to survey various additives such as KBPh$_4$, KSbF$_6$, and AgOTf, but all of these more coordinating anion

additives shut down the catalysis almost entirely (Table 5.1, entry 13-15). Since Bergman *et al.*
demonstrated that the hydroamination of alkenes with anilines could be promoted by $H(Et_2O)_{2.5}BAr^F$, we
tested the hydrohydrazination in the presence of 5 mol% of this Brønsted acid,[66] but no conversion occurred
(Table 5.1, entries 16 and 17). However, this was expected given that the basic hydrazine would
immediately deprotonate the strong acid and prevent any further transformation. The catalysis, therefore,
is ostensibly transpiring through Lewis acid in lieu of Brønsted acid catalysis. There was also the possibility
that the hydrohydrazination was catalyzed through colloidal copper nanoparticles, especially due to the
strong reducing nature of the parent hydrazine.[44,45] To determine if there was heterogeneous catalysis, we
performed a mercury drop test as mercury is known to form an amalgam with copper, but the catalysis
persisted anyway (Table 5.1, entry 18). This is consistent with a homogenous Lewis acid catalyzed process.

Table 5.2: Scope of the hydrohydrazination of terminal alkynes with NH_2NH_2.
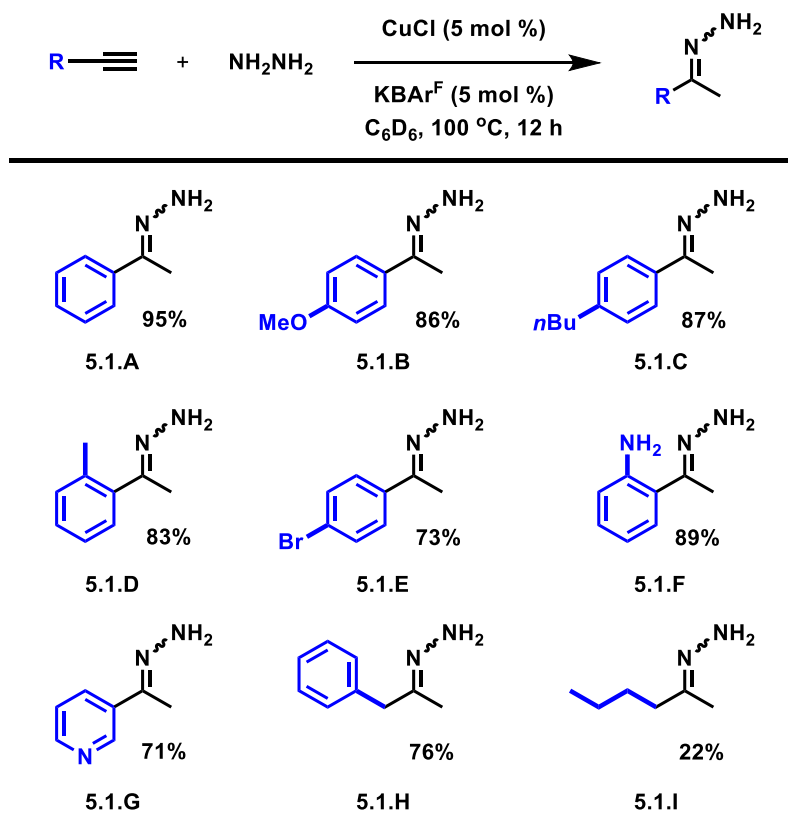
We then evaluated the scope of the reaction using our optimized conditions: CuCl (5 mol%), KBAr^F (5 mol%), and benzene as the solvent at 100 °C for 12 hours (Table 5.1, entry 8). As a result, we discovered that a broad range of terminal aryl alkynes reacted with the parent hydrazine to engender the desired hydrazones (**5.1.A**-**5.1.I**) which were isolated by neutral alumina column chromatography in good to excellent yields (Table 5.2). Interestingly, despite the presence of an *ortho*-amino substituent, **5.1.F** only led to an intermolecular hydrohydrazination reaction instead of an inter- or intramolecular hydroamination reaction with the pendant amine. Next, the more electron rich benzyl group worked well to form **5.1.H** with this catalytic system, but the limit was found upon trying an alkyl substituted alkyne, namely 1-hexyne, which required a longer reaction time and resulted in a much lower yield of **5.1.I**. To demonstrate the overall scalability of this hydrohydrazination with the parent hydrazine, we conducted a gram-scale synthesis on the phenylacetylene substrate. Under the optimized conditions, 1.17 g (89% yield) of the **5.1.A** was obtained.

Table 5.3: Scope of amine substrate in hydroamination and hydrohydrazination of phenyl acetylene.
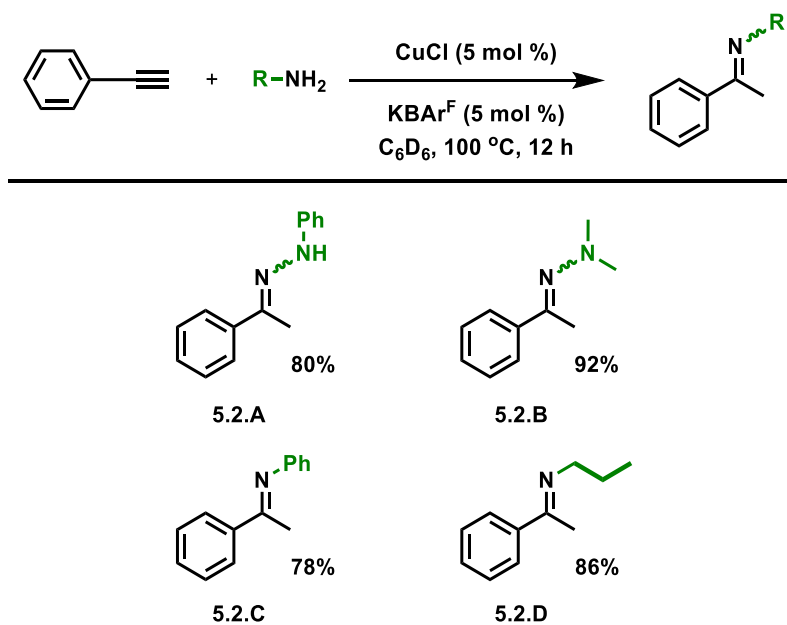
Since we were able to achieve the hydrohydrazination with the challenging parent hydrazine, we hypothesized that our reaction should extend to a broad range of amine substrates (**5.2.A**-**5.2.D**). Indeed,

upon conducting this reaction in the presence of hydrazine derivatives such as phenylhydrazine and 1,1-dimethylhydrazine, we obtained **5.2.A** and **5.2.B** in good to excellent yields (Table 5.3). Moreover, our system proved effective at catalyzing the hydroamination with aromatic amines such as aniline and even the more difficult electron rich propylamine which still gave **5.2C** and **5.2D** in good yields (Table 5.3).

Table 5.4: Bis(hydrohydrazination) of terminal alkynes.

92%	89%
5.3.A	5.3.B
85%	90%
5.3.C	5.3.D
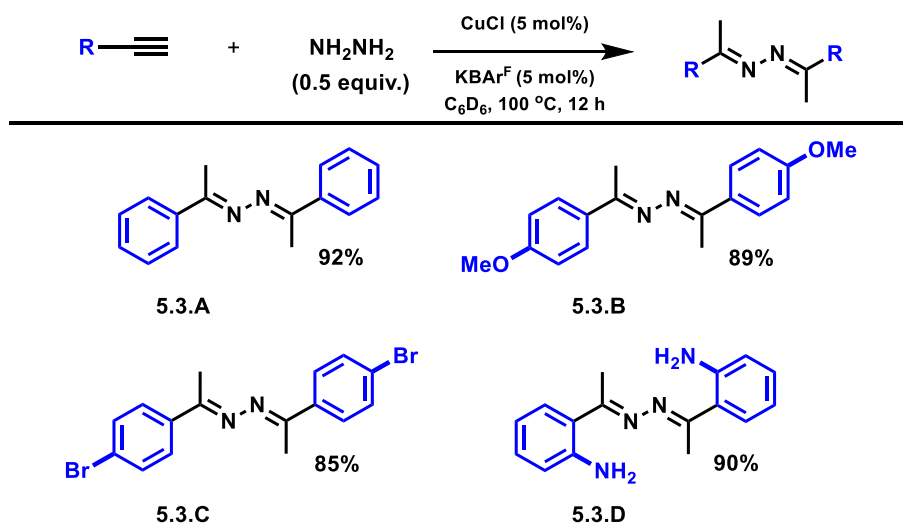
Notably, while exploring the catalytic hydrohydrazination, we observed, by ^{1}H NMR, the subtle formation of trace amounts of azine. The formation of these products resulted from a bis-hydrohydrazination reaction that occurred when the hydrazone product underwent another subsequent hydrohydrazintion of a terminal alkyne catalyzed by copper. Because azines are useful synthetic intermediates that have recently received much attention due to their interesting physical and biological properties, we decided to pursue their synthesis. Under the standard conditions, using a substoichiometric amount of parent hydrazine, a one-half equivalent, we were able to obtain the corresponding symmetrical azines (**5.3.A**-**5.3.D**) in good to excellent yields (Table 5.4). Our synthetic protocol was effective at catalyzing the formation of a broad range of aryl azines from electron poor to electron rich (Table 5.4). Furthermore, by the stepwise addition of two different alkynes, the first of which being phenyl acetylene, we were able to cleanly prepare a range of unsymmetrical azines (**5.4.A**-**5.4.D**, Table 5.5).

Table 5.5: Stepwise synthesis of unsymmetrical azines.
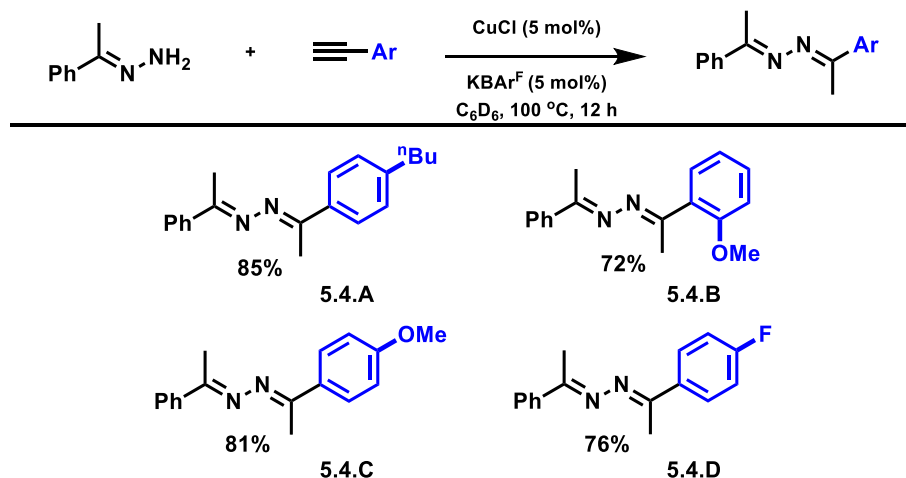
5.5 Conclusion

Despite the significant emphasis on the need for auxiliary ligands in challenging transition metal-catalyzed hydroamination processes, including hydrohydrazination, our results demonstrate that it is possible to over-engineer these systems. We discovered that simple copper salts could catalyze this challenging intermolecular hydrohydrazination previously described for sophisticated carbene gold complexes. In doing so, we have reported the first example of copper-catalyzed hydrohydrazination with the challenging parent hydrazine. Our methodology encompasses a broad range of functional groups, engenders the synthesis of symmetrical and unsymmetrical azines, and can be extended to hydrazine derivatives and amines. In contrast to other metal catalyzed reactions enabling the transformation of parent hydrazine, the catalysis reported here is ancillary ligand-free and therefore economically viable. Future directions involve finding suitable ligands to enable copper to catalyze these challenging transformations at room temperature. There is also room to potentially supplant other expensive ligated gold and precious metal catalyzed processes, including the addition of E-H bonds across unsaturated substrates such as the well-known gold catalyzed hydration of alkynes, with copper salts. Additionally, there is still the challenge of ammonia catalyzed hydroamination with copper. Overall, these results and future directions prompt us

to face the reality that if ligand design becomes superfluous, it becomes too costly to replace precious metals in desirable transformations and thus, it challenges chemists to streamline the design of catalysts to remain industrially relevant.

5.6   Appendix

5.6.1   General Methods & Materials.

All reactions were performed by using standard Schlenk or dry box techniques under an atmosphere of argon. Glassware was dried in an oven overnight at 150 °C or flame dried before use. Benzene, tetrahydrofuran, diethyl ether, n-pentane, and toluene were freshly distilled over Na metal. Hexanes, dichloromethane, and chloroform were freshly distilled over CaH_2. Reagents were of analytical grade, obtained from commercial suppliers, and dried over 4Å molecular sieves. ^1H, ^{13}C, and ^{19}F NMR spectra were obtained with a Bruker Avance 300 MHz, and a Varian INOVA 500 MHz spectrometer. Chemical shifts (δ) were reported in parts per million (ppm) relative to TMS and were referenced to the residual solvent peak. NMR multiplicities are abbreviated as follows: s = singlet, d = doublet, t = triplet, q = quartet, quin = quintet, sex =sextet, m = multiplet, br = broad signal. All spectra were recorded at 298 K unless otherwise noted. Melting points were measured with a MEL-TEMP apparatus. High-resolution mass spectrometry data was collected on an Agilent 6230 TOF-MS at the UC San Diego Mass Spectrometry Laboratory. IR spectra were recorded on thin films using a Jasco 4100 FTIR and attenuated total reflectance (ATR, 3 mm ZnSe plate). All yields were determined with respect to the terminal alkyne.

5.6.2 Experimental Procedures.

Catalytic optimization table.

Ph—≡ + NH₂NH₂ → (Cat. (5 mol %) / Additive (5 mol %) / Solvent, 100 °C, 12 h)
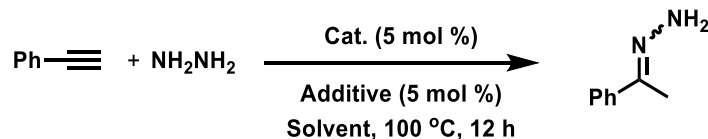
Scheme 5.10: Using Phenyl acetylene as a model substrate, a variety of conditions were optimized for the hydrohydrazination to form hydrazones.

The corresponding catalyst (5 mol.% cat. loading, 0.024 mmol), additive (0.024 mmol), and solvent (0.5 mL) were added to a J-Young NMR tube. Subsequently, the standard (hexamethylbenzene, 0.081 mmol), phenylacetylene (0.48 mmol), and hydrazine (0.53 mmol) were added. Then, the tube was heated to 100 °C for 12 hours and afterwards, ^{1}H NMR spectroscopy was used to determine the yield with respect to the standard.

Catalytic hydrohydrazination or hydroamination of alkynes.

R—≡ + NH₂R → (CuCl (5 mol %) / KBAr^F (5 mol %) / C₆D₆, 100 °C, 12 h)
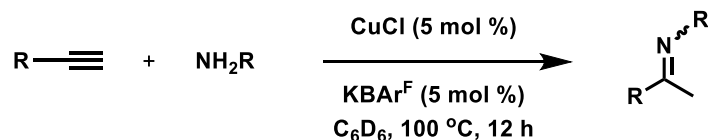
Scheme 5.11: Using optimized conditions, ketimines were synthesized from a range of terminal alkynes and amines.

CuCl (0.024 mmol), KB$_{Ar}$^{F} (B$_{Ar}$^{F}: B[C₆F₅]₄⁻) (0.024 mmol), and C₆D₆ (0.5 mL) were added to a J-Young NMR tube. Subsequently, the standard (hexamethylbenzene, 0.081 mmol), the desired alkyne (0.48 mmol), and the appropriate anhydrous hydrazine or amine (0.53 mmol) were added. Then, the tube was heated to 100 °C for the appropriate length of time. The reaction was monitored by ^{1}H NMR spectroscopy. After completion, the reaction mixture, in an inert argon atmosphere, was passed under a stream of argon through a small pipette column of 5 cm dry neutral alumina [(eluents for hydrazine hydrazones and

derivatives: 5 mL 1:10 benzene/pentane then 10 mL ether)(eluents for amines ketimines derivatives: 15 mL

2:10 ether/pentane)].

Gram-scale hydrohydrazination.

CuCl (0.49 mmol), KB_{Ar}^F (0.49 mmol), and C_6D_6 (10 mL) were added to a Schlenk pressure tube.

Subsequently, phenyl acetylene (9.8 mmol), and anhydrous hydrazine (10.8 mmol) were added. Then, the

mixture was stirred at 100 °C for 12 hours. After completion, reaction mixture, in an inert argon atmosphere,

was passed under a stream of argon through a 15 cm dry neutral alumina (eluents: 30 mL pentane then 30

mL ether); yield 1.17 g, 89%.

Catalytic hydrohydrazination to synthesize symmetrical azines.
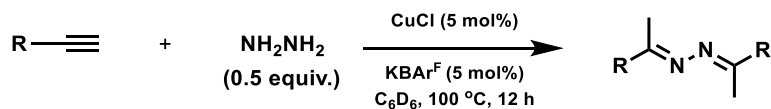
Scheme 5.12: Using a substoichiometric amount of hydrazine and optimized conditions, copper can catalyze the synthesis of symmetrical azines.

CuCl (0.024 mmol), KB_{Ar}^F (0.024 mmol), and C_6D_6 (0.5 mL) were added to a J-Young NMR tube.

Subsequently, the standard (hexamethylbenzene, 0.081 mmol), the desired alkyne (0.48 mmol), and the

anhydrous hydrazine (0.24 mmol) were added. Then, the tube was heated to 100 °C for 12 hours. The

reaction was monitored by ^1H NMR spectroscopy. After completion, the reaction mixture was passed under

a stream of argon through a small pipette column of 5 cm neutral alumina (eluent: 10 mL 1:10

benzene/pentane).

Catalytic hydrohydrazination to synthesize unsymmetrical azines.
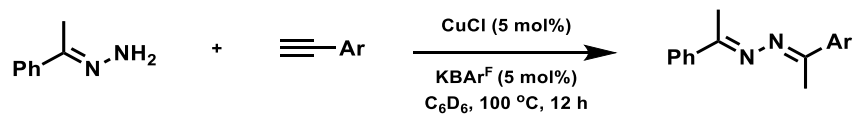
Scheme 5.13: Using a substoichiometric amount of hydrazine and optimized conditions, copper can catalyze the synthesis of symmetrical azines.

CuCl (0.024 mmol), KB_{Ar}^F (0.024 mmol), and C_6D_6 (0.5 mL) were added to a J-Young NMR tube. Subsequently, the standard (hexamethylbenzene, 0.081 mmol), phenyl acetylene (0.48 mmol), and the anhydrous hydrazine (0.48 mmol) were added. Then, the tube was heated to 100 °C for 12 hours. Afterwards, the desired alkyne (0.48 mmol) was added to the reaction mixture and heated for another 12 hours at 100 °C. The reaction was monitored by ^{1}H NMR spectroscopy. After completion, the reaction mixture was passed under a stream of argon through a small pipette column of 5 cm neutral alumina (eluent: 10 mL 1:10 benzene/pentane).

5.6.3 Characterization Data.

5.1.A (1-phenylhydrazonoethane).

Characterization data: ^{1}H NMR (300 MHz, CDCl$_3$): δ = 7.66-7.63 (m, 2H), 7.39-7.30 (m, 3H), 5.35 (br s, 2H), 2.14 (s, 3H) ppm; ^{13}C{^{1}H} NMR (125.7 MHz, CDCl$_3$): δ = 147.5 (C), 139.5 (C), 128.4 (CH), 128.2 (CH), 125.8 (CH), 11.8 (CH$_3$) ppm; **IR** (cm^{-1}): 3385 (br, NH$_2$), 3302 (br), 2921 (vs, NH$_2$) 1590 (vs, C=N); **HRMS ESI** (m/z): [M+H]$^+$ calcd. for [C$_8$H$_{11}$N$_2$]$^+$, 135.0917; found, 135.0918; yield: 61 mg, 95%.
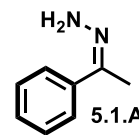
5.1.B (1-(4-methoxyphenyl)-hydrazonoethane).

Characterization data: ^{1}**H NMR** (300 MHz, C_6D_6): δ = 7.72 (d, J = 9.0 Hz, 2H), 6.80 (d, J = 9.0 Hz, 2H), 4.71 (br s, 2H), 3.30 (s, 3H), 1.60 (s, 3H) ppm; ^{13}**C{^{1}H} NMR** (125.7 MHz, C_6D_6): δ =160.1 (C), 145.3 (C), 133.0 (C), 127.1 (CH), 113.9 (CH), 54.8 (CH_3), 10.7 (CH_3) ppm; **IR** (cm^{-1}): 3393 (s), 3305 (br), 3251 (br), 2836 (m), 1602 (C=N); **HRMS ESI** (m/z): [M+H]$^+$ calcd. for $[C_9H_{13}N_2O]^+$, 165.1024; found, 165.1022; yield: 68 mg, 86%.
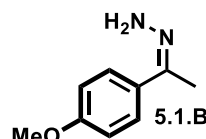
5.1.C (1-(4-butylphenyl)-hydrazonoethane).

Characterization data: ^{1}**H NMR** (300 MHz, C_6D_6): δ = 7.75 (d, J = 4.8 Hz, 2H), 7.08 (d, J = 4.8 Hz, 2H), 4.81 (br s, 2H), 2.46 (t, J = 4.5 Hz, 2H), 1.62 (s, 3H), 1.49 (quin, J = 4.5 Hz, 2H), 1.24 (sex, J = 4.5 Hz, 2H), 0.84 (t, J = 4.5 Hz, 3H) ppm; ^{13}**C{^{1}H} NMR** (125.7 MHz, C_6D_6): δ = 145.4 (C), 142.5 (C), 137.8 (C), 128.6 (CH), 125.8 (CH), 35.7 (CH_2), 33.9 (CH_2), 22.7 (CH_2), 14.2 (CH_3), 10.8 (CH_3) ppm; **IR** (cm^{-1}): 3373 (br, m), 3299 (br, m), 3213 (br, m), 2926 (s), 1600 (s, C=N); HRMS ESI (m/z): [M+H]$^+$ calcd. for $[C_{12}H_{19}N_2]^+$, 191.1540; found, 191.1543; yield: 79 mg, 87%.
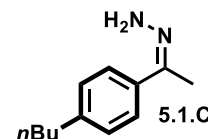
5.1.D (1-(2-methylphenyl)-hydrazonoethane).

Characterization data: (1:1 mixture of cis/trans isomers), ^{1}**H NMR** (300 MHz, CDCl$_3$): δ = 7.29-7.27 (m, 3H), 7.26-7.15 (m, 4H), 7.08-7.04 (m, 1H), 5.28 (s br, 2H), 4.88 (s br, 2H), 2.35 (s, 3H), 2.26 (s, 3H), 2.14 (s, 3H), 2.11 (s, 3H) ppm; ^{13}**C{^{1}H} NMR** (125.7 MHz, CDCl$_3$): δ = 150.0 (C), 149.7 (C), 140.8 (C), 135.5 (C), 135.4 (C), 135.2 (C), 130.7 (CH), 130.7 (CH), 128.8 (CH), 127.9 (CH), 126.8 (CH), 126.7 (CH), 125.8 (CH), 24.5 (CH_3), 20.4 (CH_3), 19.1 (CH_3), 15.7 (CH_3) ppm; **IR** (cm^{-1}): 3377 (br m), 3209 (br
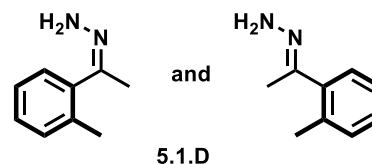
m), 1631 (s, C=N), 1603 (s, C=N); **HRMS ESI** (m/z): [M+H]$^+$ calcd. for [C$_9$H$_{13}$N$_2$]$^+$, 149.1073; found, 149.1072; yield: 59 mg, 83%.

5.1.E (1-(4-bromophenyl)-hydrazonoethane).

Characterization data: ^{1}**H NMR** (300 MHz, CDCl$_3$): δ =7.53-7.45 (m, 4H), 5.38 (br s, 2H), 2.10 (s, 3H) ppm; ^{13}**C{^{1}H} NMR** (125.7 MHz, CDCl$_3$): δ = 146.1 (C), 138.4 (C), 131.5 (CH), 131.5 (CH), 127.2 (CH), 127.2 (CH), 122.2 (C), 11.5 (CH$_3$) ppm; **IR** (cm$^-$ ^{1}): 3391 (br m), 3219 (br, m), 2917 (m), 1597 (s, C=N); **HRMS ESI** (m/z): [M+H]$^+$ calcd. for [C$_8$H$_{10}$BrN$_2$]$^+$, 213.0022; found, 213.0021; yield: 75 mg, 73%.
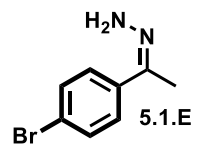
5.1.F (1-(2-aminophenyl)-hydrazonoethane).

Characterization data: ^{1}**H NMR** (300 MHz, C$_6$D$_6$): δ = 7.14 (d, J = 4.5 Hz, 1H), 7.02 (t, J = 4.5 Hz, 1H), 6.68 (t, J = 4.5 Hz, 1H), 6.44 (d, J = 4.5 Hz, 1H), 5.65 (br s, 2H), 4.46 (br s, 2H), 1.58 (s, 3H) ppm; ^{13}**C{^{1}H} NMR** (125.7 MHz, C$_6$D$_6$): δ = 150.0 (C), 147.1 (C), 128.6 (CH), 128.4 (CH), 121.2 (C), 116.5 (CH), 116.4 (CH), 12.0 (CH$_3$) ppm; **IR** (cm^{-1}): 3379 (br s), 3294 (br s), 1605 (vs, C=N); **HRMS ESI** (m/z): [M+H]$^+$ calcd. for [C$_8$H$_{12}$N$_3$]$^+$, 150.1026; found, 150.1028; yield: 64 mg, 89%.
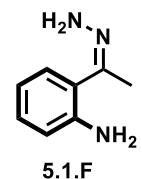
5.1.G (1-(3-Pyridinyl)-hydrazonoethane).

Characterization data: ^{1}**H NMR** (300 MHz, CDCl$_3$): δ = 8.86 (d, J = 1.2 Hz, 1H), 8.52 (dd, J = 0.9 and 3.0 Hz, 1H), 7.95 (dt, J = 1.2 and 4.8 Hz, 1H), 7.26 (ddd, J = 0.6, 3.0, and 4.8 Hz, 1H), 5.48 (br s, 2H), 2.14 (s, 3H) ppm; ^{13}**C{^{1}H} NMR** (125.7 MHz, CDCl$_3$): δ = 149.1 (CH), 147.2 (CH), 144.2 (C), 134.9 (C), 132.7 (CH), 123.3 (CH), 11.5 (CH$_3$) ppm; **IR** (cm^{-1}): 3372
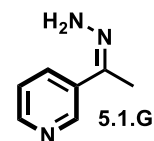
(br m), 3310 (br m), 3205 (br m), 1599 (s, C=N); **HRMS ESI** (m/z): [M+H]$^+$ calcd. for [C$_7$H$_{10}$N$_3$]$^+$, 136.0869; found, 136.0870; yield 46 mg, 71%.

5.1.H (1-phenyl-2-hydrazonopropane).

Characterization data: (Mixture of isomers); **^{1}H NMR** (300 MHz, C$_6$D$_6$): (major isomer) δ = 7.13-6.93 (m, 5H), 4.44 (s br, 2H), 3.42 (s, 2H), 1.19 (s, 3H) ppm; **^{13}C{^{1}H} NMR** (125.7 MHz, C$_6$D$_6$): δ = 149.2 (C), 148.9 (C), 138.7 (C), 136.5 (C), 129.2 (CH), 129.0 (CH), 128.8 (CH), 128.8 (CH), 126.8 (CH), 126.7 (CH), 45.5 (CH$_2$), 35.2 (CH$_2$), 23.8 (CH$_3$), 12.8 (CH$_3$) ppm; **IR** (cm^{-1}): 3350 (br m), 3325 (br m), 1642 (s, C=N), 1601 (s, C=N); **HRMS ESI** (m/z): [M+H]$^+$ calcd. for [C$_9$H$_{13}$N$_2$]$^+$, 149.1073; found, 149.1075; yield: 54 mg, 76%.
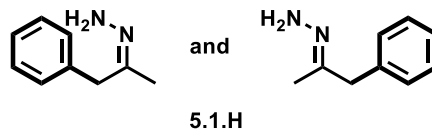
5.1.I (2-hydrazonohexane):

Despite several attempts, the product being very volatile and too unstable, we were unable to isolate the pure product by the standard protocol. Hence, purification was performed by slow evaporation of the crude reaction below 5 °C. **Characterization data: ^{1}H NMR** (500 MHz, C$_6$D$_6$): δ = 4.16 (br s, 2H), 2.00 (br t, J = 7.5 Hz, 2H), 1.32-1.18 (m, 4H), 0.84 (br t, J = 7.5 Hz, 3H) ppm; **^{13}C{^{1}H} NMR** (125.7 MHz, C$_6$D$_6$): δ = 149.6 (C), 38.1 (CH$_2$), 28.6 (CH$_2$), 22.3 (CH$_2$), 13.6 (CH$_3$), 12.6 (CH$_3$) ppm; **IR** measurements could not be obtained; **HRMS ESI** (m/z): [M+H]$^+$ calcd. for [C$_6$H$_{15}$N$_2$]$^+$, 115.1230; found, 115.1230; yield: 22% (NMR yield with internal standard).
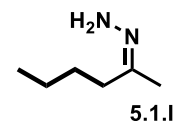
5.2.A (1-phenyl-2-phenylhydrazonoethane).

Characterization data: ^{1}H NMR (300 MHz, C$_6$D$_6$): δ = 7.70 (d, J = 4.8 Hz, 1H), 7.21-7.13 (m, 3H), 7.13-7.10 (m, 4H), 6.84 (t, J = 4.8 Hz, 1H), 6.77 (br s, 1H), 1.41 (s, 3H) ppm; **^{13}C{^{1}H} NMR** (125.7 MHz, C$_6$D$_6$): δ = 145.8 (C), 141.6 (C), 139.6 (C), 129.6 (CH) 128.6 (CH), 128.2 (CH), 125.9 (CH), 120.6 (CH), 113.8 (CH), 11.2 (CH$_3$) ppm; **IR** (cm^{-1}): 3351 (br, NH),
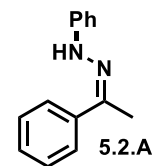
2920 (m), 1599 (vs, C=N); **HRMS ESI** (m/z): [M+H]$^+$ calcd. for [C$_{14}$H$_{15}$N$_2$]$^+$, 211.1230; found, 211.1228; yield: 81 mg, 80%.

5.2.B (1-phenyl-2,2-dimethylhydrazonoethane).

Characterization data: ^{1}H NMR (300 MHz, CDCl$_3$): δ = 7.75-7.72 (m, 2H), 7.37-7.35 (m, 3H), 2.6 (s, 6H), 2.36 (s, 3H) ppm; **^{13}C{^{1}H} NMR** (125.7 MHz, CDCl$_3$): δ = 162.2 (C), 139.3 (C), 129.4 (CH), 128.4 (CH), 126.5 (CH), 47.4 (CH$_3$), 15.7 (CH$_3$) ppm; **IR** (cm^{-1}): 2954 (m, NMe$_2$), 2855 (m, NMe$_2$), 1607 (m, C=N); **HRMS ESI** (m/z): [M+H]$^+$ calcd. for [C$_{10}$H$_{15}$N$_2$]$^+$, 163.1230; found, 163.1230; yield: 72 mg, 92%.
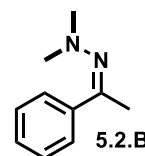
5.2.C (N-(1-phenylethylidene)-benzenamine).

Characterization data: ^{1}H NMR (300 MHz, C$_6$D$_6$): δ = 7.95-7.93 (m, 2H), 7.19-7.12 (m, 5H), 6.93 (t, *J* = 4.5 Hz, 1H), 6.75-6.73 (m, 2H), 1.81 (s, 3H) ppm; **^{13}C{^{1}H} NMR** (125.7 MHz, C$_6$D$_6$): δ = 164.4 (C), 152.6 (C), 152.2 (C), 139.9 (CH), 130.5 (CH), 129.3 (CH), 128.1 (CH), 127.7 (CH), 123.3 (CH), 119.7 (CH), 16.8 (CH$_3$) ppm; **IR** (cm^{-1}): 1600 (vs, C=N); **HRMS ESI** (m/z): [M+H]$^+$ calcd. for [C$_{16}$H$_{17}$N$_2$]$^+$, 196.1121; found, 196.1117; yield: 73 mg, 78%.
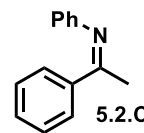
5.2.D (*N-(1-phenylethylidene)-1-propanamine*).

Characterization data: ^{1}H NMR (300 MHz, C$_6$D$_6$): δ = 7.94-7.91 (m, 2H), 7.22-7.19 (m, 2H 3.24), 7.19-7.15 (m, 1H), (t, *J* = 6.9 Hz, 2H), 1.80 (sex, *J* = 7.2 Hz, 2H), 1.74 (s, 3H), 1.04 (t, *J* = 7.5 Hz, 3H) ppm; **^{13}C{^{1}H} NMR** (125.7 MHz, C$_6$D$_6$): δ = 163.2 (C), 141.6 (C), 129.4 (CH),128.4 (CH), 127.0 (CH), 54.0 (CH$_2$), 24.9 (CH$_2$), 14.5 (CH$_3$), 12.5 (CH$_3$) ppm; **IR** (cm^{-1}): 1633 (s, C=N); **HRMS ESI** (m/z): [M+H]$^+$ calcd. for [C$_{11}$H$_{16}$N]$^+$, 162.1277; found, 162.1276; yield: 67 mg, 86%.
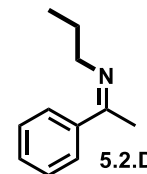
5.3.A (1,2-bis-[1-phenylethylidene]hydrazine).

Characterization data: **^{1}H NMR** (300 MHz, C$_6$D$_6$): δ = 7.94-7.92 (m, 4H), 7.21-7.15 (m, 6H), 2.16 (s, 3H) ppm; **^{13}C{^{1}H} NMR** (125.7 MHz, C$_6$D$_6$): δ = 158.4 (C), 139.2 (C), 129.7 (CH), 128.5 (CH), 127.1 (CH), 14.8 (CH$_3$) ppm; **IR** (cm^{-1}): 1603 (s, C=N); **HRMS ESI** (m/z): [M+H]$^+$ calcd. for [C$_{16}$H$_{17}$N$_2$]$^+$, 237.1386; found, 237.1385; yield: 52 mg, 92%.
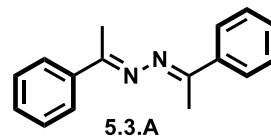
5.3.B (1,2-bis-[1-(4-methoxyphenyl)ethylidene]hydrazine).

Characterization data: **^{1}H NMR** (500 MHz, C$_6$D$_6$): δ = 7.93 (d, J = 9 Hz, 2H), 6.83 (d, J = 9 Hz), 3.30 (s, 6H), 2.31 (s, 6H) ppm; **^{13}C{^{1}H} NMR** (125.7 MHz, CDCl$_3$): δ = 161.4 (C), 158.6 (C), 132.1 (C), 128.6 (CH), 114.0 (CH), 54.8 (CH$_3$), 14.7 (CH$_3$) ppm; **HRMS ESI** (m/z): [M+H]$^+$ calcd. for [C$_{18}$H$_{21}$N$_2$O$_2$]$^+$, 297.1598; found, 297.1597; yield: 63 mg, 89%.
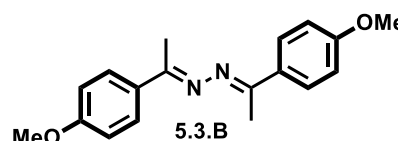
5.3.C (1,2-bis-[1-(4-bromophenyl)ethylidene]hydrazine).

Characterization data: **^{1}H NMR** (300 MHz, C$_6$D$_6$): δ = 7.52 (d, J = 8.7 Hz, 4H), 7.32 (d, J = 8.7 Hz, 4H), 1.97 (s, 6H) ppm; **^{13}C{^{1}H} NMR** (125.7 MHz, C$_6$D$_6$): δ = 158.1 (C), 137.5 (C), 131.8 (CH), 128.6 (CH), 124.6 (C), 14.6 (CH$_3$) ppm; **IR** (cm^{-1}): 2276 (s), 1618 (m); HRMS ESI (m/z): [M+H]$^+$ calcd. for [C$_{16}$H$_{15}$Br$_2$N$_2$]$^+$, 392.9597; found, 392.9596; yield: 80 mg, 85%.
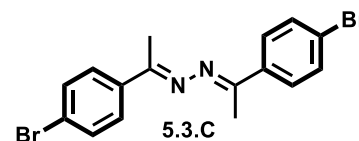
5.3.D (1,2-bis-[1-(2-aminophenyl)ethylidene]hydrazine).

Characterization data: ^{1}H NMR (300 MHz, C$_6$D$_6$): δ = 7.34 (dd, J = 0.9 and 4.8 Hz, 2H), 7.08 (td, J = 0.9 Hz and 4.5 Hz, 2H), (td, J = 0.9 and 4.5 Hz, 2H), 6.42 (dd, J = 0.9 and 4.8 Hz, 2H), 5.99 (br s, 4H), 2.13 (s, 3H) ppm; **^{13}C{^{1}H} NMR** (125.7 MHz, C$_6$D$_6$): δ = 162.2 (C), 148.64 (C), 130.6 (CH), 130.0 (CH), 119.4 (C), 116.8 (CH), 116.2 (CH), 15.8 (CH$_3$) ppm; **IR** (cm^{-1}): 3352 (sb), 1613 (s, C=N), 1565 (s); **HRMS ESI** (m/z): [M+H]$^+$ calcd. for [C$_{16}$H$_{19}$N$_4$]$^+$, 267.1604; found, 267.1607; yield: 58 mg, 90%.
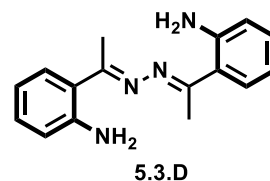
5.4.A ([1-(4-methoxyphenyl)-2-(1-phenyl)]ethylidenehydrazine).

Characterization data: (1:1 mixture of isomers); **^{1}H NMR** (300 MHz, CDCl$_3$): δ = 7.42-7.41 (m, 3 H), 6.96-6.93 (m, 2H), 3.86 (s, 3H), 2.34-2.31 (m, 6H) ppm; **^{13}C{^{1}H} NMR** (125.7 MHz, CDCl$_3$): δ = 161.0 (C), 161.0 (C), 158.1 (C), 158.0 (C), 157.8 (C), 157.8 (C), 138.8 (C), 138.6 (C), 128.5 (C), 128.5 (C), 128.3 (CH), 128.2 (CH), 126.8 (CH), 126.8 (CH), 113.8 (CH), 113.8 (CH), 55.5 (CH$_3$), 15.2 (CH$_3$), 15.1 (CH$_3$), 15.0 (CH$_3$), 15.0 (CH$_3$) ppm; **IR** (cm^{-1}): 3060 (m), 3026 (m), 1636 (vs, C=N), 1592 (vs); **HRMS ESI** (m/z): [M+H]$^+$ calcd. for [C$_{17}$H$_{19}$N$_2$O]$^+$, 267.1492; found, 267.1490; yield: 103 mg, 81%.
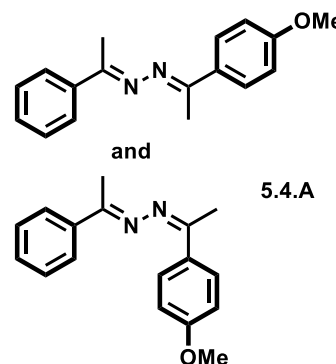
5.4.B ([1-(4-fluorophenyl)-2-(1-phenyl)]ethylidenehydrazine).

Characterization data: (1:1 mixture of isomers), **M.P.**: 116-118 °C; **^{1}H NMR** (500 MHz, CDCl$_3$): δ = 7.93-7.90 (m, 4H), 7.45-7.43 (m, 3H), 7.13-7.09 (m, 2H), 2.3 (m, 6H) ppm; **^{13}C{^{1}H} NMR** (125.7 MHz, CDCl$_3$): δ = 164.9 (C), 164.9 (C), 162.9 (C), 162.9 (C), 158.1 (d, $^1J_{CF}$ = 242 Hz, C), 157.5 (d, $^1J_{CF}$ = 242 Hz, C), 138.5 (C), 138.5 (C), 134.7 (d, $^4J_{CF}$ = 12.5 Hz, C), 134.7 (d, $^4J_{CF}$ = 12.5 Hz, C), 129.8 (CH), 129.8 (CH), 128.7 (d, $^2J_{CF}$ = 33.5 Hz, CH), 128.6 (d,
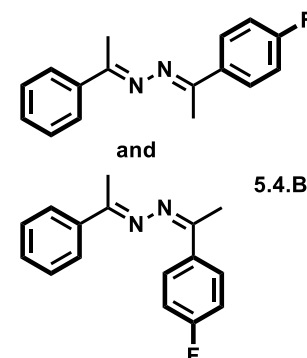
$^2J_{CF}$ = 33.5 Hz, CH), 128.5 (CH), 126.7 (CH), 126.7 (CH), 115.4 (d, $^3J_{CF}$ = 86 Hz, CH), 115.4 (d, $^3J_{CF}$ = 86

Hz, CH), 15.2 (CH$_3$), 15.2 (CH$_3$), 15.2 (CH$_3$), 15.2 (CH$_3$) ppm; ^{19}F{^{1}H} NMR (282 MHz, CDCl$_3$): δ = -

111.5 (m, C-F), -111.6 (m, C-F) ppm; IR (cm^{-1}): 1605 (vs, C=N), 1577 (s); HRMS ESI (m/z): [M+H]$^+$

calcd. for [C$_{16}$H$_{15}$FN$_2$]$^+$, 255.1292; found, 255.1294; yield: 92 mg, 76%.

5.4.C ([1-(4-butylphenyl)-2-(1-phenyl)]ethylidenehydrazine).

Characterization data: (1:1 mixture of isomers); ^{1}**H NMR** (300 MHz,

C$_6$D$_6$): δ = 7.84-7.81 (m, 2H), 7.78-7.76 (m, 2H), 7.34-7.31 (m, 3H), 7.15-

7.13 (m, 2H), 2.56 (t, J = 7.5 Hz, 2H), 2.23-2.22 (m, 6H), 1.54 (quin, J = 7.5

Hz, 2 H), 1.28 (sex, J = 7.5 Hz, 2H), 0.85 (t, J = 7.5 Hz, 3H) ppm; ^{13}C{^{1}H}

NMR (125.7 MHz, C$_6$D$_6$): 157.9 (C), 157.8, (C), 157.8 (C), 157.8 (C), 144.9

(C), 144.8 (C), 138.6 (C), 138.5 (C), 136.1 (C), 136.0 (C), 129.7 (CH), 129.7
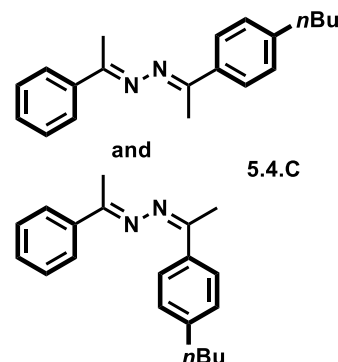
(CH), 128.5 (CH), 128.5 (CH), 128.5 (CH), 128.4 (CH), 126.7 (CH), 126.7 (CH), 126.7 (CH), 126.7 (CH),

35.6 (CH$_2$), 33.6 (CH$_2$), 22.5 (CH$_2$), 15.2 (CH$_3$), 15.2 (CH$_3$), 15.1 (CH$_3$), 15.1 (CH$_3$), 14.1 (CH$_3$) ppm; IR

(cm^{-1}): 2956 (m), 2927 (m), 1604 (s, C=N), 1565 (s); HRMS ESI (m/z): [M+H]$^+$ calcd. for [C$_{20}$H$_{25}$N$_2$]$^+$,

293.2012; found, 293.2012; yield 119 mg, 85%.

5.4.D ([1-(2-methoxyphenyl)-2-(1-phenyl)]ethylidenehydrazine).

Characterization data: (Mixture of isomers); **M. P.**, 108-110 º C; ^{1}**H NMR**

(300 MHz, CDCl$_3$): δ = 7.95-7.92 (m, 2H), 7.58-7.56 (m, 1H), 7.47-7.43 (m, 2H),

7.40-7.37 (m, 1H), 7.05-6.96 (m, 2H), 3.89 (s, 3H), 2.35-2.25 (m, 6H) ppm;

^{13}C{^{1}H} NMR (125.7 MHz, CDCl$_3$): δ = 159.5 (C), 158.7 (C), 157.8 (C), 157.7

(C), 157.0 (C), 157.0 (C), 138.6 (C), 138.6 (C), 138.6 (C), 138.6 (C), 130.3 (CH),

130.2 (CH), 129.7 (CH), 129.7 (CH), 129.6 (CH), 129.6 (CH), 128.5 (CH), 128.4

(CH), 126.7 (CH), 120.8 (CH), 120.8 (CH), 111.3 (CH), 111.3 (CH), 55.6 (CH$_3$), 55.6 (CH$_3$), 19.1 (CH$_3$),

18.9 (CH$_3$), 15.2 (CH$_3$), 15.0 (CH$_3$) ppm; **IR** (cm^{-1}): 1604 (s, C=N); **HRMS ESI** (m/z): [M+H]$^+$ calcd. for [C$_{17}$H$_{19}$N$_2$O]$^+$, 267.1492; found, 267.1491; yield: 92 mg 72%.

5.7   Acknowledgements

5.8   References

(1)   Belowich, M. E.; Stoddart, J. F. Dynamic Imine Chemistry. *Chem. Soc. Rev.* **2012**, *41*, 2003–2024.

(2)   Morales, S.; Guijarro, F. G.; García Ruano, J. L.; Cid, M. B. A General Aminocatalytic Method for the Synthesis of Aldimines. *J. Am. Chem. Soc.* **2014**, *136*, 1082–1089.

(3)   Gooßen, L. J.; Huang, L.; Arndt, M.; Gooßen, K.; Heydt, H. Late Transition Metal-Catalyzed Hydroamination and Hydroamidation. *Chem. Rev.* **2015**, *115*, 2596–2697.

(4)   Klinkenberg, J. L.; Hartwig, J. F. Catalytic Organometallic Reactions of Ammonia. *Angew. Chem. Int. Ed.* **2011**, *50*, 86–95.

(5)   Müller, T. E.; Hultzsch, K. C.; Yus, M.; Foubelo, F.; Tada, M. Hydroamination: Direct Addition of Amines to Alkenes and Alkynes. *Chem. Rev.* **2008**, *108*, 3795–3892.

(6)   Johns, A. M.; Sakai, N.; Ridder, A.; Hartwig, J. F. Direct Measurement of the Thermodynamics of Vinylarene Hydroamination. *J. Am. Chem. Soc.* **2006**, *128*, 9306–9307.

(7)   Beller, M.; Breindl, C.; Eichberger, M.; Hartung, C. G.; Seayad, J.; Thiel, O. R.; Tillack, A.; Trauthwein, H. Advances and Adventures in Amination Reactions of Olefins and Alkynes. *Synlett* **2002**, *10*, 1579–1594.

(8)   Senn, H. M.; Blöchl, P. E.; Togni, A. Toward an Alkene Hydroamination Catalyst: Static and Dynamic Ab Initio DFT Studies. *J. Am. Chem. Soc.* **2000**, *122*, 4098–4107.

(9)   Loritsch, J. A.; Vogt, R. R. The Addition of Aryl Amines to Alkynes. *J. Am. Chem. Soc.* **1939**, *61*, 1462–1463.

(10)   Suminov, S. I.; Kost, A. N. Nucleophilic Addition of Amino-Groups to an Activated Carbon–Carbon

Double Bond. *Russ. Chem. Rev.* **1969**, *38*, 884–899.

(11) Müller, T. E.; Berger, M.; Grosche, M.; Herdtweck, E.; Schmidtchen, F. P. Palladium-Catalyzed Cyclization of 6-Aminohex-1-Yne. *Organometallics* **2001**, *20*, 4384–4393.

(12) Utimoto, K. Palladium Catalyzed Synthesis of Heterocycles. *Pure Appl. Chem.* **1983**, *55*, 1845–1852.

(13) Walsh, P. J.; Baranger, A. M.; Bergman, R. G. Stoichiometric and Catalytic Hydroamination of Alkynes and Allene by Zirconium Bisamides Cp2Zr(NHR)2. *J. Am. Chem. Soc.* **1992**, *114*, 1708–1719.

(14) McGrane, P. L.; Jensen, M.; Livinghouse, T. Intramolecular [2+2] Cycloadditions of Group IV Metal-Imido Complexes. Applications to the Synthesis of Dihydropyrrole and Tetrahydropyridine Derivatives. *J. Am. Chem. Soc.* **1992**, *114*, 5459–5460.

(15) Hong, S.; Marks, T. J. Organolanthanide-Catalyzed Hydroamination. *Acc. Chem. Res.* **2004**, *37*, 673–686.

(16) Müller, T. E.; Beller, M. Metal-Initiated Amination of Alkenes and Alkynes. *Chem. Rev.* **1998**, *98*, 675–703.

(17) Pohlki, F.; Doye, S. The Catalytic Hydroamination of Alkynes. *Chem. Soc. Rev.* **2003**, *32*, 104–114.

(18) Kawatsura, M.; Hartwig, J. F. Palladium-Catalyzed Intermolecular Hydroamination of Vinylarenes Using Arylamines. *J. Am. Chem. Soc.* **2000**, *122*, 9546–9547.

(19) Åkermark, B.; Bäckvall, J. E.; Hegedus, L. S.; Zetterberg, K.; Siirala-Hansén, K.; Sjöberg, K. Palladium-Promoted Addition of Amines to Isolated Double Bonds. *J. Organomet. Chem.* **1974**, *72*, 127–138.

(20) Hartwig, J. F. Recent Advances in Palladium- and Nickel- Catalyzed Chemistry Provide New Ways to Construct C-N and C-O Bonds. *Angew. Chem. Int. Ed.* **1998**, *37*, 2046–2067.

(21) Utimoto, K.; Miwa, H.; Nozaki, H. Palladium-Catalyzed Synthesis of Pyrroles. *Tetrahedron Lett.* **1981**, *22*, 4277–4278.

(22) Corma, A.; Leyva-Pérez, A.; Sabater, M. J. Gold-Catalyzed Carbon-Heteroatom Bond-Forming Reactions. *Chem. Rev.* **2011**, *111*, 1657–1712.

(23) Gorin, D. J.; Toste, F. D. Relativistic Effects in Homogeneous Gold Catalysis. *Nature* **2007**, *446*, 395–403.

(24) Fukuda, Y.; Utimoto, K.; Nozaki, H. Preparation of 2,3,4,5-Tetrahydropyridines from 5-Alkynylamines under the Catalytic Action of Au(III). *Heterocycles* **1987**, *25*, 205–212.

(25) Widenhoefer, R. A.; Han, X. Gold-Catalyzed Hydroamination of C-C Multiple Bonds. *European J. Org. Chem.* **2006**, , 4555–4563.

(26) Bender, C. F.; Widenhoefer, R. A. Room Temperature Hydroamination of N-Alkenyl Ureas Catalyzed by a Gold(I) N-Heterocyclic Carbene Complex. *Org. Lett.* **2006**, *8*, 5303–5305.

(27)   Han, X.; Widenhoefer, R. A. Gold(I)-Catalyzed Intramolecular Hydroamination of Alkenyl Carbamates. *Angew. Chem. Int. Ed.* **2006**, *45*, 1747–1749.

(28)   Kinder, R. E.; Zhang, Z.; Widenhoefer, R. A. Intermolecular Hydroamination of Allenes with N-Unsubstituted Carbamates Catalyzed by a Gold(I) N-Heterocyclic Carbene Complex. *Org. Lett.* **2008**, *10*, 3157–3159.

(29)   Lavallo, V.; Frey, G. D.; Kousar, S.; Donnadieu, B.; Bertrand, G. Allene Formation by Gold Catalyzed Cross-Coupling of Masked Carbenes and Vinylidenes. *Proc. Natl. Acad. Sci.* **2007**, *104*, 13569–13573.

(30)   Lavallo, V.; Frey, G. D.; Donnadieu, B.; Soleilhavoup, M.; Bertrand, G. Homogeneous Catalytic Hydroamination of Alkynes and Allenes with Ammonia. *Angew. Chem. Int. Ed.* **2008**, *47*, 5224–5228.

(31)   Werner, A. Beitrag Zur Konstitution Anorganischer Verbindungen. *Zeitschrift für Anorg. Chemie* **1893**, *3*, 267–330.

(32)   Van der Vlugt, J. I. Advances in Selective Activation and Application of Ammonia in Homogeneous Catalysis. *Chem. Soc. Rev.* **2010**, *39*, 2302–2322.

(33)   Klinkenberg, J. L.; Hartwig, J. F. Catalytic Organometallic Reactions of Ammonia. *Angew. Chem. Int. Ed.* **2011**, *50*, 86–95.

(34)   Zeng, X.; Soleilhavoup, M.; Bertrand, G. Gold-Catalyzed Intermolecular Markovnikov Hydroamination of Allenes with Secondary Amines. *Org. Lett.* **2009**, *11*, 3166–3169.

(35)   Zeng, X.; Frey, G. D.; Kinjo, R.; Donnadieu, B.; Bertrand, G. Synthesis of a Simplified Version of Stable Bulky and Rigid Cyclic (Alkyl)(Amino)Carbenes, and Catalytic Activity of the Ensuing Gold(I) Complex in the Three-Component Preparation of 1,2-Dihydroquinoline Derivatives. *J. Am. Chem. Soc.* **2009**, *131*, 8690–8696.

(36)   Seo, H.; Roberts, B. P.; Abboud, K. A.; Merz, K. M.; Hong, S. Novel Acyclic Diaminocarbene Ligands with Increased Steric Demand and Their Application in Gold Catalysis. *Org. Lett.* **2010**, *12*, 4860–4863.

(37)   Dash, C.; Shaikh, M. M.; Butcher, R. J.; Ghosh, P. Highly Convenient Regioselective Intermolecular Hydroamination of Alkynes Yielding Ketimines Catalyzed by Gold(I) Complexes of 1,2,4-Triazole Based N-Heterocyclic Carbenes. *Inorg. Chem.* **2010**, *49*, 4972–4983.

(38)   Liu, L. J.; Wang, F.; Wang, W.; Zhao, M. X.; Shi, M. Synthesis of Chiral Mono(N-Heterocyclic Carbene) Palladium and Gold Complexes with a 1,1'-Biphenyl Scaffold and Their Applications in Catalysis. *Beilstein J. Org. Chem.* **2011**, *7*, 555–564.

(39)   Morozov, O. S.; Lunchev, A. V.; Bush, A. A.; Tukov, A. A.; Asachenko, A. F.; Khrustalev, V. N.; Zalesskiy, S. S.; Ananikov, V. P.; Nechaev, M. S. Expanded-Ring N-Heterocyclic Carbenes Efficiently Stabilize Gold(I) Cations, Leading to High Activity in π-Acid-Catalyzed Cyclizations. *Chem. Eur. J.* **2014**, *20*, 6162–6170.

(40)   Seo, H.; Snead, D. R.; Abboud, K. A.; Hong, S. Bulky Acyclic Aminooxycarbene Ligands. *Organometallics* **2011**, *30*, 5725–5730.

(41) Weber, S. G.; Zahner, D.; Rominger, F.; Straub, B. F. Mechanistic Investigations of a Stable, Highly Active, Extremely Sterically Shielded Molecular Gold Catalyst. *ChemCatChem* **2013**, *5*, 2330–2335.

(42) Schaper, L. A.; Wei, X.; Hock, S. J.; Pöthig, A.; Öfele, K.; Cokoja, M.; Herrmann, W. A.; Kühn, F. E. Gold(I) Complexes with "Normal" 1,2,3-Triazolylidene Ligands: Synthesis and Catalytic Properties. *Organometallics* **2013**, *32*, 3376–3384.

(43) Tolentino, D. R.; Jin, L.; Melaimi, M.; Bertrand, G. Mesoionic Carbene-Gold(I) Catalyzed Bis-Hydrohydrazination of Alkynes with Parent Hydrazine. *Chem. Asian J.* **2015**, *10*, 2139–2142.

(44) Chen, J. P.; Lim, L. L. Key Factors in Chemical Reduction by Hydrazine for Recovery of Precious Metals. *Chemosphere* **2002**, *49*, 363–370.

(45) Heaton, B. T.; Jacob, C.; Page, P. Transition Metal Complexes Containing Hydrazine and Substituted Hydrazines. *Coord. Chem. Rev.* **1996**, *154*, 193–229.

(46) Schirmann, J.-P.; Bourdauducq, P. Hydrazine. *Ullmann's Encyclopedia of Industrial Chemistry*; Major Reference Works; 2001.

(47) Lundgren, R. J.; Stradiotto, M. Palladium-Catalyzed Cross-Coupling of Aryl Chlorides and Tosylates with Hydrazine. *Angew. Chem. Int. Ed.* **2010**, *49*, 8686–8690.

(48) Kinjo, R.; Donnadieu, B.; Bertrand, G. Gold-Catalyzed Hydroamination of Alkynes and Allenes with Parent Hydrazine. *Angew. Chem. Int. Ed.* **2011**, *50*, 5560–5563.

(49) López-Gómez, M. J.; Martin, D.; Bertrand, G. Anti-Bredt N-Heterocyclic Carbene: An Efficient Ligand for the Gold(I)-Catalyzed Hydroamination of Terminal Alkynes with Parent Hydrazine. *Chem. Commun.* **2013**, *49*, 4483–4585.

(50) Manzano, R.; Wurm, T.; Rominger, F.; Hashmi, A. S. K. Room-Temperature Hydrohydrazination of Terminal Alkynes Catalyzed by Saturated Abnormal n-Heterocyclic Carbene-Gold(I) Complexes. *Chem. Eur. J.* **2014**, *20*, 6844–6848.

(51) Yazdani, S.; Junor, G. P.; Peltier, J. L.; Gembicky, M.; Jazzar, R.; Grotjahn, D. B.; Bertrand, G. Influence of Carbene and Phosphine Ligands on the Catalytic Activity of Gold Complexes in the Hydroamination and Hydrohydrazination of Alkynes. *ACS Catal.* **2020**, *10*, 5190–5201.

(52) Heininger, S. A. Cupric Acetate Catalyzed Monocyanoethylation of Aromatic Amines. *J. Org. Chem.* **1957**, *22*, 1213–1217.

(53) Müller, T. E.; Grosche, M.; Herdtweck, E.; Pleier, A. K.; Walter, E.; Yan, Y. K. Developing Transition-Metal Catalysts for the Intramolecular Hydroamination of Alkynes. *Organometallics* **2000**, *19*, 170–183.

(54) Krasnova, L. B.; Hein, J. E.; Fokin, V. V. Synthesis of 7-Aza-5-Deazapurine Analogues via Copper(I)-Catalyzed Hydroamination of Alkynes and 1-Iodoalkynes. *J. Org. Chem.* **2010**, *75*, 8662–8665.

(55) Tokimizu, Y.; Ohta, Y.; Chiba, H.; Oishi, S.; Fujii, N.; Ohno, H. Direct Synthesis of Highly Fused Perimidines by Copper(I)-Catalyzed Hydroamination of 2-Ethynylbenzaldehydes. *Tetrahedron*

2011, *67*, 5168–5175.

(56)   Pouy, M. J.; Delp, S. A.; Uddin, J.; Ramdeen, V. M.; Cochrane, N. A.; Fortman, G. C.; Gunnoe, T. B.; Cundari, T. R.; Sabat, M.; Myers, W. H. Intramolecular Hydroalkoxylation and Hydroamination of Alkynes Catalyzed by Cu(I) Complexes Supported by N-Heterocyclic Carbene Ligands. *ACS Catal.* **2012**, *2*, 2182–2193.

(57)   Chen, D. S.; Zhang, M. M.; Li, Y. L.; Liu, Y.; Wang, X. S. Copper(I)-Catalyzed Synthesis of 1-Arylpyrazolo[5,1-b]Quinazolin-9(1H)-One via Intramolecular Alkyne Hydroamination. *Tetrahedron* **2014**, *70*, 2889–2893.

(58)   Zhou, L.; Bohle, D. S.; Jiang, H. F.; Li, C. J. Synthesis of Propargylamines by a Copper-Catalyzed Tandem Anti-Markovnikov Hydroamination and Alkyne Addition. *Synlett* **2009**, *6*, 937–940.

(59)   Bahri, J.; Jamoussi, B.; Van Der Lee, A.; Taillefer, M.; Monnier, F. Copper-Catalyzed Hydroamination of Alkynes with Aliphatic Amines: Regioselective Access to (1 E,3 E)-1,4-Disubstituted-1,3-Dienes. *Org. Lett.* **2015**, *17*, 1224–1227.

(60)   Daniel W. Robbins, J. F. H. A Simple, Multidimensional Approach to High-Throughput Discovery of Catalytic Reactions. *Science* **2011**, *333*, 1423–1427.

(61)   Shi, S. L.; Buchwald, S. L. Copper-Catalysed Selective Hydroamination Reactions of Alkynes. *Nat. Chem.* **2015**, *7*, 38–44.

(62)   Jin, L.; Tolentino, D. R.; Melaimi, M.; Bertrand, G. Isolation of Bis(Copper) Key Intermediates in Cu-Catalyzed Azide-Alkyne "click Reaction. *Sci. Adv.* **2015**, *1*, e1500304.

(63)   Jurkauskas, V.; Sadighi, J. P.; Buchwald, S. L. Conjugate Reduction of α,β-Unsaturated Carbonyl Compounds Catalyzed by a Copper Carbene Complex. *Org. Lett.* **2003**, *5*, 2417–2420.

(64)   Gómez-Suárez, A.; Ramón, R. S.; Songis, O.; Slawin, A. M. Z.; Cazin, C. S. J.; Nolan, S. P. Influence of a Very Bulky N- Heterocyclic Carbene in Gold-Mediated Catalysis. *Organometallics* **2011**, *30*, 5463–5470.

(65)   Gómez-Suárez, A.; Nelson, D. J.; Nolan, S. P. Quantifying and Understanding the Steric Properties of N-Heterocyclic Carbenes. *Chem. Commun.* **2017**, *53*, 2650–2660.

(66)   Anderson, L. L.; Arnold, J.; Bergman, R. G. Proton-Catalyzed Hydroamination and Hydroarylation Reactions of Anilines and Alkenes: A Dramatic Effect of Counteranions on Reaction Efficiency. *J. Am. Chem. Soc.* **2005**, *127*, 14542–14543.

Chapter 6 – Concluding Remarks

6.1 Twisting Carbon to Behave like a Metal

Despite Lewis basic carbenes monopolizing the field of carbene catalysis, we challenged this prevailing paradigm. To achieve this, we capitalized on the intrinsic properties of ambiphilic carbenes to mimic transition metals. Specifically, we targeted the valorization of carbon monoxide, a molecule known for its stability thereby inhibiting its transformation.

To overcome this significant hurdle, we investigated the use of CAACs which are known to activate CO and generate (amino)ketenes. By exploring the reactivity of these (amino)ketenes, we have shown that they are capable of undergoing [4+2] reactions with *ortho*-quinones to form cyclic carbonates. However, we faced the difficulty of eliminating the product from our carbene catalyst. Drawing further on the parallel with transition metal catalysts, we exploited the use of a bulky CAAC with a sterically encumbered menthyl substituent to introduce significant congestion at the carbene center and trigger the release of the product through reductive elimination. To engender a catalytic system, we developed a stepwise mechanistic pathway and achieved the catalytic carbonylation of quinones as a proof-of-concept. This fundamental investigation of CAAC-catalyzed carbonylation reactions of *ortho*-quinones paves the way for the future developments of carbon centered catalysts that could one day lead to transformations that are divergent from metal catalysts.

It is reasonable to envisage that more ambiphilic carbenes, such as CAACs, will provide a strong foundation for understanding the mechanisms of these processes. However, the challenge of reductive elimination, which we have seen with CAACs, will likely plague the development of highly active catalysts based on these carbenes. Therefore, using our principles it is likely that less basic carbenes will lead to state-of-the-art carbene-catalysts. While the initial focus on the advancement of carbene technology has been on new electronic properties, the next wave will most likely involve intense research effort into carefully designed sterically bulky systems for improved organocatalysis.

6.2 (CAAC)Copper-Amides: Replacing Heavy Metal Phosphors

We have shown that an easily overlooked, but serendipitous, optical phenomenon, such as triboluminescence, can led to an investigation into photoluminescent dicoordinate copper species. Eventually, my natural curiosity blossomed into a collaboration with the Thompson group (USC). Together, we discovered that the sterics of these dicoordinate $(CAAC)Cu(NR_2)$ systems proved vital in slowing down nonradiative decay.

Although the $^{Menth}CAAC$ component turned out to be critical, further investigation revealed that a carbazolide type ligand was the ideal partner. This system facilitated emission that was tunable across the visible spectrum, had high Φ_{PL} (up to unity) in non-rigid media, and led to extremely fast radiative lifetimes. By altering the sterics of the CAAC, we experimentally demonstrated the importance of a coplanar ligand conformation thereby supplanting the RASI mechanism. Unlike heavy metals that rely on metal-to-ligand charge transfer, we discovered that the key to having an active photoluminescent copper species was in fact to have minimal participation of the metal. Instead, a combination of a strong π-donor with a strong π-acid led to ligand-to-ligand charge transfer. This process was facilitated by copper which acted as an electronic bridge through the metal d-orbitals. Therefore, we have designed copper(I) complexes with photophysical properties that are competitive with state-of-the-art heavy metal phosphors.

While these studies have already led to several rapid advancements, such as in white organic light emitting diodes (WOLEDs) to make more efficient ambient lighting, another avenue for investigation is to improve the all copper based emissive layer. Although our all copper emissive layer for the corresponding OLED devices featured $(CAAC)Cu-C_6F_5$ as the host, unfortunately it led to rapid roll-off. However, given the highly tunable nature of carbenes, a less π-acidic carbene with a higher LUMO and a more donating amide type ligand for a lower HOMO could provide a high energy emitter that would serve as an ideal host. Therefore, this would aid in overcoming the typical challenges of finding high energy hosts for blue light emitting devices.

6.3   Absolute Templating of Active Clusters in Metal Replacement

Despite galvanic exchange's broad potential, it remains primarily used in materials. Interestingly, nanoclusters have broadly displayed anti-galvanic exchange (AGR). Therefore, we demonstrated that AGR results from the lack of stable active metal clusters and the lack of strong M^0 character in existing ones. In part, this can be attributed to weak metal-metal interactions and the lower half-cell potential of active metals, which tends to result in ill-defined, polydisperse mixtures thus complicating their isolation. Upon taking advantage of the enhanced stability imparted by CAACs, we provided a rationale for the absolute templating of group 11 trinuclear M^0M^I clusters by means of galvanic exchange. During this work, extremely rare examples of copper and silver nanoclusters featuring predominantly M^0 character were isolated and used to engage in the metal replacement technique analogous to nanomaterials. By exploiting this technology, we completed the family of group 11 clusters which feature the same morphology, formal oxidation state, and ligands for the first time. Moreover, drawing on a parallel with known M(111) surfaces, we demonstrated that copper is unique among coinage metals in that it can transform CO_2, a greenhouse gas, into CO. Altogether, this work served to further bridge a gap between homogenous and heterogenous systems.

Following this study, future work could involve two different directions. One would be to design new more active metal clusters, such as the synthesis of a more active iron cluster, to test the limits of our strategy. Another pathway would be to target larger systems with a higher metal to ligand ratio that would still feature a large amount of M^0 character. In fact, I have already prepared a novel polynuclear (Cu = 5) CAAC copper chalcogenide precursor that could easily be reduced with diboron to investigate this future direction.

Furthermore, our use of boron-based reagents led to the divergent synthesis of a novel carbene copper hydride nanocluster. Stryker's reagent, a triphenylphosphine ligated Cu-H hexamer, has found broad usefulness as reducing agents in many organic transformations including catalytic conjugate addition reactions with α,β-unsaturated carbonyl compounds. Therefore, our discovery of the first atomically precise

carbene stabilized copper(I) hydride nanocluster, $[(Et_2CAAC)_6Cu_{14}H_{12}][BF_4]_2$, warrants investigation into its use in organic transformations.

6.4   Copper Ancillary Ligand Free Hydrohydrazination: Replacing Gold Complexes

Unarguably, significant research effort has focused on the use of carbenes to guide synthetic targets and catalytic reactions. In that regard, numerous reports have emphasized the need for carbene ligands to activate and stabilize heavy metals for the difficult catalytic hydrohydrazination of alkynes using the parent hydrazine. The reliance on these types of ligands stems from the many challenges associated with the use of the parent hydrazine (*e.g.*, it tends to lead to inert Werner complexes and inactive M^0 nanoparticles) which prevents efficient catalytic activity by poisoning the metal catalyst. Suspecting that existing carbene copper catalysts could be overengineered, I explored the activity of copper catalysts with and without ancillary carbenes. Unlike transformations involving gold catalysts which depend on a ligand, I unambiguously demonstrated that readily available copper salts such (CuCl) could perform ligand less in these challenging processes. Inevitably, the impact of this investigation questions the very foundations upon which we rest our scientific assumptions and supports the questioning of our initial postulates.

The purpose of ligands in catalysis is to lower the activation barrier for the transformation of substrates into products. With an appropriately designed ligand, reactions that could not be achieved under ambient conditions become feasible. In that regard, a ligand-free catalytic system does not diminish the impact of ligands in these processes. On the contrary, it emphasizes the need for the development of carefully designed ligand motifs. For example, I have shown that the ligand less catalytic systems require harsh conditions to proceed, but through an ancillary carbene ligand, milder reaction conditions are on the horizon. In fact, it is conceivable that with the appropriate carbenoid type ligand, presumably one that is extremely ambiphilic, copper could catalyze more challenging substrates such as ammonia. Therefore, this study supports the very foundation of this dissertation: carbenes as powerful tools.